



UNIVERSITY OF  
LIVERPOOL

**MAXIMISING THE UTILISATION OF TI-6AL-4V METAL POWDER IN THE  
SELECTIVE LASER MELTING PROCESS**

Thesis submitted in accordance with the requirements of  
the University of Liverpool for the degree of  
Doctor of Philosophy

by

**Robert Colin Williams**

School of Engineering  
The University of Liverpool

Submission Date: October 2021

## Abstract

In the selective laser melting (SLM) process, the heat input by the laser to create the melt pool also diffuses from the melt pool to the surrounding material promoting the growth of surface oxide layers on powder particles that surround the built part. Molten material is also ejected from the melt pool, which oxidises rapidly before landing on the powder bed, creating local variability in the oxygen content of any used powder.

Although large particles are removed when recycling by sieving, smaller oxidised particles (the size of the specified powder for the machine) and oxide residue ( $<10\mu\text{m}$ ) are not removed and become incorporated into subsequent builds on powder reuse.

This project sought to investigate the effect these oxidised particles may have on part integrity and how they affect mechanical failure. In this research, grade 23 Ti-6Al-4V metal powder was thermally oxidised to produce a range of interference colours that correspond to specific oxide thicknesses.

Powder characterisation of each coloured particle established bulk oxygen wt %, particles size distribution (PSD) and used optical spectrometry to quantify the bulk colour of each powder. Oxidised Ti-6Al-4V powder with interference colour yellow and blue powder were chosen for further investigation as in the context of this study, they represent high (0.4 wt %) and ultra-high (0.7 wt %) oxygen levels respectively.

Tensile builds were produced using SLM with a known feedstock layer, part way up the build, formed of a blend of oxidised and virgin particles. Tensile tests were performed for each build to evaluate the failure modes.

Microscopy techniques were used to examine the material near the fractured region, including chemical composition and semi-quantification of the oxygen levels, allowing any microstructural and chemical changes to be investigated. Nano-indentation was used in order to understand if the material properties near the fractured region differ from other remainder of the build.

The main findings from this investigation suggested that the region of the build doped with oxidised particles has a negative impact on the mechanical properties of the final build, as they produce mechanical (oxide films/residue) and chemical flaws (interstitial elements). Consequently, unless these particles can be removed from recycled feedstock their effects will limit the reuse of powder, especially in safety critical industries, significantly increasing the costs of components produced by this route. Robust quality control is needed for post processed powder to minimise the risk of failure and improve the reusability of post processed powder as feedstock.

## Acknowledgments

I would like to thank everybody who has made this PhD project a success. Due to the scale of the project, there are numerous people involved at various stages throughout the project who all have equally guided me and had an impact on the outcome of this work. That being said, I feel it necessary to thank the following people specifically for their significant guidance and contribution to the project.

I would like to thank my primary supervisor, Dr Peter Fox for his guidance and support throughout the project and in particular towards the latter stages of the project as the COVID-19 pandemic impacted the process significantly. His knowledge of the field, guidance and most importantly, patience, ensured a successful conclusion to this project, alongside a publication in a high-ranking journal (Additive manufacturing).

I would also like to thank Dr Matt Bilton from the Albert Crewe Centre for Electron Microscopy (ACCM), formerly known as iCal when I started the PhD. His knowledge of microscopy and patience in helping me create and analyse many complex lamella samples were invaluable to the project. I can attribute much of my microscopy knowledge, both theoretical and practical to his guidance and enthusiasm for the project.

I would like to thank Carpenter Additive, formerly known as LPW at the beginning of the PhD for their financial support in this project. I wish to thank my industrial supervisor, Dr Neil Harrison, whose work provided the foundation for the PhD and his knowledge of both AM and materials were invaluable to the project.

The greatest thanks go to my family, without their support, patience and encouragement, this project would have not been possible. Thank you and I love you all.

# Table of Contents

<b>ABSTRACT .....</b>	<b>2</b>
<b>ACKNOWLEDGMENTS.....</b>	<b>4</b>
<b>PUBLICATIONS.....</b>	<b>8</b>
<b>LIST OF TABLES.....</b>	<b>9</b>
<b>LIST OF FIGURES .....</b>	<b>10</b>
<b>LIST OF ABBREVIATIONS .....</b>	<b>16</b>
<b>NOMENCLATURE .....</b>	<b>17</b>
<b>1.0 INTRODUCTION.....</b>	<b>18</b>
1.1 PROBLEM STATEMENT .....	19
1.2 AIMS AND OBJECTIVES OF RESEARCH.....	20
1.3 THESIS STRUCTURE.....	21
<b>2.0 LITERATURE REVIEW .....</b>	<b>23</b>
2.1 SELECTIVE LASER MELTING: THE PROCESS .....	23
2.1.1 <i>Application</i> .....	24
2.1.2 <i>Controllable parameters</i> .....	25
2.2 PROBLEMS IN SLM .....	29
2.2.1 <i>High thermal and residual stress</i> .....	29
2.2.2 <i>Porosity</i> .....	31
2.2.3 <i>Powder reuse</i> .....	36
2.2.4 <i>Hot tearing crack formation</i> .....	40
2.3 OXIDATION .....	41
2.3.1 <i>Introduction</i> .....	41
2.3.2 <i>Oxidation fundamentals</i> .....	42
2.3.3 <i>Oxide growth mechanisms</i> .....	44
2.3.4 <i>Oxidation of conventional titanium alloys</i> .....	46
2.3.5 <i>Mixed Titanium-Aluminium oxide</i> .....	48
2.3.6 <i>Interference phenomenon</i> .....	50
2.4 TITANIUM ALLOYS .....	53
2.4.1 <i>Introduction and Application</i> .....	53
2.4.2 <i>Metallurgy of titanium alloys</i> .....	54
2.4.3 <i>Alloy classification</i> .....	58
2.4.4 <i>Diffusion controlled transformation</i> .....	60
2.4.5 <i>Diffusionless transformation</i> .....	61
2.5 Ti-6Al-4V ALLOY.....	63
2.5.1 <i>Microstructure of conventional Ti-6Al-4V</i> .....	64
2.5.2 <i>Microstructure of Ti-6Al-4V processed by SLM</i> .....	66
2.5.3 <i>Prior <math>\beta</math> columnar grains</i> .....	67
2.5.4 <i><math>\alpha'</math>-martensite grains</i> .....	69
2.5.5 <i>Hardness of Ti-6Al-4V processed by SLM</i> .....	70
2.6 INTERSTITIAL ELEMENTS IN TITANIUM ALLOYS .....	71

2.6.1 Mechanical effects in titanium alloys .....	71
2.6.2 Solubility of oxygen in titanium .....	76
2.6.3 Oxygen and nitrogen diffusion through titanium .....	78
2.7 ATOMISATION.....	82
2.7.1 Plasma atomisation .....	84
2.7.2 Electrode inert gas atomisation (EIGA).....	85
2.8 POWDER DEGRADATION IN SLM .....	87
2.8.1 Powder requirements.....	87
2.8.2 Gas quality .....	87
2.8.3 Marangoni effect .....	88
2.8.4 Denudation.....	90
2.8.5 Heat affected zone (HAZ) powder.....	91
2.8.6 Spatter.....	92
2.8.7 Condensate .....	94
2.8.8 Cross-contamination .....	94
2.9 CHAPTER SUMMARY .....	96
<b>3.0 EXPERIMENTAL METHODOLOGY .....</b>	<b>97</b>
3.1 Ti-6Al-4V MATERIAL.....	97
3.2 THERMAL OXIDATION OF Ti-6Al-4V .....	100
3.2.1 The process.....	100
3.3 ANALYSIS TECHNIQUES .....	101
3.3.1 Sample preparation .....	101
3.3.2 Chemical analysis.....	103
3.3.3 Laser size diffraction (LSD).....	103
3.3.4 Optical spectrometry.....	104
3.4 MICROSCOPY.....	104
3.4.1 Scanning Electron Microscope (SEM).....	105
3.4.2 Focused Ion Beam- Scanning electron microscope (FIB-SEM) .....	105
3.4.3 S/TEM sample preparation using FIB-SEM .....	109
3.4.4 Preliminary findings for S/TEM sample preparation .....	111
3.4.5 Scanning Transmission Electron Microscope (S/TEM).....	113
3.4.6 Optical Microscope (OM).....	115
3.5 TRUMPF TRUPRINT 1000 .....	115
3.5.1 Machine limitations .....	116
3.6 NANO-INDENTATION.....	117
3.7 CHAPTER SUMMARY.....	118
<b>4.0 POWDER CHARACTERISATION OF OXIDISED PARTICLES.....</b>	<b>119</b>
4.1 PRELIMINARY INVESTIGATION OF OXIDISED POWDERS .....	119
4.2 CHEMICAL ANALYSIS OF BULK POWDER.....	121
4.3 MORPHOLOGY OF POWDER PARTICLES.....	123
4.4 PARTICLE SIZE DISTRIBUTION (PSD).....	126
4.5 OPTICAL IMAGING .....	129
4.6 COLOUR CHARACTERISATION .....	133
4.6.1 Bulk colour reflectivity and LAB colour space .....	133
4.6.2 Sub-yellow powder reflectivity and LAB colour space .....	136
4.7 EFFECT OF THE SURFACE OXIDE LAYERS ON LASER ABSORPTION PROCESSING Ti-6Al-4V.....	139

4.8 CHAPTER SUMMARY.....	141
<b>5.0 INFLUENCE OF PARTICLE SIZE ON OXYGEN CONTRIBUTION IN THE BUILD .....</b>	<b>143</b>
5.1 WHAT IS THE PURPOSE OF THE EXPERIMENT? .....	143
5.2 PARTICLE SIZE OXYGEN CONTRIBUTION .....	143
.....	145
5.3 COMPARISON OF OXIDE THICKNESS RELATIVE TO PARTICLE SIZE .....	146
5.4 COMPARISON OF OXYGEN CONTRIBUTION BETWEEN PARTICLE CORE AND OXIDE LAYER .....	153
5.5 HIGH RESOLUTION IMAGING OF OXIDE LAYER .....	161
5.5.1 <i>Interface between oxide shell and core</i> .....	163
5.5.2 <i>Electron energy loss spectroscopy (EELS) analysis</i> .....	166
5.6 CHAPTER SUMMARY.....	169
<b>6.0 FAILURE ANALYSIS .....</b>	<b>171</b>
6.1 FAILURE HYPOTHESIS.....	171
6.2 VALIDATION EXPERIMENT AND RESULTS .....	175
6.2.1 <i>Tensile Build Methodology</i> .....	175
6.2.2 <i>Tensile test data</i> .....	183
.....	184
6.2.3 <i>Fracture surface imaging</i> .....	187
6.3 OXIDE FILM/ RESIDUE FORMATION IN SLM.....	190
6.3.1 <i>Oxide film on fracture surface</i> .....	190
6.3.2 <i>Microstructure analysis</i> .....	192
6.4 CHAPTER SUMMARY.....	195
<b>7.0 THE EFFECT OF OXYGEN DISSOLUTION IN THE BUILD .....</b>	<b>197</b>
7.1 QUANTIFICATION OF OXYGEN IN FRACTURE SURFACE .....	197
7.1.1 <i>Oxide film on an unbonded particle (oxide region)</i> .....	198
7.1.2 <i>Plastically deformed region (non-oxide region)</i> .....	201
7.2 THE EFFECT OF OXYGEN DISSOLUTION ON THE MECHANICAL PROPERTIES .....	207
7.2.1 <i>Nano-indentation hardness</i> .....	207
7.3 CHAPTER SUMMARY.....	214
<b>8.0 CONCLUSION .....</b>	<b>215</b>
<b>9.0 CONSIDERATIONS AND FUTURE WORK .....</b>	<b>217</b>
9.1 CONSIDERATIONS .....	217
9.2 FUTURE WORK .....	217
9.2.1 <i>Modelling of Heat affected zone (HAZ) powder</i> .....	217
9.2.2 <i>The impact of sub yellow coloured powder on tensile properties</i> .....	218
9.2.3 <i>Controlling oxide formation and disrupting oxide in the build process</i> .....	219
9.3 KEY CONTRIBUTION OF THE THESIS .....	220
<b>10 APPENDIX.....</b>	<b>222</b>
<b>11 REFERENCES .....</b>	<b>226</b>

## **Publications**

There has been one publication from this work, specifically relating to the work discussed in chapters 4-7, details of which are below. This statement acts as a reference to said publication for this work.

R. Williams, M. Bilton, N. Harrison, and P. Fox, (2021) "The impact of oxidised powder particles on the microstructure and mechanical properties of Ti-6Al-4 V processed by laser powder bed fusion, "Addit.Manuf., vol. 46, p.102181, doi: <https://doi.org/10.1016/j.addma.2021.102181>



## List of Tables

Table 1: SLM tabulated processing parameters .....	26
Table 2: Concentration of interstitial elements in titanium alloy wire [104]. .....	71
Table 3: Elemental weight % of Ti-6Al-4V powder supplied by Carpenter Additive..	97
Table 4: PSD results for oxidised Grade 23 Ti-6Al-4V .....	126
Table 5: Minimum quantity of powder required for feedstock chamber to complete doped tensile builds.....	177
Table 6: Oxygen wt % for doped powder layer blend. ....	178
Table 7: Mass of powder required for blended oxidised powder layer. ....	179
Table 8: Tensile test data for control, yellow and blue builds. Data provided by Westmoreland Mechanical Testing & Research, Ltd.....	184
Table 9: summary table of experimental data which demonstrates where each specimen broke and how close to doped band .....	186
Table 10: Summary of pre-built tensile bars and measurement of fracture location .....	222

## List of Figures

Figure 1: Schematic of SLM build process for Renishaw SLM 125 [5].....	24
Figure 2: Schematic of parameters in selective laser melting .....	28
Figure 3: Illustration of scanning strategies used in SLM [11]. .....	29
Figure 4: Illustration of the thermal gradient mechanism (TGM) [20] .....	31
Figure 5: A) Lack of fusion with un-melted particles inside and B) Gas pore [32] ....	32
Figure 6: Illustration of wetting phenomena on a solid substrate b) Transition from semi-spherical to spherical droplet dependent upon melt pool dimensions. [38].....	34
Figure 7: Schematic of SLM process and generation of unwanted by-products (Spatter and condensate).....	37
Figure 8: Schematic of the 'top up' recycling process [47].....	38
Figure 9: Hot tearing crack formation in LPBF AA-7075 along the build direction....	40
Figure 10: Schematic of mass transport across oxide layer [45].....	46
Figure 11: Ti-O phase diagram .....	47
Figure 12: Schematic of oxidation rate with respect to time and temperature. [48]..	48
Figure 13: Illustration of the formation of multi-layered oxide structure in Ti-6Al-4V by Du et al [61].....	50
Figure 14: Interference colours produced the oxide thickness, which depends upon the voltage applied during anodisation. ....	51
Figure 15: Schematic of two light waves impinging surface oxide during interference phenomena. [53] .....	52
Figure 16: Schematic of titanium crystal structure, a) $\alpha$ -phase hexagonal close-packed (HCP) and b) $\beta$ -phase body centred-cubic (BCC) [4].....	55
Figure 17: Schematic of the effect of alloying elements in titanium using binary phase diagrams. [67] .....	56
Figure 18: Ti-Al phase diagram .....	57
Figure 19: Ti-V phase diagrams .....	58
Figure 20: 3-D schematic of titanium alloy classification phase diagram [60].....	59
Figure 21: Illustration of the martensitic transformation mechanism [68].....	62
Figure 22: Adapted from Donachie, Schematic of Ti-6Al-4V microstructure development with a slow cooling rate.....	65

Figure 23: A) optical micrograph showing microstructure of as-built SLM Ti-6Al-4V lateral plane with the dominant prior $\beta$ grain growth direction B) optical micrograph showing microstructure of stress relieved SLM Ti-6Al-4V lateral plane. [72].....	67
Figure 24: SEM micrograph of SLM built Ti-6Al-4V microstructure showing primary, secondary, tertiary and quartic structure [61] .....	69
Figure 25: Interstitial element effect on the mechanical properties of $\alpha$ -phase titanium [91] .....	73
Figure 26: Comparison of commercially pure titanium alloy and Ti-6Al-4V on the relationship of oxygen concentration on a) ultimate tensile strength (UTS), b) Lattice parameters ( $c/a$ ratio), c) Vickers hardness (H) and d) elongation (%) [96].....	75
Figure 27: Schematic of close packed hexagonal (CPH) crystal structure with octahedral interstitial sites present. ....	76
Figure 28: Illustration of oxygen concentration profile in oxidised titanium from Wagner's model. [101] .....	77
Figure 29: Diffusivity of oxygen and nitrogen against temperature in titanium. ....	79
Figure 30: Different methods of melting material for gas atomisation .....	83
Figure 31: Types of nozzle used in gas atomisation .....	84
Figure 32: Schematic of plasma atomisation process .....	85
Figure 33: Schematic of EIGA process .....	86
Figure 34: a) Negative surface tension outward flow b) Positive surface tension inward flow [112] .....	89
Figure 35: schematic of high- and low-pressure interactions between laser beam and powder bed. ....	90
Figure 36: Particle size distribution of Carpenter Additive virgin Ti-6Al-4V powder..	98
Figure 37: SEM micrograph of VIGA virgin Ti-6Al-4V powder in secondary electron imaging mode.....	99
Figure 38: Bulk Ti-6Al-4V colours in clear sample holder used for spectrometry. ...	104
Figure 39: Schematic of FIB-SEM operation .....	107
Figure 40: Powder particles mounted on carbon tape inside FEI Helios Nanolab 600i FIB-SEM.....	108
Figure 41: SEM live capture micrograph of milling an oxidised powder particle to expose the cross section FEI Helios Nanolab 600i FIB-SEM.....	109

Figure 42: Images of In-situ lift out process to create a TEM lamella sample. A) Region of interest B) Pt layer C) Milling site D) Lamella sample mounted to copper grid .....	110
Figure 43: Schematic of wedge milling process .....	111
Figure 44: Thinning of blue Ti-6Al-4V lamella using a channelling method to maintain structural integrity.....	112
Figure 45: Schematic of cross section of JEOL 2100+ from the JEOL operation handbook. ....	114
Figure 46: Images of TRUMPF TruPrint 1000 machine with labelled image of build chamber .....	117
Figure 47: Thermally oxidised Ti-6Al-4V powder particles; ranging from virgin (far left) to green (far right).....	120
Figure 48: Relationship between interference colour and oxygen, nitrogen, and hydrogen in oxidised Ti-6Al-4V metal powder.....	122
Figure 49: The impact of temperature on oxygen, nitrogen, and hydrogen for oxidised Ti-6Al-4V .....	123
Figure 50: A) BSE micrograph at x300 magnification of Virgin Ti-6Al-4V B) High mag (x1000) BSE micrograph of Virgin Ti-6Al-4V .....	124
Figure 51: A) BSE micrograph at x300 magnification of yellow coloured Ti-6Al-4V B) High mag (x1000) BSE micrograph of yellow coloured Ti-6Al-4V .....	124
Figure 52: A) BSE micrograph at x300 magnification of blue coloured Ti-6Al-4V B) High mag (x1000) BSE micrograph of blue coloured Ti-6Al-4V .....	125
Figure 53: A) BSE micrograph at x300 magnification of green coloured Ti-6Al-4V B) High mag (x1000) BSE micrograph of green coloured Ti-6Al-4V .....	125
Figure 54: Particle size distribution.....	127
Figure 55: A) Low magnification (x200) optical image of yellow coloured Ti-6Al-4V powder particles B) Higher magnification (x1000) optical image of yellow coloured Ti-6Al-4V powder particles. ....	130
Figure 56: A) Low magnification (x200) optical image of blue coloured Ti-6Al-4V powder particles B) Higher magnification (x1000) optical image of blue coloured Ti-6Al-4V powder particles. ....	131
Figure 57: A) Low magnification (x200) optical image of green coloured Ti-6Al-4V powder particles B) Higher magnification (x1000) optical image of green coloured Ti-6Al-4V powder particles. ....	132

Figure 58: Relationship between reflectance (%) and wavelength (nm) for bulk colours; yellow blue and green and control colour; virgin.....	135
Figure 59: L*a*b* colour measurements of the three bulk powders; yellow, blue, and green.....	136
Figure 60: Sub-yellow relationship between wavelength (nm) and reflectance (%)	137
Figure 61: L*a*b* colour measurements of the three bulk powders; yellow, blue and green.....	139
Figure 62: A) Schematic of titanium powder particle B) Model of laser absorption at the surface of the titanium powder [9] .....	141
Figure 63: Relationship between Oxygen (O) wt% and particle size ( $\mu\text{m}$ ) for blue and yellow interference colour.....	145
Figure 64: Relationship between Nitrogen (N) wt% and particle size ( $\mu\text{m}$ ) for blue and yellow interference colour.....	145
Figure 65: Relationship between oxide thickness (nm) and particle size ( $\mu\text{m}$ ).....	147
Figure 66: Relationship between mass fraction ratio of oxide shell to whole particle with respect to coloured particle size ( $\mu\text{m}$ ) .....	148
Figure 67: concentration of oxygen in oxide layer with respect to the whole particle .....	149
Figure 68: A) Green Ti-6Al-4V chosen for investigation. B) Cross sectional view of the blue Ti-6Al-4V powder particle. ....	150
Figure 69: A) High magnification cross sectional view of the oxide layer showing oxide satellites B) EDX map of the cross-sectional view.....	152
Figure 70: A) High magnification micrograph of blue Ti-6Al-4V particle B) Cross sectional view of FIB milled particle.....	152
Figure 71: High magnification micrograph of oxide layer on blue Ti-6Al-4V particle B) EDX mapping of oxide layer interface .....	153
Figure 72: EDS line scan of 20 $\mu\text{m}$ yellow Ti-6Al-4V powder particle cross section with elemental wt % tabulated.....	156
Figure 73: EDS line scan of 45 $\mu\text{m}$ yellow Ti-6Al-4V powder particle cross section with elemental wt % tabulated.....	157
Figure 74: EDS line scan of 20 $\mu\text{m}$ blue Ti-6Al-4V powder particle cross section with elemental wt % tabulated. ....	158
Figure 75: EDS line scan of 45 $\mu\text{m}$ blue Ti-6Al-4V powder particle cross section with elemental wt % tabulated. ....	159

Figure 76: EDS line scan of 20µm green Ti-6Al-4V powder particle cross section with elemental wt % tabulated. ....	160
Figure 77: EDS line scan of 45µm green Ti-6Al-4V powder particle cross section with elemental wt % tabulated. ....	161
Figure 78: High resolution TEM micrograph of oxide interface of blue powder particle in both Annular dark field (ADF) and bright field (BF) illumination.....	163
Figure 79: EDS mapping of the oxide interface showing oxygen (green) and aluminium (grey) mapping.....	164
Figure 80: TEM micrograph of oxide interface at high magnification showing nano-pores depicted by red circles.....	165
Figure 81: Micrograph of region of interest for EELS analysis; A is the core of material and B is the oxide layer. ....	166
Figure 82: EELS spectra for location A (Material core) .....	168
Figure 83: EELS spectra for location B (oxide layer).....	169
Figure 84: Schematic of how heavily oxidised particles can be present within a batch of powder, but the bulk powder measurement still be within specification.....	172
Figure 85: Image of heat affected zone powder surrounding Ti-6AL-4V parts inside the TRUMPF TruPrint 1000.....	173
Figure 86: Schematic of out of specification region of powder within the build, the blue and yellow particles represent oxidised powder particles and the grey represent Ti-6Al-4V powder within ASTM limits. ....	174
Figure 87: Diagram of experimental design to simulate local concentration of high oxygen wt% particles within volume of ASTM B348 Gr 23 Ti-6A4V powder .....	175
Figure 88: Stacking arrangement for doped tensile builds .....	177
Figure 89: Technical drawing of cylindrical tensile bars .....	180
Figure 90: Schematic of tensile test specimen adhering to ASTM E8/E8M-16A, the red dashed box denotes the specimen dimensions chosen. [161].....	181
Figure 91: Image of build layout and control tensile build from the TRUMPF TruPrint 1000. ....	182
Figure 92: Dimensions of as built tensile bar: A) Length of bar excluding support, B) length of bar including support and C) diameter of bar.....	182
Figure 93: Image showing evidence of cracking in the approximated doped layer of the tensile build. ....	183
Figure 94: Optical image of ductile (control build) fracture. ....	184

Figure 95: Optical image of brittle fracture (blue doped build).....	185
Figure 96: SEM micrograph of tensile fracture surface of A) Virgin C) Yellow and E) Blue, enhanced magnification micrographs of region of interest B), D) and F) .....	189
Figure 97: Non-melted oxidised Ti-6A4V powder particle embedded into fracture surface B) high contrast solid-state backscatter electron detector (CBS) image of embedded oxidised particle surface in fracture surface .....	192
Figure 98: SEM micrograph of tensile build cross sections displaying fracture surface for A) Virgin, C) Yellow and E) Blue. Region of microstructure away from fracture surface for the three respective builds B), D) and F).....	193
Figure 99: A) ROI with un-bonded particle in contact with oxide film, B) ROI plastically deformed region not in contact with an oxide film. ....	198
Figure 100: EDX elemental mapping of blue Ti-6Al-4V tensile build fracture surface lamella sample. A) EDX elemental overlay map B) Oxygen (O) element map.....	199
Figure 101: EDX elemental line scan of blue tensile build fracture surface lamella of embedded oxidised particle. A) HAADF-STEM image of lamella region of interest with graphing overlay B) Line scan graph .....	199
Figure 102: EDX elemental map of blue tensile non-embedded particle region of interest. A) EDX elemental overlay map B) EDX oxygen (O) map .....	201
Figure 103: EDX elemental line scan of blue tensile build fracture surface lamella of non-embedded oxidised particle. A) TEM image of lamella region of interest with graphing overlay B) Line scan graph.....	202
Figure 104: EDX elemental map of the yellow build fracture surface lamella.....	204
Figure 105: EDX line scan of the yellow fracture surface lamella overlaid onto to the O elemental map.....	205
Figure 106: EDX line scan plot of elements for yellow non embedded particle region lamella.....	206
Figure 107: Indentation plan illustrated on SEM micrograph of tensile cross section sample.....	208
Figure 108: Relationship between hardness (GPa) and distance from the fracture surface ( $\mu\text{m}$ ) .....	209
Figure 109: Relationship between distance from fracture surface ( $\mu\text{m}$ ) and modulus of elasticity, E (GPa) determined by the NanoSuite® software. ....	212

## List of Abbreviations

AM	- Additive Manufacturing
SLM	- Selective Laser Melting
CAD	- Computer Aided Design
XRD	- X-Ray Diffraction
EDX	- Electron Diffraction X-Ray
EDM	- Electrical Discharge Machining
UTS	- Ultimate Tensile Strength
HIP	- Hot Isostatic Press
HAZ	- Heat Affected Zone
FCC	- Face Centre Cubic
BCC	- Body Centre Cubic
HCP	- Hexagonal Centre Cubic
TGM	- Thermal Gradient Mechanism
EDS	- Energy Dispersive Spectroscopy
DOE	- Design of Experiment
SEM	- Scanning Electron Microscope/Microscopy
FIB	- Focused Ion Beam
STEM	- Scanning Transmission Electron Microscope/Microscopy
TEM	- Transmission Electron Microscopy
SE	- Secondary Electron (Imaging mode)
OM	- Optical Microscopy
LSD	- Laser Size Diffraction
PPM	- Parts per Million
PD	- Point Distance
LT	- Layer Thickness
ET	- Exposure Time
FO	- Focus Offset
HS	- Hatch Spacing
BD	- Beam Diameter



## Nomenclature

$T$	- Temperature
$m$	- Mass of material
$t$	- Time
$Q$	- Energy
$t_{\text{exp}}$	- Exposure time
$P$	- Laser power
$L$	- Length
$\rho$	- Density
$E$	- Young's modulus or elastic modulus
$H$	- Enthalpy
$V$	- Volume
$K$	- Thermal conductivity
$T_0$	- Initial temperature
$A$	- Surface area
$\sigma_y$	- Yield strength
$\sigma_{\text{tens}}$	- Tensile stress
$\epsilon_{\text{pl}}$	- Plastic strain
$\sigma_{\text{comp}}$	- Compressive stress
$D_0$	- Independent temperature coefficient
$C_x$	- Concentration
$C_i$	- Initial concentration
$C_0$	- Final concentration

## 1.0 Introduction

Additive manufacturing (AM), commonly known as 3-D printing is a process of successive fusion of layers of material to construct a 3-D component. Raw material can be deposited and fused in many different processes such as suspension based, liquid or solid in particular position so that cross sectional layers are sequentially added to create the 3-D structure. A variety of different materials can be used to create a component such as plastics, resins, rubbers, ceramics, metals, glass and concretes [1].

In comparison, traditional techniques used for manufacturing such as computer-generated numerical controls (CNC) are all subtractive methods to cut, drill, frame and fit an object from raw materials such as billets. CNC can achieve complex external geometries and give accurate dimensional tolerances; however, this process is not ideal for the manufacture of internal features as the cutting instruments cannot reach the desired location. Parts with complex internal structure such as cooling channels may be manufactured by different methods such as casting, which involves the creation of a complex mould to cast the component. The creation of mould can be time consuming and costly; casting is only cost effective if high volumes of the part are being made in order to reduce the costing of the mould. However, additive manufacturing (AM) overcomes all the problems that the traditional methods present as manufacturing geometric complexity comes at little to no extra cost.

AM was primarily used for rapid prototyping as this significantly reduced the time to market and innovation of products. Rapid prototyping can be defined as the process of rapidly creating a prototype of a part so that the part can be tested and scrutinised before mass production occurs. However, AM technologies have matured significantly over recent years and wide industrial acceptance of their advantages has shifted the technologies to serial production of parts as opposed to rapid prototyping [2]. In particular, throughout 2019-2020, the demand for AM technologies have increased as many companies have shifted their manufacturing chains to AM due to the impact on the global supply chain from the Covid-19 pandemic, whilst most of the conventional manufacturing processes are still based in China [3].

A popular AM technique for serial production is selective laser melting (SLM) which is a powder bed fusion technique. SLM utilises a laser beam to selectively melt the powder bed on a layer-by-layer basis predetermined by computer aided design (CAD) data. SLM is utilised by manufacturers for its performance, high resolution, and inert gas operating environment in the processing of titanium alloys Ti-6Al-4V powder. Ti-6Al-4V is commonly processed in SLM and is extremely useful to industries such as aerospace, biomedical and maritime due to its superior material properties such as the high strength to weight ratio, biocompatibility and corrosion resistance [4]. Therefore, Ti-6Al-4V is commonly researched in AM to optimise the material properties and produce the highest quality finished parts. However, Ti-6Al-4V is an expensive feedstock material and the reuse of the material can be low due to lack of understanding of the impact reused powder has on build quality, therefore in some instances, driving the cost of processing the material higher.

### **1.1 Problem statement**

It is understood that Ti-6Al-4V metal powder used for selective laser melting (SLM) degrades with repeated use as it picks up oxygen in significant quantities throughout the build process believed to be a result of by-products of the powder melting and handling processes involved [5].

It is essential that critical and high-end manufacturing techniques understand the impact this degradation has on the final build's quality and mechanical properties however, this is poorly understood. The need to understand powder degradation is prominent now as users are moving towards serial production of structurally critical parts. AM is transitioning from prototyping and small batch production technique so the need to understand degradation is now increasingly prominent.

Degradation due to repeated use of Ti-6Al-4V metal powder promotes a lack of confidence in additive manufacturing (AM) industries that develop high end and critical applications [6]. This typically results in companies specifying build limits on the same batch of powder as little is known about the effect degraded powder has on build

quality, resulting in high raw material cost as poor understanding of the impact degraded powder has on final build quality if reused in feedstock.

The degradation is caused by by-products of the melting process which produce re-melted 'weld splatter' and a soot-like condensate of nanoparticles. Understanding the nature of these newly created by-products and the impact on build quality utilising them would build confidence in used powder and enable solutions to be found to monitor and eliminate the negative effects of powder degradation.

The project will investigate the fundamental mechanisms which lead to powder degradation of Ti-6AL4V in selective laser melting (SLM) process, evaluate solutions for monitoring the rate of degradation and evaluate End-of-life solutions for powder which is degraded beyond acceptable limits.

## **1.2 Aims and objectives of research**

The aim of this work is maximising the utilisation of Ti-6Al-4V powder metal processed by laser powder bed fusion (LPBF).

Below are the main objectives in order to achieve this aim:

- To investigate and understand the root cause of Ti-6AL-4V powder degradation in the SLM process.
- To investigate the impact degraded powder particles, have on reuse in the build process.
- To investigate the oxide layer interface between core and particle to understand the relationship between interference colour and oxygen wt %.
- To develop a method of identifying degraded powder particles in post processed powder and evaluate the re-use/end of life application for the powder.

### **1.3 Thesis structure**

This section briefly outlines the main structure of the thesis and introduces the content within each of the chapters.

Chapter 1 introduces the background research as well as the objectives, problem statement and thesis structure.

Chapter 2 is dedicated to reviewing current technology regarding the processing of material using SLM with details on the operation, process parameters and literature on the oxidation and metallurgy of titanium alloys, specifically Ti-6Al-4V. The critical aspects of powder reuse and degradation mechanisms through oxidation are discussed which range from powder production to manufacturing defects, microstructure, and phase transformation of as built parts.

In chapter 3, the experimental procedure and methodology for the project. Specific methodology will be discussed in the respective chapters, however, methods for sample analysis and equipment details are discussed here. Inert gas fusion (IGF), commercially known as LECO was used to characterise oxygen, nitrogen, and hydrogen. Malvern Mastersizer 3000 was used to analyse the particle size distribution of the metal powders using laser size diffraction. SEM imaging and TEM lamella sample preparation were conducted using a JEOL 6610 SEM and a FEI Helios Nanolab 600i FIB-SEM. Advanced microscopy techniques were carried out using a JEOL 2100f C<sub>s</sub> corrected FEG S/TEM (80-200kV) and a JEOL 2100+ S/TEM (200kV LaB6 thermionic emission source).

Chapter 4 consists of preliminary investigations into powder oxidation and the characterisation of the artificially oxidised powder particles by investigating the key characteristics such as chemical analysis, morphology, and Particle size distribution. The preliminary investigations into powder oxidation try to establish relationships between interference colours, oxide formation and bulk powder oxygen content. These fundamental properties are key in understanding the impact and contribution of oxidised powder in the powder bed. Additionally, this chapter investigates the role of

the interference colours on the powder particles and how they are quantified to ensure consistency in imaging post processed powder and identifying coloured oxidised particles. This understanding is key in the development of a quality control methodology for post processed powder.

Chapter 5 investigates the influence of particle size and colour and their contribution to the oxygen contribution to the build process. This chapter features various analysis methods to characterise the oxygen contribution from the key particle colours. Scanning transmission electron microscopy (S/TEM) was used to identify regions of interest and quantify the oxygen present through techniques such as EDX and EELS.

Chapter 6 investigates the failure modes of the tensile specimens built with a region of doped oxidised powder and compare the results to a virgin, control sample. This section features tensile test data of each of the specimens and high-resolution microscopy images to understand the fracture surface features and identify region of interest. Additionally, the chapter finishes with the microstructure analysis of the tensile specimens to try and establish whether the failure occurred due to a mechanical flaw in the build process.

Chapter 7 investigates the oxygen dissolution within the build and whether the failure of the tensile specimens occurs due to a chemical flaw within the build. This chapter utilises S/TEM techniques to quantify the oxygen present within fracture surface lamellas of an oxidised region and a non-oxidised region of the fracture surface. Nano-indentation is used to measure the hardness change of the localised known doped layers around the fracture surface and compare it to regions of virgin powder build to evaluate whether an oxygen increase in the titanium matrix has embrittled the build.

Chapter 8 concludes the project and evaluates all the evidence and discussion throughout each chapter to summarise the project and present the main findings.

Chapter 9 discusses future work based on the key findings throughout the investigation alongside the key contributions of the thesis.

## 2.0 Literature review

### 2.1 Selective laser melting: The process

Selective laser melting (SLM) is an additive manufacturing (AM) process which utilises a laser beam to selectively melt a metallic bed of powder on a layer-by-layer basis. This technique produces fully dense, three-dimensional components based on imported geometry data from a 3-D Computer Aided Design (CAD) model. This technology has been widely adopted by numerous different industries; in particular aerospace and medical, as it allows complex designs and difficult to manufacture components to be produced with relative ease. However, serial production of SLM technologies has been hindered by poor build-to-build consistency. In particular, the mechanical properties of SLM built parts can vary significantly compared to wrought due to the presence of residual stresses [7] and defects such as cracks [8], porosity and balling [9]. A study using Ti-6Al-4V found that the SLM built Ti-6Al-4V had higher yield strength, ultimate tensile strength (UTS) and hardness, but produced significantly lower elongation compared to wrought Ti-6Al-4V. [10]

Additive manufacturing technologies and SLM have seen a rapid growth in recent years due to significant interest from both industry and research sectors due to the large design flexibility and ability to manufacture complex components. The layer-by-layer build process allows geometries to be constructed that conventional techniques cannot achieve, such as internal lattice structures. The build process allows complex detail to be incorporated into the final components which conventional techniques would not be able to achieve. SLM allows non-fused powder to be recycled using sieving and usually a powder recycling regime, which uses a top up process of virgin material blended with the sieved post processed powder in order to re-use the material as feedstock, which reduces waste. However, little is known about the impact recycled powder has on the final build quality and the mechanical properties of components processed by SLM.

The SLM process manufactures components via the successive deposition of metallic powder layers, 20 to 150 $\mu$ m thick onto a substrate material, each layer and part of the underlying component is then melted by a high-power laser (50W – 1kW),

predetermined by 3-D CAD model data, forming a metallic bond between the two respective layers, thus creating a 3-D metal structure as shown in Figure 1 [11].

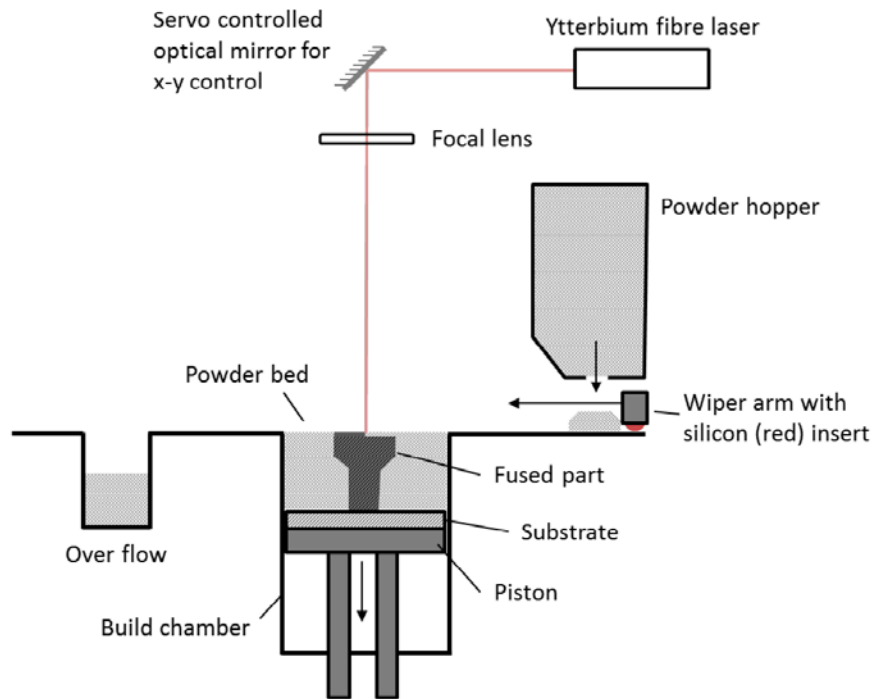


Figure 1: Schematic of SLM build process for Renishaw SLM 125 [5]

### 2.1.1 Application

Although large SLM manufacturers have been established for numerous years now, it is still considered a developing technology as it moves towards a phase of serial production. However, there are still fundamental limitations to achieving industrial serial production of parts via the SLM process such as large start-up costs (machine cost typically >£250,000), machine running cost and low production volumes relative to conventional techniques. However, similar to any technology, there are certain applications that SLM is better suited to such as high-end manufacturing in industries such as aerospace, dentistry, medical and jewellery [12].

The competitive advantages of SLM are geometric design freedom, mass customisation, material flexibility, reduction in process steps, shortened design to



product time and no tooling costs unlike those associated with conventional techniques such as moulds and tooling heads [13].

The scope of the application for SLM is varied between industries but includes customised medical orthopaedics, veterinary implants and tooling inserts with high geometrical complexity [14]. Additionally, the aerospace sector has shown great interest and investment in the use of SLM for high end component manufacture as the safety standards require high levels of performance and component integrity. The material of choice for the aerospace industry is generally high-performance alloys such as titanium- and nickel-based alloys due their superior properties of strength, corrosion resistance and high temperature application. Applications such as gas engine turbine blades, airframes, fuel injection nozzles and many more utilise SLM to create high performance components. Optimised SLM technology offers huge cost reduction for the aerospace industry due to its high flexibility and ability to process numerous different high-performance materials. An example of a successful AM built application within the aerospace industry is the Rolls Royce Trent XWB-97 engine as it features large Ti-6Al-4V, EBM built, 1.5m diameter compression vanes [15].

### **2.1.2 Controllable parameters**

There are many controllable processing parameters in SLM dependent upon the machine used. However, there are numerous factors affecting the built part which are not controllable and are locked in by the machine manufacturer or are dependent upon supplier specification such as the material. Table 1 illustrates the processing parameters throughout the SLM process broken down into four categories: Materials, Environment, Laser and Scan.

Table 1: SLM tabulated processing parameters

Material composition	Type of inert gas	Laser power	Scan pattern
Particle size distribution (PSD)	Gas flow rate	Laser scan mode	Scan velocity
Morphology (Particle shape)	Temperature of the build platform	Wavelength	Scan distance
Powder relative density	Build chamber pressure	Laser spot size	Hatch spacing
Powder flowability	Part placement	Type of laser	Layer thickness
Powder interstitial content	Part orientation	Offset point	Scan sectors

Layer thickness is the thickness of the deposited powder for each layer of the build and determines the energy input into the powder layer required to melt and bond to the substrate completely. Layer thickness also has a big impact on production time, a greater layer thickness results in a shorter production time but can produce poor dimensional accuracy and surface quality [16][17].

Throughout the SLM process, the laser beam moves, defined by the scanning speed, across the powder bed which in turn determines the production time of the build. Increased scanning speed reduces the overall production time, however, high scanning speed with low laser power may result in insufficient fusion across the build resulting in a build fail.

Laser power, hatch spacing, layer thickness and scan speed has been investigated by numerous authors as primary processing parameters for SLM which define the laser energy density that is delivered to the powder bed. The volumetric unit for the energy delivered to the powder bed is energy density (E), and is defined by the following equation 1 [14][16]:

$$E = \frac{P}{V \cdot h \cdot t} \quad (1)$$

Where E is energy density, P is laser power, V is scan velocity, h is the hatch spacing and t is the powder layer thickness. The energy density can have a large impact on the mechanical properties of a built part as it directly effects the physical densification of a part.

The Trumpf TruPrint 1000 that was used throughout this project utilised a continuous scan of the laser along the track length rather than a point-to-point regime and, therefore, point distance (PD) is not a controllable parameter in the case of this machine. However, with machines such as the Renishaw SLM 125, a scan length can be separated into a series of exposure points at a set point distance and a set exposure time. In this case, the laser moves between each point by the defined point distance and when the exposure, defined by the exposure time of each point is complete, the laser pauses and moves to the next exposure. Hatch spacing is the distance between the centre point of two adjacent melt tracks as shown by Figure 2.

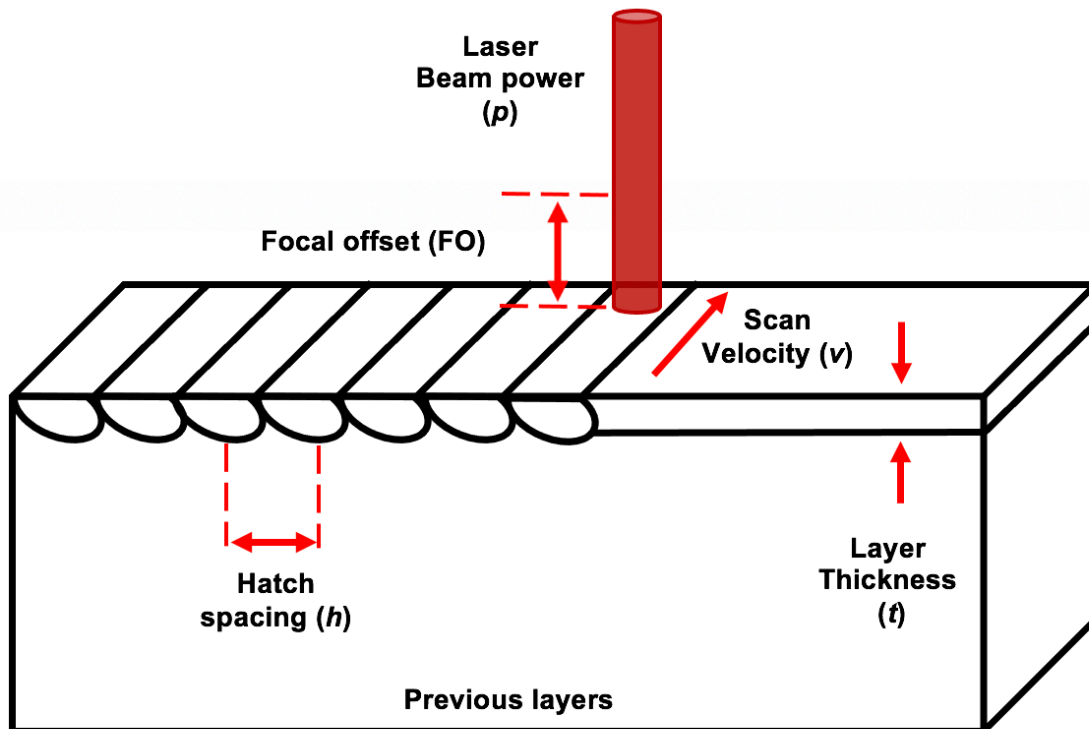


Figure 2: Schematic of parameters in selective laser melting

The scan strategy or sometimes referred to as the hatch pattern, is the laser pattern used for the melting of a two-dimensional shape in the powder bed. Usually, the scan strategy consists of straight and parallel scan vectors which can be modified either between consecutive layers or modified inside layers. Generally, the specific purpose of the scan strategy is to reduce residual stress or reduce build time. Figure 3 illustrates some examples of common scan strategies such as meander, stripes and chessboard.

The meander scan strategy consists of straight-line vector paths from each side of the border which makes for a quick and efficient build, ideal for small XY cross sectional parts. However, this strategy can produce inconsistent heat distribution throughout each layer.

The stripes scan strategy splits the scan area into strips around 5-100mm wide and utilises the meander technique within these strips to process the material. The key advantage to this method is that it maintains a consistent temperature distribution

throughout the part which is ideal for large XY cross sectional parts [18]. However, a key disadvantage is that this strategy is slower than meander as an increased number of laser jumps is required.

The chessboard strategy splits the scan area up into squares similar to that of a chessboard and is generally used in order to minimise the residual stress of the built part. However, a key disadvantage of this is longer scanning times and is generally not favoured when productivity is favoured [18].

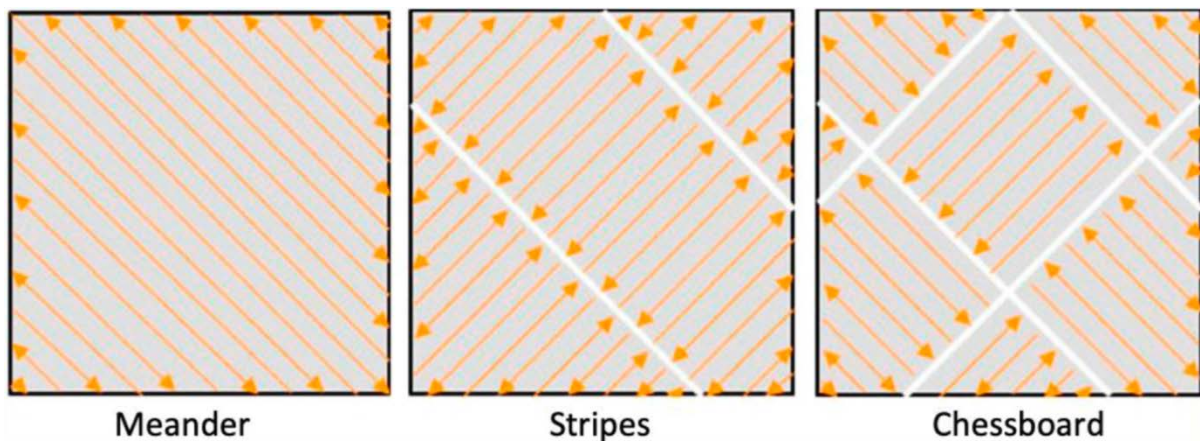


Figure 3: Illustration of scanning strategies used in SLM [11].

## 2.2 Problems in SLM

Similar to any processing technique, SLM has numerous process limitations that create problems for final component quality and the associated mechanical properties. Understanding these limitations and controlling the problematic process characteristics is essential for industry wide adoption of SLM for serial production. The order of the sub sections illustrating each common problem are in no order of priority.

### 2.2.1 High thermal and residual stress

Residual stress can be associated with the processing of a material and defined as the internal stress present within a component without the presence of an external applied force. However, residual stress is associated with all material processes as the introduction of residual stress in some form is inevitable across every process [19].

Therefore, control and manipulation of residual stress has been studied and implemented across industry for many years to tailor the material for a desired application. Residual stress is the result of elastic misfits between regions creating elastic strain from cold deformation. Residual stress is usually relieved via heat treatment processes, however, in sufficient concentration, residual stress can lead to reduced tensile strength, micro-crack formation and part deformation [20].

Residual stress is categorised into three types; Type-1 macro-residual stress, Type-2 micro-residual stress and Type-3 sub-micro residual stress. Type-1 residual stress develops in several grain boundaries and varies in length relative to the part size. The formation of Type-1 residual stress occurs in processes that results in inhomogeneous distribution of strains. Type-2 micro-residual stresses form in one grain but vary in size in different grains. The formation of type-2 residual stress occurs from misfit strains from processes such as martensitic transformation. Thus, the volume difference between martensite and austenite creates residual stresses. The formation of type-3 residual stress is caused by lattice defects such as interstitial solutes and dislocations [21]. Type-1 stress can also occur via thermal elastic strains which is prevalent within the SLM process caused by the temperature gradient and differential shrinkage. Type-1 stress also has the largest impact on material strength in comparison with Type-2 and Type-3 due to the varying size over numerous grain boundaries [19].

A study of residual stress found in SLM from Mercelis and Kruth [20] suggested that residual stress arises from two mechanisms in the SLM; the cooling of molten top layers and the thermal gradient mechanism (TGM). The thermal gradient mechanism (TGM) is the result of thermal gradients produced by the laser interaction with the metallic powder bed. The top surface is rapidly heated to fuse material together, however the heat conduction through the remaining material is relatively low compared to the top surface and thus creates a large temperature gradient. The thermal expansion of the top layer is restricted, at lower temperatures, by the comparatively cooler layer below, thus creating induced elastic compressive strain. However, at elevated temperatures, the top layer yield strength is reduced, resulting in plastic compression. The cooling of the plastically compressed top layer results in a bending angle towards the laser due to the differential shrinkage of the cooled top layer as different areas of the part cool at different rates, thus introducing a tensile stress in the

direction of the build. Figure 4 illustrates the thermal gradient method (TGM) for a laser incident on solid material (the mechanism occurs in the solid phase) where  $\epsilon_{th}$  is thermal strain,  $\epsilon_{pl}$  plastic strain,  $\sigma_{tens}$  is the tensile stress and  $\sigma_{comp}$  is the compressive stress. The freezing mechanism of the molten top layer introduces stress into the build in a similar process to the thermal gradient mechanism (TGM). Thermal contraction occurs during the cooling of the solidified material, resulting in tensile stress in the top layer and compressive stress in the layer below.

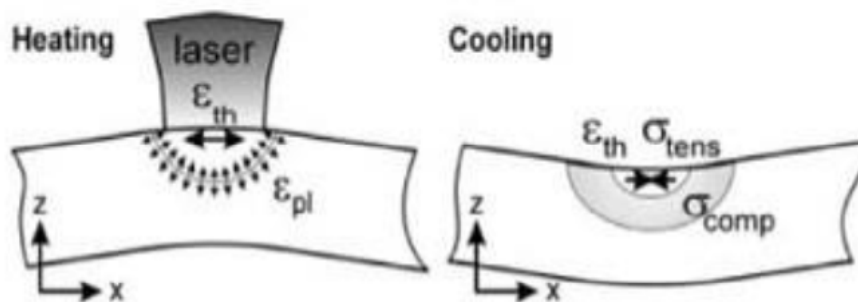


Figure 4: Illustration of the thermal gradient mechanism (TGM) [20]

This section discussed the presence of residual stress in SLM and the link to problematic changes in mechanical properties induced via the fusion process. However, residual stress may be relieved via post process heat treatment commonly referred to as stress relief. That being said, defects in the material due to thermal stress can be problematic as the material is at greater risk of deformation and fracture which are significantly harder to remedy.

### 2.2.2 Porosity

Selective laser melting in theory can produce a fully dense structure, however, non-optimised melting parameters will result in porosity. Porosity is a common problem within SLM which causes problematic defects in built parts. Porosity is defined as a pore or number of pores within a given volume, usually stated in units of volume % or commonly as density ( $\text{kgm}^{-3}$ ). Uncontrolled pores are considered to be problematic in

SLM as they are considered to be crack initiation sites as they are effectively a region (microscopic) of space in the build in which no fused material is present. Biswas et al [22] found that the pores in the microstructure of SLM built parts are likely to become nucleation site for adiabatic shear bands and microcracks. However, controlled porous structures can be used to tailor mechanical properties to a specific application to address the stress shielding effect [23][24].

Therefore, achieving fully dense parts is essential in order to minimise the risk of uncontrolled pores leading to crack initiation and detrimental mechanical properties. Early investigations of SLM built parts primarily focused on achieving high values of density (99.9%) as suggested by many authors [25][26]. The reasons for the formation of pores within SLM builds are highlighted by numerous investigations where the main causes are found to be insufficient melting/fusion depth (lack of fusion), trapped gas and balling.

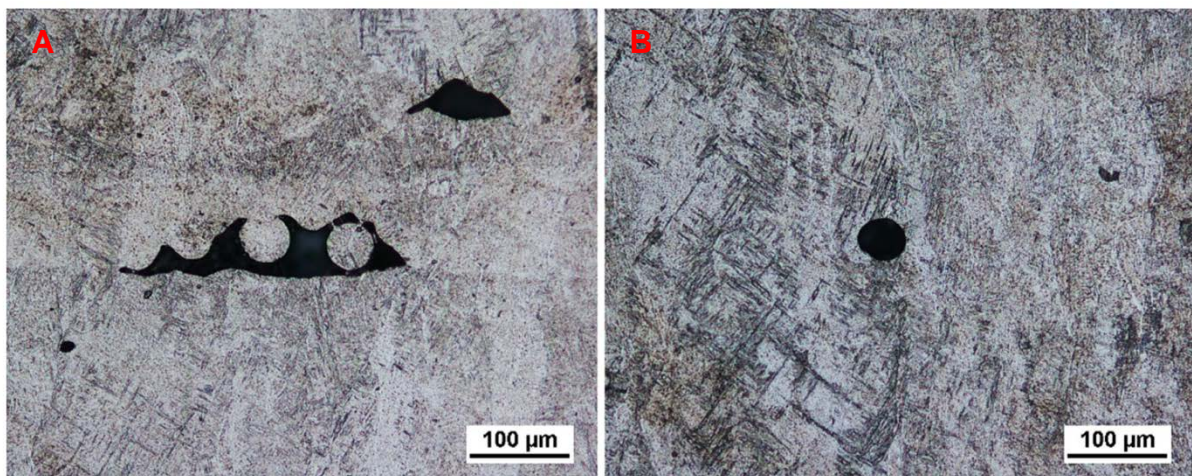


Figure 5: A) Lack of fusion with un-melted particles inside and B) Gas pore [32]

Figure 5 shows the morphology of a lack of fusion and gas pore in a part manufactured by SLM [27]. Figure 5A shows a lack of fusion pore which is irregular in shape with sharp tips and is notably larger than gas pores. These pores are generally formed and spread in the joint region over two adjacent layers and are formed due to a deviation from the optimal processing conditions such as insufficient energy input or insufficient overlap leading to poor melting and bonding [28][29]. Additionally, the sharp tips on



the lack of fusion pores are prone to high localised stress and can result in premature failure when subjected to loading [28][30][31].

Rickenbacher et al [32] demonstrated the effect process parameter optimisation can have on porosity in IN738LC starting with a build which had no parameter optimisation which produced a porosity of 53% compared with a build with process optimisation which resulted in 0.2% porosity. The 0.2% porosity present in the optimised build showed numerous spherical pores varying in size, these phenomena were due to trapped gas within the build process creating spherical voids; trapped gas expands uniformly, creating the spherical shape.

A study by Shrestha [33] investigated the relationship of laser energy density (LED) and pore formation in Ti-6Al-4V in SLM using a micro-CT scanner to analyse single track builds. The study showed that at the same laser energy density, an increase in laser power showed a distinct transition from incomplete melting to conduction melting and to keyhole melting. At low power, balling formation occurred due to lack of substrate wetting. In contrast, high power resulted in keyhole pores and the depth of the pores increased with laser power. The study concluded that the power/speed are highly influential toward the formation of keyhole porosity. This is significant as it provides evidence to the importance of optimising process parameters to ensure sufficient melting and balancing the processing power with the formation of keyhole pores.

Kasperovich et al [34] showed that optimised process parameters using Ti-6Al-4V in SLM could significantly reduce porosity achieving a residual porosity of <0.05%. The study found that excessive energy density produced circular/spherical pores with a diameter >50 $\mu\text{m}$  due to the keyhole effect. Low energy density produced elongated, crack like voids of length >100 $\mu\text{m}$ , these pores were due to lack of fusion caused by a combination of the powder layers not sufficiently melting and the balling effect.

Balling is another phenomenon which contributes to the formation of pores within the build process. Balling is defined as solidified metal beads on the surface as opposed to hemi-spherical droplets. The formation of the balling phenomenon is due to insufficient wetting of the molten material to the underlying solid material, the spherical

shape is created by the surface tension forces [35]. The balling phenomenon obstructs the formation of continuous melt lines, forming solidified metal beads and which in severe cases can aggravate in subsequent layers and jam the powder coater in the SLM machine.

The spherical droplets form a rough surface resulting in altered mechanical properties detrimental to the final build quality, as the number of pores increase if the balling phenomenon is present, the pores forming in-between discontinuous metal balls. This is because the layer above the solidified balls on the surface does not uniformly melt, thus, leaving pores. Similarly, the melted underlying layers also leave pores between the balls.

Additionally, the surface roughness is increased by the presence of the balling on the surface, therefore post processing surface polishing is needed in order to improve part quality. However, polishing can reduce the dimensional accuracy. In severe cases, the metal balls on the surface of the melted layer hinder the movement of the powder spreading roller/wiper resulting in either a defected layer in the build or a stopped powder coater.

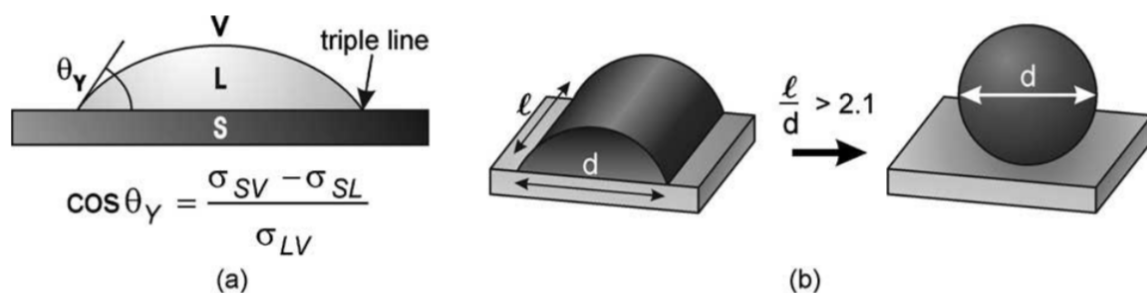


Figure 6: Illustration of wetting phenomena on a solid substrate b) Transition from semi-spherical to spherical droplet dependent upon melt pool dimensions. [38]

Figure 6 illustrates the wetting phenomena showing the process of transformation from semi-spherical to spherical droplets, where S is a flat, chemically homogenous surface, L is liquid, V is vapor phase,  $\theta$  is the angle of intersect between liquid and

surface and  $\Theta$  is the minimum total free energy of the system. The laser interaction time in the melting process inside SLM is small and thus  $\theta$  obeys the classical Young's equation (1804) as shown in Figure 6 where,  $\sigma_{SV}$ ,  $\sigma_{SL}$  and  $\sigma_{LV}$  are the surface energies of the system and  $\theta_Y$  is the intersection angle [35].

If the melt pool is considered as a half cylinder, the balling phenomenon occurs when the total surface of the melt pool is larger than a sphere with the same volume ( $L/d > 2.1$ ) unless the molten material has wetted to the underlying substrate. Therefore, in order to avoid the balling phenomena,  $L/d < 2.1$ , which can be achieved through the optimisation of process parameters such as laser scan velocity and power. A study by Kruth et al [35] showed that high laser power fully melt the metallic powder and high scan velocity satisfies  $L/d < 2.1$  as it reduces the length of the melt track, thus reducing the effect of balling. However, studies by Gu et al [36] showed in contrast to the previous study, low scan speeds can also reduce the effect of balling due to the low scan velocity producing increased melt track width, thus satisfying  $L/d < 2.1$ .

Oxides are less reactive and can considerably affect the ability for a material to wet to the underlying substrate. According to Young's law, wetting between solid steel and liquid aluminium should be possible, however, in practical conditions, this is not observed. Jia et al [37] showed that the wetting of the two materials does not occur in practical conditions due to the presence of an oxide layer on the molten aluminium surface which needs to be removed in order for the two materials to wet.

Liu et al [38] Studied the influence of surface morphologies on wettability and flow of molten metal during the formation of single tracks. The study concluded that a small amount of molten metal of the single track on the uneven surface decreased the amount of melt for wetting and resulted in shrinking of the single track. Additionally, the study concluded that oxide films formed on the balls resulted in poor wetting to the substrate of molten material.

The balling effect can also be reduced by decreasing the oxygen content within the build chamber atmosphere. A study processing stainless steels and pure nickel powder by Li et al [39] showed that a build chamber oxygen content of 0.1% produced a smooth melted surface with no balling whereas an oxygen content of 2% and 10% produced clear balling formation. Additionally, the study concluded that balling can be

divided into two categories: ellipsoidal balls and spherical balls. Ellipsoidal balls are caused by a poor ability to wet, these can form in dimensions up to 500µm which can be highly detrimental to SLM build quality. Spherical balls are formed as explained earlier and have no apparent detrimental effect on final build quality with dimensions of 10µm.

Das and Kruth et al [40] explained that the oxide film on the preceding build layer obstructs bonding between layers (which would reduce the surface energy) and leads to balling as molten metal do not readily wet oxide films unless a chemical reaction occurs (in soldering this effect is achieved by the use of fluxes). Delamination can also occur as there are high thermal stresses combined with poor interlayer bonding. Therefore, the study suggested that the low oxygen level would reduce the presence of oxide and repeated laser exposure would break up any oxide films and thus reduce the balling phenomenon.

### **2.2.3 Powder reuse**

The production cost of processing with powder feedstock in SLM is high. A practical solution to overcome the high material costs is to recycle the feedstock from previous builds as only 10-50% of the powder is utilised in the build volume and the cost of a built part can double without the inclusion of a recycling regime [41]. However, once the virgin powder is exposed to the building environment within the SLM process, degradation of the powder occurs, and quality is compromised with repeated use.

Metal powder used in SLM degrades with repeated use through the pick-up of interstitial elements such as oxygen and nitrogen [42][6]. The degradation is considered to be caused by by-products from two main mechanisms within the SLM process, the powder melting process which produce re-melted 'weld splatter', agglomerates and a soot-like condensate of nanoparticles [43] as shown in Figure 7, and contamination from the handling process of powder. These particles can settle on the powder, which can affect powder distribution, layer uniformity and even be incorporated into the build.

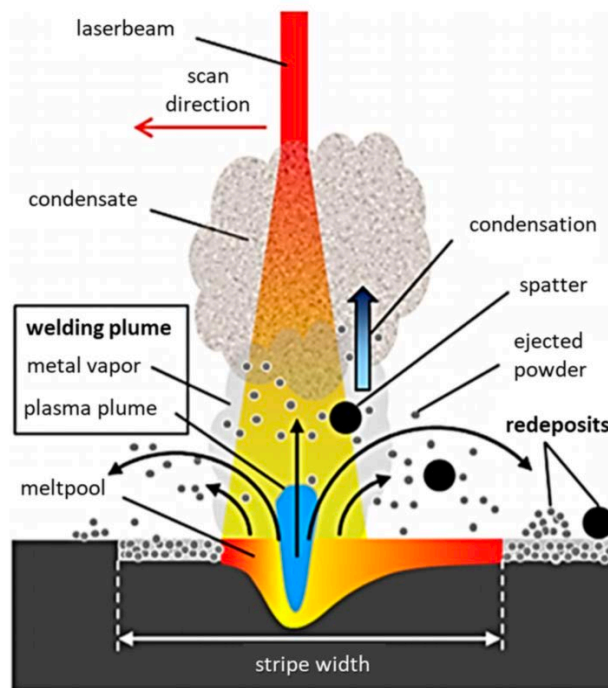


Figure 7: Schematic of SLM process and generation of unwanted by-products (Spatter and condensate)

Adoption of AM in high end, critical applications for industries such as aerospace are hindered by the high raw material cost of metal powder attributed to excessive scrappage of powder due to poor understanding of the degradation mechanism. There is a lack of confidence in the re-use of metal powder even though reuse has long been a unique selling point for the technology as it has the potential to yield large material utilisation.

The cost reduction through powder re-use could be significant for the aerospace industry as the 'buy-to-fly' ratio has the potential to exceed 0.9 in comparison to conventional technique such as machining which yields a buy-to-fly ratio of 0.1. The buy-to-fly ratio is defined as the quantity of material used in flight compared to the total material purchased. However, as powder is degraded with repeated use, combined with a lack of understanding of the impact it has on the final build mechanical properties, confidence in powder re-use is low. Therefore, many manufacturers for high end, critical components such as aerospace applications have specified limits on

the amount of times powder can be used. The reuse of powder is necessary to make the process economically viable [44][45].

Incorporating a robust recycling strategy into processing is important to improve the sustainability of the SLM. There are two common recycling strategies used for SLM fabrication processes; single batch and top up [46].

A single batch recycling strategy allows the powder batch quantity to deplete by completing a series of manufacturing builds without replenishing the powder quantity. Post processed powder is sieved in order to remove out of range oxidised particles, contaminants and agglomerates. The sieved powder is then reintroduced as feedstock into the SLM process, this process is then repeated until there are insufficient powder quantities left to complete any further build cycles.

By contrast, a top-up recycling strategy uses a blending process of virgin powder in order to replenish the feedstock as shown by Figure 8. Post processed powder is collected after the build cycle and a sample of powder is taken from the batch for analysis to evaluate the powder quality from build-to-build to ensure that the powder properties still meet build specifications. The post processed powder is replenished and blended with virgin powder, known as 'top up', and finally reintroduced back into the SLM process as feedstock ready for a new build cycle. This process is repeated until the quality of post processed powder and virgin powder no longer meets the required build specifications. It is important to note that the number of cycles that a powder can be reused for, using the top up method, varies between materials used and process parameters used.

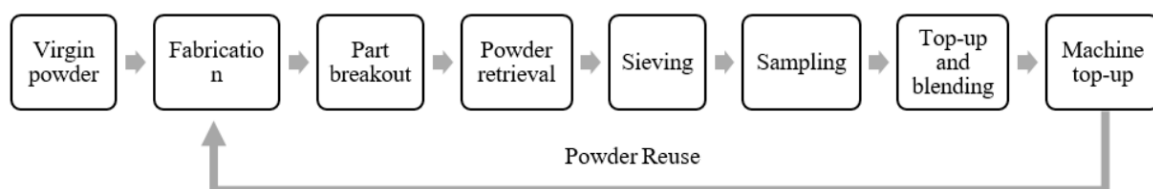


Figure 8: Schematic of the 'top up' recycling process [47]

A study by E. Santecchia *et al* [41] suggested that the production of condensate and spatter by-products leads to laser muting (attenuation) and drift, local changes in process conditions, leading to a change in the mechanical properties of final part and variations in the microstructure. The results concluded that the process parameters and inefficient removal of by-product by gas flow is a key factor in the development of the problems mentioned.

H.P.Tang *et al* [48] investigated the effect of powder reuse on Ti-6Al-4V by selective electron beam melting. The study showed that the oxygen wt % increased significantly as the number of powder reuses increased; reuse number 0 (0.08 wt %) and reuse number 21 (0.19 wt %). The increased oxygen content resulted in an increase in yield strength and ultimate tensile strength from reuse 6 to 20. Additionally, the powder became less spherical and the particle size distribution narrowed with increased powder use. The oxygen specification for grade 23 titanium alloys is a max of 0.13 wt % and 0.2 wt % for grade 5. Thus, based on the evidence presented by H.P.Tang *et al*, the titanium powder was out of specification for grade 23 after reuse 4 and approaching the grade 5 specification limit of 0.2 wt % at reuse 21. The number of reuse cycles also had a direct impact on the elongation of the sample, after 6 reuse cycles, the elongation % dropped from 16 % (virgin) to 13.5%. However, at 21 reuse cycles, the elongation result was 15.5%, although a reduction compared to virgin, the relationship between elongation and oxygen may not be linear.

The featured literature focussed on the effect of re-used powder in the SLM process and the potential consequences it can have on final build quality. The effects of powder re-use differ significantly and are mainly dependent upon the material, process parameters and gas quality. Thus, re-iterating the uncertainty and lack of confidence around the re-use of powder within industry. Understanding the nature of the degradation mechanisms, in particular, the by-products (condensate and spatter) would build confidence within the industry to re-use powder and enable a solution to identify, monitor and if possible, remove problematic particles within post processed powder. The need to understand powder degradation is prominent as industry is transitioning from rapid prototyping and driving towards serial production of components.

## 2.2.4 Hot tearing crack formation

In the form of cracks, hot tearing is a common defect that occurs in processes with rapid cooling rates. Hot tearing forms throughout the semi-solid phase where alloys are in a slurry state during solidification. Hot tearing is more prominent in alloys with a large freezing range due to longer time spent by the alloy in a vulnerable state where a thin film of liquid exists between dendrites. In LPBF, the high cooling rates may promote columnar dendrites which may lead to a higher amount of hot tearing in comparison to equiaxed structures.

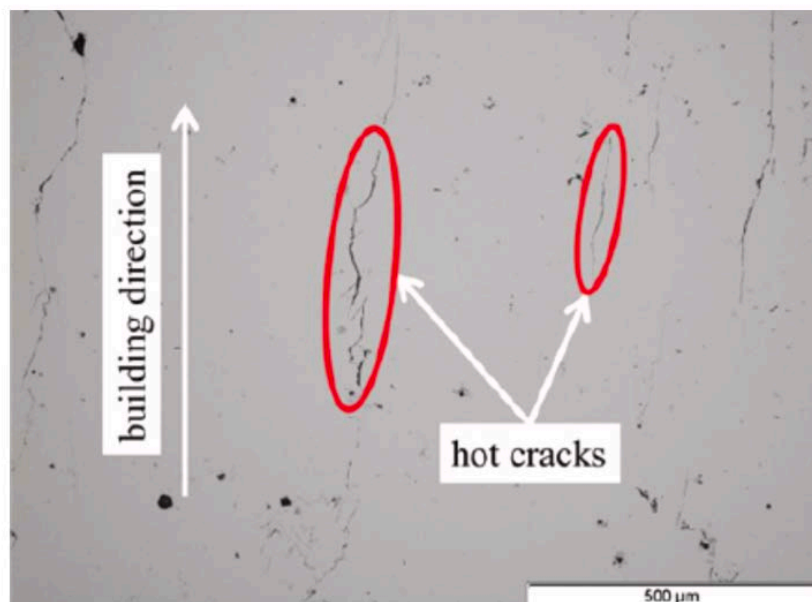


Figure 9: Hot tearing crack formation in LPBF AA-7075 along the build direction

Martin et al [49] showed the formation of cracks in AA-6061 parallel to the build direction which agreed with findings for AA-7075 from Kaufmann et al [50] as shown in Figure 9. Zhang et al [51] reported that the crack formation increased in AA-2024 as the scan speed increased due to the Mg and Cu widening the materials solidification range.

Throughout the solidification process in high strength aluminium alloys, columnar grains form in the direction of the thermal gradient. This results in inter-dendritic liquid



at the interface and in combination with shrinkage, lead to crack formation suggesting that the formation of cracks can be correlated to the melting mode.

The solidification cracks form and grow along the grain boundaries in the latter stages of the solidification due to the thermal stresses, shrinkage, and a lack of liquid filling. The formation of residual stresses exceeding the yield strength of the material during the process of solidification promotes the crack formation [52].

Sun et al [53] studied the hot tearing mechanism for high entropy alloys manufactured using LPBF. The results suggested that intergranular solidification cracks are present regardless of the process parameters and severe stress induced by the large grain size is the root cause for intergranular cracking.

## **2.3 Oxidation**

### **2.3.1 Introduction**

Oxidation of metals is widely used across industry for different applications. However, in SLM, oxidation of the powder bed can create undesirable changes to the mechanical properties of a component. Interstitial elements such as oxygen can dissolve (for some alloys) into the substrate material which can locally embrittle regions of the build. Additionally, oxide layer formation may occur within the build process which coats the particles with an oxide surface layer. This can result in oxide being broken up during the melting process and stirred into the melt pool increasing the risk of delamination between build layers and lead to the formation of micro cracking of the built component.

This section reviews the literature of oxidation fundamentals, specifically, oxidation of titanium alloys. Additionally, the interference phenomenon is reviewed as the interference colours produced from the oxide layer formation formed a crucial part of later investigations.

### 2.3.2 Oxidation fundamentals

Oxidation of metals is considered to be a complex process as it depends on various different factors. Free energy change associated with oxide formation from the reactants is the dominant factor in the oxidation process and oxide layer formation, but reaction kinetics and diffusion play a significant role in the structures formed. Oxide layers will only form if the dissociation pressure of the oxide in equilibrium is less than the ambient oxygen pressure as shown in Equation 2, where  $\Delta G^\circ(M_aO_b)$  is defined as the standard free energy change.

$$pO_2 \geq \exp \left\{ \frac{-2\Delta G^\circ(M_aO_b)}{bRT} \right\} \quad (2)$$

The Ellingham diagram illustrates oxide formation standard free energy as a function of dissociation pressure and temperature. The Ellingham diagram is a useful tool for qualitatively measuring the stability of oxides at different partial pressures of oxygen and temperature. However, the Ellingham diagram does not account for oxidation kinetics and provides no information. Understanding the oxidation kinetics is essential as it forms the basis for elucidation of the oxidation process. Reaction rate is dependent upon numerous variables such as temperature, surface preparation and time of reaction, these relationships can be categorised into the three growth rate laws:

- Logarithmic
- Parabolic
- Linear

Many metals obey logarithmic law at temperatures below 400°C; the reaction rate is rapid initially and then reduces to a negligible rate. Low temperature oxidation of metals can be considered by this direct law and the inverse logarithmic equation as shown in Equation 3 and 4 [54]. Where,  $x$  is the oxide thickness,  $A$  and  $B$  are constants,  $k_{il}$  and  $k_{log}$  are the rate constants and  $t$  is the oxidation process time.

$$\text{Direct law: } x = k_{log} \log(t + t_o) + A \quad (3)$$

$$\text{Inverse law: } \frac{1}{x} = B - k_{il} \log(t) \quad (4)$$

At elevated temperatures metals mainly obey the parabolic law with respect to time rather than the logarithmic law observed at lower temperatures. Parabolic law oxidation rate can be illustrated by Equation 6 [54]. Where  $x$  is the oxide thickness,  $k'_p$  and  $k_p$  are rate constants,  $C$  is the integration constant and  $t$  is time of oxidation.

$$\text{Differential: } \frac{dx}{dt} = \frac{k'_p}{x} \quad (5)$$

$$\text{Integrated: } x^2 = 2k'_p t + C = k_p t + C \quad (6)$$

The linear law differs from logarithmic and parabolic as the linear growth relationship is constant with time and therefore does not depend upon the thickness of the oxide. The linear oxidation law can be described by Equation 8 [54]. Where  $x$  is oxide thickness,  $t$  is time,  $C$  is an integration constant and  $k_i$  is linear rate constant.

$$\frac{dx}{dt} = k_i t \quad (7)$$

$$x = k_i t + c \quad (8)$$

The oxidation process is complex and varies between materials and not often obeys only one standardised oxidation law, instead most metals obey a combination of oxidation rate laws mentioned due to the changing nature of the oxide with respect to time. At the initial stages of oxidation, a primary oxidation law is dominant whilst the second oxidation law is dominant after a prolonged period of time into the oxidation process. At low temperatures, the cubic rate can be observed to combine logarithmic and parabolic rate laws. Whereas at elevated temperatures, the para-linear rate occurs, combining an initial oxidation rate obeying parabolic law and then after a prolonged period of time, the oxidation rate obeys linear rate law. Thermogravimetry is the conventional way to measure oxidation rates and is widely used by material scientists to determine behaviour of metals by studying the change in mass of a heated material of defined surface area with respect to time. The mass change is dependent upon the thickness of the oxide layer and diffusion of oxygen into the substrate material. Determination of oxidation rate and oxidation kinetics can be achieved by factoring the weight gain data into Equation 9 [54] [55].

$$\left(\frac{\Delta W}{A}\right) = Kt^n \quad (9)$$

Where  $\Delta W$  is the weight gain,  $K$  is the rate constant,  $A$  is surface area,  $t$  is time and  $n$  is the reaction index; where  $n=1$  (Linear),  $n=2$  (Parabolic) and  $n=3$  (Cubic). Calculation of the reaction indices is conventionally achieved through regression analysis of a log-log plot of time and weight gain per surface area. Arrhenius law can describe the temperature dependence of the reaction constant as shown by Equation 10, where  $k_o$  is the frequency factor,  $Q$  is the activation energy,  $R$  is the universal gas constant and  $T$  is absolute temperature. Arrhenius plot of  $1/T$  and  $\log k$  values allows a comparison of different metals oxidation resistance over a larger temperature range.

$$k = k_o \exp\left(\frac{-Q}{RT}\right) \quad (10)$$

### 2.3.3 Oxide growth mechanisms

The growth of an oxide can be categorised into four main steps that results in the formation of a uniform layer that covers a substrates surface:

1. Adsorption of oxygen
2. Oxide nucleation
3. Oxide growth laterally
4. Compact oxide layer formation

The primary step in oxide growth is the adsorption of oxygen which results in oxygen attaching onto the substrate surface via physical adsorption or chemisorption [54]. The bonding of the gas molecules to the substrate surface defines the type of adsorption process that occurs. Chemisorption forms stable chemical bonds, whereas in physical bonding, gas molecules are held to the substrate surface via weak van der Waals forces. Chemisorption is generally a slow process in comparison to physical adsorption, however, if the surface of the substrate metal is clean, the process is rapid without significant activation energy. Physical adsorption is a fast process as it commences upon impingement of the metal surface by the gas molecules without, the requirement of activation energy. Upon sufficient adsorption of the oxygen molecules, the molecules dissociate and are absorbed as atoms until a saturated state occurs. Once the metal is saturated with oxygen atoms, the formation of oxide nuclei occurs, and they grow laterally resulting in a thin, compact oxide layer covering the metal surface.

Metal oxides are compounds, therefore further growth of the oxide is dependent upon the mass transport of electrons and ionic species through the oxide layer as shown in Figure 10. Oxide layers have numerous different imperfections which significantly aid the mass transport such as metal/non-metal ions located at the interstitial position and metal/non-metal ion vacancies. Dependent upon the imperfections present and conductivity, oxides can be categorised into two types:

- p-type oxide
- n-type oxide

p-type oxides grow outwards relative to the substrate metal, whereas, n-type oxides grow inwards [56]. In the case of oxidation of titanium alloys, oxygen ions diffuse to react with the metal via n-type anions, resulting in the oxide growing inwards.

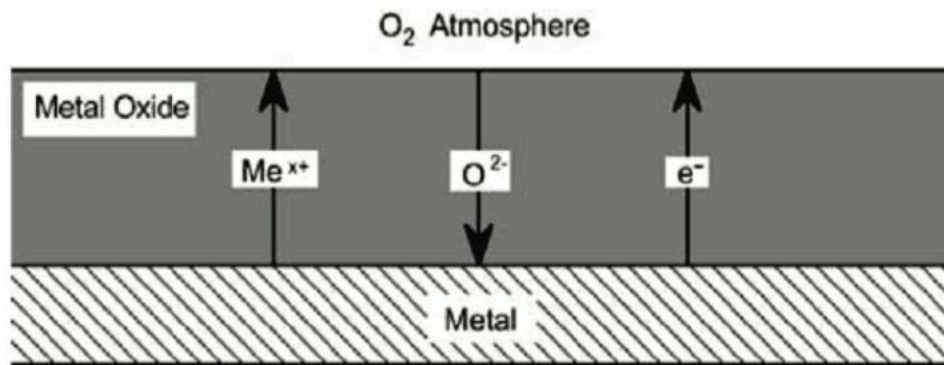


Figure 10: Schematic of mass transport across oxide layer [45]

### 2.3.4 Oxidation of conventional titanium alloys

Titanium has a high affinity to react with oxygen. The rate of the reaction is dependent upon the environmental conditions in which the titanium is exposed such as temperature and pressure. At room temperature, a thin passive  $TiO_2$  oxide film forms due to the reaction between oxygen and titanium which provides protection for the metal surface from corrosion. However, as the temperature increases, the oxide layer no longer protects the metal surface and allows oxygen to dissolve into the core titanium. The solubility of oxygen in titanium is dependent upon the phase;  $\alpha$ -phase titanium is around 34 at % with little variation with temperature whereas  $\beta$ -phase titanium increases in solubility as the temperature increases, peaking at 8 at % at  $1700^\circ C$ . Figure 11 shows the Ti-O phase diagram indicating that many stable titanium oxides can form such as  $TiO$ ,  $Ti_2O_3$  and  $Ti_2O$ . However, at near atmospheric pressure and oxidation temperatures below  $1000^\circ C$ , only the  $TiO_2$  rutile type oxide scale is normally observed [54].

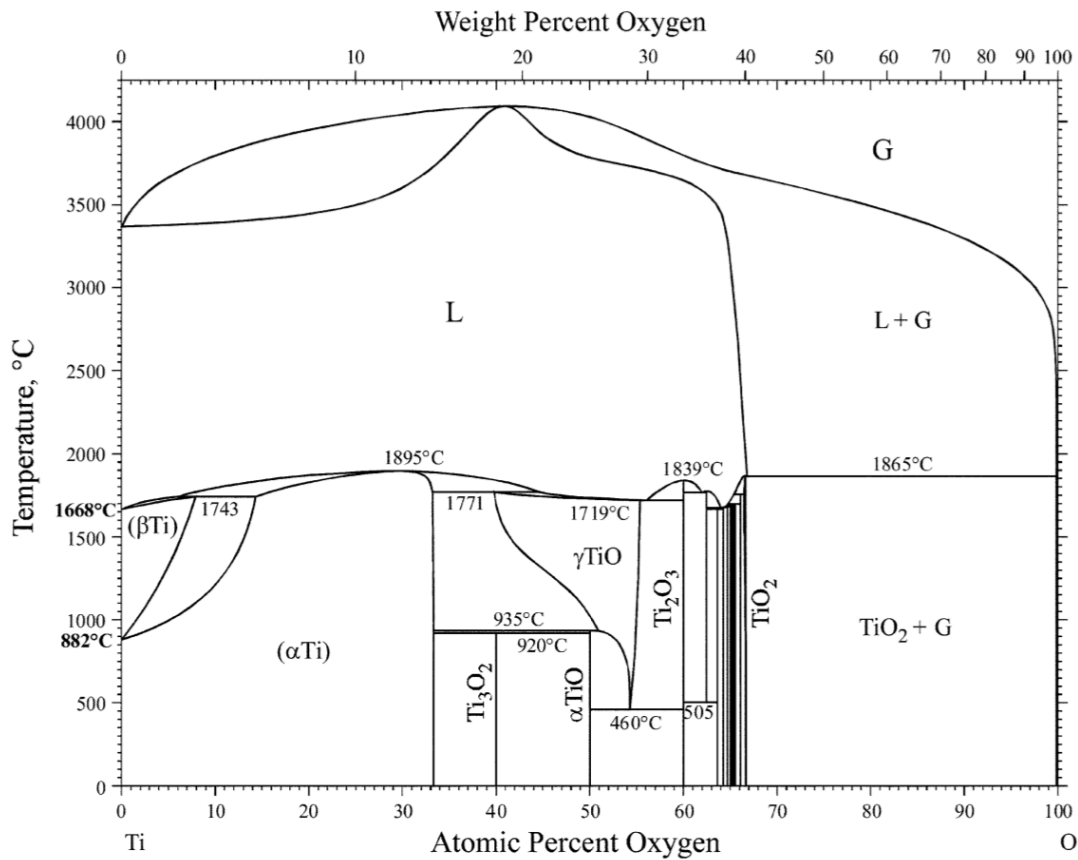


Figure 11: Ti-O phase diagram

The oxidation rate of titanium is heavily dependent upon the alloying elements. Commercially pure (CP) titanium has been investigated extensively to understand how temperature effects oxidation rate and with respect to time as shown in Figure 12. Kofstad et al [57] showed that temperature <400°C followed logarithmic law, temperature in the range of 400-600°C followed cubic law, temperature in the range of 600-700°C followed parabolic law and temperatures >900°C followed linear law. However, at elevated temperature (>600°C), the oxidation rate changes with respect to time, as the exposure time increases, the rate of oxidation shifts to a linear rate. Logarithmic oxidation produced a thin passive oxide layer whereas cubic and parabolic oxidation rates produced a thick surface oxide layer and oxygen diffusion into the titanium core, resulting in a change in mechanical properties as a brittle, hard oxide layer formed. Linear oxidation resulted in cracking and porosity in the oxide layer this was accredited to the high stresses in the oxide layer and titanium core [58][59].

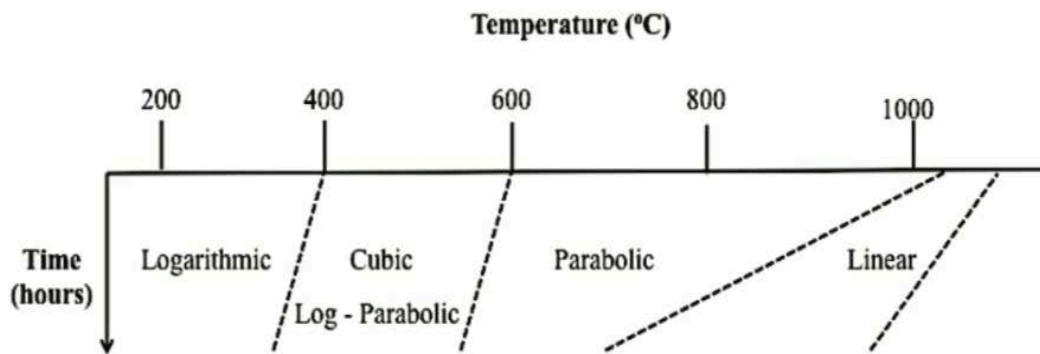


Figure 12: Schematic of oxidation rate with respect to time and temperature. [48]

Alongside CP titanium, there are many other titanium alloys utilised in various industries due to their superior mechanical properties such as Ti-6Al-4V. However, the alloying elements change the oxidation behaviour significantly and add complexity due to the different microstructures. There are many titanium alloys to be considered other than Ti-6Al-4V, however the following section will focus on Ti-6Al-4V as this was the material of choice for this project.

### 2.3.5 Mixed Titanium-Aluminium oxide

Various authors have studied the oxidation of Ti-6Al-4V exposed to different environmental conditions and temperatures. A study by Frangini et al [60] investigated the oxidation behaviour of Ti-6Al-4V between 600-700°C exposed for 300 hours and concluded that between 600-700°C, parabolic law was observed. However, at temperatures above 700°C, linear law was observed after an exposure time of 50 hours. The change in oxidation rate is due to the change of morphology of the formed oxide layer; dense and compact structures are formed at low temperatures whereas higher temperatures result in porous structures and increase the rate of oxidation.

A subsequent study by Du et al [61] showed that Ti-6Al-4V exposed to temperatures of 650-850°C over prolonged periods of time produced a multi layered oxide structure consisting of TiO<sub>2</sub> and Al<sub>2</sub>O<sub>3</sub>. The study concluded that formation of this multi-layered



oxide structure is a phenomenon dependent upon time and temperature where the number of  $\text{Al}_2\text{O}_3$  layers increases with an increase in either dependent variable.

Du et al [61] also discussed a formation mechanism for multi-layered oxide scale structure in Ti-6Al-4V with regards to oxygen and oxygen partial pressure within the oxide scale. As the  $\text{TiO}_2$  forms on the surface of the titanium alloy, the alloy is separated from the environment by the oxide layer whereby the partial pressure of the oxygen in the oxide drops from the gas/oxide interface to the oxide/metal interface resulting in a partial pressure decrease to close to the dissociation pressure of  $\text{TiO}_2$ . The disassociation pressure of aluminium oxide is much lower than that of titanium oxide and would suggest that the aluminium will still oxidise. The earlier oxidation may have depleted the aluminium in the substrate near the metal/oxide interface and therefore it is unlikely that  $\text{Al}_2\text{O}_3$  will form at the oxide/metal interface.

In contrast, aluminium diffuses outwards in the direction of the gas/oxide interface where it reacts with oxygen to form an outer layer of  $\text{Al}_2\text{O}_3$ , this results in the formation of a double oxide layer consisting of  $\text{TiO}_2$  and  $\text{Al}_2\text{O}_3$  [61]. The continued growth of the oxide layers causes cracks at the oxide/metal interface when the critical thickness of the oxide layer is achieved because of the different thermal expansion coefficients between the oxide and substrate metal. At the initial stages of oxidation, the contact remains good between the oxide scale and the substrate [62], however since the plasticity of the oxide is limited, cracking will occur once critical thickness is achieved. The cracking and detachment of the oxide from the substrate metal makes the oxide less protective and so increases the partial pressure of the oxygen close to the oxide/metal interface which promotes the formation of a second  $\text{TiO}_2$  layer. This process repeats itself as the oxidation continues and results in the formation of a multi-layered structure of  $\text{TiO}_2$  and  $\text{Al}_2\text{O}_3$  structure in Ti-6Al-4V as shown in Figure 13 between 650-800°C.

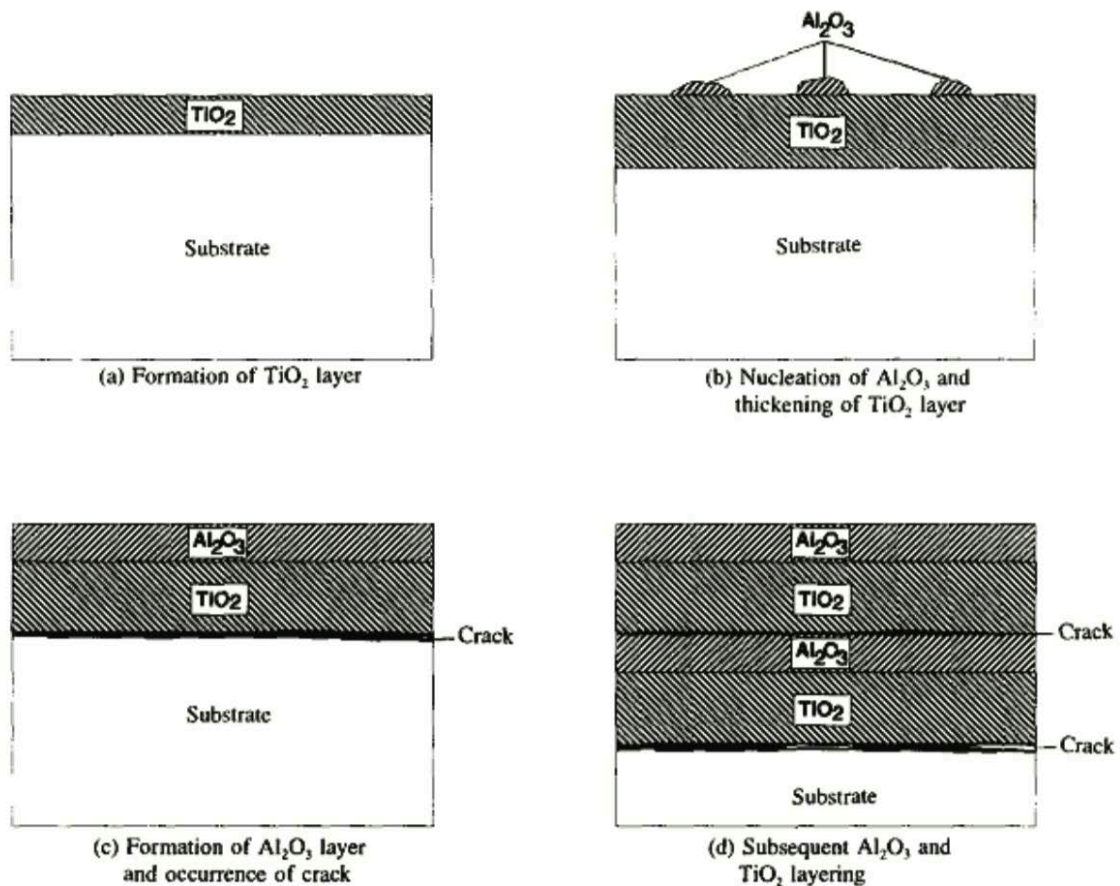


Figure 13: Illustration of the formation of multi-layered oxide structure in Ti-6Al-4V by Du et al [61]

### 2.3.6 Interference phenomenon

Interference phenomena is observed when reflected waves of light are out of phase, such as when light is reflected and refracted by a thin film, this is commonly known as thin film interference, and a common example of the phenomena is observed when there is oil on a wet road.

The colouring of titanium has been used in various different industries such as jewellery, architecture and design for its desired colours and in some applications, the protection associated with the oxide layer formed. Titanium alloys exposed to an oxygen atmosphere, results in a colourless passive nanometre thick oxide film.

However, increasing the thickness of this native oxide film, the surface acquires colour due to the interference phenomena. The colour produced by the thickening oxide layer is observed over a range of thicknesses, which follow the well-established oxidation spectrum for titanium alloys. Interference colours can occur twice over two different thickness ranges, known as first-order colour and second-order colour as shown in Figure 14. The thickening of the oxide can be achieved by thermal oxidation or commonly, anodization.

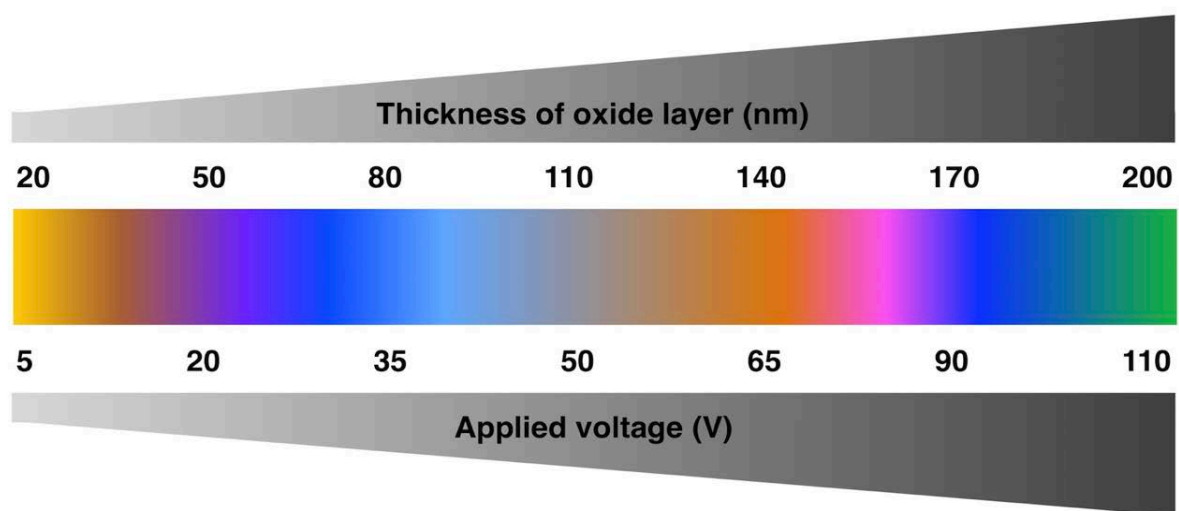


Figure 14: Interference colours produced the oxide thickness, which depends upon the voltage applied during anodisation.

When the oxide is irradiated with light, the surface oxide reflects only a portion of the incident photons, the remaining portion experiences refraction inside the oxide and is reflected by the metal surface. Therefore, after impinging the surface, two different distances are covered by the light wave resulting interference phenomena which is considered to be constructive for in-phase waves and destructive for waves in the opposing phase [63][64], as shown by Figure 15. The refracting film layer makes the light travel a longer path resulting in the light waves reflected from the upper and lower thin film surfaces being out of phase and interfere to cancel wavelengths out and promote others. The cancellation of a wavelength occurs when the reflected and refracted light waves are out of phase, resulting in destructive interference and a colour is observed using white light, here some wavelengths are enhanced, and some

are suppressed. As the oxide thickness layer increases and different colours are observed, the wavelength that is cancelled varies. The surface finish is essential as it influences the colour produced as it determines the behaviour of the light scattering across the surface and thus effects brightness of colours [65].

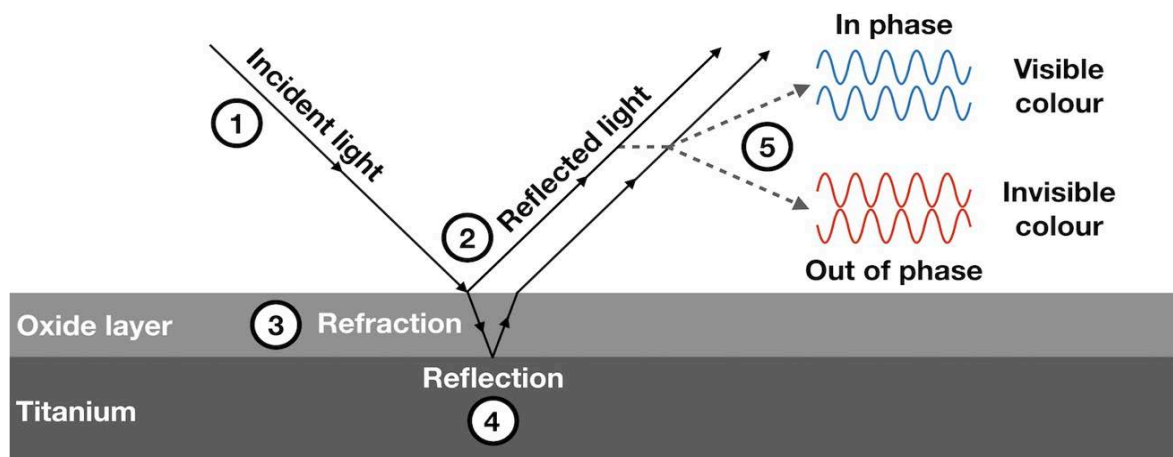


Figure 15: Schematic of two light waves impinging surface oxide during interference phenomena. [53]

The extra distance that is travelled by the refracted wave compared to the reflected wave is called the optical path difference. The optical path difference is a combination of the extra distance travelled by the refracted wave and its retardation due to the refractive index of the material on which the layer has formed. The optical path difference is important as it determines the phase of light and governs the interference and diffraction of the light wave. The refractive index of a material is defined as the ratio of speed of light within the material to the speed of light in a vacuum, this ratio is a measure of a material's optical density. The optical density varies between materials; however, a material must be sufficiently transparent to ensure the incident light wave is not totally absorbed [65].

The ratio is quoted using Snell's law [66] by comparison of the sine of the incident angle of the light wave through a less dense medium and sine of the angle of refracted light in a denser medium as shown in Equation 11.

$$n_1 \sin \theta_1 = n_2 \sin \theta_2 \quad (11)$$

Where  $n_1$  is incident index,  $n_2$  is refracted index,  $\theta_1$  is incident angle and  $\theta_2$  is refracted angle. The optical path difference is the product of two variables; the thickness (t) and the difference in refractive index (n) given by Equation 12.

$$OPD = d_1 n_1 - d_2 n_2 \quad (12)$$

Where  $d_1$  and  $d_2$  is the distance the wave has travelled through the respective medium,  $n_1$  is the largest refractive index and  $n_2$  is the smaller refractive index. The physical thickness of the oxide layer and optical density both significantly influence the optical path difference. Using the OPD, the phase can be calculated using Equation 13 [67].

$$\delta = OPD \left( \frac{2\pi}{\lambda} \right) \quad (13)$$

## 2.4 Titanium Alloys

### 2.4.1 Introduction and Application

This section illustrates the background theory of the titanium research field and includes a literature review for Ti-6AL4V alloy.

Titanium is the fourth most dominant structural elements found in the earth's crust after aluminium, magnesium and iron, overall, it is the ninth most abundant element present within the earth's crust. However, titanium does not naturally occur in its pure state, it

is found in a variety of different states naturally in minerals such as rutile ( $\text{TiO}_2$ ) and ilmenite ( $\text{FeTiO}_3$ ), isolating titanium to a free element is a difficult and expensive process. However, although the processing cost is high, the mechanical properties of titanium make it a perfect metal to be used across a variety of industries such as medical and aerospace. In the case of SLM, titanium alloys undergo an atomisation process in order to get the alloy into powder form.

Titanium is widely used across many different industries, in particular, the aerospace industry, due to titanium's high strength to weight ratio and excellent corrosion resistance. The titanium usage within the aerospace is continually growing as the high strength to weight ratio allows a weight reduction for aircraft. Other industries such as biomedical and marine utilise titanium for components but are only used for high end applications due to the high raw material cost of titanium alloys mainly associated with the processing.

#### **2.4.2 Metallurgy of titanium alloys**

There are two allotropic forms in which pure titanium exists:  $\alpha$ -titanium ( $\alpha$ -phase) and  $\beta$ -titanium ( $\beta$ -phase). The  $\alpha$ -titanium has a hexagonal close packed (HCP) crystal structure and the  $\beta$ -titanium has a body centred cubic (BCC) crystal structure. Figure 16 displays the crystallographic structure and unit cells of the  $\alpha$  and  $\beta$  phases of titanium. Figure 16a displays the hexagonal close packed (HCP) structure of  $\alpha$ -phase titanium displaying different planes such as the basal planes  $\{0002\}$ , the prismatic planes  $\{10\bar{1}0\}$  and pyramidal planes  $\{10\bar{1}1\}$ , Axes  $a_1$ ,  $a_2$  and  $a_3$  display the close pack directions. By comparison, Figure 16b displays the  $\beta$ -phase body centred cubic (BCC) crystal structure with one of six  $\{110\}$  planes [4].

In pure titanium, allotropic phase transition from  $\alpha$ -phase to  $\beta$ -phase occurs at  $882 \pm 2$  °C, this temperature is widely known as the  $\beta$ -transus temperature. At low temperatures (room temperature) to the  $\beta$ -transus temperature,  $\alpha$ -phase is stable, however, temperatures exceeding the  $\beta$ -transus temperature,  $\beta$ -phase is stable.

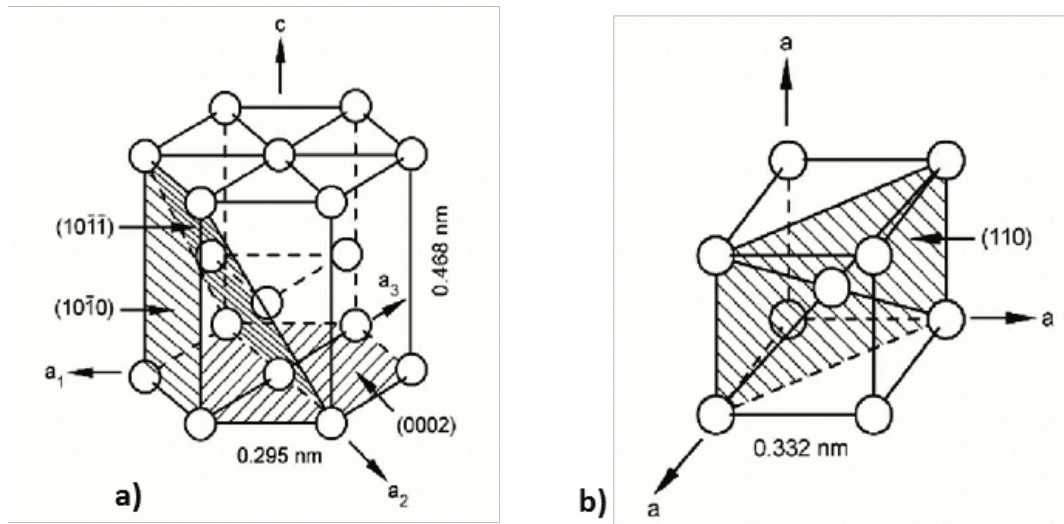


Figure 16: Schematic of titanium crystal structure, a)  $\alpha$ -phase hexagonal close-packed (HCP) and b)  $\beta$ -phase body centred-cubic (BCC) [4]

The presence of titanium in two phases alongside the allotropic phase transformation temperature is essential for titanium alloy processing which allows different mechanical properties to be achieved dependent upon the alloying elements. The stability of the phases at a given temperature is dependent upon the alloying elements, thus the  $\beta$ -transus temperature changes with the alloying element. The aerospace industry has widely alloyed titanium with various different elements for applications such as high temperature compressor blades, jet engine components and many structural components, all requiring slightly different compositions to achieve the given application.

The  $\alpha$ -phase exhibits higher creep resistance in comparison with the  $\beta$ -phase but produces lower ductility due to the lack of symmetry in the HCP structure. Additionally, the  $\alpha$ -phase produces higher strength and stiffness, the Young's modulus varying from 100GPa 145GPa dependent upon the applied load direction relative to the orientation of the crystal [68]. Volume and phase distributions also affect the material properties; the  $\beta$ -phase is both thermally [69] and electrically [70] more conductive than the  $\alpha$ -phase.

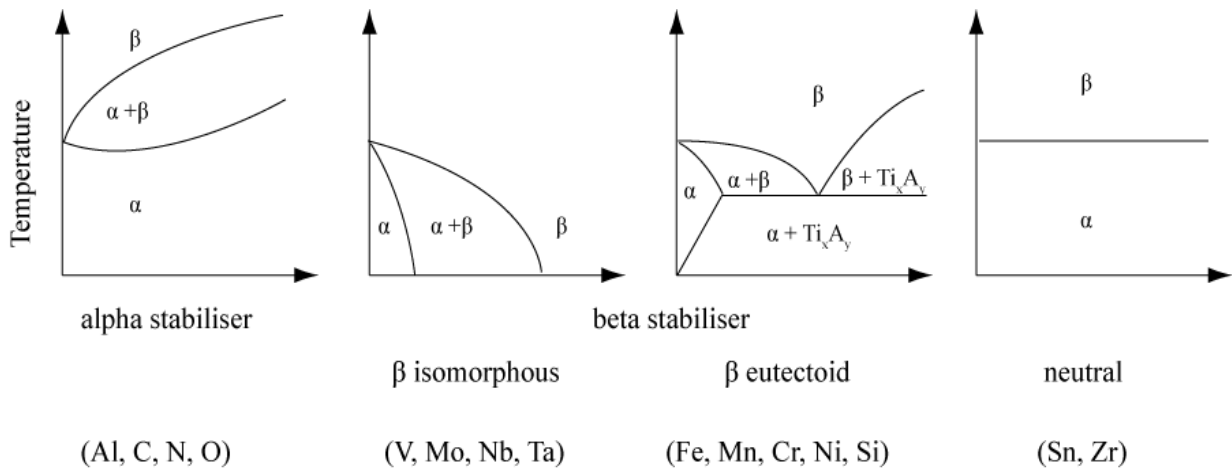


Figure 17: Schematic of the effect of alloying elements in titanium using binary phase diagrams. [67]

Figure 17 illustrates titanium alloy phase diagrams and shows the impact different alloying elements have on the  $\beta$ -transus temperature. There are three categories of alloying elements to titanium,  $\alpha$ -stabilizer,  $\beta$ -stabilizer and neutral elements. Elements added to titanium in order to increase the  $\beta$ -transus temperature are called  $\alpha$ -stabilizers whereas elements added to reduce the  $\beta$ -transus temperature are called  $\beta$ -stabilizers. Alloying elements that have no effect on the  $\beta$ -transus temperature are called neutral elements. There are two categories of  $\beta$ -stabilizing elements;  $\beta$ -isomorphous and  $\beta$ -eutectoid.  $\beta$ -isomorphous is categorised as elements with a high solubility in titanium whereas  $\beta$ -eutectoid is categorised as elements that have limited solubility in titanium and form intermetallics.

The most commonly used  $\alpha$ -stabilizing element is aluminium (Al) due to its high solubility in both  $\alpha$  and  $\beta$  -phase alongside the ability to raise the  $\beta$ -transus temperature as shown in Figure 17. However, to avoid the formation of titanium aluminide ( $Ti_3Al$ ) precipitates in the  $\alpha$ -phase, the aluminium content of most titanium alloys is limited to around 6 wt %. Figure 18 displays that an aluminium content of 6 wt % in titanium can increase the  $\beta$ -transus temperature from 882 °C (pure titanium) to 1000°C.



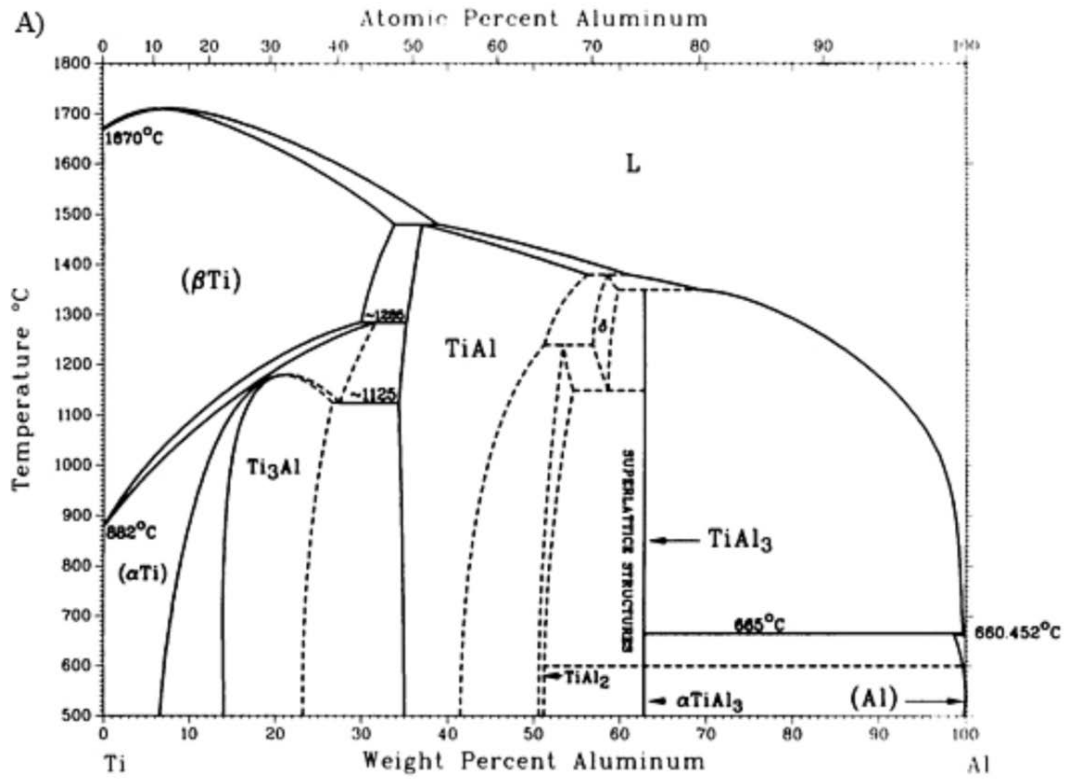


Figure 18: Ti-Al phase diagram

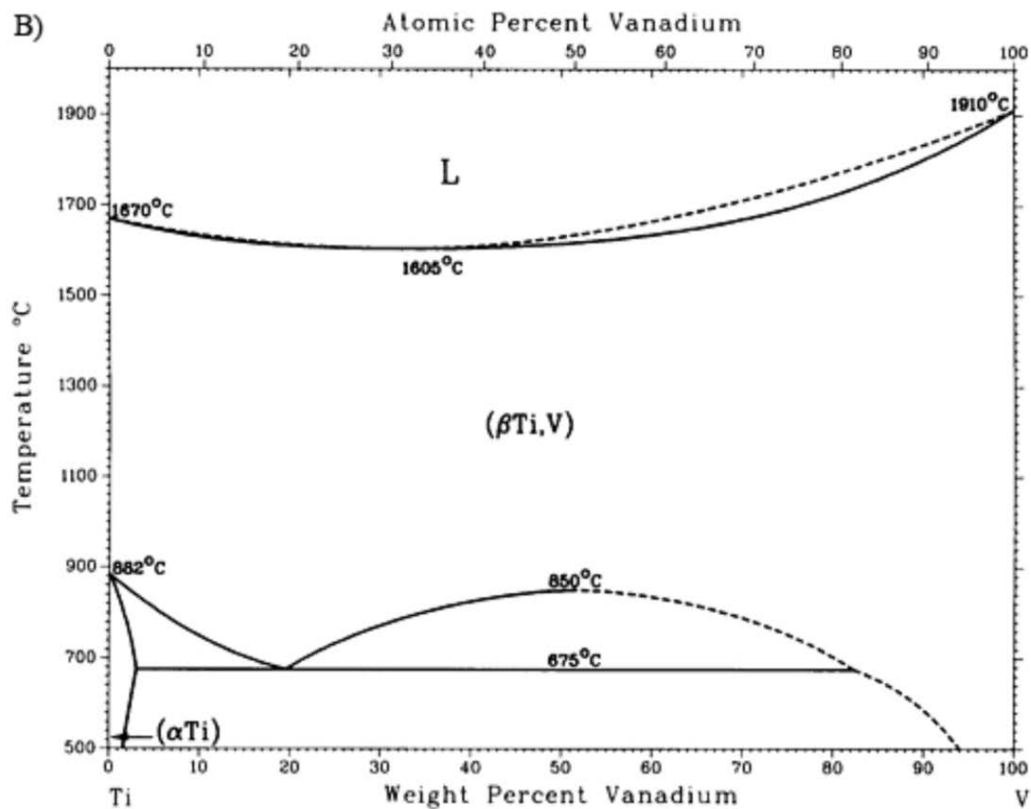


Figure 19: Ti-V phase diagrams

Commonly used  $\beta$ -isomorphous stabilizing elements are Vanadium (V) and Molybdenum (Mo) and in sufficient amount stabilize the  $\beta$ -phase at room temperature. Different quantities of these stabilising elements are present for different alloying applications, in the case of Ti-6Al-4V, the vanadium (V) content is around 4 wt %. Commonly used  $\beta$ -eutectoid stabilising elements are chromium (Cr) and iron (Fe) to reduce the  $\beta$ -transus temperature whereas zirconium (Zr) and hafnium (Hf) do not significantly impact the  $\beta$ -transus temperature and are considered to be neutral alloying elements. Oxygen also plays a key role as an  $\alpha$ -stabilising element due to its high solubility and ability to significantly increase the strength of titanium alloys.

### 2.4.3 Alloy classification

There are three main classes of titanium alloy;  $\alpha$ -phase,  $\beta$ -phase and  $\alpha+\beta$ -phase. Two subclasses of these alloys are near  $\alpha$ -phase and near  $\beta$ -phase (metastable). The alloy

classification is dependent upon the type of alloying elements and the quantity present which in turn defines the dominant phase at room temperature as shown in Figure 20.

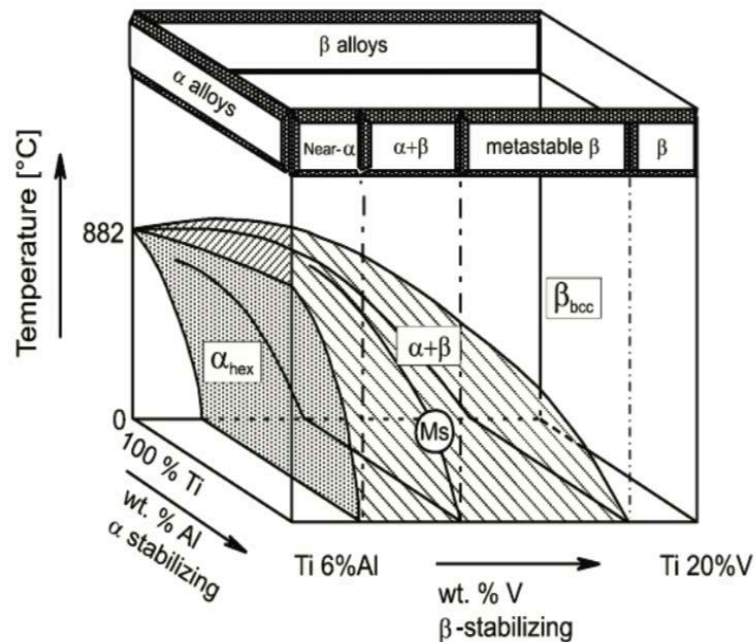


Figure 20: 3-D schematic of titanium alloy classification phase diagram [60].

The  $\alpha$ -phase and near  $\alpha$ -phase alloy classification consists of commercially pure titanium (CP) and alloys that comprise of  $\alpha$ -stabilising elements and/or neutral alloying elements. Commercially pure titanium (CP) is graded based upon the oxygen content which dependent upon the level of oxygen results in reduced ductility and increased strength. Chemical analysis of these alloys will often detect small amounts of contamination/impurities from the manufacturing process such as carbon and iron elements. The  $\alpha$ -phase alloys are characterised by high deformability and excellent corrosion resistance and thus used in engineering and chemical applications. Whereas, near  $\alpha$ -phase alloys have small volume fractions of  $\beta$ -stabilising elements such as silicon that segregate to dislocations and grain boundaries forming titanium disilicide ( $\text{TiSi}_2$ ) precipitates that resist deformation. This results in high strength and excellent creep resistance, making these alloys excellent for high temperature applications operating up to 500-550°C [71].

The  $\beta$ -phase and near  $\beta$ -phase (metastable) alloy classification are located in the  $\alpha+\beta$ -phase region and usually consist of  $>15$  wt %  $\beta$ -stabilising element. Martensitic formation does not occur within these  $\beta$ -phase alloys upon fast cooling from high temperature. These alloys are typically used in applications for orthodontics, medical and aerospace sectors due to its high strength, fatigue strength and high toughness. However, in comparison to  $\alpha+\beta$ -phase alloys, these alloys have a high cost and a small processing window.

The  $\alpha+\beta$ -phase alloy classification is located in the  $\alpha+\beta$ -phase region consisting of both  $\alpha$ -stabilising and  $\beta$ -stabilising elements which are in larger quantities compared to  $\alpha$ -phase alloys. These  $\alpha+\beta$ -phase alloys are typically used in both commercial and military aircraft applications due to the excellent corrosion resistance, high damage tolerance and high strength. Ti-6Al-4V is the most commonly used  $\alpha+\beta$ -phase alloy, accounting for approximately 50% of total titanium alloy production worldwide due to its excellent workability, weldability and heat treatability.

#### **2.4.4 Diffusion controlled transformation**

A diffusion-controlled transformation occurs when the rate of cooling is controlled or slower than that of a diffusionless transformation. A diffusion-controlled transformation in Ti-6Al-4V impacts the orientation, morphology and distribution of the equilibrium  $\alpha + \beta$  phases. The determining characteristic of this transformation is the Burger orientation relationship between the  $\alpha + \beta$  phases and is defined as:  $\{110\}_{\beta} // (0001)_{\alpha}$  and  $\langle 111 \rangle_{\beta} // \langle 11-20 \rangle_{\alpha}$  [72][73].

The Burger orientation relationship can result in twelve potential crystallographic  $\alpha$  structures in one parent  $\beta$  grain. In the case of the Widmanstätten morphology, the nucleating  $\alpha$  phase forms high aspect ratio laths, resulting in a crystallographic relationship with the prior  $\beta$  matrix [72].

At the primary of the transformation, the  $\alpha$  grain boundary nucleates on the prior  $\beta$  boundary to form Widmanstätten  $\alpha$  plates which can produce colonies (similarly arranged platelets) or a basketweave structure. A basketweave structure suggests

that more rapid cooling has occurred or an enrichment of  $\beta$  stabiliser during phase transformation. An increase in temperature and time in the  $\beta$  solution results in an increase of the number of Widmanstätten  $\alpha$  plates. However, the number of Widmanstätten  $\alpha$  plates will decrease with rapid cooling rates and higher  $\beta$  stabilising elements [74].

#### **2.4.5 Diffusionless transformation**

The martensitic transformation is a diffusionless transformation which is achieved with high cooling rates, conventionally in the form of water or oil quenching. A diffusional transformation occurs at slower cooling rates such as air cooling or furnace cooling. The high cooling rates from the  $\beta$ -phase field transform the titanium alloys from  $\beta$ -phase (bcc) to  $\alpha$ -phase (hcp) occurs via a displacive transformation to form  $\alpha'$  martensitic structure. A range of  $M_s$  temperatures have been stated for Ti-6Al-4V from 575 °C [75] to 800 °C [76] dependent upon initial microstructure, impurity elements and composition homogeneity [77].

Banerjee et al [72] investigated the martensitic transformation and suggested that there are three main steps in the displacive mechanism as shown in Figure 21. The first mechanism is the Bain distortion which turns the cubic lattice into orthombic or hexagonal. The second step is a lattice shear by either slipping or twinning relative to the invariant plane. The third step is a shuffling in the [1-10] direction on the (110) plane to orientate the atoms into the proper hexagonal positions of the martensite.

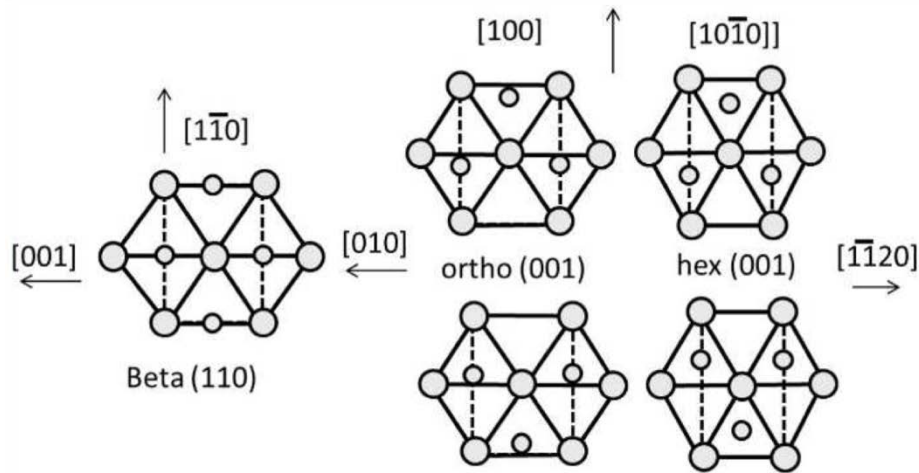


Figure 21: Illustration of the martensitic transformation mechanism [68]

The morphology of the  $\alpha'$  martensitic structure is dependent upon the alloy content and is classified into two different microstructures; acicular martensite and massive (packet) [78]. Acicular martensite comprises of combinations of individual  $\alpha'$  plates belonging to different Burger orientations [79]. In contrast, massive packet martensite comprises of large irregular regions with packets of small parallel  $\alpha'$  plates belonging to the same  $\alpha'$  variants, there being no observable features under the optical microscope.

The microstructure formed by rapid cooling rates from the  $\beta$ -phase varies dependent upon the amount of isomorphous  $\beta$ -phase stabilisers present such as vanadium, niobium and molybdenum. The microstructural differences influence the mechanical properties of the titanium alloy such as the hardness and the Young's modulus [80]. The addition of  $\alpha$ -phase stabilising elements such as tin or aluminium to alloys that exhibit  $\beta$ -phase to  $\alpha''$  martensitic transformation (Ti-V, Ti-Nb or Ti-Mo) leads to the  $\beta$ -phase to  $\alpha''$  transformation is suppressed.

A study by Ikeda et al [37] showed that the  $\beta$ -phase to  $\alpha''$  martensitic transformation was suppressed by an addition of 3 at % aluminium in Ti-11 at % Molybdenum alloys quenched from the  $\beta$ -phase. The transformation suppression is caused by lattice distortion in the  $\beta$ -phase, the addition of aluminium increases the resistance for lattice displacement of the martensitic transformation [81][82].

The  $\beta$ -phase to  $\alpha''$  martensitic transformation can also be suppressed by the addition of oxygen as this is also an  $\alpha$ -phase stabilising element. Tahara et al [83] investigated the  $\alpha$ -phase martensitic transformation in Ti-20-at% Nb alloy and showed that the transformation was suppressed by the addition of 0.7 at % oxygen. The study suggested the addition of oxygen to the alloy created a strain field induced by the oxygen atoms, resulting in the suppression of the martensitic transformation.

Salloom et al [84] investigated the effect of oxygen on phase stability and  $\beta$ -phase to  $\alpha''$  martensitic transformation in Ti-Nb alloys. The study showed that the oxygen atoms created significant lattice distortions occupying octahedral interstitial sites. The oxygen interstitials oppose the atomic reshuffle required for martensitic transformation but also stabilise the  $\beta$ -phase by inducing local elastic shear strains at low oxygen concentrations of 1 at %. The cancelling of the fields stabilises the  $\beta$ -phase and suppress the  $\beta$ -phase to  $\alpha''$  martensitic transformation and consequently decrease the martensitic start temperature ( $M_s$ ). The study concluded that an increase in oxygen concentration increases the stabilisation of the  $\beta$ -phase.

## **2.5 Ti-6Al-4V alloy**

Ti-6Al-4V is a combination of  $\alpha$ -phase and  $\beta$ -phase stabilising elements, ranging 5.5-6.75 wt % aluminium (Al) as the  $\alpha$ -phase stabiliser and 3.5-4.5 wt % vanadium (V) as the  $\beta$ -phase stabilising element. These  $\alpha$ + $\beta$ -phase stabilising elements increase the  $\beta$ -transus temperature from 882°C (pure titanium) to 995 °C and allow both phases to be present at room temperature.

Ti-6Al-4V is the most popular titanium alloy used throughout industry and accounts for more than half of all industrial titanium applications [85][86]. The aerospace industry utilises Ti-6Al-4V extensively for gas turbine engine fan blades and airframe structures due to the high strength to weight ratio and ability to tailor its mechanical properties for high temperature applications. However, other industries such as marine and biomedical have increased their usage of Ti-6Al-4V due to the excellent corrosion resistance, high tensile strength and excellent biocompatibility.

### 2.5.1 Microstructure of conventional Ti-6Al-4V

The microstructure of Ti-6Al-4V is highly dependent upon its thermal processing history. Thermomechanical processing allows the mechanical properties to be tailored according to the specific end use application. The resultant microstructures are categorised as lamellar, bi-modal and equiaxial.

The process of annealing the alloy above the  $\beta$ -transus temperature produces recrystallisation of beta grains resulting in lamellar microstructures. If lamellar microstructures are required for a given end use application, industrial processes beta anneal Ti-6Al-4V to produce beta recrystallisation, however the recrystallised microstructure produced highly depends on the cooling rate. As shown in Figure 22, If the cooling rate is slow from above the  $\beta$ -transus temperature, alpha plates nucleate at the  $\beta$ -phase grain boundaries. The alpha plates grow into the beta phase grain parallel to  $\alpha$ -phase plane  $\{\bar{1}\bar{1}00\}$  and  $\beta$ -phase plane  $\{\bar{1}12\}$ . This alpha plate growth will continue in this direction until other colonies of alpha plates are met that have also nucleated from the beta grain boundary. However, when the cooling rate is increased, an acicular  $\alpha$ -phase forms whereby the lamella size and thickness decreases. If the cooling rate is  $>1000^{\circ}\text{C}\cdot\text{min}^{-1}$ , a martensitic reaction occurs from the  $\beta$ -phase decomposition, dependent upon the temperature the Ti-6Al-4V is being quenched from, alpha prime,  $\alpha'$  (CPH) or alpha double prime,  $\alpha''$  (orthorhombic) forms resulting in a decrease in material ductility [87][4].



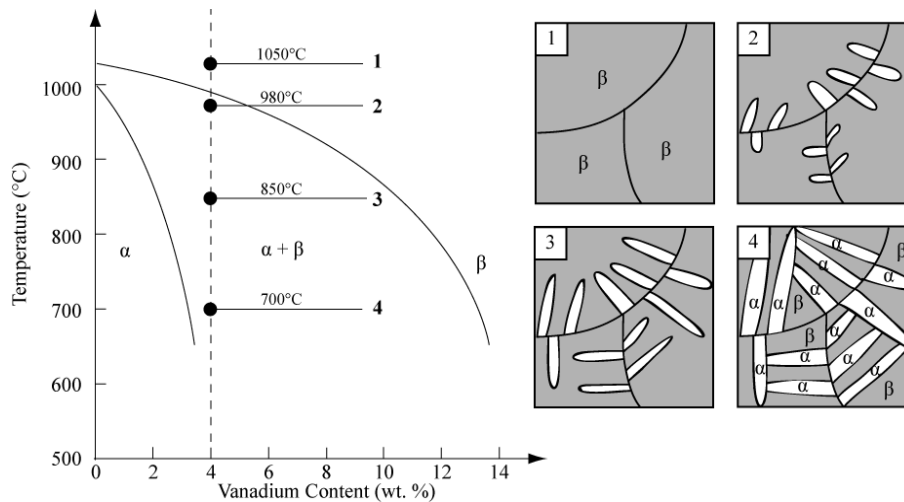


Figure 22: Adapted from Donachie, *Schematic of Ti-6Al-4V microstructure development with a slow cooling rate.*

The formation of bimodal microstructures is a multi-step process. The Ti-6Al-4V alloy is homogenised above the  $\beta$ -transus temperature and then cooled to room temperature. The width of the  $\alpha$ -phase lamellae and thus the primary alpha size ( $\alpha_p$ ) is dependent upon the cooling rate from the homogenisation temperature. The lamellae are then plastically deformed within the  $\alpha+\beta$  phase region in order to introduce dislocations and aid recrystallisation of  $\alpha+\beta$  phases. The volume fraction of the isolated equiaxed primary alpha ( $\alpha_p$ ) that forms at the triple points of  $\beta$  grains is dependent upon the temperature of recrystallisation. The formation of the primary alpha ( $\alpha_p$ ) in this way produces an  $\alpha+\beta$  lamellar microstructure whereby the  $\alpha$  grains are isolated [88][4].

A similar thermomechanical process is involved in the formation of equiaxed microstructure, however, equiaxed microstructures can be obtained via two different processes. The first process promotes the growth of the alpha grains instead of the alpha lamellae within the beta grain by utilising a low cooling rate at recrystallisation. Whereas the second process utilises a low recrystallisation temperature to achieve equilibrium volume fraction of the  $\alpha$ -phase forming from deformed lamella microstructures. In the case of Ti-6Al-4V alloys, the recrystallisation temperature utilised for this process ranges between 800-850°C.

The addition of alloys and thermomechanical processing can significantly change the mechanical properties and microstructure of titanium alloys to optimise for a given application. However, unwanted interstitial elements can diffuse into the titanium during the process, therefore these processes are usually conducted under inert atmospheres or a vacuum to prevent pickup from elements such as oxygen and nitrogen. In selective laser melting (SLM), the inert gas atmosphere (Argon) still has residual oxygen and nitrogen present within the build chamber, along with the very high surface area of the powder, and consequently the titanium alloys pick up oxygen and nitrogen during the process altering the mechanical properties of the final build fairly easily. The next section investigates the effect of interstitial elements have on titanium alloys and impact they have on the mechanical properties of finished components.

### **2.5.2 Microstructure of Ti-6Al-4V processed by SLM**

During the SLM process, the powder layer is melted rapidly by the focused laser beam which bonds the present layer with the subsequent layer. As the subsequent layers are melted, the previously melted layers undergo repeated thermal cycles of cooling and reheating. By comparison with conventional thermomechanical processes, SLM exhibits large thermal gradients ( $10^6\text{K/m}$ ), rapid cooling and solidification rates ( $10^8\text{K/s}$ ).

Due to the rapid cooling and solidification conditions, Ti-6Al-4V (bcc  $\beta$ -phase) processed using SLM produces a metastable hcp  $\alpha'$  martensitic phase, through a shear type transformation process which is diffusionless. Consequently, the microstructure produced consists of fine  $\alpha'$  martensite within columnar prior  $\beta$  grains which favour intergranular failure degrading the alloys ductility [89][90]. The fine  $\alpha'$  martensitic structures also hinder dislocation movement resulting in further reduced ductility. It is also important to note that the  $\alpha'$  martensite produced using SLM is noticeably different from that of conventional processing methods [91].

The microstructures tend to have a fine basketweave contained within large elongated  $\beta$  grains that extend across multiple build layers in the direction of the temperature

gradient (heat flux) because of repeated epitaxial growth of previously deposited titanium [92]. During the SLM process, the molten pool solidifies via transformation into the  $\beta$  phase when it cools down to solidus temperature followed by the formation of  $\alpha'$  phases within the prior  $\beta$  grains. This is due to high cooling rates as the temperature falls to the  $M_s$  which has been reported to be  $10^4$ - $10^6$  °C  $s^{-1}$  [16][93].

### 2.5.3 Prior $\beta$ columnar grains

The large  $\beta$  grains are formed due to the solidification conditions combined with the phase relationship of the titanium alloy being processed. The laser melts the deposited powder layer and some of the substrate beneath it, raising the temperature of a small portion of substrate material to above the  $\beta$ -transus which transforms it to a cubic  $\beta$ -phase. The  $\beta$ -phase returns to the orientation prior to the transformation because of regrowth of the residual  $\beta$  retained between laths. As the laser moves along the scan path, the molten materials rapidly cools and solidifies, the low solute partitioning in titanium combined with large thermal gradients in the melt pool result in insufficient super cooling of the solidification front and thus, no nucleation ahead of the growth front occurs [93]. The solidification of the molten material occurs epitaxially on to the  $\beta$  grain at the fusion boundary, therefore continuing the grain. This process is repeated for each powder layer deposited in SLM and as no nucleation occurs ahead of the solidification front, the columnar  $\beta$  structure forms across many powder layers [94].

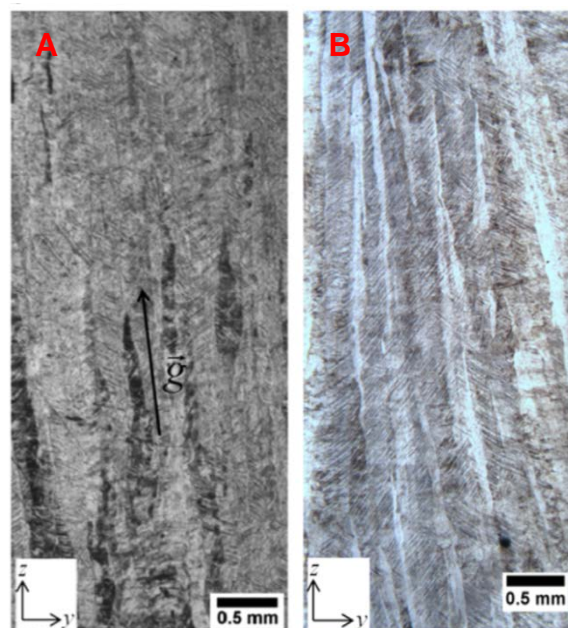


Figure 23: A) optical micrograph showing microstructure of as-built SLM Ti-6Al-4V lateral plane with the dominant prior  $\beta$  grain growth direction B) optical micrograph showing microstructure of stress relieved SLM Ti-6Al-4V lateral plane. [72]

The morphology of the  $\beta$  prior columnar grains in SLM Ti-6Al-4V can be seen in Figure 23 and produces continuous multi layered structures which are much higher than layer thickness with reported size varying between 0.2 to 4mm in width and 1 to 20mm in length [31][95][96][90].

Microstructure plays a crucial role in governing the material properties of a part built by SLM. Therefore, numerous studies have investigated the built part microstructure of titanium processed by SLM. Thijs et al [16] studied the impact scanning strategy and process parameters had on the microstructure in SLM and reported that the as-built parts displayed a microstructure with fine acicular  $\alpha'$  precipitates in the columnar original  $\beta$  grains and the average width of the  $\beta$  grains is directly associated with the scan track width. However, Simonelli et al [97] disagreed suggesting that the average columnar grain width is equal to the hatch distance.

Simonelli et al [98] processed Ti-6Al-4V using SLM into cubic blocks in order to analyse the microstructure of the SLM built part compared to wrought. The study concluded that the microstructure from the SLM part produced fine martensitic and secondary alpha phase, orientated columnar grains, periodic band structures and flat defects. L Wang et al [99] studied the microstructure of Ti-6Al-4V using optimised process parameters and found that the SLM built part featured anisotropy between the X-Z section and X-Y section. The X-Z section featured a columnar microstructure, and the X-Y section featured an equal axis microstructure due to epitaxial growth.

Similarly, Facchini et al, Thijs et al [16] and Gong et al [100] all-reported similar findings with regards to the microstructure of titanium processed by SLM using the same process parameters; layer thickness of 60 $\mu$ m, focal offset distance of 2mm and energy density of 50.62 J/mm<sup>3</sup> concluding that the printing parameters were key to achieving such microstructure. However, Xu et al [101] reported a ultrafine lamellar  $\alpha + \beta$  structure in the as built part without having noticeable grain coarsening.

## 2.5.4 $\alpha'$ -martensite grains

The large thermal gradients coupled with fast cooling rates in the SLM process produce  $\alpha'$ -martensite grains. At room temperature, the  $\alpha'$ -martensite phase dominates the SLM as-built Ti-6Al-4V microstructure producing fine needle-shaped grains embedded within prior columnar  $\beta$  grains.

Yang et al [102] suggested that  $\alpha'$ -martensite has a hierarchal structure and is composed of four martensite's; primary, secondary, tertiary and quartic  $\alpha'$ -martensite's as shown in Figure 24. The morphology of these martensite's can be controlled by the processing parameters in the SLM process resulting in sizes of 1-3 $\mu\text{m}$  for primary and secondary  $\alpha'$  and up to 20nm for quartic  $\alpha'$ .

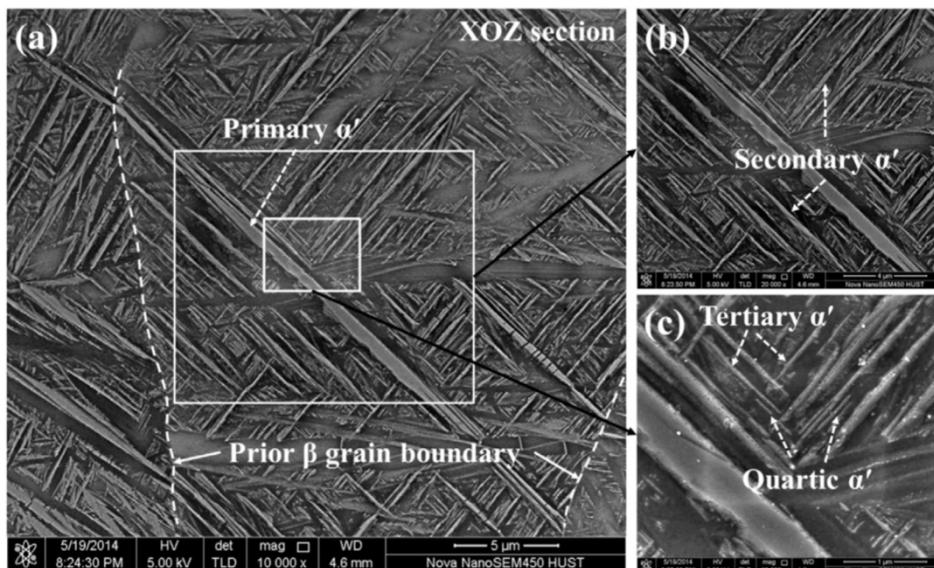


Figure 24: SEM micrograph of SLM built Ti-6Al-4V microstructure showing primary, secondary, tertiary and quartic structure [61]

Do et al [103] suggested that the grain size of the  $\alpha'$ -martensite increases with the increase in laser energy input because the increasing energy density contributes to a slower cooling rate and thus a higher  $\alpha'$ -martensite grain morphology is produced. The thermal conductivity of Ti-6Al-4V at room temperature is very low and therefore the heat produced from subsequent layers amasses in the built part. The amount of heat in the built part increases with the number of build layers which results in higher

temperatures and consequently a lower cooling rate, in particular towards the centre of the built part resulting in coarse grains [104].

A study by Borisov et al [105] showed that Ti-6Al-4V alloy processed by SLM undergoes a significant phase transformation. Heat treatment of the built Ti-6Al-4V SLM part, martensitic phase continues to decompose with the formation of  $\alpha$  and  $\beta$  phases. The study concluded that the microstructure produced of the built SLM parts produced needle shaped fine  $\alpha'$ -martensite phase and the heat treatment produced the formation of free fine  $\alpha$ -phase and  $\beta$ -phases at the grain boundaries. The mechanical properties of the resulting microstructure prior to heat treatment produced high strength but low ductility, limiting their application. However, post heat treatment, the samples agreed with ASTM F2924 by strength and ductility [106].

### **2.5.5 Hardness of Ti-6Al-4V processed by SLM**

A recent study by Khoransani et al [107] showed the effect of SLM process parameters on hardness, tensile strength and surface quality of Ti-6Al-4V using Taguchi design of experiment where 25 samples were manufactured and five repetitions for each were printed. The study varied the processing parameters and found that higher laser power and lower scanning speed produced higher hardness as the melt pool quality was good, resulting in better energy transfer. Lower than optimum hatch spacing resulted in an increase in hardness and vice versa, higher than optimum hatch spaces reduced the hardness of the part. Additionally, low scan pattern angle produced higher hardness due to double remelting of overlap of previous layers.

Ti-6Al-4V processed by SLM produces a range of Vickers hardness which is considerably higher than that of conventional Vickers hardness for cast Ti-6Al-4V which produce a hardness value of around 200Hv [108]. The reason for the increased Vickers hardness values is likely due to the fine martensitic alpha structure which impedes movement of dislocations. Thijs et al [16] Investigated the Vickers microhardness for Ti-6Al-4V processed by SLM with varying scanning velocities. The study reported an average Vickers microhardness of  $409 \pm 36$  Hv for the reference

specimen and concluded that the Vickers microhardness values increased as the scanning velocity increased.

## 2.6 Interstitial elements in titanium alloys

### 2.6.1 Mechanical effects in titanium alloys

Solid solution strengtheners are commonly used within titanium alloys, utilising elements such as carbon, nitrogen, and oxygen (also sometimes present as impurities), to alter the mechanical properties. This is especially true of commercially pure (CP) titanium, the levels present being dependent upon the end use application of the material. Commercially pure titanium (CP) is predominately graded by the content of oxygen present resulting in increased strength and reduced ductility. Grade 1 commercially pure titanium (CP) has the lowest quantity of interstitial elements present resulting in low strength; thus, this grade is typically used for its excellent corrosion resistance. As the concentration of interstitial elements such as oxygen increase, the tensile strength increases but resistance to corrosion decreases, thereby resulting in end use applications trying to find the optimum trade-off between tensile strength and resistance to corrosion.

Table 2: Concentration of interstitial elements in titanium alloy wire [104].

ASTM Grade	Max Element Concentration (wt. ppm)				Tensile Strength (MPa)
	O	C	N	Fe	
Grade 1	1800	800	300	20	240
Grade 2	2500	800	300	30	345
Grade 3	3500	800	500	30	450
Grade 4	4000	800	500	50	550
Grade 5 (Ti-6Al-4V)	2000	800	500	500	895
Grade 23 (ELI Ti-6Al-4V)	1300	800	300	250	793

Similarly, the two grades of Ti-6Al-4V alloy are also graded dependent upon the concentration of oxygen within the alloy as seen in Table 2. [109] Grade 5 alloy has a maximum oxygen concentration of 0.2 wt % and is most commonly used in applications for the aerospace and oil industry, due to the excellent mechanical properties such as fatigue resistance, low thermal expansion and high strength to weight ratio. Whereas grade 23 has a maximum oxygen concentration of 0.13 wt % and is generally used in applications such the medical industry and military aerospace due its high damage tolerance and excellent biocompatibility, however, the cost of grade 23 is typically higher than grade 5.

The effect on mechanical properties of titanium alloys based on the content of oxygen, nitrogen and carbon all differ although they are all  $\alpha$ -stabilising elements. A study from Finlay and Snyder [110] demonstrated that an increase in interstitial elements in  $\alpha$ -phase titanium alloys resulted in an increase in strength and a decrease in ductility. The study concluded that the individual effect of the interstitial elements all differs, with the dominant effect being nitrogen, followed by oxygen and then carbon as shown by Figure 25. [110]



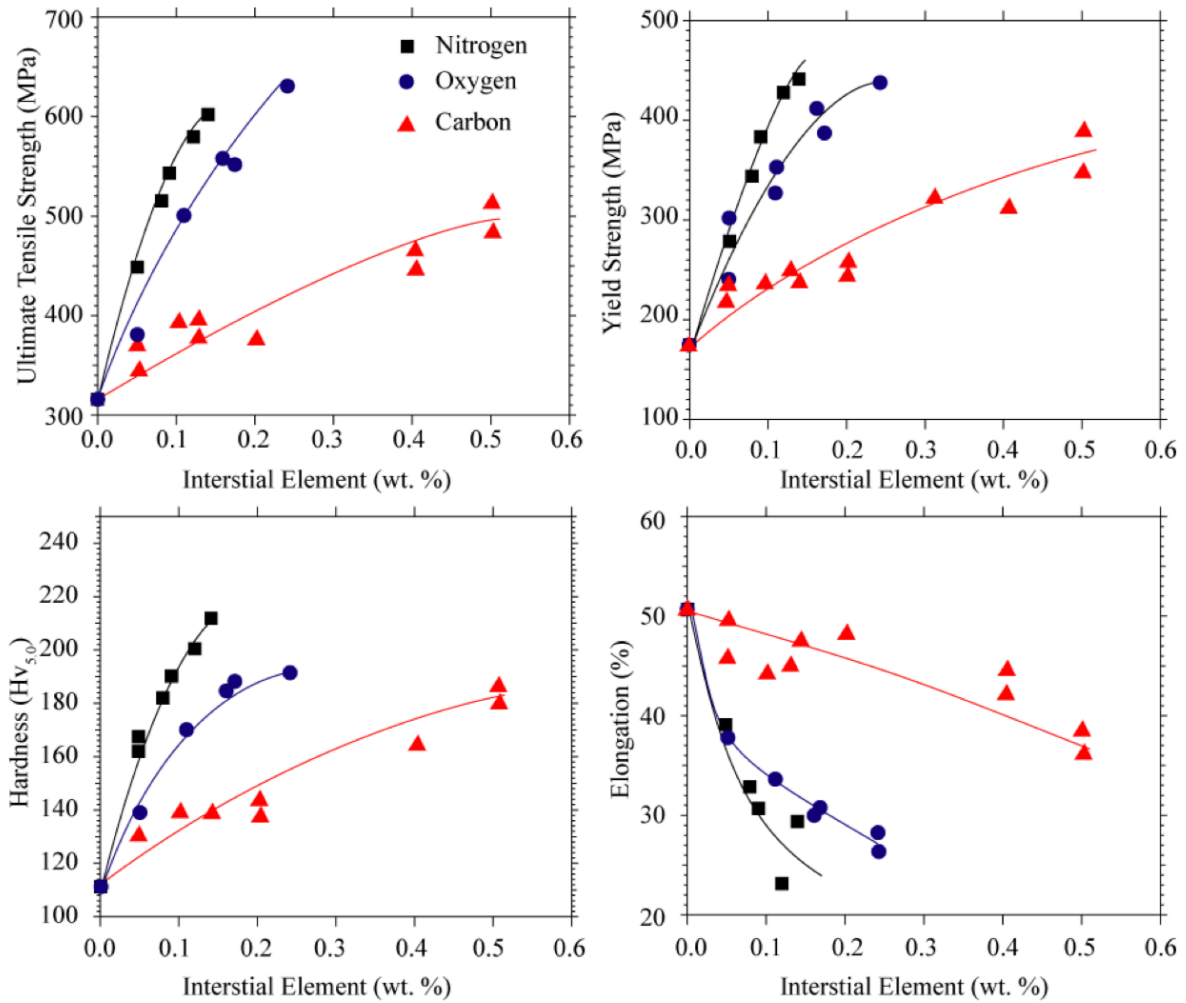


Figure 25: Interstitial element effect on the mechanical properties of  $\alpha$ -phase titanium [91]

These conclusions were later validated by Jafee *et al* [111] suggesting an equivalent oxygen concentration relationship indicating the overall effect on mechanical properties of a commercially pure titanium alloy from combined interstitial elements as shown in Equation 14.

$$[O]_{equivalent} = O + 2N + \frac{2}{3}C \quad (14)$$

However, the effect of the interstitial element oxygen on Ti-6Al-4V was studied by Oh *et al* [112] suggesting that oxygen had a limited effect on the Ti-6Al-4V alloy by

comparison with commercially pure titanium (CP). Figure 26a suggests that difference in gradients between commercially pure titanium and Ti-6Al-4V for ultimate tensile strength (UTS) with respect to oxygen concentration are very similar with no significant change. However, comparison between elongation and Vickers hardness between the two alloys shows a significant change in gradient displaying at an oxygen concentration of 3000ppm, a difference of 100 Hv in Vickers hardness and a difference of 4% elongation. This evidence comparison suggests that the addition of alloying elements aluminium and vanadium changes the effect of oxygen concentration on mechanical properties.

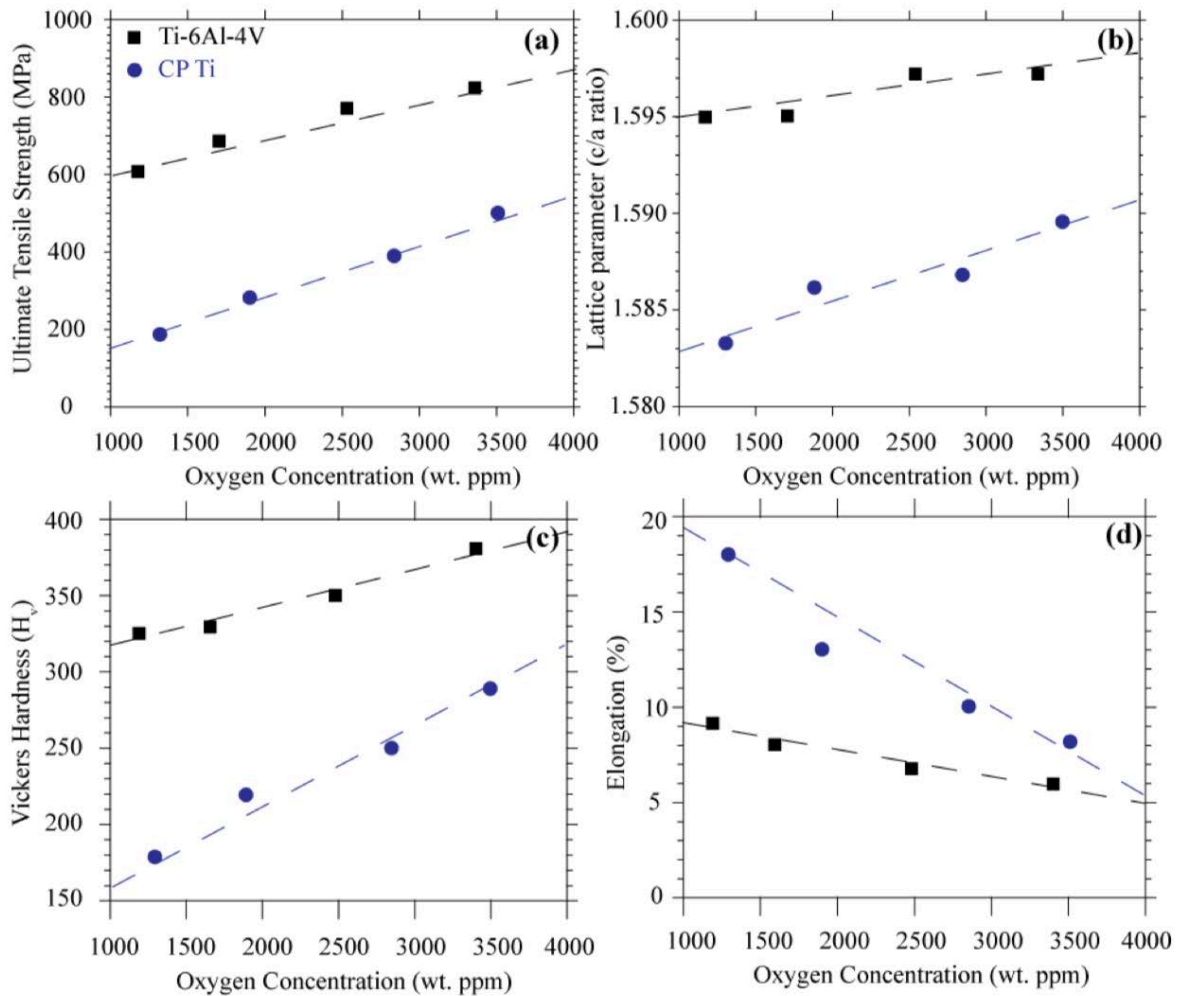


Figure 26: Comparison of commercially pure titanium alloy and Ti-6Al-4V on the relationship of oxygen concentration on a) ultimate tensile strength (UTS), b) Lattice parameters (c/a ratio), c) Vickers hardness (H) and d) elongation (%) [96]

Furthermore, the lattice parameter ratio ( $c/a$ ) increased as the oxygen concentration increased shown by Figure 26b, the rate of change between this relationship is dependent upon the alloy. Oxygen and nitrogen elements occupy the octahedral interstices in close pack hexagonal (CPH) alloys as shown in Figure 27, an increase in their respective concentration in a material results in an increase in  $c/a$  ratio. Changes in the  $c/a$  ratio due to interstitial element concentration is considered to change the material mechanical properties. An increase in the  $c/a$  ratio due to increased lattice strain reduces the number of slip planes resulting in increased strength and hardness in the hexagonal close packed structure (HCP) [113][112].

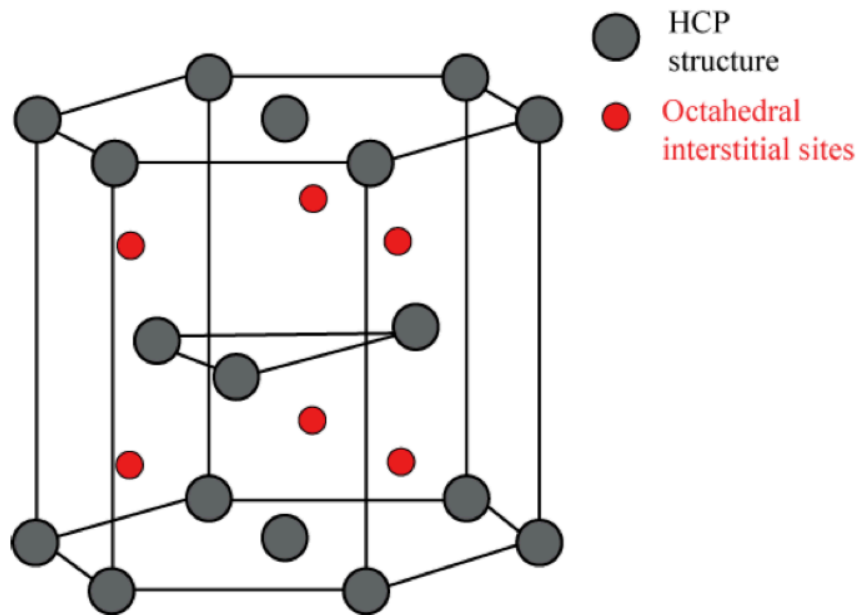


Figure 27: Schematic of close packed hexagonal (CPH) crystal structure with octahedral interstitial sites present.

Oxygen and nitrogen have substantial effects on the lattice parameters and thus impact on the mechanical properties within hexagonal close packed (HCP) titanium alloys. Therefore, the control of interstitial elements during production is essential in order to minimise the lattice strain and change to mechanical properties, although nitrogen has the dominant effect, oxygen must be controlled due to the high solubility it has within titanium alloys.

### 2.6.2 Solubility of oxygen in titanium

The solubility limit of oxygen in titanium is 32 at % in the alpha phase as titanium has the highest solubility of oxygen in the periodic table. The properties of oxygen in the interaction with titanium can be explained by the large number of unfilled shells which form the basis for the formation of a wide range of interstitial solid solutions alongside transformations to form suboxides. Many studies have shown the presence of three suboxides of titanium in the Ti-O system:  $Ti_2O$ ,  $Ti_3O$  and  $Ti_6O$ . The formation of  $Ti_2O$  and  $Ti_3O$  occur during solidification and  $Ti_6O$  is a precipitate from the alpha solid

solution of oxygen in titanium, all three suboxides have a HCP lattice of alpha titanium with an ordered structure [114].

When titanium is exposed to elevated temperatures ( $>400^{\circ}\text{C}$ ), the oxidation reaction forms oxide and inward diffusion of oxygen towards the titanium core. The result of the oxygen diffusion is an oxygen enriched layer below the oxide scale which is commonly known as the oxygen diffusion layer or alpha-case layer. The high solubility of oxygen in alpha titanium and the stabilising effect of the oxygen on the HCP crystal structure of alpha titanium allows the oxygen diffusion to occur resulting in a hard, continuous brittle layer that can significantly alter the mechanical properties of the material. Wagner's model [115] shows the oxygen concentration profile of oxidised titanium as shown by Figure 28.

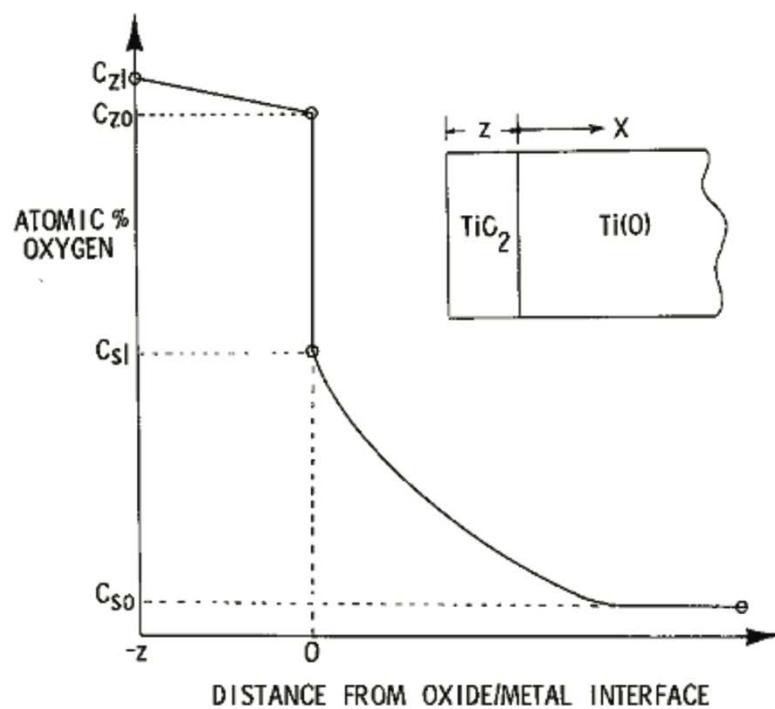


Figure 28: Illustration of oxygen concentration profile in oxidised titanium from Wagner's model. [101]

The oxygen concentration profile shown in Figure 28 consists of two individual concentration profiles: one for the oxygen diffusion layer and one for the oxide ( $\text{TiO}_2$ ). In the case of Wagner's model, they both have specific thicknesses, oxygen diffusion layer has thickness  $x$  and the oxide has thickness  $z$ . The oxygen diffusion layer has a

large oxygen solubility range, the highest oxygen concentration is at point  $C_{sl}$  which can be considered to be the oxide/metal interface and the lowest oxygen concentration is  $C_{so}$ , this is where the oxygen content reaches the bulk core titanium matrix oxygen concentration. However, the solubility of oxygen in the oxide scale can be considered to be linear as the oxygen solubility is limited as it can be seen that the oxygen concentration in the core titanium matrix decreases gradually. The concentration of oxygen in the oxide/metal interface ( $C_{sl}$ ) depends upon the exposure time and temperature and has a maximum solubility limit of 14.3 wt % in alpha titanium. Gaddam et al reported similar oxygen concentration profiles for Ti-6Al-4V using microhardness testing [116] and EPMA analysis [117].

### **2.6.3 Oxygen and nitrogen diffusion through titanium**

As mentioned in 2.5.1, the presence of interstitial elements such as oxygen, nitrogen and carbon in solid solution titanium alloys can negatively alter the mechanical properties if not controlled. The manufacturing process is accredited with the majority of the interstitial element pickup and in some cases, the formation of  $\alpha$ -case in finished products. In order to control the interstitial elements during manufacturing, the process environments are under vacuum or inert gas atmosphere such as argon.

The formation of  $\alpha$ -case is a well-studied field of metallurgy due to the largely negative impact of the mechanical properties and brittle phase formation in a finished component. The formation of  $\alpha$ -case occurs as thick and coherent  $\alpha$ -phase surface layers enriched with interstitial elements. The prevention and removal of  $\alpha$ -case has become an important process to titanium manufactures to avoid problematic properties in finished titanium components.

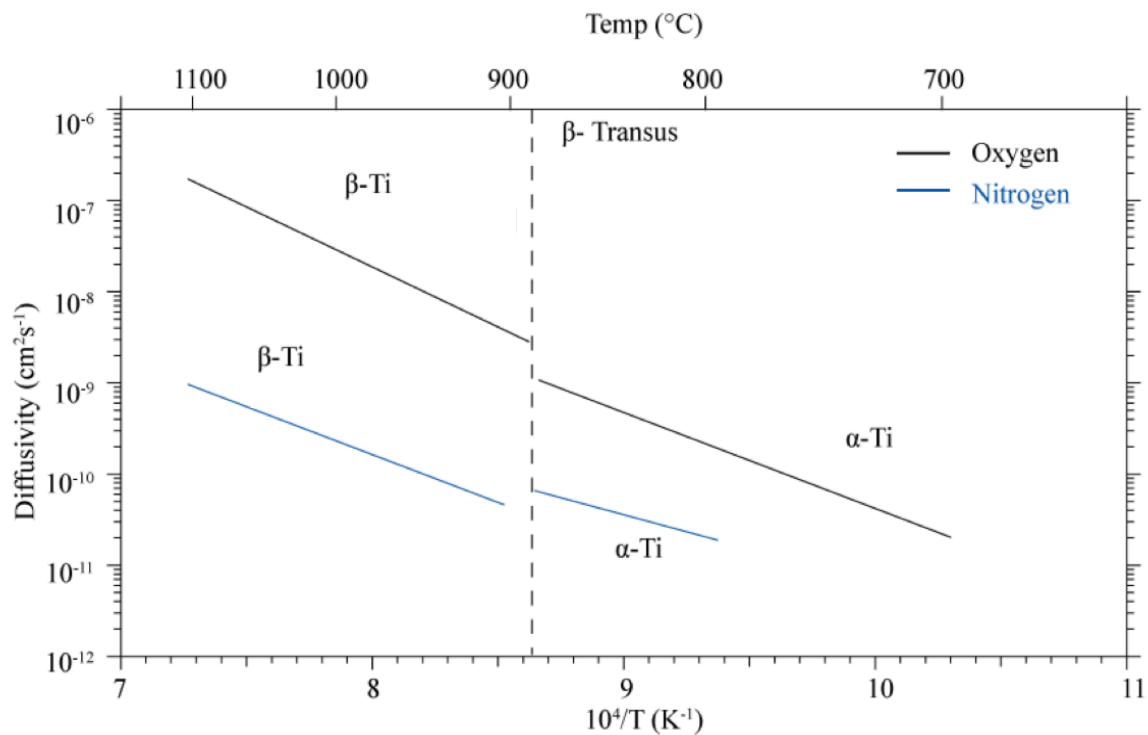


Figure 29: Diffusivity of oxygen and nitrogen against temperature in titanium.

Figure 29 illustrates the relationship between temperature and diffusivity of oxygen and nitrogen between  $\alpha$ -phase and  $\beta$ -phase. Diffusivity increases significantly in the  $\beta$ -phase due to the crystal structure change because interstitial elements diffuse more readily through body centred cubic (BCC) compared to hexagonal close packed (HCP). The diffusivity gradient of oxygen is greater than nitrogen as shown in Figure 29, due to the effect of atomic radii and solubility saturation of the element within the titanium matrix [118]. The diffusivity of metallic elements increases as the atomic radii decreases, this relationship can be applied to non-metallic elements such as oxygen (60pm) and nitrogen (65pm). However, there are some exceptions such as carbon (70pm) as the diffusivity gradient is faster than oxygen but has a larger radius (10pm bigger) [119].

The Arrhenius equation describes how the diffusion coefficient changes with temperature through the relationship of the dominate reaction kinetics with rate of diffusion as shown in Equation 15.

$$D = D_0 \exp\left(\frac{-Q}{RT}\right) \quad (15)$$

Where D is the coefficient of diffusion,  $D_0$  is an independent temperature coefficient, Q is diffusion activation energy, R is molar gas constant and T is absolute temperature. Fick's second law analyses the interstitial element concentration gradient assuming a semi-infinite solid with non-steady state diffusion shown in Equation 16.

It is important to note, if there are more than two elements then this is an approximation, it is possible that if more than two elements are present, then an element can diffuse up its own concentration gradient under the influence of the other solute atoms. A common example of this can be seen in super alloys where the concentration gradient of one element effects the movement of the other. In these cases, concentration should be replaced by activity.

$$\frac{\delta C}{\delta t} = D \frac{\delta^2 C}{\delta x^2} \quad (16)$$

Solving for a 1-D semi-infinite plane results in Equation 18,

$$\frac{C_x - C_i}{C_0 - C_i} = 1 - \operatorname{erf}\left(\frac{x}{2\sqrt{Dt}}\right) \quad (17)$$

Where  $C_x$  is the concentration, x is distance,  $C_i$  is the initial concentration,  $C_0$  is the final concentration, D is diffusion, erf is the error function and t is time. Diffusion coefficients can be compared for  $\alpha$ -phase and  $\beta$ -phase titanium with the solution to Equation 16 as previously illustrated in Figure 29.



It is important to note that the error function is a standard error derived from a statistical table and is not directly linked to diffusion. The equation uses a standard set of statistical tables that are related to normal distributions, not because there is an 'error'. However, concentration gradients in titanium are commonly produced via two experimental methods: low temperature, internal friction method and high temperature oxidation in a controlled atmosphere. The first method is dependent upon interstitial solute atom movement to minimise local strain energy when a uni-directional stress is applied on a sample. Therefore, the measurement of the diffusivity of oxygen can occur under oscillating stress conditions by measuring jump distance and frequency. This relationship is shown in Equation 18.

$$D = \frac{\Gamma x^2}{6} \quad (18)$$

Where  $D$  is temperature of diffusion,  $\Gamma$  is jump frequency and  $x$  is jump distance. Whereas the second method produces an oxygen concentration gradient in the metal substrate through the use of an oxide scale. However, the oxidation method is limited due to surface oxide formation such as rutile ( $\text{TiO}_2$ ) and non-stoichiometric oxides such as  $\text{Ti}_2\text{O}_3$ , limiting the accuracy of measurements.

The effect of interstitial element diffusion in titanium alloys has driven numerous techniques to determine activation energy and diffusivity coefficients in  $\alpha$ -phase and  $\beta$ -phase titanium alloys at elevated temperatures. However, although different methods have highlighted different factors for diffusion, each method has accuracy limitations resulting in numerous diffusion coefficients creating uncertainty. That being said, further research into diffusion mechanisms will minimise the risks caused by uncertainty in the accuracy of the diffusion coefficient and allow the exploitation of interstitial elements to further enhance titanium alloy mechanical properties.

## 2.7 Atomisation

SLM utilises metallic powder feedstock in order to construct three-dimensional (3-D) geometries using a laser to melt powder in a layer-by-layer process. Process parameters are optimised based upon the metallic material being processed to avoid problematic defects such as lack of fusion, porosity and more. High end component manufacture such as the load critical parts for the aerospace industry require a high level of build integrity and repeatability in the process. Apart from controlling machine process parameters, the initial powder feedstock is an essential controllable in order to ensure good final build quality and repeatability of final component manufacture. Due to the high influence of powder feedstock quality on the final build properties, the AM process is highly dependent upon the quality of the upstream processes such as powder manufacture, powder handling and transport. SLM uses spherical powder particles due to the good flowability properties to form a uniform powder bed. A variation in PSD will lead to variation in distribution and packing density of powder beds which are essential characteristics to influence heat distribution and component density. There are many key characteristics that effect powder quality and are essential for powder suppliers to control in order to meet mandatory requirements for SLM such as:

- Particle size / Size Distribution
- Flowability
- Reflectivity/absorptivity
- Thermal conductivity
- Oxidation
- Humidity, hydrogen
- Morphology

Metal powder is generally manufactured using four different methods: chemically, electrolysis, mechanically or atomisation. Metallic powders for AM are largely manufactured via atomisation in an inert gas atmosphere due to superior quality of powder produced. High energy gas flows atomise liquid molten metal, upon impact, resulting in spherical droplets which rapidly cool in the inert atmosphere. The spherical

particles are then sorted via particle size in order to meet different AM powder application requirements. Packaging of the metal powder slightly varies dependent upon the reactivity of the material, if the material is highly reactive such as titanium alloys, aluminium alloys and more, the material are packaged in an inert atmosphere to reduce the risk of interstitial impurities from altering mechanical properties of the powder. Atomisation of metallic powder processes can be categorised based on the method used to melt the feedstock material and the choice of nozzle used (geometry and type) [120]. Figure 30 shows the four different processes used to melt material for atomisation. It is worth noting that there are other methods are also used for AM powder production such as Plasma Rotating Electrode Process (PREP), centrifugal atomisation and plasma spheroidization, however, the material used throughout this project are manufactured for AM via EIGA.

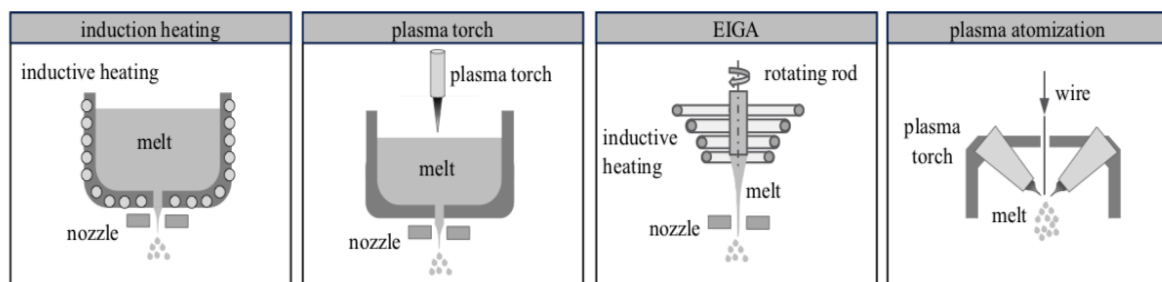


Figure 30: Different methods of melting material for gas atomisation

There are three different nozzles commonly used throughout the different atomisation processes as shown in Figure 30:

- Free fall nozzle
- Closed coupled nozzle
- De Laval nozzle

The free fall nozzle utilises gravitational forces to pull the melt flow into the atomisation chamber for atomisation to occur. The particle diameter produced are usually large (>50 $\mu\text{m}$ ) due the limited flow rate, the particle size produced from this nozzle type does not meet AM requirements for PSD of 15-45  $\mu\text{m}$  [120]. Closed coupled nozzle utilise a turbulent flow of the atomisation gas to pull the molten flow into the atomisation

chamber. The flow can be adjusted by the altering the gas flow velocity, which in comparison to free flow nozzles, this nozzle type has high flow rates and thus produces small particle diameters as small as  $10\mu\text{m}$ . The De Laval nozzle utilises a laminar flow of the atomisation gas and is accelerated to supersonic speeds resulting in narrow PSD in the range of  $15\text{-}45\mu\text{m}$  [121]. This nozzle is favoured by AM powder manufacturers as it produces powder within the PSD requirements for AM and utilises less gas compared to closed coupled nozzles.

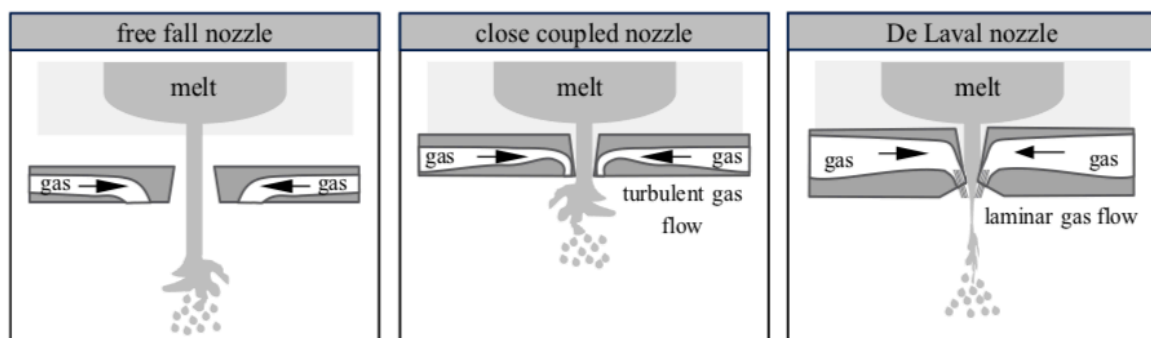


Figure 31: Types of nozzle used in gas atomisation

### 2.7.1 Plasma atomisation

Plasma atomisation production utilises a pre-alloyed wire which is melted via plasma torches as shown in Figure 32. [122] The material is directly atomised via the heat and kinetic energy of the plasma. The molten material melts into droplets that rapidly cool and solidify whilst falling in the inert atmosphere forming highly spherical morphology and PSD of  $5\text{-}250\mu\text{m}$ . The plasma atomisation process produces powders with low levels of interstitial impurities such as oxygen and nitrogen which is essential for materials such as titanium which has a high solubility to oxygen. However, in comparison to EIGA, plasma atomisation is expensive and, in some case, not cost effective as the wire feedstock which is an expensive material option which does not offer any cost advantage if up scaled.

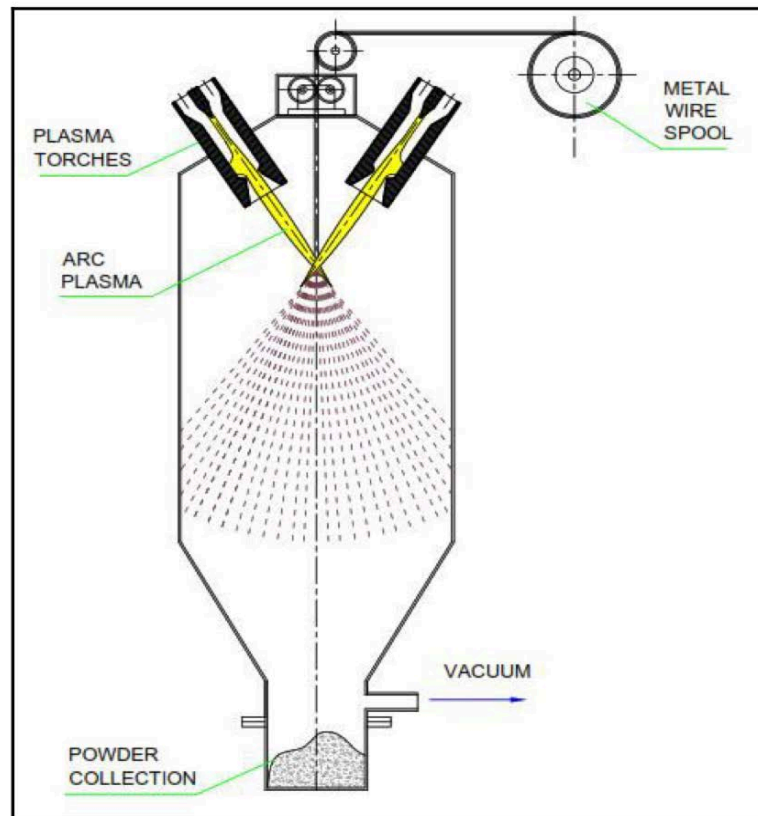


Figure 32: Schematic of plasma atomisation process

### 2.7.2 Electrode inert gas atomisation (EIGA)

Electrode inert gas atomisation (EIGA) melts metal bar feedstock via an induction heated rod allowing the molten metal to drop into the atomisation nozzle without contact from surrounding components as shown by Figure 33. This reduced contact combined with the absence of a crucible reduces contamination of the atomised powder. However, contamination can occur from previously atomised material if the atomiser isn't locked down to produce a single material. This process produces PSD of 0-500 $\mu\text{m}$  with a good morphology similar to that of plasma atomisation. EIGA is utilised for high end materials such as titanium alloys as it is clean, reducing the risk of contamination and impurities which are essential for high end applications for industries such as aerospace and medical. The process is considered to be relatively cheap in comparison to other powder production processes and is used for small production batches.

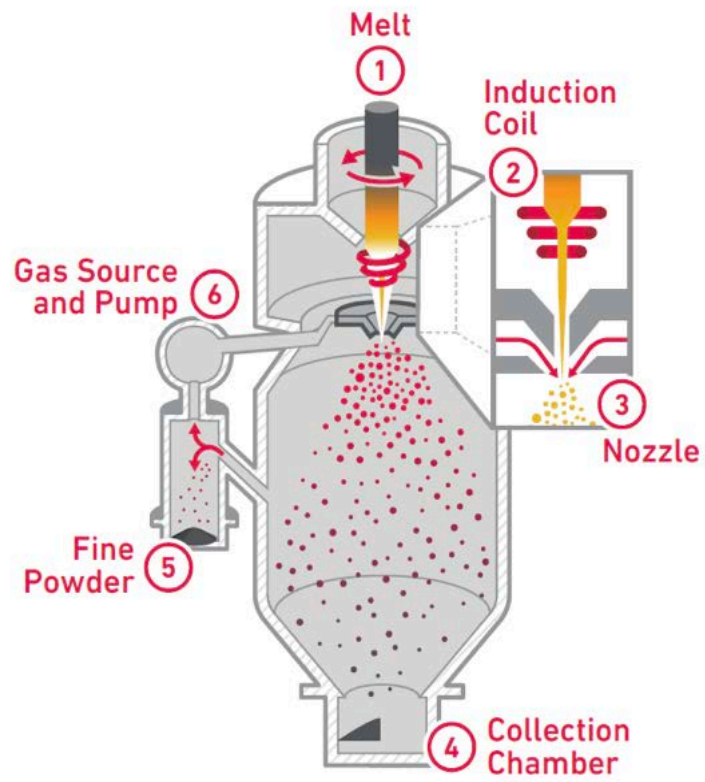


Figure 33: Schematic of EIGA process

## **2.8 Powder degradation in SLM**

### **2.8.1 Powder requirements**

Throughout SLM there are over 50 different parameters that can be optimised to achieve the desired properties in the final build such as microstructure and mechanical behaviour. However, a key requirement of repeatability is the quality of the powder feedstock. In SLM, usual PSD of powder feedstock is 15-45 $\mu\text{m}$  which must meet specific requirements of chemical composition, flowability to spread the powder across the build platform. There are various techniques to quantify these requirements such as the LECO method (bulk powder vaporisation for chemical composition), SEM (Morphology), laser size diffraction (size), Hall flow funnel (flowability of powder) and more. In high end applications such as aerospace, medical and structural load components, further requirements need to be met such as the feedstock must be free from any foreign particulate contamination such as cross contamination (exogenous) and elemental contamination (oxidation). A study by Gatto et al [123] suggested that the mechanical properties were detrimentally affected by cross contamination for maraging steel and metal oxides.

### **2.8.2 Gas quality**

The SLM process is always performed in an inert gas atmosphere in order to reduce the risk of interaction between metallic powder particles and impurities such as interstitial elements, humidity and in the case of highly reactive metals, reduce the risk of ignition. The interaction between impurities and powder particles can lead to changes in localised chemical composition, thus changing the mechanical properties of final builds and increasing the risk of brittle phase formation, crack propagation and more.

The most common inert gases used to purge the build chamber in SLM are argon (Ar) and nitrogen (N). However, dependent upon the material being processed, nitrogen is not always a viable option as the inert gas due to the formation of nitrides in highly

reactive materials, therefore in these cases argon is used. A study by Pauzon et al [124] studied the effect of a combined inert atmosphere of argon and helium in order to process Ti-6Al-4V. This study shown that the build rate increased by up to 40% alongside an improved material cooling rate suggesting that combined inert gases may offer superior gas quality in comparison to singular inert gases in the build process. However, more research is needed to understand the effect such combined inert gases have on other materials prior to wide scale adoption.

Furthermore, gas flow plays another key role of removing by-products ejected by the melt pool ensuring they are captured by the outlet filter. Thus, reiterating the importance of a continuous gas flow, if the gas flow is not effective in the removal of by-products, the risk of laser attenuation is increased due to the partial absorption of laser energy in the newly formed vapor plume from powder laser interaction. Grünberger and Domröse [125] studied these effects and found that a good quality, continuous gas flow was essential in order to avoid the occurrence of laser attenuation as the investigation discovered that areas with low velocity gas flow in the build chamber there was increased beam scattering. Thus, the study concluded that gas flow was a crucial parameter in order to reduce the presence of by-products and defects within built parts in the SLM process.

### **2.8.3 Marangoni effect**

The Marangoni effect is a mass transfer phenomenon where a fluid from a low surface tension region is transferred to a region with higher surface tension [126]. In terms of SLM, the Marangoni flow of molten material is driven by the melt pool surface tension gradient ( $dy/dT$ ) as shown in Figure 34. The sign of the gradient determines the direction of the fluid flow. A positive surface tension gradient results in a radial inward flow leading to a narrower and deeper melt pool, however, a negative surface tension gradient results in a radial outward flow producing a shallow and wider melt pool [127]. The difference in surface tension is normally due to the temperature gradient but is also affected by composition.



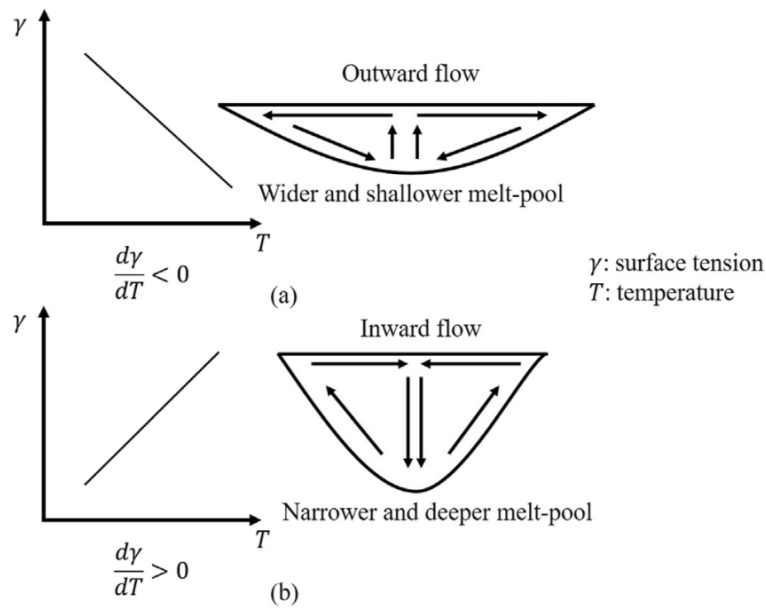


Figure 34: a) Negative surface tension outward flow b) Positive surface tension inward flow [112]

A study by Kidess et al [128] processing stainless steel using laser welding showed that the melt pool fluid flow is dominated by the Marangoni convection effect caused by the surface tension gradient despite many other physical phenomena acting on the fluid in the melt pool such as recoil pressure, buoyancy and the Lorentz force.

The surface tension gradient is dependent upon both the temperature and composition. A study by Keene et al [129] investigated the variation of the surface tension with temperature during TIG welding of two stainless steels with different sulphur concentrations (13ppm and 152ppm respectively). The study found that steel with the lower sulphur concentration resulted in a negative surface tension gradient as the surface tension decreased as the temperature increased. In contrast the steel with the higher sulphur concentration showed a positive surface tension gradient as the surface tension increased as the temperature increased.

A recent study by Le et al [130] found that the sulphur level of SS316 metal powder was critical in governing the fluid flow behaviour of the molten melt pool, a higher sulphur content changes from an outward radial direction to an inward radial direction resulting in a deep and narrow melt pool. Additionally, the study concluded that the

presence of inverse Marangoni flow inside the melt pool sweeps the gas bubbles away from the solidification front resulting in lower porosity of the scanning track

### 2.8.4 Denudation

Denudation is a phenomenon defined as the formation of clearing zones around a single laser track. The surface tension forces present within the melt pool spread the molten material and surrounding powder particles in the powder bed forming tracks with a larger width than the laser beam [131]. The large thermal gradients created by temperature difference between surface regions of the melt pool generate Marangoni flow. The Marangoni flow and vapor recoil momentum dominate the transition region resulting in denudation as the combined phenomenon pulls in adjacent powder particles to the melt pool.

The effect of denudation is highly dependent upon process parameters such as power and speed alongside gas flow velocity. A study by Mathews et al [131] showed the relationship between the Knudsen number, size of denudation area and laser scan track height. The Knudsen number,  $Kn$ , is defined as the ratio of length scale of the system to the mean free path of gas molecules. It was shown that when  $Kn < 1$ , powder particles are ejected in an upwards direction or pulled into the melt pool whereas when the  $Kn > 1$ , the vapor plume will expand and force the particles outward from the melt pool as shown in Figure 35.

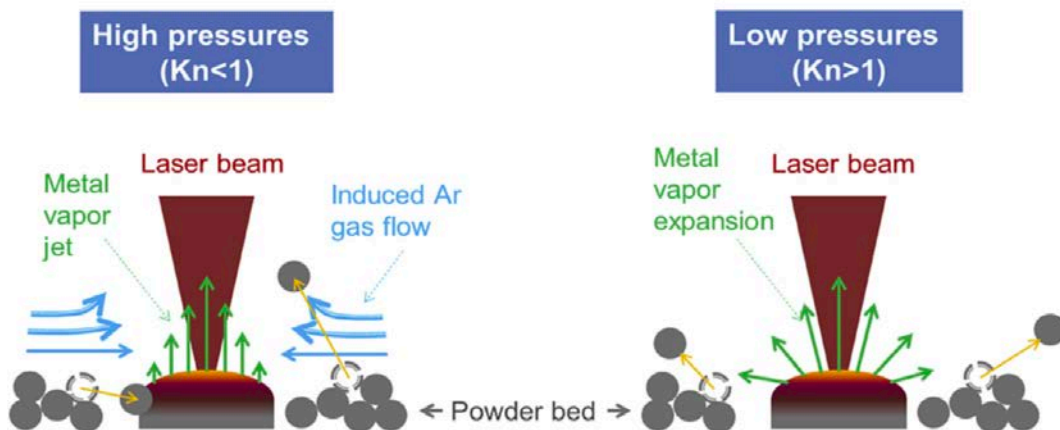


Figure 35: schematic of high- and low-pressure interactions between laser beam and powder bed.

Process parameters can generate keyholes in SLM through the formation of humping (undulation of track profile). Increased scan speed and laser power produces a thin melt pool, resulting in a common laser welding phenomenon called humping. Humping phenomenon is considered an instability by product of process parameters as it results in vertical deformation of the melt pool close to the laser interaction with the powder. However, a dynamic melt pool is formed by the Marangoni convection where the size between powder particles and laser spot. The Marangoni convection is dominated by vapour recoil and variation in absorptivity. Denudation is dominated by process parameters within the SLM process and as both physical phenomena of Marangoni flow and recoil pressure display the same characteristic in single track scans shown by Matthews et al [131], thus, conclusions made on single track scans can be extended to the total powder bed in the SLM process.

#### **2.8.5 Heat affected zone (HAZ) powder**

Throughout the SLM process, a common phenomenon is the ejection of bright particles away from the melt pool and laser interaction zone. The melt pool experiences high thermal gradients and superheat from the laser interaction with the powder resulting in a material ejection and vaporisation. Although vapor recoil pressure and Marangoni flow are the dominant mechanisms for denudation as previously mentioned, Ly et al [132] suggested that formation of particle ejection from the melt pool is driven by a vapor entrainment of micro particles. In order to avoid localised difference in chemical composition due to redeposition of ejected particles within the powder bed, in-situ monitoring of the vapor plume must be a top priority to ensure final build quality as SLM utilises varying high temperatures and rapid cooling rates to process material.

Heat effected zone powder can be divided into two categories based on the metallic powder interaction with the laser: hot ejections and cold ejections. Hot ejections are defined as the particles that are entrained by the vapor plume and are ejected as incandescent particles from the interaction with the heat source. Whereas as the cold ejections are still entrained by the vapor plume but are ejected in an upwards direction

contrary to the laser scan direction, these particles are not properly heat by the laser interaction when high scan speed are utilised in the build process.

Significant differences in thermal conductivity of bulk alloys and pre-alloyed powders lead to superheat in the melt pool which exceeds the melting temperature of the alloy resulting in evaporation of the metallic powder. As the evaporation expands, recoil pressure in the melt pool is increased resulting in the emission of hot ejections. The ejections all originate from the laser interaction zone and the angle at which the ejection leaves are dependent upon vapor pressure and melt pool geometry. The use of high-power laser parameters significantly influences the expansion of the evaporation and formation of a depression in the melt pool and additional vapor plume. Optimising process parameters is essential in order to control the formation and orientation of the vapor plume to reduce the chances of problems with the final built component. L. Criales et al [133] demonstrated via in-situ thermal imaging that between 20-35% of total processing area along a single-track produced spatter ejected particles resulting in significant losses in material and heat.

### **2.8.6 Spatter**

Ejected Spatter particle formation is known to originate from the melt pool area and the interaction zone of the laser and powder bed. The formation of spatter can significantly impact the properties of built components and also generate sub surface defects as spatter particles are difficult to remove via post processing procedures due to their varied size, shape and ability to distinguish them. Spatter particles that are larger than the layer thickness in the build process pose a large risk for lack of fusion defects as the process parameters may not be sufficient to melt them, thus remaining un-sintered across build layers. Additionally, the presence of large spatter particles across build layers lead to problems with the re-coating and spreading of the above layer for the next melting cycle. The generation of spatter occurs from the melt pool where surface tension forces produce particles with non-uniform chemical composition and various shapes. A study by Sutton et al [134] categorised spatter formation based on morphology:

- Spherical: ejected molten particle rapidly cools and solidifies during flight through inert atmosphere without collision with other particles.
- Aggregates: ejected particles collide with another neighbouring spatter in flight and/or after contacting the metallic powder bed.
- Coarse aggregates: numerous ejected spatter particles collide with each other throughout flight.

The low cooling rate of the ejected particles from the melt pool allows surface tension forces to shape the molten material creating mostly spherical spatter particles. A study by Simonelli et al [135] suggests that the shape of the spatter particle is not dependent of the material. Spatter particle size heavily depends on the power input from the laser, as the power input increases, so does the size of the spatter particle ranging from  $>100\mu\text{m}$  diameter coarse to usual PSD range (15-45  $\mu\text{m}$ ) [136]. Approximately 90% of the ejections from the melt pool are within the PSD of 15-45 $\mu\text{m}$  consisting of both heat affected zone powder and spatter particles [134]. Therefore, post processing operations such as sieving post processed feedstock prior to re-use will not remove these particles. The presence of such particles within build layers changes the localised chemical composition and promotes further generation of condensate, spatter and metal vapor. Studies from several authors [136][137], suggest that if the even if process parameters remain constant throughout the build, the quantity of spatter produced can vary. This varying generation of spatter particles is accredited to the vapor plume partially absorbing and scattering the laser beam.

The ejection of spatter particles can occur at the front and the back of the melt pool dependent upon the movement of the laser. The ejection movement at the front of the melt pool follows the scan direction of the laser and moves similar to that of a wave. However, spatter ejection at the back of the melt pool moves in an opposite direction to the laser scan direction. Additionally, the depression formed from the laser interaction with the melt pool and the vapor plume influences the elongation and breaking of molten material resulting in spatter generation which is then deflected by the radiation from the laser into surrounding powder bed. This highlights the variation in spatter ejection location and that spatter is generation is not completely dependent upon the motion of laser beam. A study by Yin et al [138] shown that only a few spatter

particle ejected horizontally with the majority ejecting backwards in the direction of the scan. A relationship was established between the location of the generated spatter particles and process parameters (scan speed and power).

### **2.8.7 Condensate**

An additional side effect of the melting process caused by metal evaporation is the formation of vapor plumes. The continuous gas flow and atmospheric conditions inside the build chamber influence the rapid solidification of vaporised material, resulting in small condensate particles ( $<5\mu\text{m}$ ) being distributed around the build chamber. A study by Sutton et al [134] shown that the condensate can deposit on the surface of spatter particles as well as the surrounding powder bed. Condensate was observed in the form of nanoparticles due to the decrease in solubility of the metal vapor during cooling, resulting in a supersaturated solution which has high undercooling; thus, influencing the formation of nanoparticles. Nanoparticles would not be removed by conventional post processing operations such as sieving, It is worth noting that if a large amount of condensate is generated and redeposited into the powder bed, the surface properties of the powder may change the flowability of the reused powder [134][139][140][41].

The need to find a solution to the problem of condensate is prominent as the AM industry is transition from rapid prototyping to serial production, however, there is still much debate about the methodologies used in different research to reach a common solution.

### **2.8.8 Cross-contamination**

Cross contamination occurs in many forms within the AM industry originating from feedstock supplied, powder handling when changing over builds/powder, condensate contamination from previous builds of different material and many more. The impact of contamination within the SLM process is significant as it can change the localised materials properties and produce build failures, crack propagation or altered final build mechanical properties. These scenarios lead many industries to locking down SLM

machines to one material for production in order to reduce the risk of cross-contamination.

A study by A. Brandão et al [141] investigated the impact cross contamination has on SLM built parts using Ti-6Al-4V. It was determined that the main source of cross contamination; tungsten (W) originated from two different scenarios. The first was the Plasma Rotating Electrode Process (PREP) for powder manufacture, the tungsten electrode used for manufacture was wearing out and as it degraded, it contaminated the powder batch. Secondly, cross-contamination of the AM machine was concluded to be a source as a build using tungsten material was processed in batches previous to the Ti-6Al-4V builds. The impact of the tungsten contamination on the build was clear as fracture elongation was significantly reduced for contaminated powder batch (Lowest fracture elongation value of 2%) compared to a non-contaminated batch (lowest elongation value of 8%). However, the strength values across both batches remained similar. It is also worth noting, the study concluded that detection of contamination was difficult and characterisation methods used for certification were insufficient for detection, instead x-rays were used to detect the tungsten leading the study to suggest use of one powder type per AM machine for component manufacture.

A later study by Santecchia et al [142] investigated the impact and quantification of contamination in SLM suggesting new procedures for identification of contamination. The study intentionally contaminated powder samples and compared them to virgin samples via energy dispersive x-ray spectroscopy (EDS) and concluded that the cross contamination was accurately detected through the comparison of elemental quantification of the two samples. The evidence also suggested that the most relevant physical property for detection and measuring contamination was the contaminant density.

Thus, the numerous studies of contamination all reiterate the importance to control powder quality and enable full traceability back to source to identify problematic contamination and reduce the risk of reoccurrence. Additionally, the evidence suggests that contamination is a problematic variable to identify and control as usual certification methods do not detect the presence of contamination, more advanced techniques such as EDS is required. However, the cost of using EDS for certification

could be high, therefore further research is required into cost effective techniques for identifying contamination in certification methodology.

## **2.9 Chapter Summary**

Oxidation theory of titanium is a well-established and researched field with an abundance of literature. However, the oxidation of Ti-6Al-4V powder metals and the impact oxidised particles have in the SLM is poorly understood, at the time of writing, there was no published research on thermal oxidation of Ti-6Al-4V powder metal. Therefore, it was necessary to seek theory and understanding on research similar to this field, allowing for a holistic consideration for the potential problems for the reuse of degraded powder and oxidised particles in the SLM process. Together with a review of conventional oxidation theory of titanium alloys combined with the literature surrounding powder reuse helped form a full hypothesis for the impact of degraded powder as feedstock will have on final build quality.



### 3.0 Experimental methodology

This chapter explains the experimental methodology for the project and the preliminary investigations will be discussed. The operation of the SLM system and the sample analysis equipment are discussed here. The preliminary investigations focus on understanding the powder metal interference colours produced by thermal oxidation and correlating the colour to an oxygen wt %.

#### 3.1 Ti-6Al-4V Material

The powder used throughout this project was gas atomised Ti-6Al-4V supplied by Carpenter Additive with a size range of 15-45µm. Table 3 shows the ‘as received’ elemental weight % of the powder supplied.

Table 3: Elemental weight % of Ti-6Al-4V powder supplied by Carpenter Additive

Element	Titanium (Ti)	Aluminium (Al)	Vanadium (V)	Oxygen (O)	Nitrogen (N)	Hydrogen (H)	Iron (Fe)	Carbon (C)
Weight %	Balance	6.39	3.89	0.091	0.028	0.0019	0.19	0.01

Particle size analysis was conducted to confirm the particle size range and obtain information with regards to the particle size distribution (PSD). Additionally, SEM imaging was utilised to analyse the powder morphology.

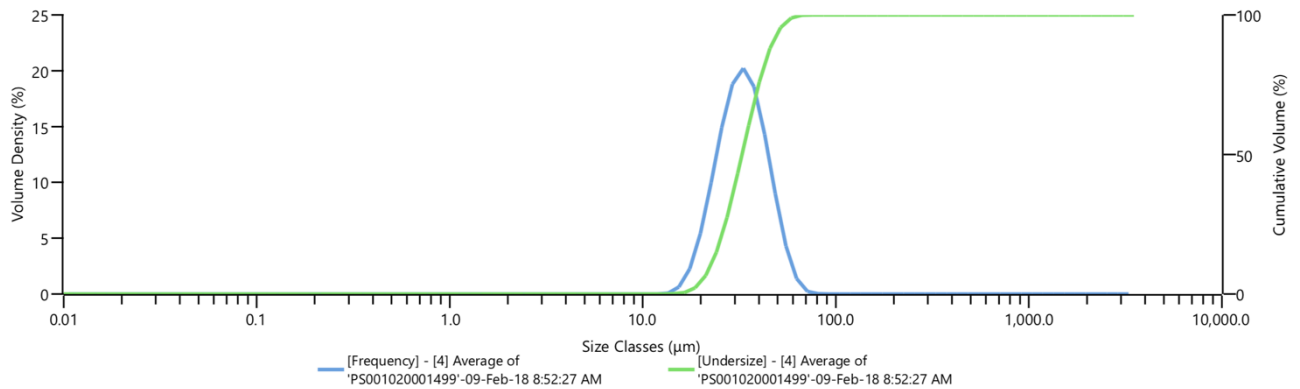
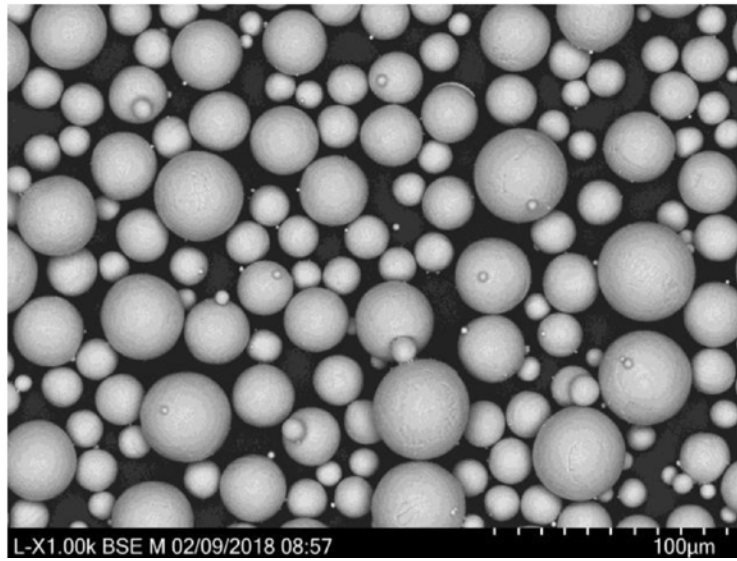


Figure 36: Particle size distribution of Carpenter Additive virgin Ti-6Al-4V powder

The particle size distribution was measured using a Malvern ® Mastersizer ® 3000 utilising the laser size diffraction (LSD) process. A Fraunhofer scatter model was used with the assumption that the particle shape was spherical. Dry dispersion was used for the powder delivery to reduce the possibility of smaller particles conglomerating and being identified as one larger particle. Figure 36 shows the particle size distribution for the virgin Ti-6Al-4V powder. A total number of 3 cycles was used for the laser size diffraction analysis. The Dv (%) values were as follows: Dv (90) 47.2μm, Dv (50) 32.7μm and Dv (10) 22.3μm. Although the powder size range was 15-45μm, 13.3% of the powder volume consisted of particles >45μm and 0.4% <15μm.



*Figure 37: SEM micrograph of VIGA virgin Ti-6Al-4V powder in secondary electron imaging mode.*

Figure 37 suggests that there are no particles in the field of view greater than 50 $\mu$ m in size with no evidence of distorted particles or agglomerates, given the sample size it is likely you would see them. Additionally, the particles all display spherical shapes with no evidence of oxide scaling or satellites.

With respect to processing, the volume distribution enables the user to understand what percentage of a deposited powder layer consists of particles smaller, or larger, than a chosen layer thickness. The SEM micrographs complements the volume distribution from a quality control aspect as it allows the user to assess the quality of the powder qualitatively.

## 3.2 Thermal oxidation of Ti-6Al-4V

### 3.2.1 The process

The thermal oxidation process was conducted using a Carbolite CSF 1200 air furnace. The process used is described below:

1. Heat the furnace to the prescribed temperature.
2. Prepare powder samples, measure ceramic crucible on weighing scales (+/- 0.0001g) and zero the crucible. Take a spatula and measure 10g of Ti-6Al-4V powder into the crucible.
3. Once the furnace has reached the prescribed temperature, use the tongs to place crucible into the centre of the furnace and close shut (The time it takes to place the crucible in the furnace and then shut was measured numerous times averaging around 5 seconds). Allow 2 minutes for the box furnace to reach prescribed temperature due to temperature fluctuation between furnace and room temperature.
4. Once the furnace has reached the prescribed temperature, start the stopwatch for 60 minutes.
5. When 60 minutes is complete, remove the crucible using the tongs (ensure ends of tongs are wrapped in wool to avoid thermal shock and potential shattering of the crucible), shut the furnace and place the crucible into a desiccator. Slide the desiccator lid shut slowly to ensure a seal and powder dries in dry atmosphere. Note: the desiccant used for this project was silica gel.
6. After 2 hours of cooling inside the desiccator, remove the crucible via the tongs. Take a spatula and test the flow ability of the powder by moving the spatula through the powder. Note; if any powder has bonded together, this needs to be ground in a mortar and pestle to keep the flow ability of the powder.
7. Use a spatula to place the oxidised Ti-6Al-4V into test sample vials.
8. Label each vial with relevant temperature and time exposure.
9. Repeat steps 1-8 for each new sample.

Manufacture of the yellow, blue and green powder utilises steps 1-9, however set the desired temperature to 530°C for yellow, 630°C for blue powder and 680°C for green.

It's important to note, in the case of this project, it was found that up scaling the powder batch to larger quantities still produced the bulk interference colour desired, however upon further inspection using optical microscopes, the powder particles did not produce a uniform colour on the particle level. Therefore, in order to maintain quality control and produce powder colour that is uniform at both the bulk level and the particle level, 10g batch sizes was used throughout the project to artificially oxidise even when larger quantities of powder were needed for the build experiment.

### **3.3 Analysis techniques**

#### **3.3.1 Sample preparation**

Throughout the project many different samples were made for different applications. A large proportion of the samples made in the latter stages of the project were produced using Focused ion beam milling (FIB) in order to create thin nano-meter thick lamella samples ready for TEM analysis, this is explained in greater detail in section 3.5.2. Here sample preparation concerns metallography specimens that were used for the remaining analysis throughout the project.

For initial experiments, samples were vertically sectioned using a Buehler Isomet 1000 wafering saw with a T2- type abrasion cutting blade operating at 1250 RPM. The fracture surface was gold coated using an Edwards S150 sputter coater. The gold coating gave some protection to the surface features but also allowed any damage to the surface when it was sectioned to be identified.

The cross sections were mounted in a thermo-setting phenol-urea based resin called Conducto-mount using a hot mounting press in the form of 32mm diameter pucks. The Conducto-mount features graphite which allows for conduction of electrons through the mounting which negated the application of conductive tape or paint. This allowed

for better quality micrograph under the SEM, therefore all samples were mounted in Conducto-mount as SEM analysis was always a possibility.

The mounted cross sections were all polished using the following procedure:

Primarily, sequentially finer grades of silicon carbide paper were used for the first stage, progressively from 800, 1200, 2500, with water lubrication, on a metallographic grinding machine. After this grinding sequence, specimens were cleaned scrupulously in aqueous detergent solution and rinsed with distilled water, then ethanol, before drying in a stream of hot air, prior to the initial polishing stage.

Initial polishing was achieved, using a Memphis napped synthetic cloth doped with 1 $\mu$ m alumina paste, again with water lubrication, on a carousel-type polishing machine, at ~250 RPM.

After cleaning as before, the specimens were finely polished, down to 40nm surface integrity, using an Opus colloidal suspension of silica on fresh "Memphis" cloth as before, again at ~250 RPM. Specimens were finally cleaned ultrasonically in distilled water and detergent, before rinsing with distilled water, then ethanol and drying in a stream of hot air.

Etching was performed on samples to expose microstructural features of the specimen, as the same material was used throughout the project, Keller's etching reagent in order to expose microstructure features of the Ti-6Al-4V samples. The Keller's etching agent comprises of the following:

- Distilled water, 190ml
- Nitric acid, 5ml
- Hydrochloric acid, 3ml
- Hydrofluoric acid, 2ml

The preferred method of etching for the samples utilised the swabbing method. A small amount of Keller's etching solution was placed into a beaker and soaked up using

cotton wool. The sample was placed in a separate beaker with the exposed specimen facing upwards. Using tweezers, the saturated cotton wool was placed on top of the sample using tweezers and a timer was started to ensure all samples received the same amount of time etching. The Keller's saturated cotton wool was moved around the sample face, remaining in contact with the sample surface at all times. Once the elapsed time was up, the sample was removed from the beaker and placed into a neutralising solution.

Once neutralised, the sample was then rinsed under cold running water, placed into a beaker of deionised water and finally rinsed using ethanol. The sample was then placed into a drying station where warm air dried out the sample to avoid residue from forming. The sample was then placed under an optical microscope to assess the quality of the etching process and ensure that the microstructural features had been exposed.

### **3.3.2 Chemical analysis**

Inert gas fusion (IGF-IR) spectroscopy, commercially known as LECO, this IGF testing method adheres to test standard ASTM E1409-13 [143] and was used to characterise the oxygen wt % of each batch of powder alongside nitrogen and hydrogen values. 1g of Ti-6Al-4V material was vaporised to measure the oxygen, nitrogen and hydrogen content (in wt %). Each IGF batch sample utilised 3g of material for three separate vaporisations, with average values for oxygen, hydrogen and nitrogen being calculated.

### **3.3.3 Laser size diffraction (LSD)**

The particle size distribution was measured using a Malvern ® Mastersizer ® 3000 [144] utilising the laser size diffraction (LSD) process. A Fraunhofer scatter model was used with the assumption that the particle shape was spherical. Dry dispersion was used for the powder delivery in order to reduce the possibility of smaller particles conglomerating and being identified as one larger particle. A total number of 3 cycles was used for the laser size diffraction analysis.

### 3.3.4 Optical spectrometry

The spectrometry used throughout this project was completed using a Konica Minolta CM-2600d portable spectrophotometer. Each powder colour being analysed was placed into a clear sample holder as shown in Figure 38 and were placed under the aperture (35mm). Prior to any data measurement, the CM-2600d was calibrated using a white Konica Minolata calibration standard. Each powder was shaken and the bottom of the uDish was wiped with an optical wipe in order avoid any dirt or residue hindering the colour measurement. Reflectance measurements were recorded every 10nm from 360nm to 740nm and data collection was input into SpectraMagic NX software for analysis.



*Figure 38: Bulk Ti-6Al-4V colours in clear sample holder used for spectrometry.*

### 3.4 Microscopy

Throughout this project, four different microscopes were used for analysis of various specimens. The suitability of a specific microscope for imaging is dependent upon the specimen and the image resolution the investigation desires. In this project, optical microscopes (OM) were used to characterise particle colour and evaluate whether an artificially oxidised batch of powder was a series of different coloured particles that produced one large bulk colour or if the whole batch of powder was the same colour throughout. Scanning electron microscopy (SEM) was used in order to characterise microstructure, fracture surface analysis and image oxidised powder particles. Focused ion beam scanning electron microscope (FIB-SEM) was used for particle



cross sectional analysis and lamellae sample preparation for high resolution imaging and quantification of elemental diffusion in the scanning transmission electron microscope (STEM).

### **3.4.1 Scanning Electron Microscope (SEM)**

Scanning electron microscopes (SEM) utilises a beam of electrons to view specimen features at much higher resolution than optical microscopes due to the smaller wavelength of the electron beam relative to visible light. The beam of electrons in SEM is generated via an electron gun situated at the top of the microscope, then passes through a series of lenses to focus the electron beam on the specimen for imaging. In order to maintain the stability of the electron beam, the chamber is under vacuum during operation. The focused electron beam interacts with material at and near the surface of the specimen producing secondary electrons, backscattered electrons and auger electrons. Different detectors within the SEM can be used to utilise each type of signal respectively.

A JEOL 6610 SEM was used for particle imaging, fracture surface analysis and microstructure analysis throughout this project. The microscope has a range of accelerating voltage, but throughout this project, 10kV was widely used for imaging. However, the microscope is limited to a resolution of 3nm at 30kV, new SEM microscopes can achieve much higher resolution of 1nm at 30kV. This microscope was also equipped with a multi axis stage, allowing tilting and rotation of sample to better image specific features on specimen. Additionally, the microscope is equipped with an Oxford INCA X-act EDX detector which can be used to study elemental distribution of a specimen. However, due to the relative low energy resolution and availability of more accurate EDX detectors, this was not used throughout this project.

### **3.4.2 Focused Ion Beam- Scanning electron microscope (FIB-SEM)**

The FEI Helios Nanolab 600i FIB-SEM utilises a Focused Ion Beam column which can be used in conjunction with an SEM; scanning electron microscope in order to focus and scan an accelerated ion beam onto, in this case, a metallurgical sample within a

vacuum chamber. The FIB column is generally used for two main purposes; the primary function being to generate a scanning ion image of the sample. The secondary function being the localised sputtering of the sample materials surface to directly fabricate arbitrary nanostructures.

In most commercial and academic systems, a liquid metal ion source (LMIS) is utilised for micromachining applications. These sources are considered to be point sources meaning their based-on field emission to produce ions and their brightness is higher than any other common sources such as plasma ion sources. In comparison to other common sources such as plasma ion source (PIS), LMIS have finite virtual source size of around 50nm which allows the ions to be focused within 1-2nm.

LMIS can consist of several different ion species such as Sn and Au, however, the most common ion used in commercial and academic systems is gallium (Ga); this is utilised in a blunt needle source [145]. Gallium has various advantages over other ion sources such as the ions previously mentioned due to combination of a low melting temperature of 30°C, low vapour pressure and good wetting of tungsten needles for in-situ lift out procedures. The low melting temperature allows for easy operation at room temperature and enables ease of design. The needle is typically made of tungsten (W) as gallium (Ga) does not react with the material and evaporation of Ga is negligible. Gallium based LMIS have a long lifetime and are the most stable of the commercial options; this combination is essential for high resolution imaging and longevity of system operation. The SEM uses the same operating principles as previously mentioned but is built in-situ with the FIB column as shown in Figure 39.

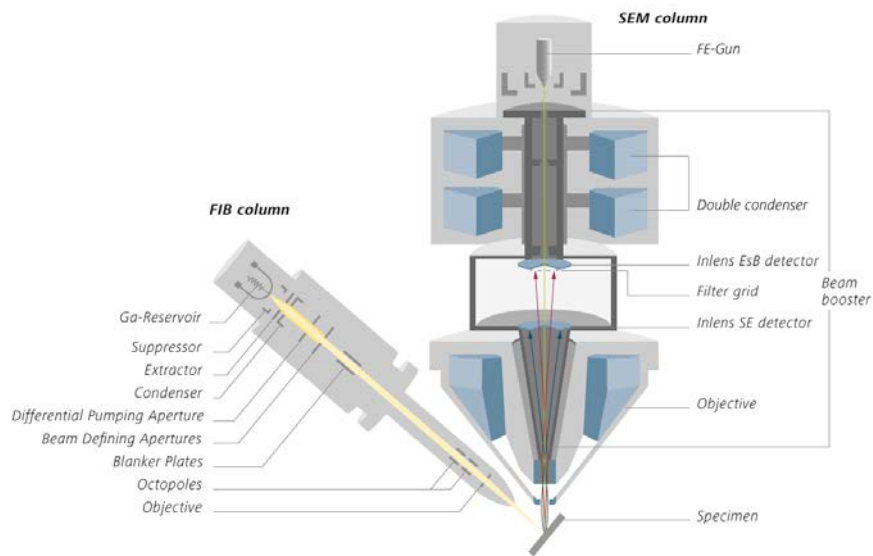


Figure 39: Schematic of FIB-SEM operation

In the case of this project, a dual beam FEI Helios Nanolab 600i FIB-SEM was used for two main purposes, primarily, the FIB was used for sample preparation for STEM analysis (Discussed in later section). Secondly, the FIB column was used to mill and cross section powder particles in order to characterise oxide thickness and microstructure.

The flexibility of the FEI Helios Nanolab 600i FIB-SEM allowed multiple samples to be processed at once, in the case of the powder samples, the three main powders coloured could be processed at once using the same mounting stage as shown in Figure 40. Thin layers of the respective powder colour were mounted to carbon tape on top of an SEM stub and labelled A, B and C in order to see which colour was being processed under the SEM as no colour is produced under the microscope. This method reduced cost, saved time and most importantly reduced the risk of contamination as the opening of the chamber was reduced.

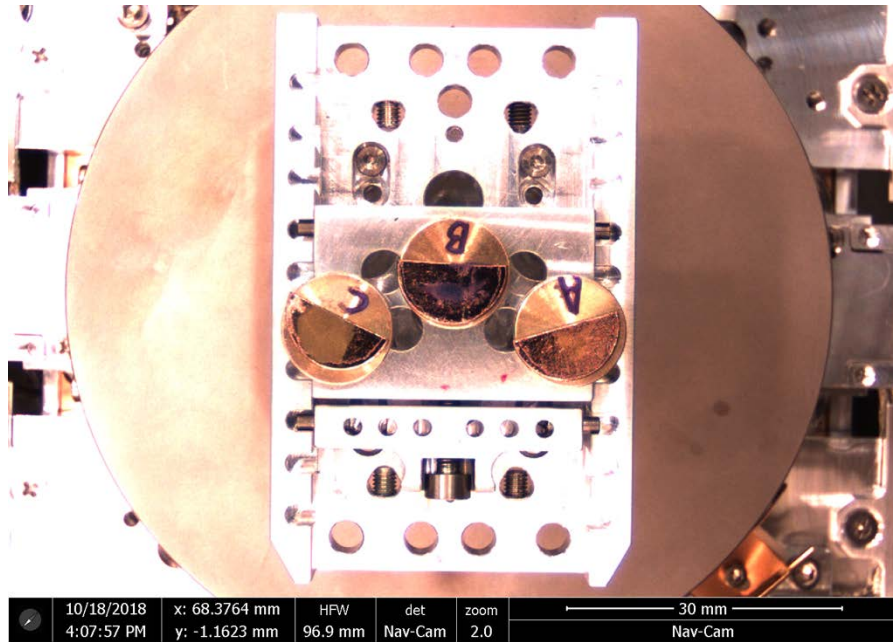


Figure 40: Powder particles mounted on carbon tape inside FEI Helios Nanolab 600i FIB-SEM.

In the case of analysis of the powder cross section, powder samples were milled, thinned and polished using a gallium (Ga) ion source. Using the SEM column to inspect the powder sample, a whole powder particle of interest was chosen (Figure 41A) and using the ion beam from the FIB column, half of the powder material is removed from the particle leaving an exposed cross-sectional face.

Dependent upon the diameter of the particle, the size of the Pt layer may vary in order to coat the relevant area of the particle surface, a  $\sim 2\mu\text{m}$  thick layer of Pt of size  $10\mu\text{m} \times 2\mu\text{m}$  is deposited on the surface using the electron and ion beams (Figure 41B). This helps protect the powder particle top surface from damage and protect any features that may be near such as an oxide layer from the high current Ga-ions.

The milling process started with an accelerating voltage of 30kV and a current of 0.28nA (Figure 41C). Once the bulk material is removed from the powder particle, the voltage and current are incrementally decreased to a voltage of 2kV and current of 15pA in order to polish the cross-sectional surface of the particle ready for analysis (Figure 41F).

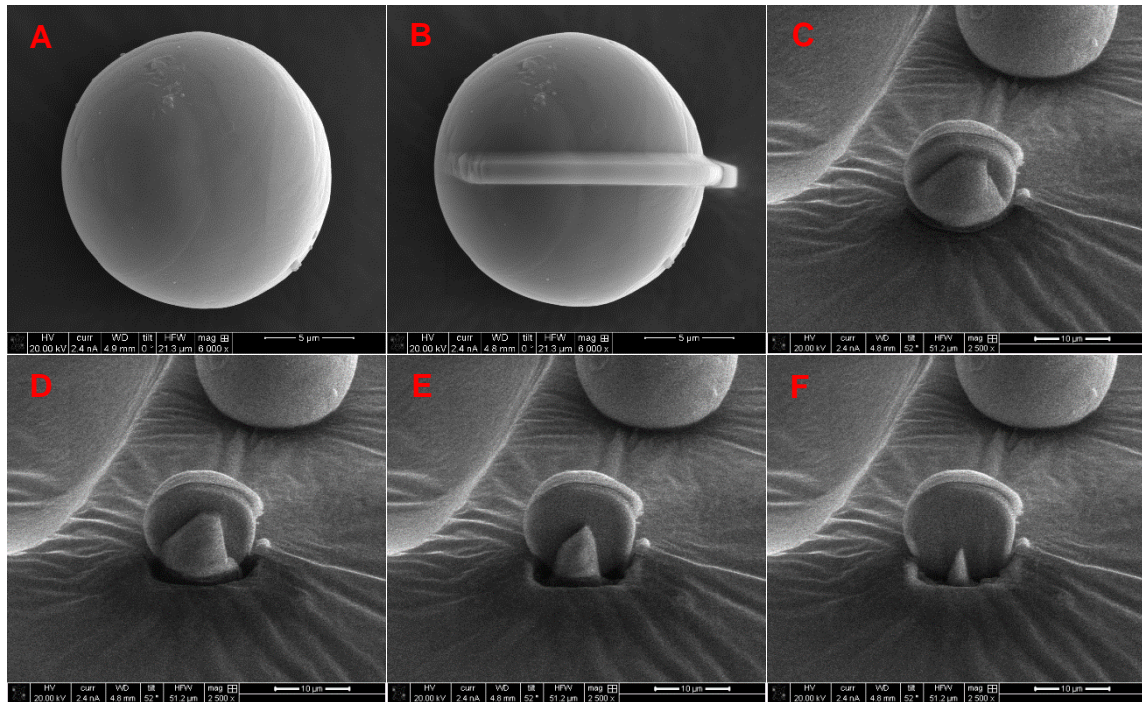


Figure 41: SEM live capture micrograph of milling an oxidised powder particle to expose the cross section FEI Helios Nanolab 600i FIB-SEM.

### 3.4.3 S/TEM sample preparation using FIB-SEM

Numerous lamella specimens were made throughout this project originating from different samples such as powder particles and tensile fracture bar surfaces. The process of creating a lamella for the fracture surface of the tensile bar and powder particles followed the same process each time in order to keep the results consistent. The region of interest (ROI) was selected for its surface characteristics in order to create the desired lamella in the fracture surface.

Once the lamella location is selected (Figure 42A), a  $\sim 2\mu\text{m}$  thick layer of Pt of size  $25\mu\text{m} \times 5\mu\text{m}$  is deposited on the surface, using the electron and ion beams (Figure 42B). This helps protect the region of interest from damage from the high current Ga ions used during preparation. Bulk material is then milled in the surrounding area to the Pt-protected ROI to a depth of  $\sim 20\mu\text{m}$  to expose preliminary lamella (Figure 42C). The lamella is then removed using an Omniprobe needle and mounted to a copper TEM grid where thinning and polishing at incrementally reducing beam currents and accelerating voltages produce a final lamella thickness of  $\sim 50\text{nm}$  (Figure 42D).

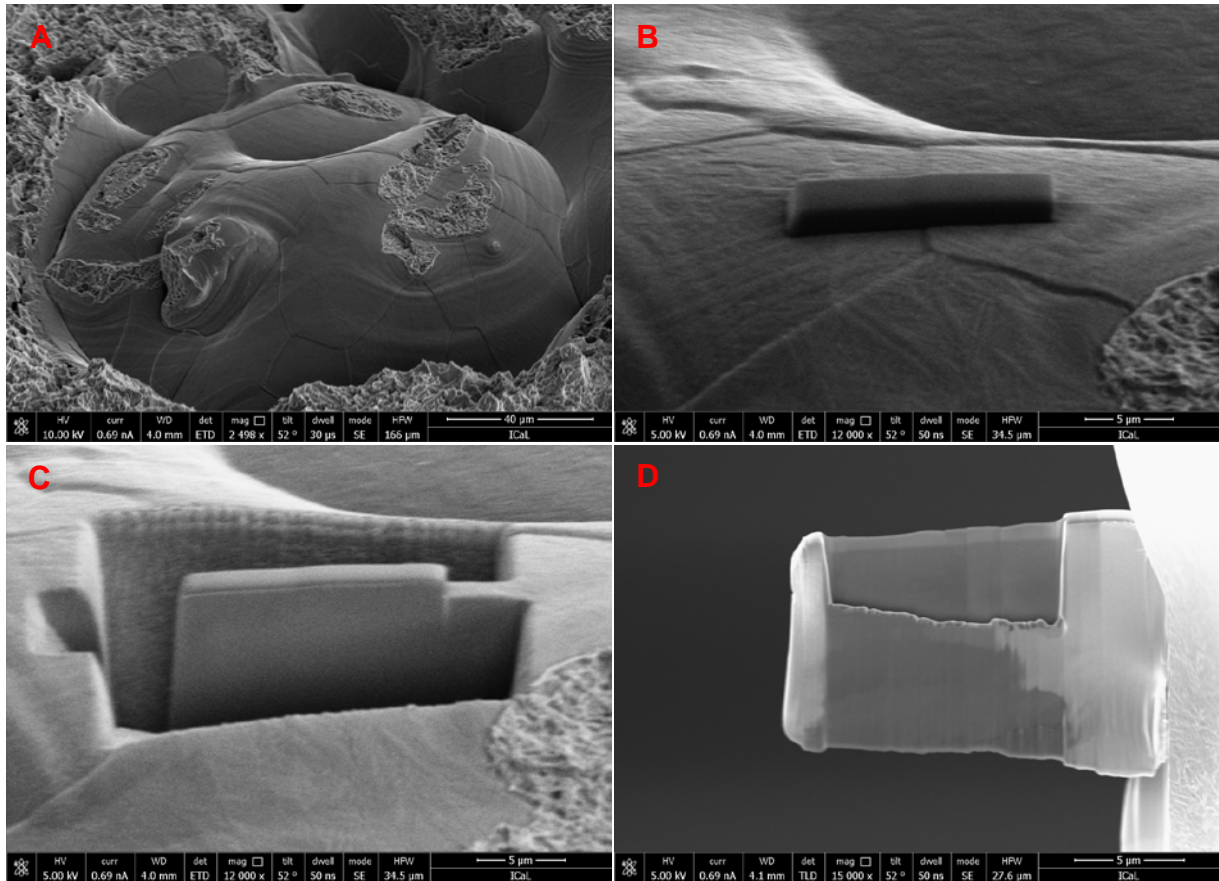


Figure 42: Images of In-situ lift out process to create a TEM lamella sample. A) Region of interest B) Pt layer C) Milling site D) Lamella sample mounted to copper grid

The thinning process started with an accelerating voltage of 30kV and a current of 0.28nA when the lamella sample is at its thickest (5µm). The voltage and current are incrementally decreased as the lamella thickness decrease until a final polishing voltage of 2kV and current of 15pA at a lamella thickness of ~50nm. The thinning process utilises a wedge milling process suggested in a study by M Schaffer *et al* [146] in order to best protect surface features and create a flat lamella for atomic resolution imaging as shown in Figure 43. Similar to accelerating voltage and current, at the lamellas thickest point, high angle tilt is used to thin both side of the lamella, at a thickness value of 5µm,  $\pm 5^\circ$  tilt angle is used incrementally decreasing to a final thinning tilt angle of  $\pm 1^\circ$  at a thickness of ~50nm. The final polishing tilt angle is  $\pm 5^\circ$  to remove any amorphous structure created by the gallium (Ga) ion source.

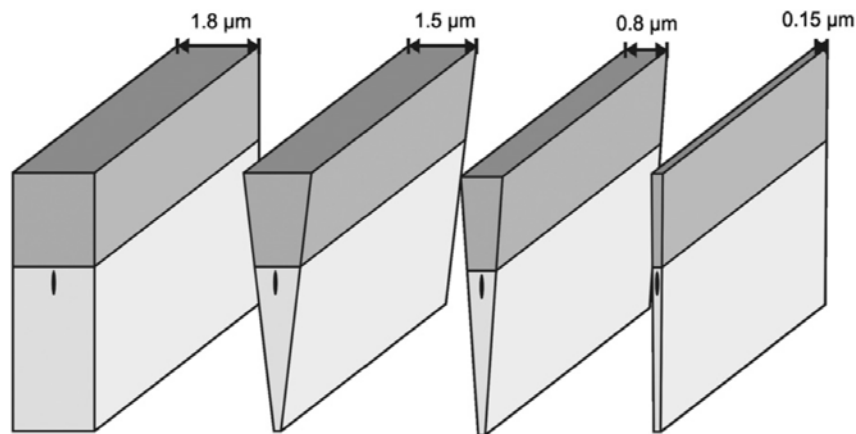


Figure 43: Schematic of wedge milling process

The process of creating a lamella sample for powder particles followed a very similar process as the same material was used. The significant difference between the processes was the region of interest (ROI), being a stand-alone powder particle mounted on carbon tape as discussed in 3.4.5.3. The in-situ lift out parameters, thinning and polishing all followed similar steps using the same equipment as methods.

### 3.4.4 Preliminary findings for S/TEM sample preparation

Throughout the FIB milling process there were a variety of problems producing lamella samples for STEM analysis due to several different factors. Primarily, the main finding from preliminary lamella production was the use of a Gallium source focused ion beam (FIB), the Gallium (Ga) atoms implanted onto the lamella surface creating amorphous structures and thus requiring lengthy cleaning procedures at low voltage and current to achieve atomic resolution as detailed in section 3.4.5.4. However, despite the cleaning routine of the lamella, small amounts of Gallium (Ga) implantation remained on the surface of the lamella making it hard to achieve consistent atomic resolution. The use of a plasma FIB negated this problem and was utilised for the cross-sectional measurements of the oxide layer thickness which is discussed in later sections. However, the plasma FIB had a high cost to the project and was not viable to conduct any remaining work on, therefore a Gallium source FIB was utilised for remaining work.

Another major finding in sample preparation for STEM was the bending of the lamella samples once mounted to the copper (Cu) TEM grids once the thinning process from the ion beam had started. Therefore, in order to achieve atomic resolution, two different methods were utilised for STEM analysis. Primarily, the in-situ lift out process featured a similar method to that illustrated in Figure 42 where it was found that some lamella may bend when milling with the ion beam, this would not make the lamella suitable for EELS analysis and would require consistent realignment as the region of interest changed on the lamella. Therefore, a second technique was utilised where sections of the lamella were thinned strategically for the desired analysis. This method used a 'channelling' technique, three channels were thinned to different thickness depending on the application, the locations between each channel did not receive any thinning from the ion beam and were left at the initial thickness of the lamella to keep the structural integrity of the lamella as shown in Figure 44. The three channels thinned were utilised for three separate analysis techniques, one for atomic resolution imaging, second for EDX analysis and the third for EELS analysis. Typically, the imaging channel was thinned to ~50nm as documented in the previous section. The second window featured a similar thickness for EDX analysis but did not require the intensive cleaning procedure that the first channel did, reducing the milling time of the FIB, finally the third channel was thinned the most achieving ~30nm to maximise the number of electrons passing through the lamella and captured by the EELS detector.

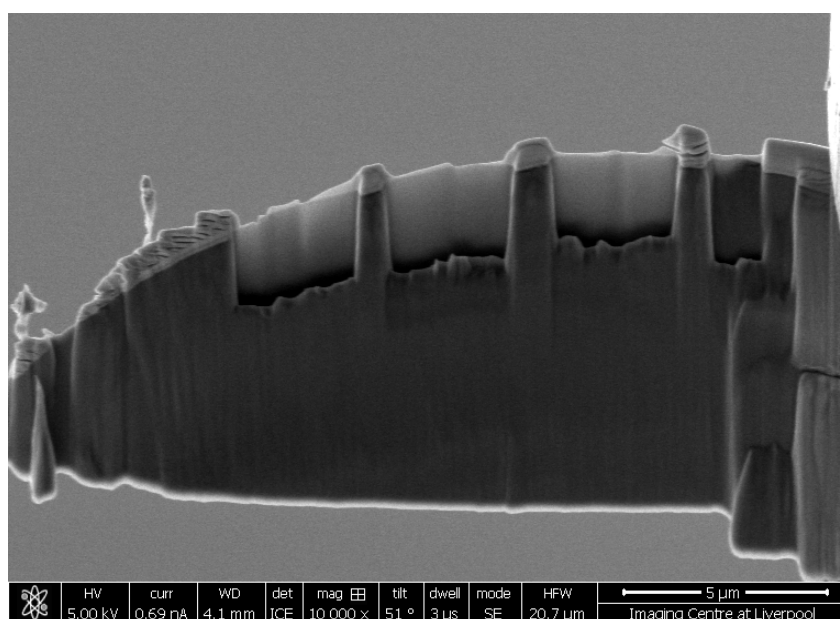


Figure 44: Thinning of blue Ti-6Al-4V lamella using a channelling method to maintain structural integrity.



This technique was used extensively for the particle STEM analysis in order to run the different types of analysis. However, it is important to note that the technique displayed in Figure 44 was not utilised in the latter stages of the project for the fracture surface lamella due to the complexity of the lift out process, because the uneven fracture surface, it proved challenging to topcoat and mill out the lamella, therefore due to the thin layer of Pt coating on the lamella surface, only one channel was thinned in order to avoid any damage to the surface.

The findings from these early investigations for FIB milling provided essential information to improve the time and efficiency of the FIB process for sample preparation for STEM as numerous lamella samples were made throughout the project for different particles and fracture surfaces.

### **3.4.5 Scanning Transmission Electron Microscope (S/TEM)**

Transmission electron microscopy utilises a beam of electrons generated from an electron emission source situated at the top of microscope. In comparison to SEM, the electron beam is transmitted through the specimen to achieve an image of the specimen. The beam of electrons is focused through a series of condenser lens in order to focus the beam onto the specimen. However, beam profiles vary dependent upon the grade of microscope and can significantly change the resolution and information limit of the microscope [147]. Higher grade microscopes feature  $C_s$  aberration correctors in order to correct the beam profile and produce better resolution. In order for the electron beam to transmit through the specimen, the sample has to be extremely thin. Samples vary in their nature and dependent upon the information required from the analysis, they are prepared using different methods. Typically, lamella samples are <50nm thick in order to achieve a high-resolution imaging [146]. There are two imaging modes: bright field (BF) and annular dark field (ADF).

A JEOL 2100f  $C_s$ -corrected FEG S/TEM (80-200kV) and JEOL 2100+ S/TEM (200kV, LaB6 thermionic emission source), as shown in Figure 45, was used throughout this project for high resolution imaging and quantification of elemental distribution. The microscopes have a point resolution of 0.19nm and a maximum magnification of

x1,500,000. The analysis conducted throughout this project was conducted with an accelerating voltage of 200kV, in both bright field (BF) and annular dark field (ADF). Scanning- TEM mode was used with all samples throughout the project and due to the nature of the sample, double tilt holder was used for all specimens. An EDAX Octane T Optima windowless 60mm<sup>2</sup> SDD EDX detector was used to quantify elemental distribution within lamella samples and help understand the concentration of interstitial elements such as oxygen due to diffusion in the SLM build process.

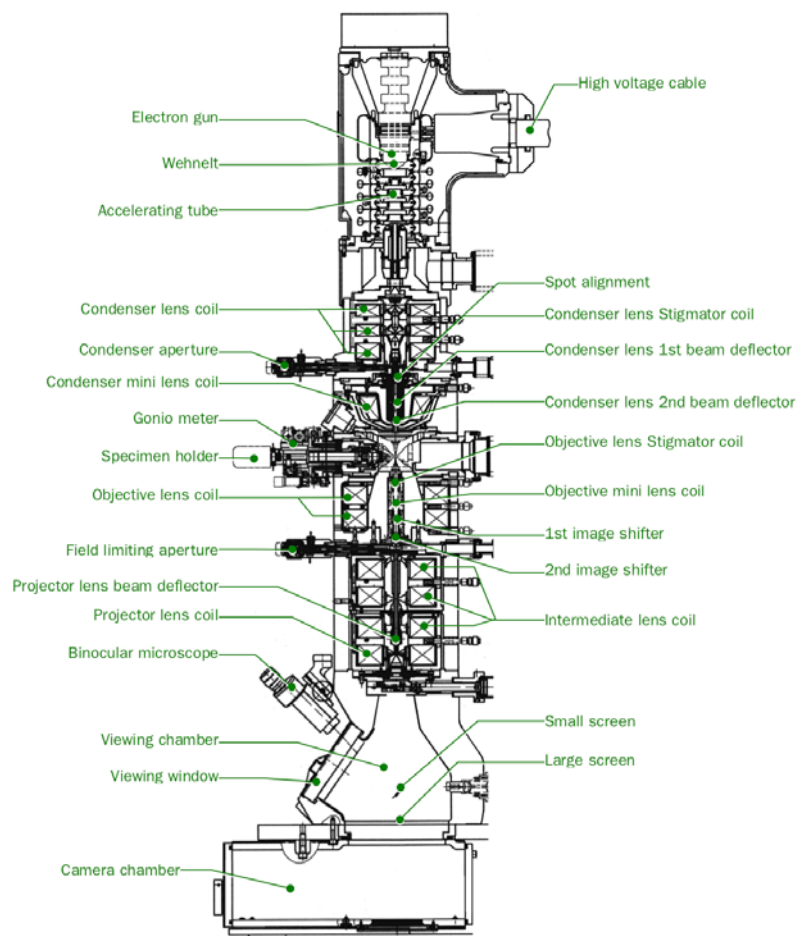


Figure 45: Schematic of cross section of JEOL 2100+ from the JEOL operation handbook.

### **3.4.6 Optical Microscope (OM)**

Optical microscopy utilises visible light through a series of compounding lenses to create a magnified image of a specimen. The primary objective lens is used to collect visible light from the specimen which is then focused inside of microscope to display an image, usually there are three or four objective lenses of different magnification. Most modern microscopes utilise a digital camera system in order to view and capture images of specimens due to the user-friendly interfaces and allows more than one user to view the specimen on a screen as opposed to the microscope eye piece. A Nikon "Epiphot TME" inverted microscope, fitted with M-Plan objective lenses, in brightfield illumination was used to image basic microstructure features and interference colours from oxidised particles. Images were captured employing an "Infinity 2-2C" CCD digital camera and "Infinity Capture v7.0" software.

### **3.5 TRUMPF TruPrint 1000**

All built samples throughout this project have been fabricated on a TRUMPF TruPrint 1000 machine. The TRUMPF TruPrint 1000 uses a 200W Ytterbium fibre laser to process deposited metallic powder within a 100mmx100mmx100mm build volume. However, the laser 200W Ytterbium laser is capped at 175W for processing to allow for calibration drift and drop off in power.

To minimise the potential for oxidation during the melting process, the build chamber is flooded with argon and the metallic powder is processed in an argon atmosphere. The build chamber is initially purged with argon to remove residual air from the build chamber and once a residual oxygen content <1000ppm is achieved, a running flow of argon across the powder is used to remove partially sintered and oxidised particles during the build process. The oxygen content reduces throughout the build process as more argon is introduced into the build chamber. The flow of argon is continuously filtered to remove fine powder particles and any particulates produced from the melting process.

### 3.5.1 Machine limitations

There are numerous limitations to the TRUMPF TruPrint 1000 (Figure 46) like that of every AM machine. However, in the context of this project, four key limitations are discussed that had the most significant potential to affect the build quality of the tensile specimens.

1. There is poor/inconsistent laminar gas flow across the build plate, this can lead to poor removal of spatter from the fusion zone and result in the creation of pores/defects if spatter particles are incorporated into fused material (parts). This can in turn mean that there is a variation in the part density as a function of build plate location, however this is not necessarily consistent.
2. There is a short time between layers (this is an unfortunate result of an aspect which is usually considered a positive). However, on the TRUMPF TruPrint 1000, the time between layers is short resulting in very little time for parts to cool down between laser exposures. This problem becomes more prominent over long build periods, the parts ambient temperature increases to levels at which thermal expansion and oxidation of the part become more significant. This effect is exacerbated when there is a step change (reduction) in cross sectional area, resulting in drop-in layer time. Note, a solution for this was provided in a software update, which allowed for the setting of a minimum layer time, however this software update was not available at the time of the tensile builds for this project.
3. The glass build and feed chambers are optional on the TRUMPF TruPrint 1000 and in the case of this project, Carpenter Additive chose this option for their research and development team as it allowed easy removal and cleaning as they processed multiple different alloys. However, previous builds using Ti-6Al-4V for a research project lead by Carpenter had caused the glass build and feed chamber to suffer thermal fatigue and consequently it cracked. This required a new cylinder to be bought and therefore delayed the tensile builds for this project by four weeks as we were unable to process without the glass build and feed chamber.
4. Relatively low power in comparison to other SLM machines. The 175W power is quite low relative to production focused SLM machines resulting in the laser

scan velocities being low to meet necessary energy densities. It's important to note, there is not an option to specify a higher power laser for the TRUMPF machines, but this was not available at the time of the tensile builds for this project.

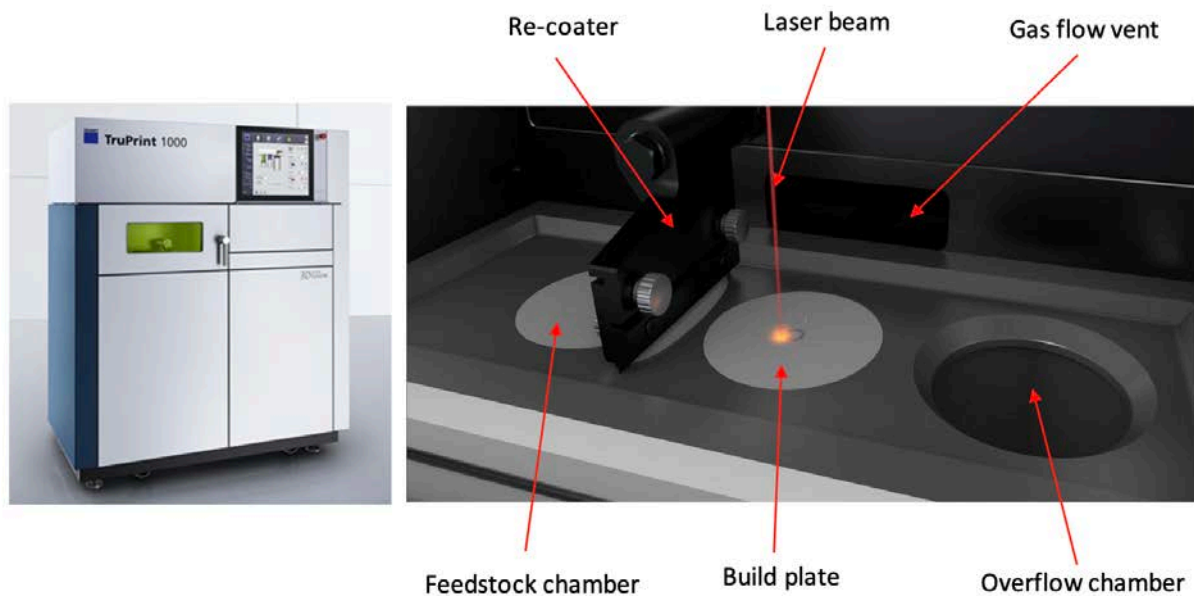


Figure 46: Images of TRUMPF TruPrint 1000 machine with labelled image of build chamber

### 3.6 Nano-Indentation

All tests were performed using the Nano Indenter G200 equipped with a DCM-II head and a Berkovich sharp (Synton) pyramidal tip. Prior to any testing, the pyramidal tip was calibrated using a fused silica sample. All nano-indentation testing was conducted using the Oliver-Pharr analysis [148]

Three samples were mounted into the Nano indenter, the samples consisted of cross sectioned tensile bars mounted in 32mm Conducto-mount pucks which had been polished using the procedure described in section 3.4.1. The three samples were loaded to 10 mN with a 15 second time to load and unload and a 10 second hold time. The drift rate was set to 0.1 nm/s and a Poisson's ratio of 0.31 was used. Three locations were chosen on each sample to show the variation in hardness with respect to the fracture surface, 5 indents were made in each chosen location. The first location

was the fracture surface, the second location is 50µm offset from the fracture surface and the third location is 100µm offset from the fracture surface.

### **3.7 Chapter summary**

In this chapter, the methodology for each analysis technique used throughout the project was explained in detail and several preliminary but key experiments were performed. The purpose of these experiments was to gain an understanding of the interference colours produced by thermal oxidation of the Ti-6Al-4V powder particles and optimise techniques to characterise them for later experiments.

Yellow and blue interference colours were chosen for the tensile builds as these coloured particles produced a uniform colour both on the bulk and particle level, whereas green produced a uniform bulk colour, however, on inspection of the individual particles, the colour varied.

It was found that two different techniques would need to be used for S/TEM analysis throughout the project; the particle analysis would require a technique which milled three channels out the lamella to avoid the bending effect from the internal stresses allowing multiple types of analysis on one lamella. However, the fracture surface lamella would use a wedge milling process due to the complexity of the lift process because of the uneven fracture surface.

## **4.0 Powder Characterisation of oxidised particles**

This chapter presents and discusses the results from the powder characterisation of the thermally oxidised Ti-6Al-4V powder particles.

Optical imaging was used to validate the consistency of the artificial manufacturing process in its ability to produce the same interference colour on the bulk and particle level. Chemical analysis investigated bulk powder material oxygen contribution, SEM imaging investigated the morphology of the powder batches and finally, particle size distribution investigated the effect of thermal oxidation on the change in particle size and distribution.

The results from these investigations formed the basis of the failure hypothesis as it furthered the understanding of the impact thermal oxidation had on powder properties on the bulk and particle level.

### **4.1 Preliminary investigation of oxidised powders**

There was little literature on thermal oxidation of Ti-6Al-4V powder metals, the existing literature focused on anodising titanium as this was the preferred industrial method for processes such as jewellery. Therefore, temperature and interference colour due to oxide layer growth was investigated over a range of 400°C to 700°C as it is well documented that >400°C oxygen begins to rapidly dissolve into titanium. As previously mentioned in section 3.2, the procedure utilised 10g batches for 60 minutes and produced an interference colour based on the oxide growth. This process was repeated at 10°C intervals to investigate all major interference colours produced within the given temperature range. The interference colours followed established literature with regards to order in which they appear with respect to oxide thickness, and this was correlated with the respective temperature to form the basis of the preliminary findings.



*Figure 47: Thermally oxidised Ti-6Al-4V powder particles; ranging from virgin (far left) to green (far right).*

Figure 47 displays the prominent colours from the preliminary investigations, there were many variants/shades of the colours displayed in Figure 47, however these colours were chosen for further investigation and the respective temperatures noted. Preliminary investigations such as chemical analysis was conducted to establish the correlation of colour and oxygen wt %. The results of these findings established that the oxygen wt % increased with temperature. This led to the coloured powder being narrowed down into three colours of interest: yellow, blue and green, these colours were chosen as they represented, in terms of this project, low, medium and high oxygen wt %.

These powders represented highly oxidised particles within a post processed powder bed which were significantly higher in oxygen content than the rest of the powder bed. This provided an idealised system with which to study the effects of oxidised Ti-6Al-4V powder particles in a powder bed.

This allowed efficiency in terms of powder utilisation for the project, instead of producing numerous different colours and thus using large quantities of powder, the decision to focus on three colours benefitted the project both in terms of cost and allowed a greater amount of analysis to be conducted on three distinct points in Ti-6Al-4V powder particle oxidation scale.



## 4.2 Chemical analysis of bulk powder

Throughout this research, interference colours were used to categorise different oxidation points throughout the Ti-6Al-4V oxidation spectrum. The aim being to develop a quality-controlled methodology with quantified levels of oxidation that match those observed in real reused powder, so as to observe their effect on part behaviour. This would increase understanding of the impact, if any, they would have on final build quality in real parts, and it would identify if post processing were likely to be helpful.

Inert gas fusion (IGF-IR spectroscopy) results in Figure 48 suggest that at temperatures  $<400^{\circ}\text{C}$ , the oxygen wt % increases at a slow rate. As the temperature increases ( $>400^{\circ}\text{C}$ ), the dissolution of oxygen into the core of the Ti-6Al-4V particles increases rapidly and an oxide layer begins to thicken on the particle surface. Figure 49 suggests that the temperatures  $>400^{\circ}\text{C}$  have reached the maximum acceptable oxygen content (wt %) of 0.13 wt % according to ASTM F136-13 for grade 23 Ti-6Al-4V powder. However, temperatures below  $400^{\circ}\text{C}$  are still below 0.13 wt % and within ASTM limits, therefore the powder can be considered for use as feedstock.

Oxides formed on Ti-6Al-4V are more stable than nitrides, under normal SLM processing conditions, and an oxide layer forms on any exposed surfaces at temperatures  $>400^{\circ}\text{C}$ , with titanium nitrides only forming readily in nitrogen rich atmospheres that are not normally used. Dependent upon the desired built component application, the maximum level of oxygen and nitrogen wt % in a build volume may differ across industry to meet safety standards. In medical applications, oxygen levels exceeding 0.2 wt % and nitrogen levels exceeding 0.05 wt % are out of specification as determined by ASTM F2924 ALM Ti6Al-4V. [149]

Both the yellow and blue powder (Figure 48) would be considered out of range for the medical industry (oxygen wt % of 0.4 wt % and 0.7 wt % respectively) if they made up the bulk of the powder but spread within powder of lower oxygen content they may not be observed, the overall powder being within specification. Little is known about the interaction of the oxidised powder within a build and the effect on the final build local oxygen content.

The error bars in Figure 48 and 49 are calculated using standard deviation of the IGF (LECO) results, this IGF technique adheres to test standard ASTM E1409-13 [143] and utilises triplicate testing; the measurement uses three, 1g batches of powder to vaporise and measure the O, N and H values to gain an average result.

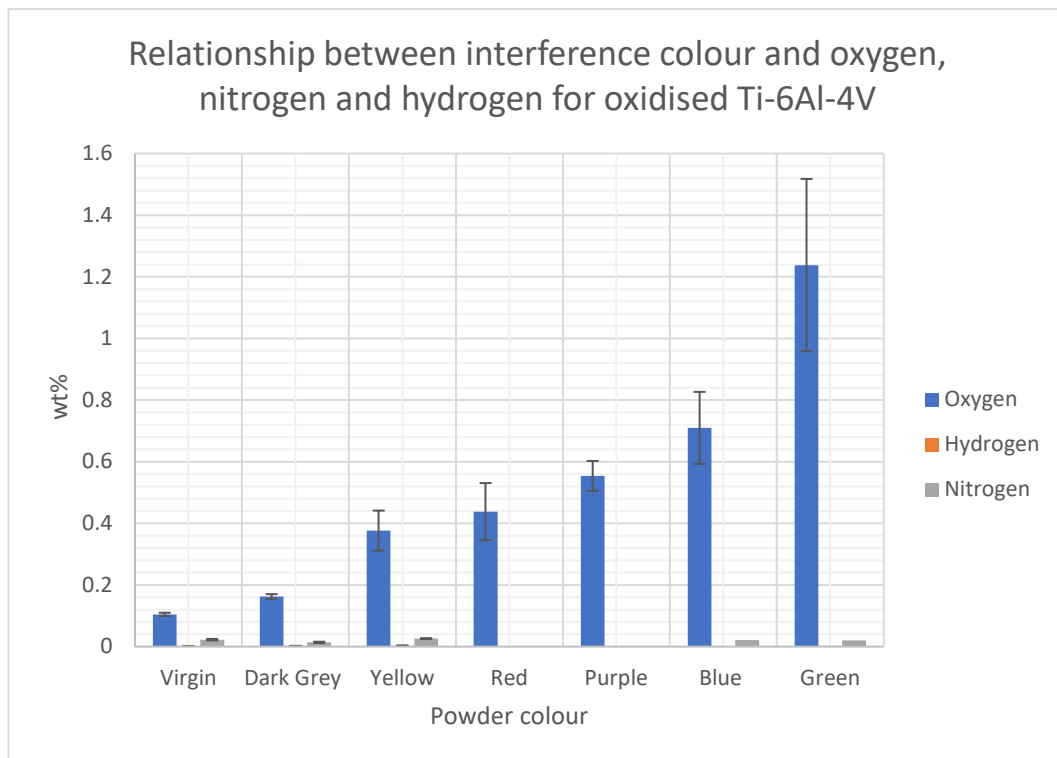


Figure 48: Relationship between interference colour and oxygen, nitrogen, and hydrogen in oxidised Ti-6Al-4V metal powder.

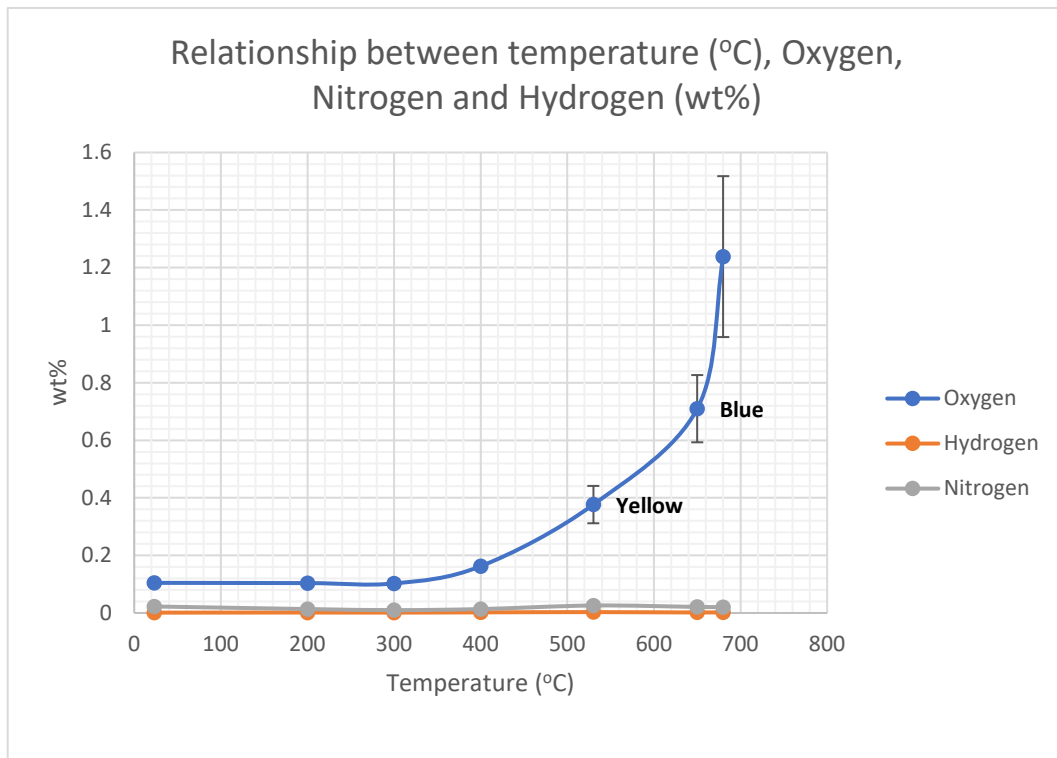


Figure 49: The impact of temperature on oxygen, nitrogen, and hydrogen for oxidised Ti-6Al-4V

### 4.3 Morphology of powder particles

The morphology of each powder batch was investigated to understand the potential impact of the oxidation process on key powder properties such as flowability and packing density.

Scanning electron microscopy (SEM) was used to image the powder at different magnifications, the morphology investigation features a low magnification micrograph and a high magnification micrograph to compare each powder batch in detail.

Figure 50A displays a low magnification micrograph of virgin Ti-6Al-4V, the image shows many powder particles which all appear uniform in shape and a similar spherical morphology. The image suggests a variety of particle sizes distributed evenly throughout. Figure 50B displays a high magnification micrograph of the same virgin Ti-6Al-4V showing large and small particles all spherical in morphology and shows little to no evidence of satellites or contamination. However, it is worth noting that there are small particles (<math><5\mu\text{m}</math>) attached to the surface of the larger particles present within

the high magnification image, this is likely due to the manufacturing process of the virgin Ti-6Al-4V.

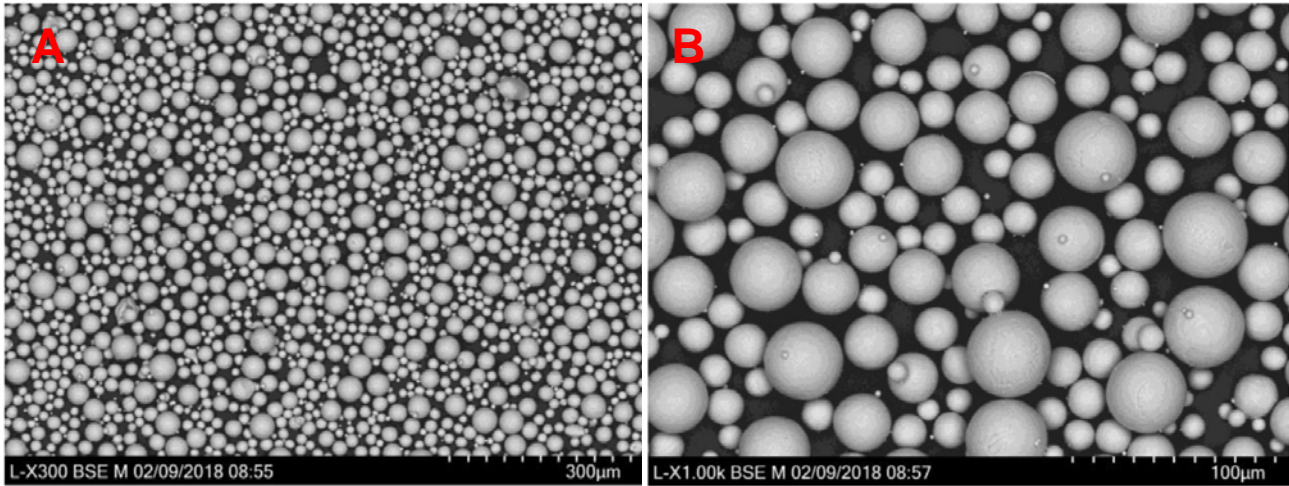


Figure 50: A) BSE micrograph at x300 magnification of Virgin Ti-6Al-4V B) High mag (x1000) BSE micrograph of Virgin Ti-6Al-4V

Figure 51A displays a low magnification BSE micrograph of yellow coloured Ti-6Al-4V, the image displays a large variation in particle size and a similar morphology to that of virgin Ti-6Al-4V. Figure 51B displays a high magnification BSE micrograph of yellow coloured Ti-6Al-4V, the image displays large and smaller particles with some evidence of satellites and potential oxide growth on the particle surface denoted by the red circle.

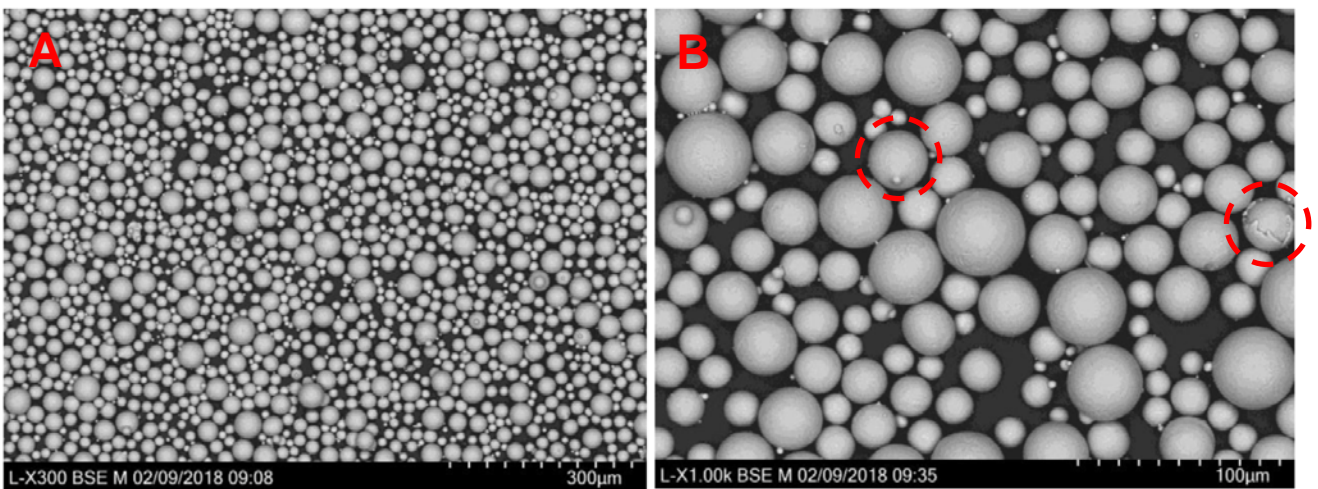


Figure 51: A) BSE micrograph at x300 magnification of yellow coloured Ti-6Al-4V B) High mag (x1000) BSE micrograph of yellow coloured Ti-6Al-4V

Figure 52A displays a low magnification BSE micrograph of blue coloured Ti-6Al-4V powder, the image displays a large variation in particle size and morphology with evidence of oxide growth and satellites throughout. Figure 52B shows a high magnification BSE micrograph of blue coloured Ti-6Al-4V with strong evidence of satellites on the surface of powder particles alongside evidence of a textured structure on the surface of the particle as denoted by the red circle.

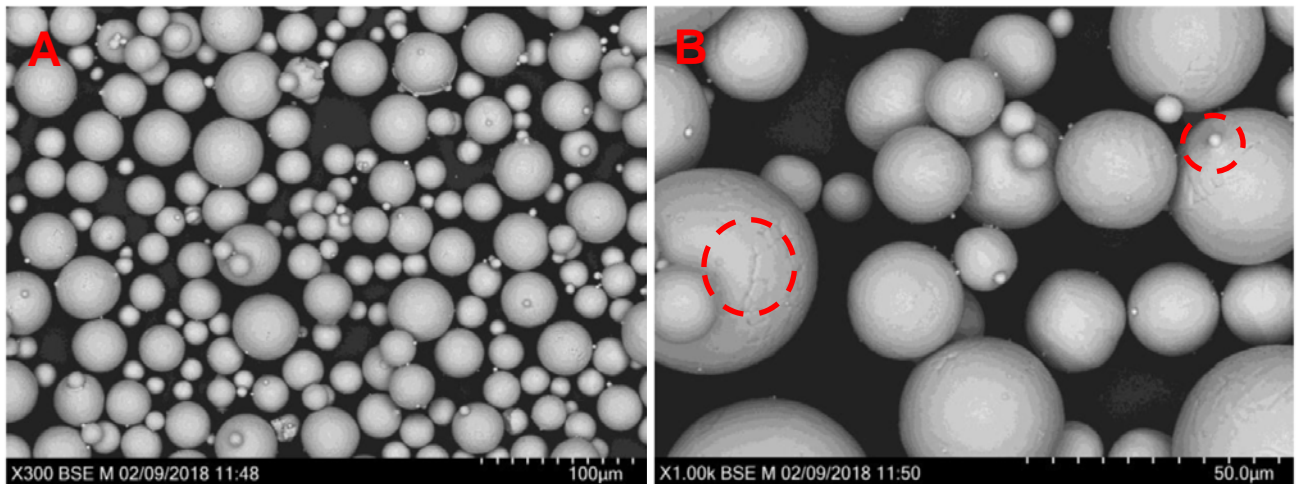


Figure 52: A) BSE micrograph at x300 magnification of blue coloured Ti-6Al-4V B) High mag (x1000) BSE micrograph of blue coloured Ti-6Al-4V

Figure 53A displays a low magnification BSE micrograph of green coloured Ti-6Al-4V powder, the image displays a large variation in particle morphology with evidence of satellites on the particle surface denoted by the red circle. Figure 53B displays a high magnification BSE micrograph of green coloured Ti-6Al-4V, here there is further evidence of satellites on the surface of powder particles alongside potential oxide layer growth on the surface of powder particles as a rough texture can be observed.

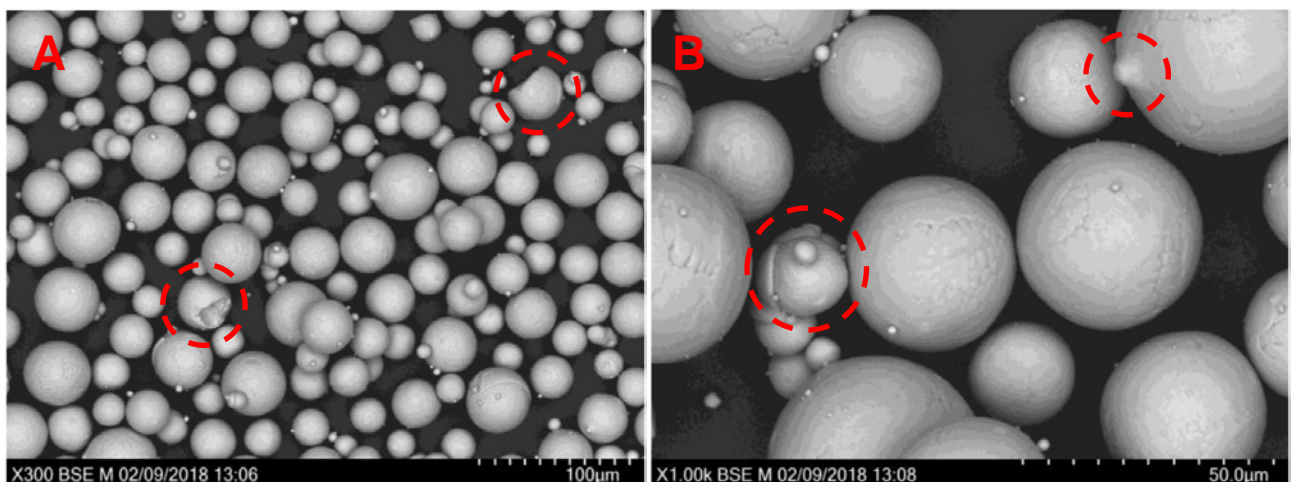


Figure 53: A) BSE micrograph at x300 magnification of green coloured Ti-6Al-4V B) High mag (x1000) BSE micrograph of green coloured Ti-6Al-4V

#### 4.4 Particle size distribution (PSD)

Particle size analysis was conducted to confirm the particle size range and obtain information with regards to the particle size distribution (PSD). Table 4 shows the  $D_v$  values for each oxidised powder condition, the results shown are averages of three passes on the Malvern Mastersizer 3000.

Table 4: PSD results for oxidised Grade 23 Ti-6Al-4V

$D_v$ Value	Virgin	Yellow	Blue	Green
$D_v 10$ ( $\mu\text{m}$ )	22.3	22.0	22.8	22.5
$D_v 50$ ( $\mu\text{m}$ )	32.7	32.3	32.8	33.4
$D_v 90$ ( $\mu\text{m}$ )	47.2	46.8	45.7	49.0
Particles $<16\mu\text{m}$	0.4%	0.49%	0.34%	0.29%
Particles $>45\mu\text{m}$	13.3%	12.63%	11.37%	16.14%

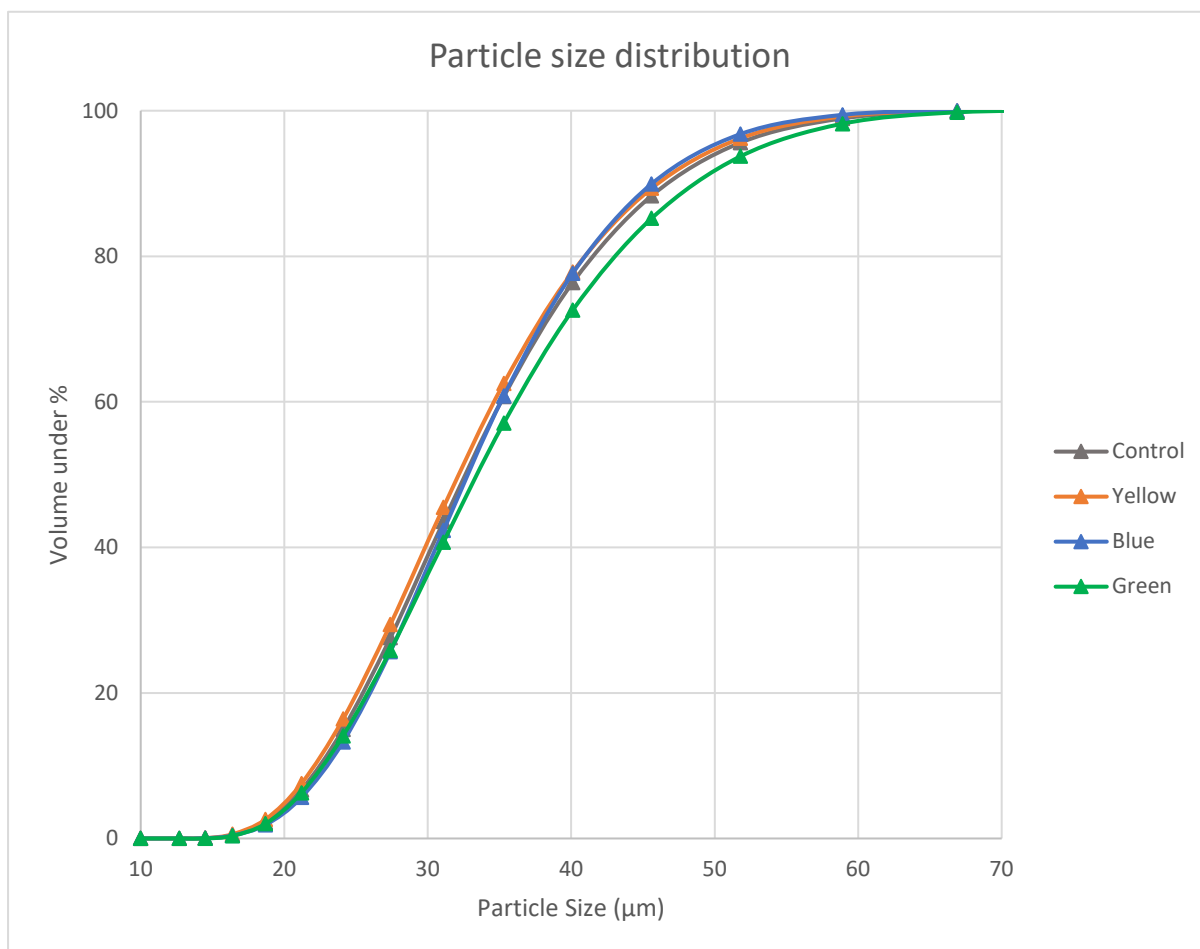


Figure 54: Particle size distribution

Overall, Figure 54 suggests that the particle size distribution remained relatively consistent across the control (virgin), yellow and blue powder with a change of 1.5µm for Dv (90), 0.1µm for Dv (50) and 0.5µm Dv (10). However, relative to the control (virgin), green yielded a significant increase in particle size with a change of 1.8µm for Dv (90), 1.1µm for Dv (50) and 0.2 µm for Dv (10). Additionally, the data suggested no significant change in particle size >45 µm with only a 1.93% change between virgin, yellow and blue. However, the green powder >45 µm increased 2.84% relative virgin. This increase is likely accredited to large oxide layer covering the surface of the particles and potentially agglomerates or oxide satellites distorting LSD measurements.

In terms of processing, these findings suggest the particle size of yellow and blue are not significant differently from that of virgin but may still detrimentally affect the ability of the powder to flow and packing density during the build process. However, the green powder suggests there are significant differences across all the size classes and the number of particles  $>45\mu\text{m}$  is significantly larger than that of virgin, resulting in reduced packing density and flowability of the powder. The green  $D_v(90)$  is an increase of  $1.8\mu\text{m}$  compared to virgin  $D_v(90)$  suggesting an increased number of large particles. Interestingly, there was a decrease in the number of fine particles ( $<16\mu\text{m}$ ) as volume (%) reduced by 0.11% between virgin (0.4%) and green (0.29%) powder.

The reduction in smaller particles can aid the flowability of the powder as the smaller, fine particles can inhibit the flow of powder due to their increased inter-particle adhesion resulting in friction. Harkin et al [47] investigated powder recycling in SLM using grade 23 Ti-6Al-4V and found that the powder flowability increased from 30s per 50g to 23.6s for 50g for recycled powder where the number of fine particles ( $<14.5\mu\text{m}$ ) as volume (%) has reduced from 0.06% to 0.03%.

However, in terms of processing, the larger particles ( $>50\mu\text{m}$ ) will likely be removed by the wiper/re-coater and transferred into the collection cylinder. The finer particles ( $<50\mu\text{m}$ ) are spread across the build plate and likely participate in the melting and solidification during manufacturing. Although the larger particles ( $50\mu\text{m}$ ) are likely to be removed by the wiper if they are bigger than the build height, it is possible that they could scrape across the surface of the powder creating lines in the powder leading to zones of lack of fusion or increased porosity. This could be detrimental to the build as under loading conditions, lack of fusion and increased porosity can result in premature failure. Yellow powder particles have an oxide layer thickness of around 20-40nm, Blue powder particles around 60-80nm and green around 200nm thick [150][65]. Therefore, the diameter of the particles will slightly increase as the oxide layer grows for the respective colour as seen in the particle size distribution in Figure 54. However, this change is small relative to the particle size, and it is likely powder variation is also a large contributing factor in the different PSD.

After each completed build, the powder will likely pass through a series of sieves and mixed with the feedstock dependent upon the chosen recycling strategy. If this process



is repeated, then the PSD of recycled powder will begin to narrow as the larger particles ( $>50\mu\text{m}$ ) are removed via sieves and the smaller particles ( $<50\mu\text{m}$ ) are present within the melting process. Therefore, it is likely that the smaller particle size class poses a larger threat to the built component in comparison to the larger particles as they are likely to be removed. Smaller particles with a high oxygen content and oxide layer may remain within the powder as neither the re-coater/wiper and the post sieving may not remove these problematic particles. Patrico et al [151] investigated recycling of Ti-6Al-4V in SLM and reported a narrowing of PSD as powder reuse increased alongside better flowability compared to new powder due to lower cohesion and interparticle frictions.

#### **4.5 Optical Imaging**

Optical imaging proved a useful tool for the investigation into the powder characterisation as it showed the bulk and individual particle colour under the illumination of white light from the objective lens. 1g of each powder colour was spread across a glass slide and sealed with a clear piece of tape to ensure no movement of the powder particles under the optical microscope.

Optical imaging served two main purposes throughout the project; it was initially used to understand if the artificially oxidised bulk powder interference colour consisted of numerous smaller particles of the same interference colour.

Optical imaging was initially used to understand the relationship between the bulk colour and the individual particle colour by imaging the bulk colour of the powder and comparing this to individual powder colour. In the case of the bulk powder colour matching the individual particle colour, this would validate the thermal oxidation process used to create these particles as they produced consistent colours on the particle and bulk level. It was vital that the bulk powder colour and the particle colour was the same for the later stages of the project as analysis using SEM and FIB-SEM, produces a black and white image and it would not be possible to distinguish between colours without preparing an individual particle for analysis.

The yellow powder proved to be successful in terms of producing a uniform colour both on the particle level and the bulk powder colour. Therefore, the conditions for the artificial oxidation process were successful and made it reasonable to assume all the particles were of the same colour for chemical analysis to understand the oxygen contribution of the colour.

Figure 55A shows a low magnification optical image of the powder batch displaying a uniform distribution of the 'yellow' colour with all particles showing a spherical morphology. Figure 55B shows a higher magnification image displaying a uniform colouring of the particle with no evidence of any other colours.

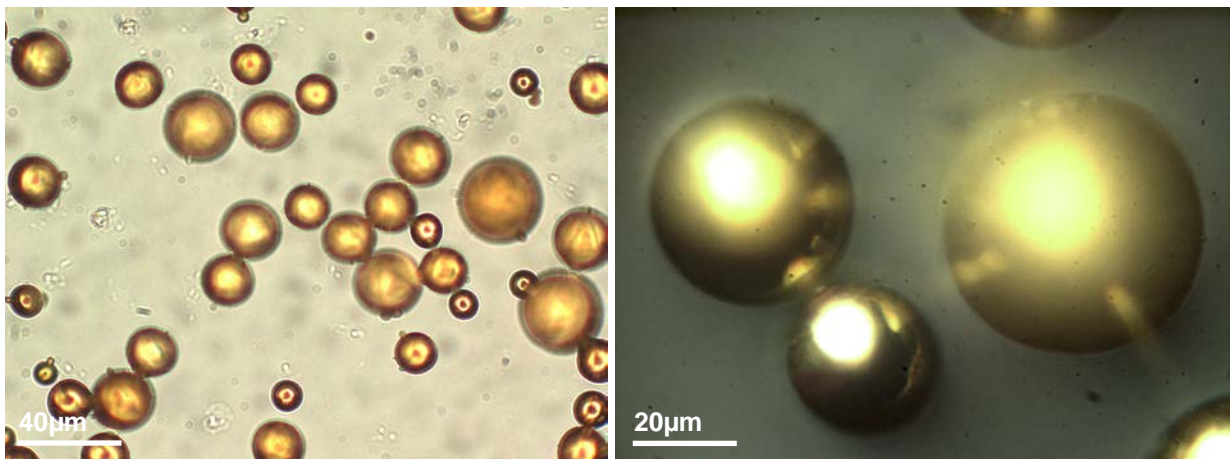


Figure 55: A) Low magnification (x200) optical image of yellow coloured Ti-6Al-4V powder particles B) Higher magnification (x1000) optical image of yellow coloured Ti-6Al-4V powder particles.

The blue coloured powder showed a blue interference colour both at the bulk powder level and the same colour at the particle level. Figure 56A displays a low magnification optical image of the powder sample and displays a uniform colour throughout all of the particles of a blue interference colour. Figure 56B displays a high magnification optical image of the powder sample and again displays a uniform blue colour on the particles alongside a spherical shape.

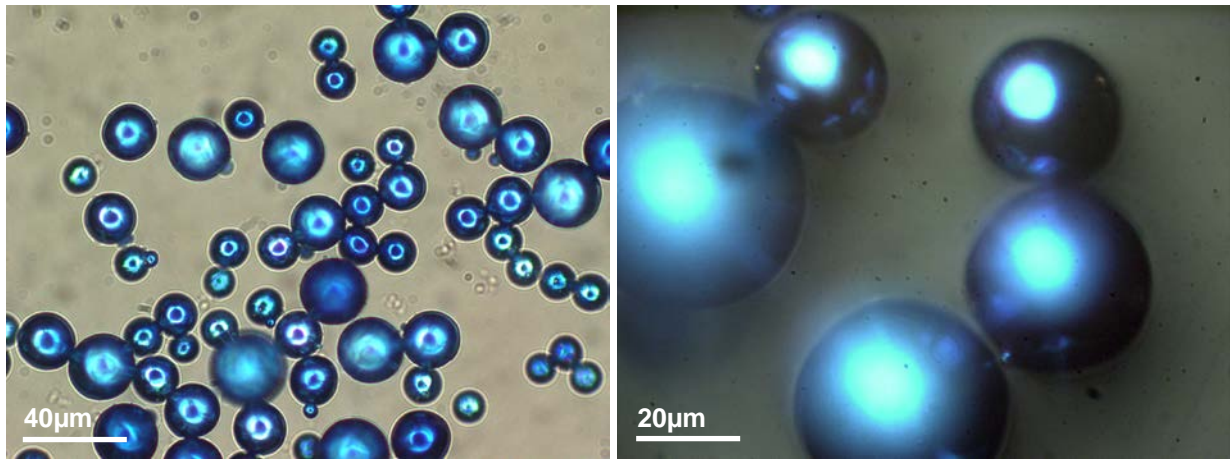


Figure 56: A) Low magnification (x200) optical image of blue coloured Ti-6Al-4V powder particles B) Higher magnification (x1000) optical image of blue coloured Ti-6Al-4V powder particles.

The green powder sample displayed a non-uniform distribution of colours throughout the particle sample. Figure 57A displays a low magnification optical image of the powder sample and clearly indicates a variety of different interference colours present throughout the sample. The bulk colour may appear to be green to the human eye, however, under the microscope, it is a variety of different colours from the oxidation spectrum that comprise the powder samples bulk colour. Figure 57B further reiterates this in a high magnification image of the interference colours on the particle surface clearly indicating the presence of purple, green, yellow, and blue coloured particles.

The green coloured powder proved to be problematic to achieve a uniform distribution of green coloured particles. It is possible that this is due to the rate of heating, smaller particles will heat up faster than larger particles and consequently reach the prescribed oxidation temperature quicker. However, the larger particles will take longer and therefore will need to be held at the oxidation temperature longer to achieve the same oxide thickness as the smaller particles. Due to the small exposure time of 60 minutes, some of the larger particles may not have had enough time held at the oxidation temperature to reach the required oxide thickness to create the interference colour green, whereas the smaller particles may have reached this colour in the 60-minute exposure time. Therefore, this creates a mixed batch of coloured powder as observed in Figure 57. Additionally, it is possible that because the powder is effectively in a pile in the crucible dish during oxidation, the oxygen cannot get to all the particles and the particles on the outer of the sample will heat up faster than the particles on the inner of the sample. However, due to the small batch size of 10g for oxidation, this is unlikely, and this problem becomes more significant in larger batch quantities.

NOTE: it is possible to achieve a uniform colour of green powder both on the bulk scale and the particle level but requires a change in the key variable such as exposure time and atmospheric conditions. However, the decision was taken to not up scale the manufacture of the green powder as it was hard to consistently manufacture to ensure all the particles featured the same colour and from this point on in the project for further investigation, the blue coloured powder would act as the high oxygen contributing particle.

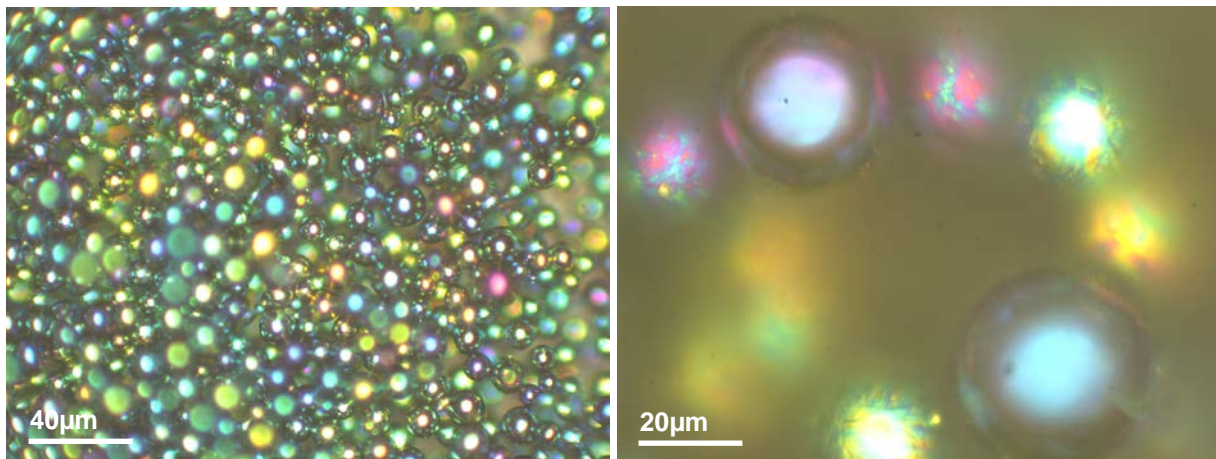


Figure 57: A) Low magnification (x200) optical image of green coloured Ti-6Al-4V powder particles B) Higher magnification (x1000) optical image of green coloured Ti-6Al-4V powder particles.

The optical imaging proved a valuable aspect to the project investigation as it validated the manufacturing process for yellow and blue powder particles. The green powder displayed a mixture of different colours that comprise of the bulk powder colour, although achievable, this proved difficult to control the quality of the powder created in ensuring uniformity within the powder particle colour. Therefore, the decision was made that the blue powder material would act as the high oxygen contributing particle for the tensile builds as the validity of the green build could not be ensured. However, for the purpose of the investigation, the green powder particles would still undergo the same powder characterisation as the yellow and blue.

## 4.6 Colour characterisation

Colours created by the interference phenomenon are a crucial element of the project as they are the foundation for building a quality control methodology. Understanding the interference colours and quantifying their presence within powder beds allows SLM users to identify problematic particles within post processed powders by identifying these particle colours and choosing the necessary action to prevent them entering the build process. The interference phenomenon is created by oxide layers on the particle surface, therefore, different oxide layer thickness results in different colours. Therefore, the three main colours chosen for this project, yellow, blue and green represent, in relation to this project, low, medium and high oxygen wt %.

L\*a\*b\* colour space was used to quantify the colour of the bulk powder, L\*a\*b\* colour space is quantitative colour model defined by the Commission Internationale de l'Eclairage (CIE) measuring three main components: lightness ( $L^*$ ), red/green coordinate ( $a^*$ ) and yellow/blue coordinate ( $b^*$ ).

Quantifying the reflectance and L\*a\*b\* coordinates of each colour and relating them to an oxygen wt % range would form the basis for a preliminary quality assessment of post processed powder bed. If an image of the post processed powder can identify the coloured particles and correlate an oxygen wt % range, it would allow a user to understand if there are problematic particles present within the post processed powder bed.

### 4.6.1 Bulk colour reflectivity and LAB colour space

Understanding the reflectivity of the coloured powder particles relative to the virgin Ti-6Al-4V powder is crucial as the interference colour due to the oxide thickness may also affect the behaviour as the reflectivity of the particle will change with interference colour. Interference colour studies of thin titanium oxide layers suggest that the refractive index decreases at larger oxide layer thickness.[65] Therefore, the thermal energy absorbed by the blue particles may not always be sufficient to melt the shell oxide and the core particles, resulting in un-fused/ partially fused particles into the

surrounding build layer. Each interference colour has a different oxide thickness and thus produces a different reflectance value. Utilising Konica Minolta colour spectrometry, each powder colour was analysed across wavelength of 360nm to 740nm to evaluate the reflectance (%) value and quantify the colour to understand whether the interference colour being observed on the bulk level matched the same colour on the known L\*a\*b\* colour charts.

Figure 58 shows the relationship between reflectance and wavelength of the three interference colours relative to the virgin Ti-6Al-4V powder. The virgin powder displays a consistent high reflectance starting at 15% at 360nm, gradually increasing to 22% at 740nm suggesting that the virgin powder will have a consistent refractive index which will aid consistent thermal absorption of the laser energy across the build process. The yellow powder displays a steady increase from 3% at 360nm to 13% at 740nm suggesting that powder may not absorb energy as readily as virgin. Blue powder shows a steady decrease from 13% at 360nm to 2% at 740nm suggesting that this powder has low reflectance across the majority of wavelengths [152] and may potentially increase the thermal absorption from the laser energy [153]. Interestingly, although green has the largest oxide thickness, this colour produces a steady increase from 5% at 360nm to 15% at 740nm. Diamanti et al [150] reported similar reflectance values for two step anodised TiO<sub>2</sub> for oxide thickness of 80nm, 100nm and 120nm.

Carrion et al [151] measured the thermal conductivity of reused powder and showed that the thermal conductivity slightly increased as the number of reuses increased alongside a slight increase in PSD for reused particles agreeing with the results from Figure 54. The thermal conductivity of the powder is significant in this case as it plays a significant role in cooling rates and thermal histories, therefore effecting the resultant microstructure of the built part [154].

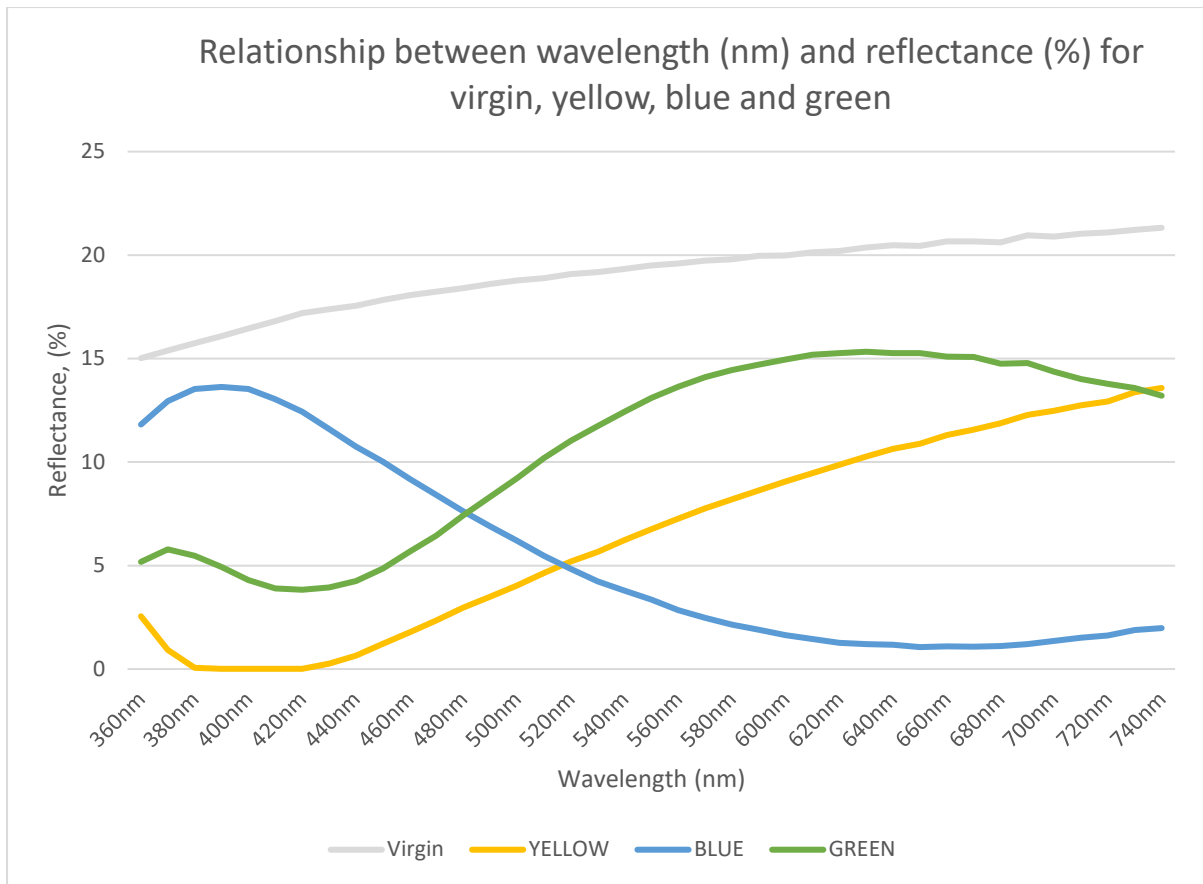


Figure 58: Relationship between reflectance (%) and wavelength (nm) for bulk colours; yellow blue and green and control colour; virgin.

As previously mentioned,  $L^*a^*b^*$  colour space is the industry standard for measuring different colours and quantifying them. Here each powder is assigned a quantitative value and plotted on the  $L^*a^*b^*$  colour space chart to show where the colour sits relative to other colours. The axis are defined as lightness ( $L^*$ ), red/green coordinate ( $a^*$ ) and yellow/blue coordinate ( $b^*$ ).

The colour measurements in Figure 59 are conclusive with known  $L^*a^*b^*$  values for the three bulk-coloured powders being investigated. The three powder colours are present across two different quadrants of the  $L^*a^*b^*$  colour space and yellow sits on the vertical  $L^*$  axis, this suggests that there are significant differences in lightness ( $L^*$ ) and chromatic colouring ( $a^*$  and  $b^*$ ). This is expected as the three powders display distinct differences in their colour both on the bulk level and the particle level as shown by the optical micrographs in section 4.0.

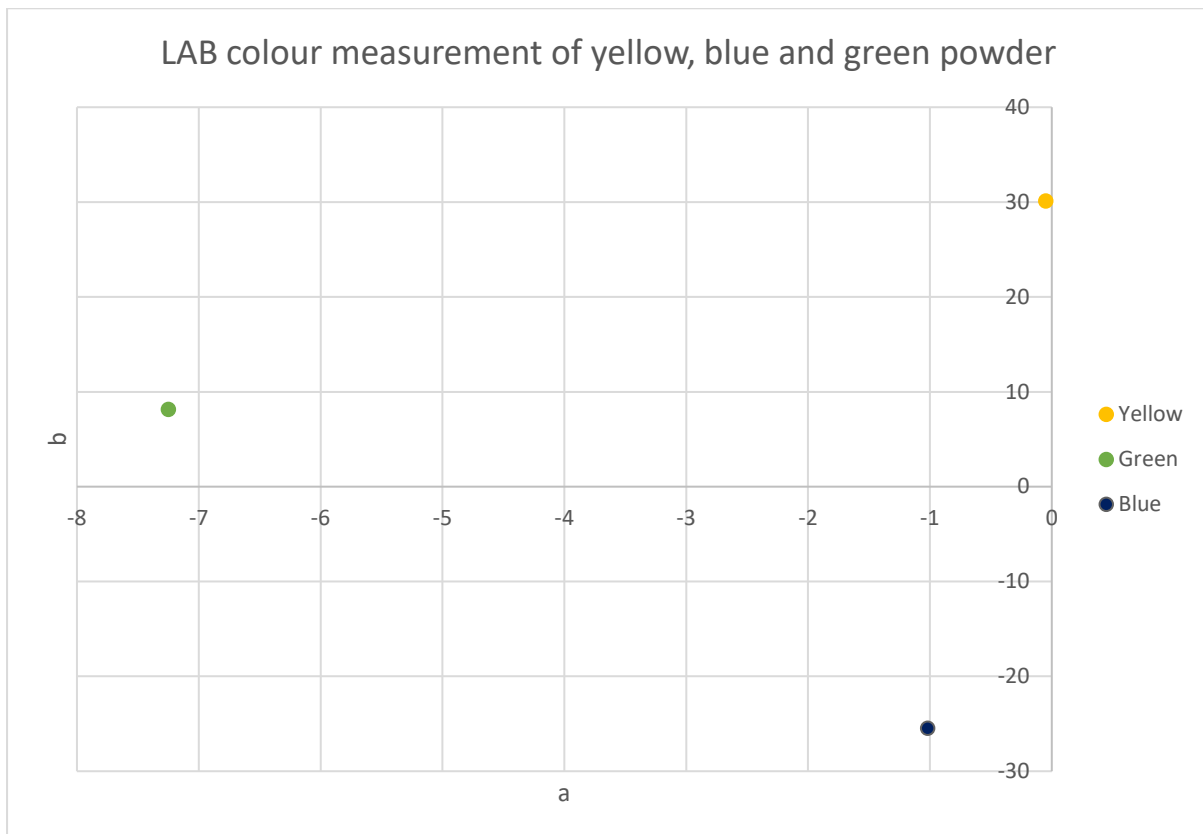


Figure 59:  $L^*a^*b^*$  colour measurements of the three bulk powders; yellow, blue, and green.

#### 4.6.2 Sub-yellow powder reflectivity and LAB colour space

Similar to the bulk colour study, the reflectance relationship with wavelength was conducted for powders that did not show any apparent interference colour change but produced increased oxygen contents across temperatures of 200°C, 300°C and 400°C. Understanding the reflectance changes of these powder particles was important as they represented heat affected zone powder which is commonly found around built parts. Establishing the relationship between reflectance and wavelength aided understanding of whether the heat absorption changes as they are subjected to varied temperatures between 200-400°C.

Figure 60 shows the relationship between reflectance (%) and wavelength (nm) for three different heat effected powders: 200°C, 300°C and 400°C. The 200°C powder shows similar results to the virgin powder as it produces a consistent slight increase



in reflectance from 12% at 360nm to 20% at 740nm. Similarly, 300°C also displays similar results with a slightly lower starting value of 6% at 360nm and peaking at 18% at 740nm. Lastly, the 400°C powder displayed a similar relationship but produced significantly lower starting reflectance of 2% at 360nm and peak of 17% at 740nm.

Overall, the result across the three heat affected zone powders showed similar results in terms of the relationship across the given wavelengths, the only distinguishable difference appears to come from the starting value and the peaks which differ slightly due to slightly larger oxide thicknesses on each powder (in the order of nm). In comparison to the bulk colours, these powders produce consistent high reflectance results which are favourable for the conditions inside the SLM process as it allows consistency.

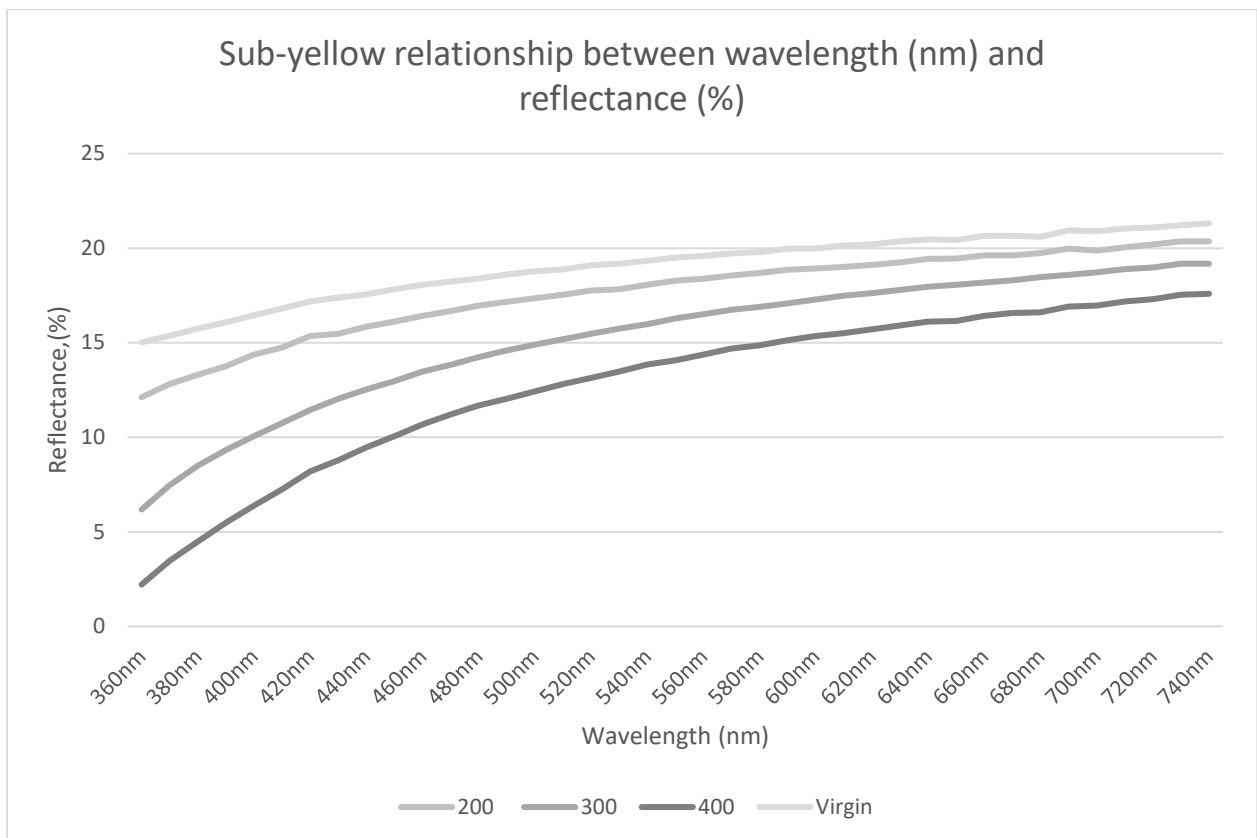


Figure 60: Sub-yellow relationship between wavelength (nm) and reflectance (%)

Similar to the bulk colour study, the sub yellow powder was all quantified using a spectrometer and plotted in  $L^*a^*b^*$  colour space. The values obtained using the spectrometer are in the same quadrant suggesting that there is little variation in the lightness ( $L^*$ ), and chromatic axis ( $a^*$  and  $b^*$ ). This suggest that although the powder increases in oxygen as the temperature increases, the change in colour below  $400^\circ\text{C}$  is not significant. The similar values in the  $L^*a^*b^*$  readings can be accredited to the small oxide layer covering the surface of the powder particles, the oxide layer is not thick enough to create the interference phenomenon to change the colour of the particle and thus displays similar values across the different heat-treated powders.

Similar to Figure 59, the axis in Figure 61 are defined as lightness ( $L^*$ ), red/green coordinate ( $a^*$ ) and yellow/blue coordinate ( $b^*$ ). Interestingly, for the sub yellow powders, there is no distinct difference in the colour of powder to the naked eye but there are differences in colour and reflectance measured by the spectrometry results in Figure 58 and Figure 60.

In comparison, the bulk colours yellow, blue, and green are noticeably different to the naked eye and the spectrometer, suggesting that although the bulk colours present the largest oxygen contribution to the powder bed as individual particles (Figure 48), they can be easily identified and potentially controlled. Identifying the highly oxidised particles, allows the user to make decisions whether to proceed with the feedstock or potentially develop a process to remove the oxidised particles. However, the sub yellow powders are not easily identifiable from the naked eye but are different in the spectrometer potentially presenting a higher risk to build material properties due difficulty in identifying and isolating these particles.

The sub yellow powders may present a considerable challenge in terms of controlling the quality of post processed powder as the sub yellow powders can be present in the large numbers within the powder bed and avoid detection as they are a very similar colour to the virgin powder as shown in Figure 60 and 61. These particles are most likely to occur in the heat affected zone where increased localised temperatures radiating away from the melt pool increase the temperature of the immediate surrounding powder.

Although the oxygen contribution from an individual particle from the sub yellow particles may be small and within the ASTM limits, large quantities of these particles may raise the bulk oxygen content of the powder considerably and bring the overall powder feedstock close to or above the ASTM limits for oxygen.

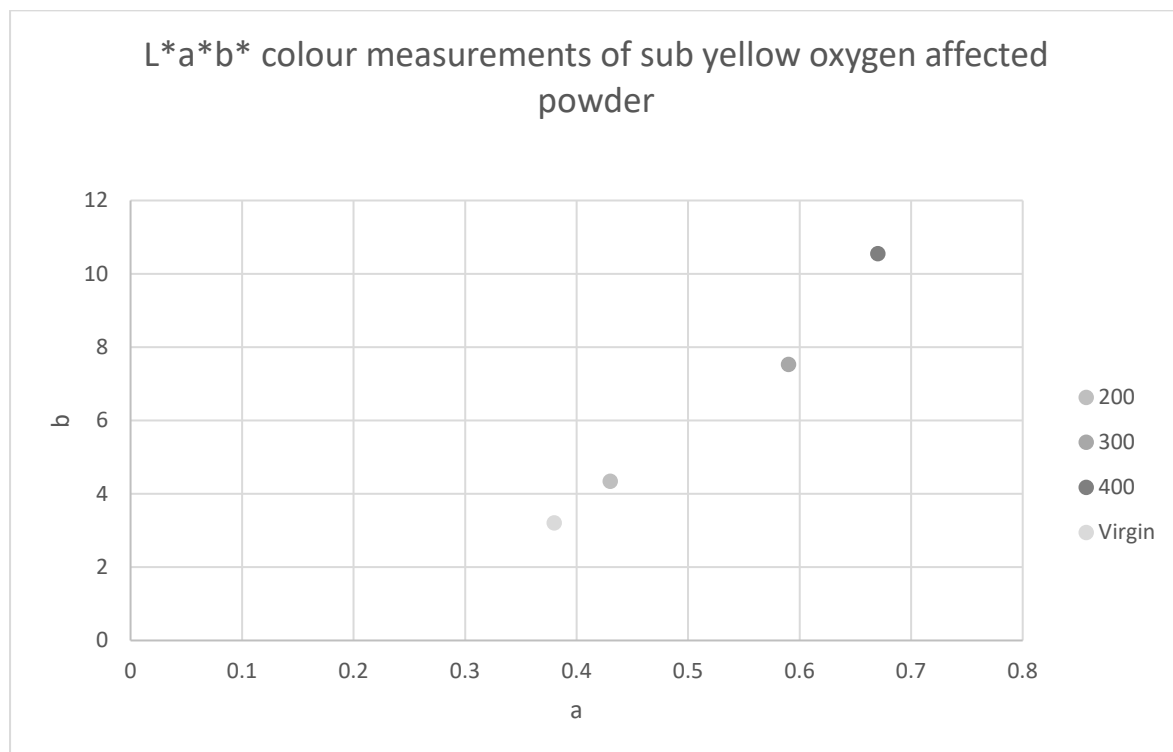


Figure 61:  $L^*a^*b^*$  colour measurements of the three bulk powders; yellow, blue and green.

#### 4.7 Effect of the surface oxide layers on laser absorption processing Ti-6Al-4V

The spectroscopy results have revealed that there is a variation in results between a virgin powder particle and an oxidised particle (yellow and blue) in terms of reflectance. The intention of this section tries to understand whether the different reflectance values can significantly change the ability for the laser radiation to penetrate the oxide. It is worth noting that this section is used an indication rather than a way to obtain absolute values.

According to the SEM results, it has been concluded that there is a surface oxide layer on the outer surface of the particle and a core metal matrix on the inner surface of the

particle. King et al [155] proposed a simple model presenting the surface structure of a powder particle as shown in Figure 62. As the laser irradiates the powder bed, a proportion of the radiation is reflected, another part of it is absorbed by the surface oxide layer whilst the remaining radiation is absorbed or reflected by the metal matrix. The intensity  $I$  decays exponentially with the depth  $z$  as the absorbed laser radiation penetrates through the powder according to the Beer-Lambert law:

$$I(z) = I \exp\left(\frac{-4\pi kd}{\lambda}\right) \quad (29)$$

Where  $I$  is equal to  $[(1-R) \times I_0]$  and is defined as the intensity inside the surface after the reflection loss as shown in Figure 62.  $K$  is the extinction coefficient at given wavelength  $\lambda$  and  $d$  is the penetration depth across the metal matrix.

Due to the extremely small extinction coefficient of Titanium oxide ( $\text{TiO}_2$ ) being close to 0, the calculated intensity of the laser almost does not decay across the oxide layer, suggesting that it is possible that the oxide layer on the particle surface does not significantly impede the radiation of the laser into the titanium powder matrix.

It is important to note that Equation 1 assumes that the oxide species is uniform and is  $\text{TiO}_2$ , it is a possibility that the oxide species may be a mixed Ti-Al oxide species. Additionally, Equation 1 also does not consider any contaminants or trace elements that may be present. However, this simple model gives an indication as to the effect of the oxide layer of  $\text{TiO}_2$  on the ability of laser to irradiate the metal matrix

The Beer-lambert model was later used by Yan et al [156] to understand the effect of  $\text{Fe}_2\text{O}_3$  surface oxide layers on the laser material interaction in SLM. The study concluded that the presence of the oxide layer on the powder surface does not impede laser radiation on the metal matrix and instead the oxide layer can enhance the effect of laser radiation absorptivity of the steel powder.

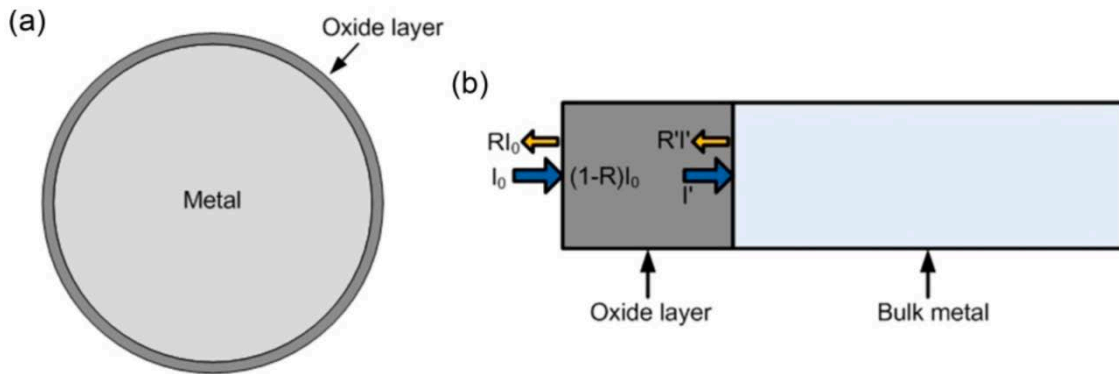


Figure 62: A) Schematic of titanium powder particle B) Model of laser absorption at the surface of the titanium powder [9]

#### 4.8 Chapter summary

Chemical analysis suggested that below 400°C oxygen pick up from heat treated powders is not significant and is still within Grade 23 specification below 0.2 wt %. However, above 400°C, the oxygen contents increase significantly as the temperature increases peaking at 1.24 wt % for green powder. Yellow, blue and green were chosen for further analysis as the chemical analysis suggested that they represented, in the context of this study, the low, medium, and high points of the oxygen wt %, additionally, these colours are also commonly observed in post processed Ti-6Al-4V powder.

Particle size distribution remained relatively consistent across the control (virgin), yellow and blue powder with slight differences across the  $D_v(90)$ ,  $D_v(50)$  and  $D_v(10)$  values and not significant change in particle size  $>45 \mu\text{m}$  with only a 1.93% change between virgin, yellow and blue. However, the green powder produced significantly different results, all size classes increased in value and the % of particles  $>45 \mu\text{m}$  increased 2.84% relative virgin. This increase is likely accredited to large oxide layer covering the surface of the particles and potentially agglomerates or oxide satellites distorting LSD measurements.

Morphology analysis suggests that there is no significant change in powder morphology between virgin and yellow as they still display spherical particle with little

evidence of oxide scaling or satellites. However, the blue and green powder particles display evidence of oxide scaling and in particular, the green powder shows the presence of significant oxide satellites which would be detrimental to the SLM process as it would hinder the ability for the powder to flow and adversely affect powder packing density.

Optical imaging showed that the bulk powder colour for yellow and blue matches the particle level colour and thus validated the artificial oxidation process used for this experiment. However, the optical micrographs showed that green powder bulk colour was not the same as the particle level and instead consisted of numerous different particle level colours. Numerous attempts were made to achieve consistency across bulk and particle level, however, without atmospheric control, this was not possible and thus a decision to not use green in further analysis such as the tensile builds was chosen in order to ensure reliability and validity of the results.

Finally, the colour characterisation further complemented the optical microscopy as it showed that the bulk colours are different quantitatively using LAB colour space and varied in reflectance measurements with yellow displays the high reflectance and blue displaying low reflectance. However, more interestingly, the LAB measurements showed that the sub yellow powder particles showed little difference in reflectance and LAB measurements suggesting that the oxide growth is not significant between virgin and  $<400^{\circ}\text{C}$  to change the colour of the powder particle. Section 4.6 suggested that it is likely that the oxide layers do not significantly impede the ability for the laser radiation to reach the titanium metal matrix. However, many assumptions were made using the Beer-Lambert equation. Chapter 5 further investigates the particle surface oxide layer and the oxygen contribution it has to the build process.

## **5.0 Influence of particle size on oxygen contribution in the build**

### **5.1 What is the purpose of the experiment?**

This chapter builds on the previously characterised oxidised powder particles in chapter 4 by investigating where the main oxygen contribution is located in the oxidised powder particles and if particle diameter has an influence on the amount of oxygen inside a particle.

As previously discussed in chapter 4, if the larger oxidised particles are likely to be removed by the wiper/re-coater, then it is important to understand the impact of the remaining smaller oxidised particles by characterising the oxide layers and comparing the oxygen contribution between different particle diameters. Sieving separated the size classes of the oxidised powder and used microscopy techniques and inert gas fusion (LECO) to establish the material properties and chemical composition of the different size classes. The key findings from the investigations in this chapter will allow the development of the failure hypothesis.

Testing and validating the hypothesis will feature building tensile bars with a layer of powder doped with oxidised particles, the specific details are explained in chapter 6. In order to accurately conduct these validation builds, it is important to investigate and quantify the oxidised particles.

### **5.2 Particle size oxygen contribution**

This section investigates the relationship between the particle size class for coloured Ti-6Al-4V powder (yellow and blue) and the bulk oxygen contribution measured by the IGF technique (LECO).

The data in Figure 63 and 64 was obtained via a series of sieving processes; 53 $\mu$ m, 45 $\mu$ m, 32 $\mu$ m and 20 $\mu$ m. The yellow and blue oxidised powder passed through each of the previously mentioned sieve sizes and the oversize from each sieve process was collected and measured by the inert gas fusion (IGF) technique. It is important to note

that no results were obtained for 53 $\mu$ m as there was not enough powder collected to gain a valid LECO result, this is likely due to the virgin powder PSD specification being 15-45 $\mu$ m, this agrees with the PSD results in chapter 4.

Figure 63 suggests that as the particle size distribution increases, the oxygen wt % decreases. Similarly, Figure 64 suggests that as the particle size distribution increases, the nitrogen wt % decreases. The larger surface area to volume ratio of the smaller powder particles allows the oxygen percentage of the powder to rise more rapidly. Therefore, as the smaller particles have a higher surface to volume ratio, so for a given oxide thickness the overall levels is higher. This suggests that powders that use a wide particle size distribution (PSD) with many small particles, to increase packing density, would have a greater problem with oxygen pick up.

The errors bars in Figures 63 and 64 use the standard deviation of the IGF (LECO) results, the error bars appear smaller for the larger particles size (45 $\mu$ m) due to the lower surface area to volume ratio of these particles, resulting in lower variation in oxide thickness and thus lower deviation between O, N wt % values.



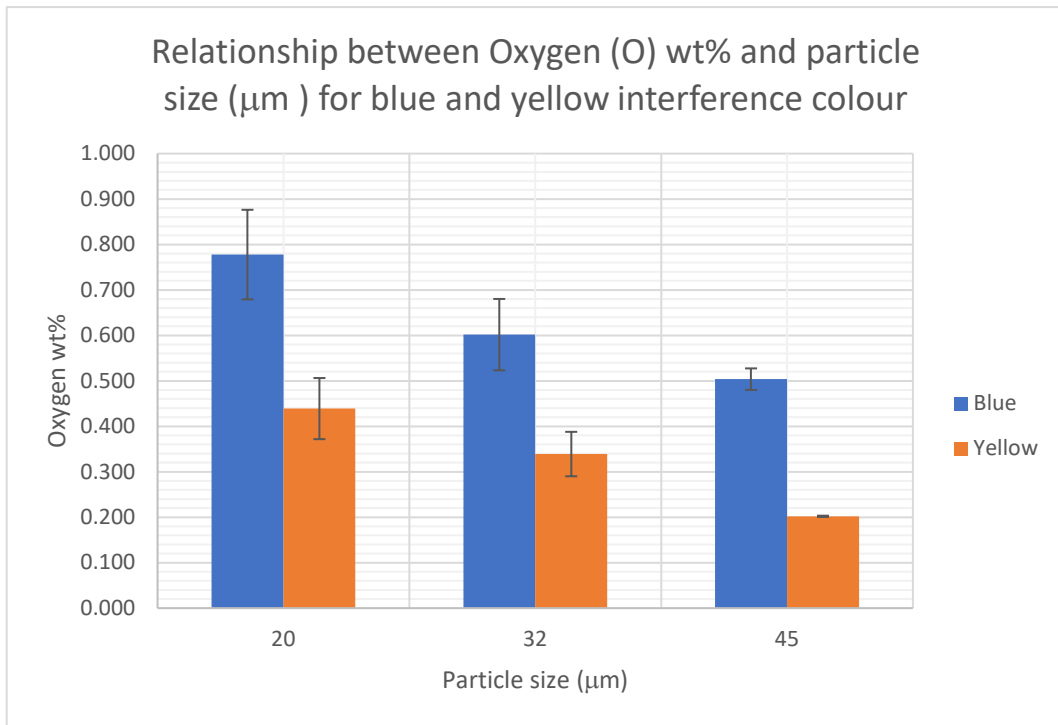


Figure 63: Relationship between Oxygen (O) wt% and particle size ( $\mu\text{m}$ ) for blue and yellow interference colour

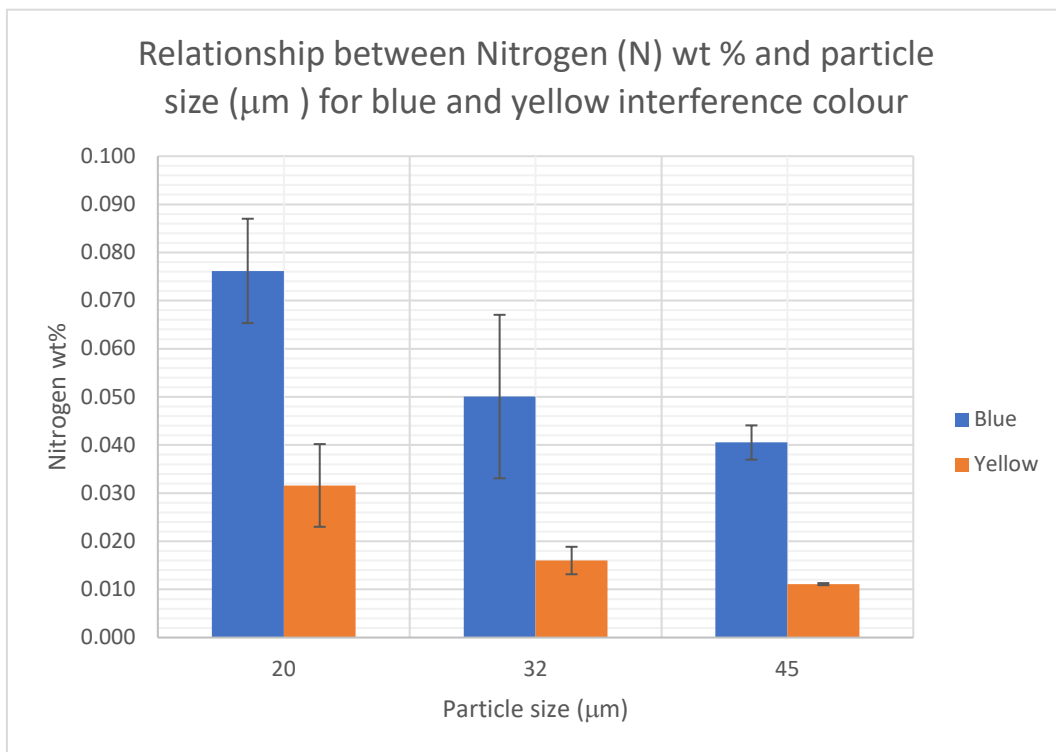


Figure 64: Relationship between Nitrogen (N) wt% and particle size ( $\mu\text{m}$ ) for blue and yellow interference colour

### 5.3 Comparison of oxide thickness relative to particle size

The oxide layer thickness data in Figure 65 suggests that the thickness of the oxide layer is not affected by the particle size, the oxide thickness trend is consistent across all three size classes. These results are expected as the colour of the oxide is due to the interference phenomenon which suggests that to achieve a specific colour, the oxide thickness has to be within a certain range. The oxide thickness data also agrees with the known values of layer thickness to achieve the colour yellow and blue for the oxidation of Ti-6Al-4V [157][158][150]. The data in Figure 65 suggests that although the oxide thickness is not affected by the particle size, the time taken to reach the desired oxidation temperature may be affected by particle size.

This would explain why the smaller particles have a slightly larger oxide thickness in comparison to the larger particles, but the difference is small around 10nm. This is likely due to the smaller particle having less mass resulting in a faster heating rate compared to the larger particles. Therefore, the smaller particles will reach the desired oxidation temperature faster and potentially have a longer exposure time at this temperature in comparison to the larger particles. Although, it's worth noting as the oxidation time was set at 60 minutes for the manufacture of the oxidised particles, it is likely that the difference in the time held at the desired oxidation temperature between the smaller and larger particles is small, resulting in a small difference between the oxide layer thickness as seen in Figure 65.

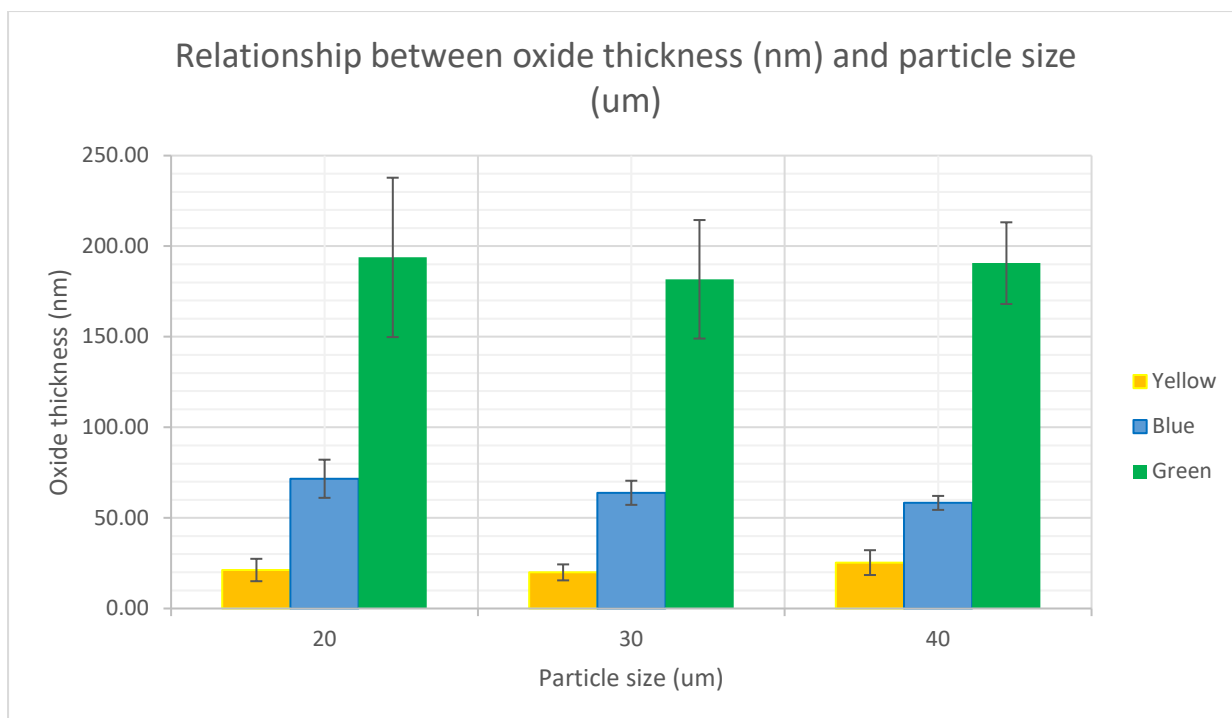


Figure 65: Relationship between oxide thickness (nm) and particle size (μm)

Interestingly, comparing the data from Figure 63 and Figure 65, this suggests that although there is not a large difference in the oxide thickness across the different size classes for each coloured particle, the oxygen contribution of the smaller particles is still higher than the larger particles. This is likely due to the ratio of the volume of oxide to the volume of core particle, in the smaller particles, the oxide layer thickness is still relatively similar to the larger particles, however, the core particle is much smaller, therefore the overall oxygen contribution of the smaller particles is larger compared to the larger particles.

To further understand why the oxygen contribution of the smaller particles is greater than the larger particles even though the oxide thickness is relatively similar, the volume fraction of oxide shell to whole particle with respect to particle size was calculated.

The volume of the oxide was calculated using the average oxide layer thickness measurement for each coloured particle size class as shown in Figure 65. Utilising the calculated volume ratio, the mass fraction was calculated using the assumption that the density of the particle core is consistent throughout the material core and is the

same as established literature for Ti-6Al-4V ( $4430000 \text{ g/m}^3$ ). The same assumption is applied to the oxide shell that the density is consistent throughout the layer and the oxide is  $\text{TiO}_2$  ( $4230000 \text{ g/m}^3$ ), although the oxide probably is a mixed oxide with traces of  $\text{Al}_2\text{O}_3$  [61]. It is important to note that these calculations make numerous assumptions of ideal conditions such as a uniform oxide phase and material density, in reality they are used to illustrate the trend of the relationship between the mass fraction and the particle size, these values cannot be considered absolute values.

Figure 66 shows that for all three coloured particles, the smaller particle size class ( $20\mu\text{m}$ ) have the highest mass fraction ratio of oxide shell to whole particle at 0.056 compared to  $45\mu\text{m}$  size class with a mass fraction of 0.025, suggesting that the smaller particles may pose a significant problem for the build process as they have a large quantity of oxide relative to the particle size. This likely due to the high surface area to volume ratio but any oxide defects are going to be less for smaller particles.

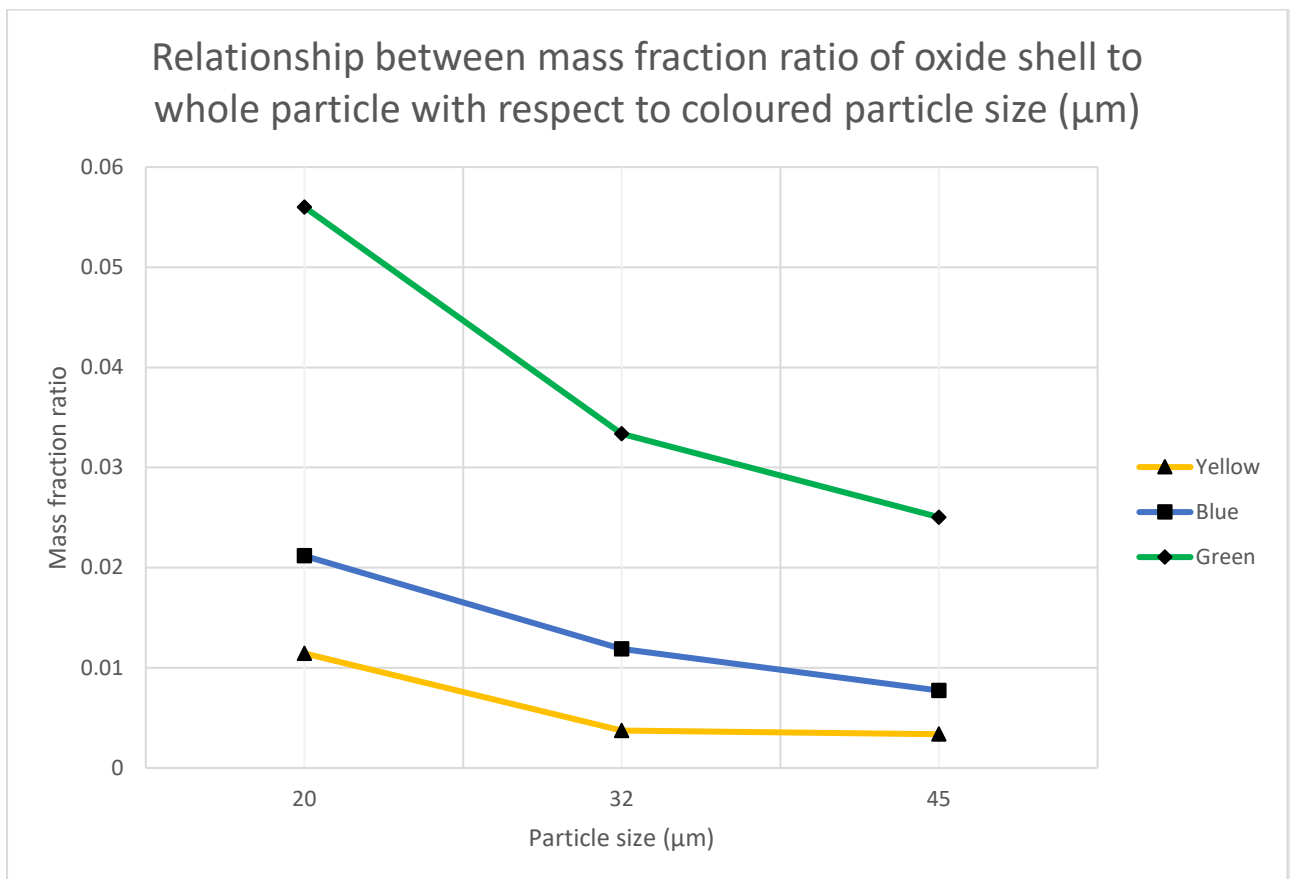


Figure 66: Relationship between mass fraction ratio of oxide shell to whole particle with respect to coloured particle size ( $\mu\text{m}$ )

This data in Figure 66 can be utilised in order to calculate the concentration of oxygen in the oxide layer with respect to the whole particle by multiplying the values obtained by a known mass percent of oxygen in  $\text{TiO}_2$  phase (40.066%) [159]. It is important to note that the calculated data shown in Figure 67 is calculated based on oxide thickness measurements as shown in Figure 65, however this calculation carries the error associated in Figure 66 based on a set of assumptions as previously discussed alongside a new assumption used for this calculation that the oxygen mass percentage is exactly 40.066% as suggested in literature [159].

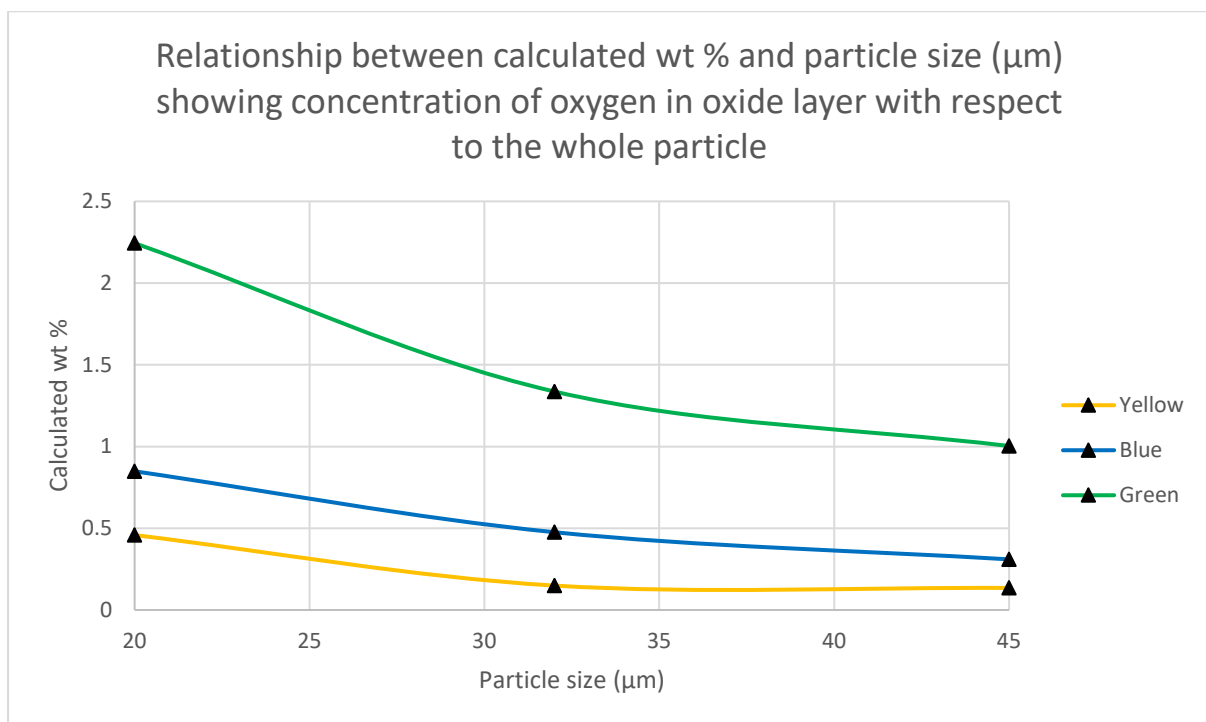


Figure 67: concentration of oxygen in oxide layer with respect to the whole particle

Figure 67 shows the calculated concentration of oxygen in the oxide layer with respect to the whole particle. Interestingly, the calculated data shows similarity to the measured oxygen wt % of the different size class oxidised powder as shown in Figure 63.

The calculated data suggests that at  $20\mu\text{m}$ , the yellow and blue are 0.45 wt % and 0.84 wt % respectively compared to a bulk powder measured value using IGF of 0.439 wt % and 0.779 wt % as shown in Figure 67. Similarly, the calculated values for  $32\mu\text{m}$

are 0.149 wt % and 0.47 wt % compared to the bulk powder measured values using IGF in Figure 67 at 0.339 wt % and 0.602 wt %. Finally, the 45 $\mu$ m size class measured values were 0.14 wt % and 0.31 wt % compared to bulk powder measured values using IGF in Figure 67 at 0.2 wt % and 0.5 wt %.

Although the data in Figure 67 utilises IGF which is a bulk analysis technique, this suggests that the calculated data is within range of the measured values. Additionally, it's reasonable to assume given the data thus far that the largest oxygen contribution comes from the oxide shell as opposed to the core particle.

The data obtained thus far suggests that the smaller particle size class for each colour have a greater percentage of oxide present due to the high particle surface area to volume ratio. Therefore, using the same FIB process for oxide measurement, a 10  $\mu$ m particle of the green powder colour was selected to show how the oxide layer forms on smaller particles. Figure 68A shows a SEM micrograph of a single green Ti-6Al-4V particle with evidence of a rough surface finish associated with an oxide film alongside the presence of oxide satellites. Figure 68B shows the cross-sectional view of the milled particle showing formed pores on the oxide interface.

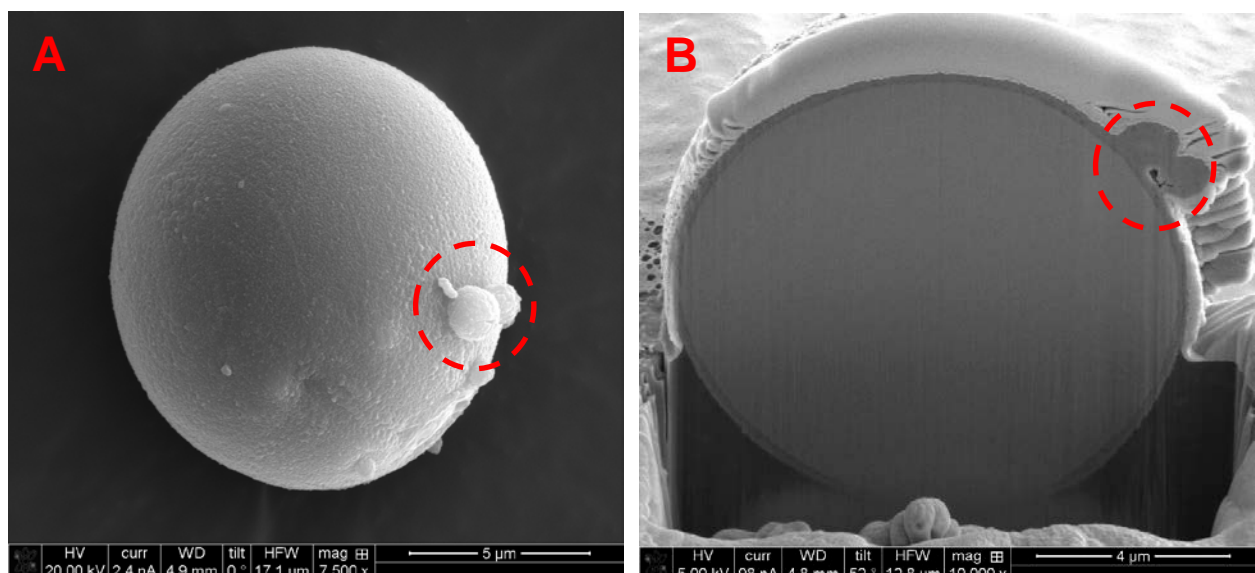


Figure 68: A) Green Ti-6Al-4V chosen for investigation. B) Cross sectional view of the blue Ti-6Al-4V powder particle.

Figure 69A shows a high magnification micrograph of the oxide layer with satellites present on the surface, the oxide thickness is measured to average around 260nm for

the layer excluding the satellites. The oxide satellite extends the oxide thickness for that section to measure  $1.37\mu\text{m}$  which is considerably larger than that measured for a particle size of  $20\mu\text{m}$  with an average layer thickness of  $190\text{nm}$ .

Figure 69B shows an EDX map of the elements present within the cross section and was used to understand the oxygen distribution in both the oxide layer and the core of the particle. The EDX map shows the oxygen is concentrated in the oxide layer on the surface of the particle and has a high concentration in the oxide satellites. Interestingly, Figure 69B shows oxygen is present throughout the core suggesting that oxygen may have diffused into the core of the Ti-6Al-4V particle. It is reasonable to assume that the oxygen is present interstitially within the alloying elements in the core of the material but is still significantly less present in the core in comparison to the oxide layer. It is likely that the main oxygen contribution comes from the oxide layer, this would also agree with Figure 67.

The presence of oxide satellites significantly increases the local oxide thickness by up to 80% as shown in Figure 69A. This could result in the powder particle not fully fusing to the surrounding material and remaining as a partially fused particle in the build layer acting as a mechanical flaw and increasing the risk of crack propagation. Alternatively, the oxide may break up into numerous smaller residues and stir up into the build layer creating problematic microstructures.

It is also possible that the laser interaction vaporises the oxide and enters the gas or dissolves and enters the molten liquid. If the oxide enters the molten liquid and dissolves into the surrounding material, this is likely to change localised microstructure and mechanical properties. It is also likely that the oxide is broken up under the laser interaction and stirred into the melt pool under the Marangoni forces and resulting in oxide residue/films being present within the surrounding build layers microstructure. An investigation into oxide formation in aluminium alloys in SLM by Louvis et al [160] showed that the oxide may break up and stir into the surrounding layers present problematic microstructures detrimental to the build.

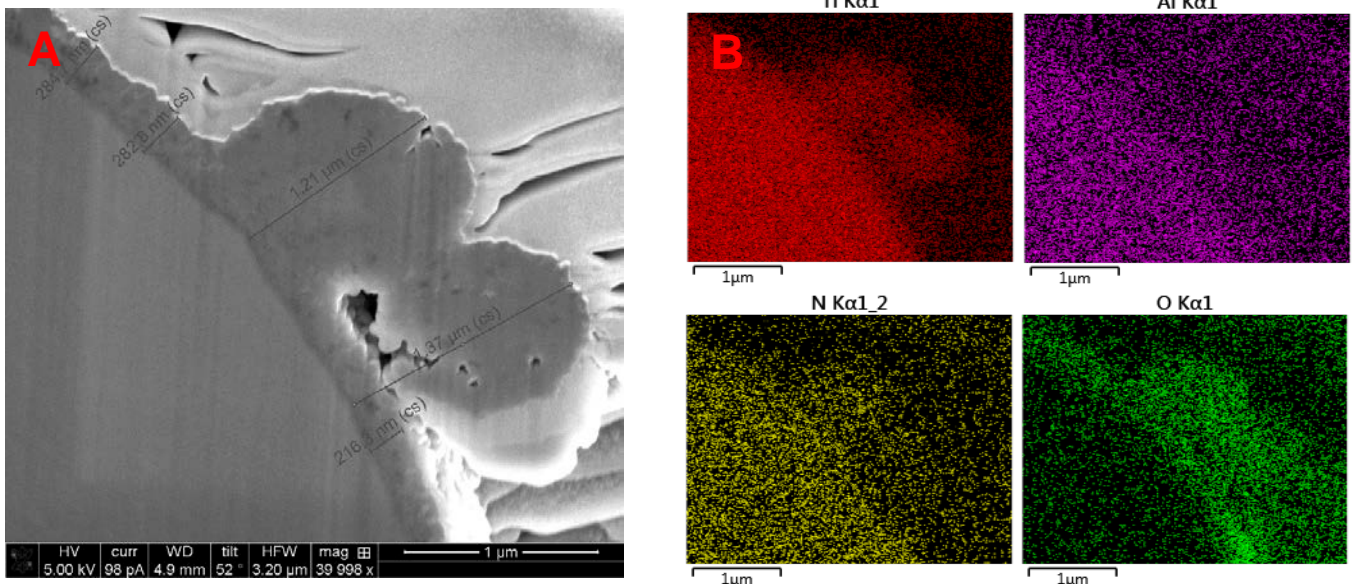


Figure 69: A) High magnification cross sectional view of the oxide layer showing oxide satellites B) EDX map of the cross-sectional view

Figure 70A shows a high magnification micrograph of a blue oxidised particle with no apparent satellites on the surface. Figure 70B shows the cross-sectional view of the milled particle.

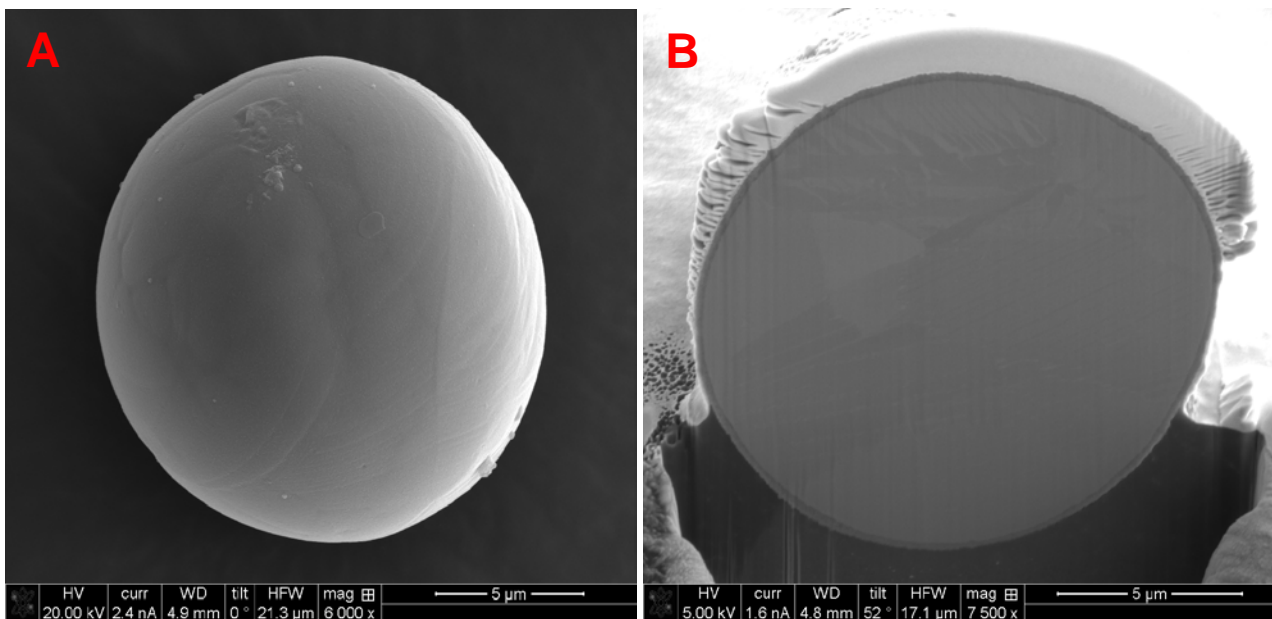


Figure 70: A) High magnification micrograph of blue Ti-6Al-4V particle B) Cross sectional view of FIB milled particle



Figure 70A shows a high magnification micrograph of the oxide layer on the particle surface of Figure 70B showing evidence of small pores (~5-10nm) denoted by the red circles. The oxide thickness measured an average of 80nm which agrees with the oxide thickness data in Figure 64 for a particle size of 20 $\mu$ m.

Figure 71B shows an EDX map of the elements present within the cross section and was used to understand the oxygen distribution in both the oxide layer and the core of the particle. Similar to Figure 69B, Figure 71B shows the presence of oxygen in core of the material but its significantly more concentrated within the oxide layer. It's important to note that the EDX mapping does not yield absolute values and is mainly used as a qualitative technique to illustrate where the elements are concentrated. In this case, it is used to show how the oxygen concentration is significantly higher within the oxide layer compared to the core of the material.

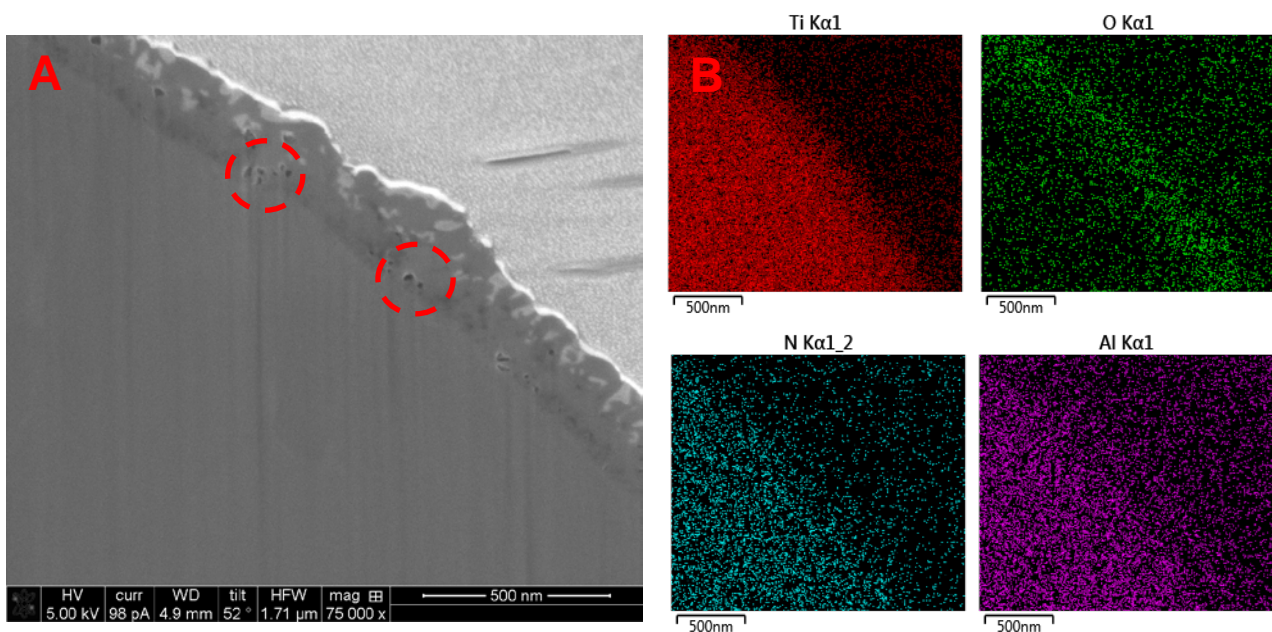


Figure 71: High magnification micrograph of oxide layer on blue Ti-6Al-4V particle B) EDX mapping of oxide layer interface

#### 5.4 Comparison of oxygen contribution between particle core and oxide layer

Further investigations of the oxygen contribution with respect to particle size were conducted via EDS line scans of the particle cross sections comparing the material core and oxide shell. Each coloured particle size class was cross sectioned via the

FIB milling process and measured using EDS line scan to correlate the relationship between the oxygen contribution and particle size. To understand whether the main contribution of oxygen comes from the core or the oxide layer, 20 $\mu\text{m}$  diameter particles were compared with 45 $\mu\text{m}$ , because in the context of this study, these represent the lower and upper size class limits.

The three EDS line plots comparing the oxide layer to the particle material core for 20 $\mu\text{m}$  and 45 $\mu\text{m}$  coloured particles show similar data in terms of oxygen peak locations. However, the overall oxygen wt % of the line scan data in Figures 72-75 shows slight variation in oxygen content between particle size with the smaller particle sizes typically yielding the highest oxygen wt % in the oxide layer in comparison to the material core for the EDS line scan summary.

It is important to note that EDS analysis detection limit of EDS for bulk materials is usually 0.2-0.5 wt % and therefore cannot detect trace elements <0.2 wt % [161]. Additionally, the surface conditions of the region of interest for the EDS analysis can hinder the detection limit, the smoother the surface, the lower the detection limit. In the case of this data, the surface is relatively smooth as the FIB process cleans the surface with the Ion beam to ensure detection is optimal. Major and minor elements can be detected by EDS with different detection limits, concentrations between 1 wt % and 10 wt% (Oxygen, nitrogen) are considered to be the minor concentrations and above 10 wt % (Titanium) are considered to be the higher concentrations [161].

Yellow:

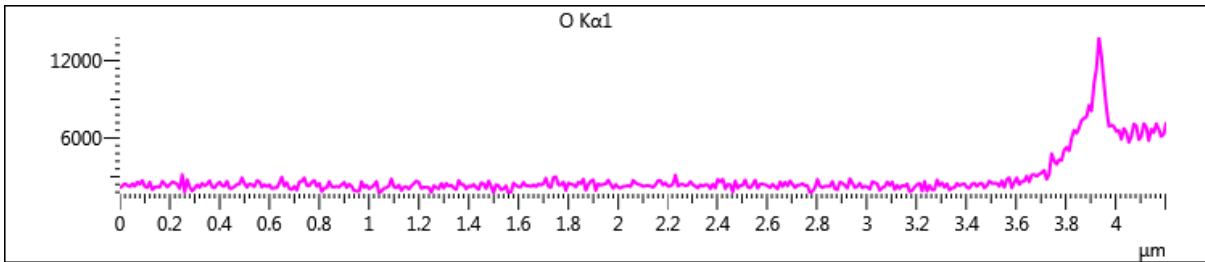
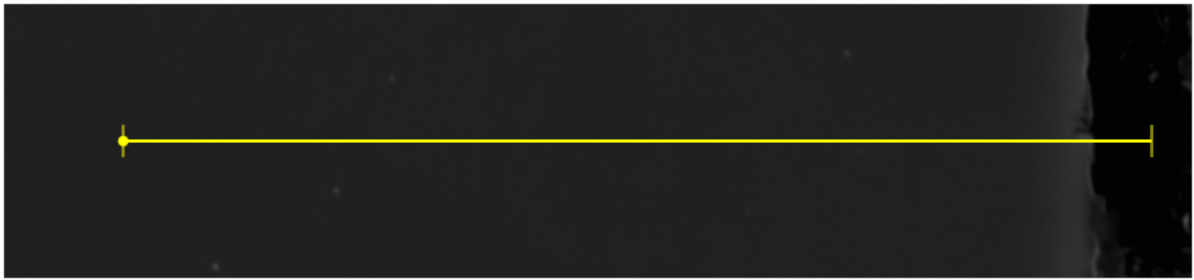
The yellow 20 $\mu\text{m}$  particle EDS line scans shows that the oxygen contribution in the core of the material is consistent throughout and remains at relatively low levels in comparison to the oxide layer as shown in Figure 72. Between 0 $\mu\text{m}$  (core of particle material) and 3.7 $\mu\text{m}$  (material surrounding the oxide layer), the oxygen content in the core of the material does not change with respect to distance from the oxide interface. In contrast, the oxide layer shows a rapid increase in oxygen content from 3.7 $\mu\text{m}$  and peaking at 3.9  $\mu\text{m}$ . The oxygen increase occurs over a 0.2 $\mu\text{m}$  distance before it peaks, the oxide thickness measurement data for the smallest yellow particle size class suggests that the average layer thickness is around 20nm. Therefore, this suggests

that around 0.18 $\mu\text{m}$  of core material closest to the oxide layer has a higher oxygen content relative to the remaining material in the core.

It is important to consider the effect of the sample shape in this analysis as it is effectively a cut sphere which can affect the signal received towards the edge of the sample. This is due to the sample thickness from the edge of the sphere to the centre, whereby the penetration depth of the beam for the generation of X-rays may go through the whole material where it is at its thinnest (the edges). Beam penetration depth can be several  $\mu\text{m}$ 's depending on beam conditions (voltage/current) and the density of the material, in this case, Ti-6Al-4V. Therefore, this would mean that the X-ray counts generated from the edge of the sphere will be a lot fewer than those from the centre. At the edge it is possible to get signal from the substrate/carbon tape as well as background signal. Signal from the centre of the sphere will be more reliable, and also come from deeper in the sample. This is true for all the samples analysed using the EDS line scans throughout this chapter.

Additionally, the escape of low energy x-rays near the edge is a problem worth considering, if the beam goes all the way through the sample (i.e. transmission) if its thin enough at the edges and this can cause an increase in background radiation (bremsstrahlung or braking radiation) [162][163]. This background radiation can be considered low energy and therefore can interfere with low energy x-rays from low Z elements. It is also possible to detect radiation effects if the peak transmits through the sample and hits other materials such as the substrate.

This suggests that the oxygen dissolves into the localised core material around the oxide layer, however, the oxygen content of the oxide layer is still significantly higher than that of the bulk core material and core material surrounding the oxide layer.

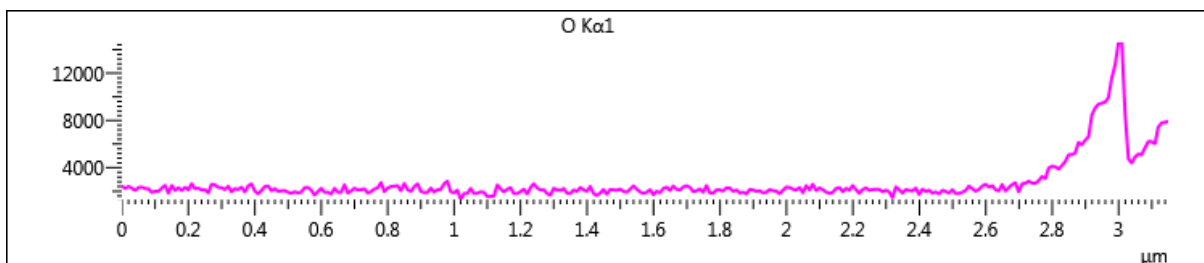
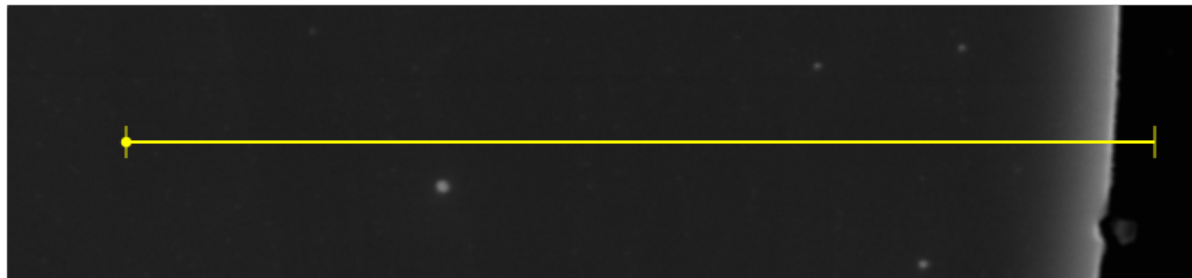


Element	O	Al	Ti	V
Wt %	3.26	4.45	89.55	2.74

Figure 72: EDS line scan of 20µm yellow Ti-6Al-4V powder particle cross section with elemental wt % tabulated.

Similar to the yellow 20µm particle results in Figure 72, the line scan in Figure 73 for a 45µm yellow particle shows a consistent oxygen level throughout the core of the material (0µm-2.8µm) with no noticeable difference in CPS throughout the core material compared to the 20µm yellow particle. The oxygen peak starts to increase at 2.8µm rising rapidly as the scan enters the oxide layer and the material close to the oxide layer until a distance 3µm is achieved where the peak rapidly decreases as the line scan enters the resin. By comparison with the results in Figure 72, there is noticeable difference in the oxygen content within the core of particles material. The results show a similar trend as the line scan approaches the oxide layer on both the 20µm and 45µm particle as the immediate surrounding material next to oxide layer shows a slight increase in oxygen content followed by a sharp oxygen peak as the scan enters the oxide layer. Additionally, the oxygen wt % for the 45µm (3.06 wt %) yellow particle is slightly lower than 20µm particle (3.26 wt %) showing little difference between the size classes.

The comparison of the results in Figure 72 and 73 for the 20 $\mu\text{m}$  and 45 $\mu\text{m}$  yellow particles suggest that the main oxygen contribution comes from the oxide layer showing little difference in oxygen within the core of the material between both size classes. The results also suggest a slight increase in oxygen is present in the surrounding material next to the oxide layer across both the 20 $\mu\text{m}$  and 45 $\mu\text{m}$  particles.

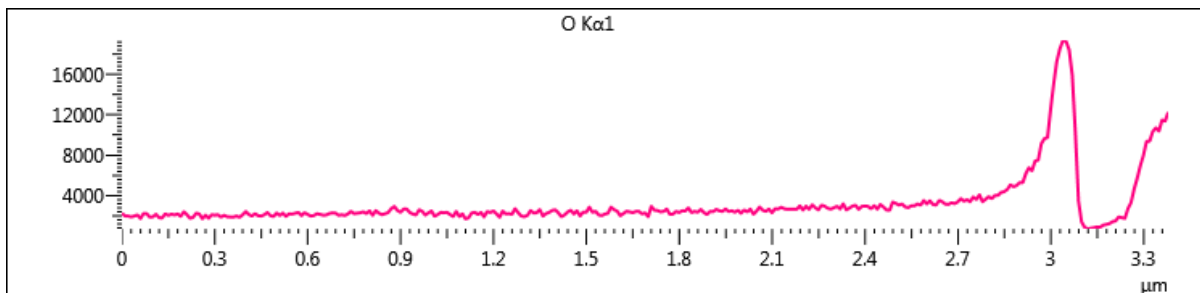
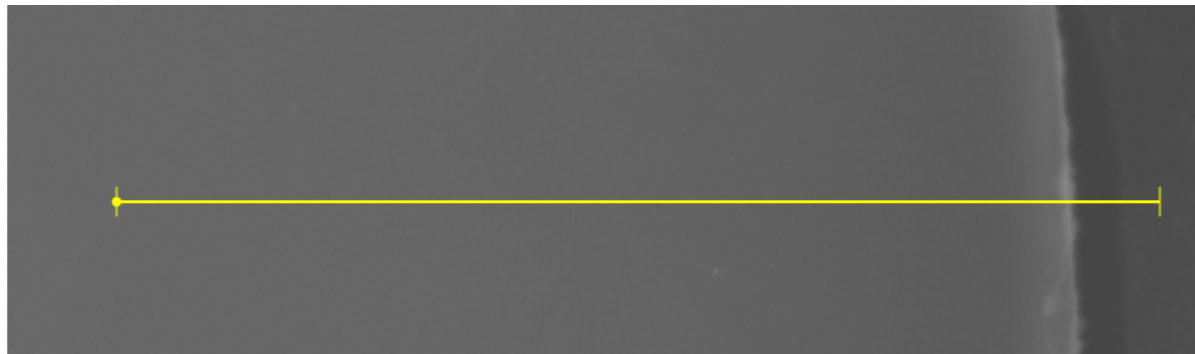


Element	O	Al	Ti	V
Wt %	3.06	4.61	90.42	1.91

Figure 73: EDS line scan of 45 $\mu\text{m}$  yellow Ti-6Al-4V powder particle cross section with elemental wt % tabulated.

Blue:

The blue 20 $\mu\text{m}$  particle shows a consistent oxygen content throughout the core of the particle material (0 $\mu\text{m}$ -3 $\mu\text{m}$ ) which is significantly lower in comparison to the oxide layer as shown in Figure 74. The oxygen content begins to rapidly increase between 2.9-3.0 $\mu\text{m}$  as the scan enters the oxide layer and peaks at 3.1 $\mu\text{m}$  before rapidly decreasing around a distance of 3.15 $\mu\text{m}$  as the scan leaves the oxide layer and enters the resin.



Element	O	Al	Ti	V
Wt %	4.9	5.5	86.1	3.4

Figure 74: EDS line scan of 20µm blue Ti-6Al-4V powder particle cross section with elemental wt % tabulated.

Similar to the blue 20µm particle results in Figure 74, the line scan for a 45µm blue particle in Figure 75 shows a consistent oxygen level throughout the core of the material (0µm-3.4µm) with no noticeable difference in CPS throughout the core material compared to the 20µm blue particle.

The oxygen peak starts to increase around 3.5µm rising rapidly as the scan enters the oxide layer (3.6-3.7µm) and the material close to the oxide layer (3.5-3.6µm). The oxygen peak rapidly decreases around 3.7µm as the line scan leaves the oxide layer and enters the resin. By comparison with the results in Figure 74, there is noticeable difference in the oxygen content within the core of particles material.

The results show a similar trend as the line scan approaches the oxide layer on both the 20µm and 45µm particle as the immediate surrounding material next to oxide layer

shows a slight increase in oxygen content followed by a sharp oxygen peak as the scan enters the oxide layer. Additionally, the oxygen wt % for the 45 $\mu\text{m}$  (3.90 wt %) yellow particle is slightly lower than 20 $\mu\text{m}$  particle (4.9 wt %) showing a difference of 1 wt % between the two size classes.

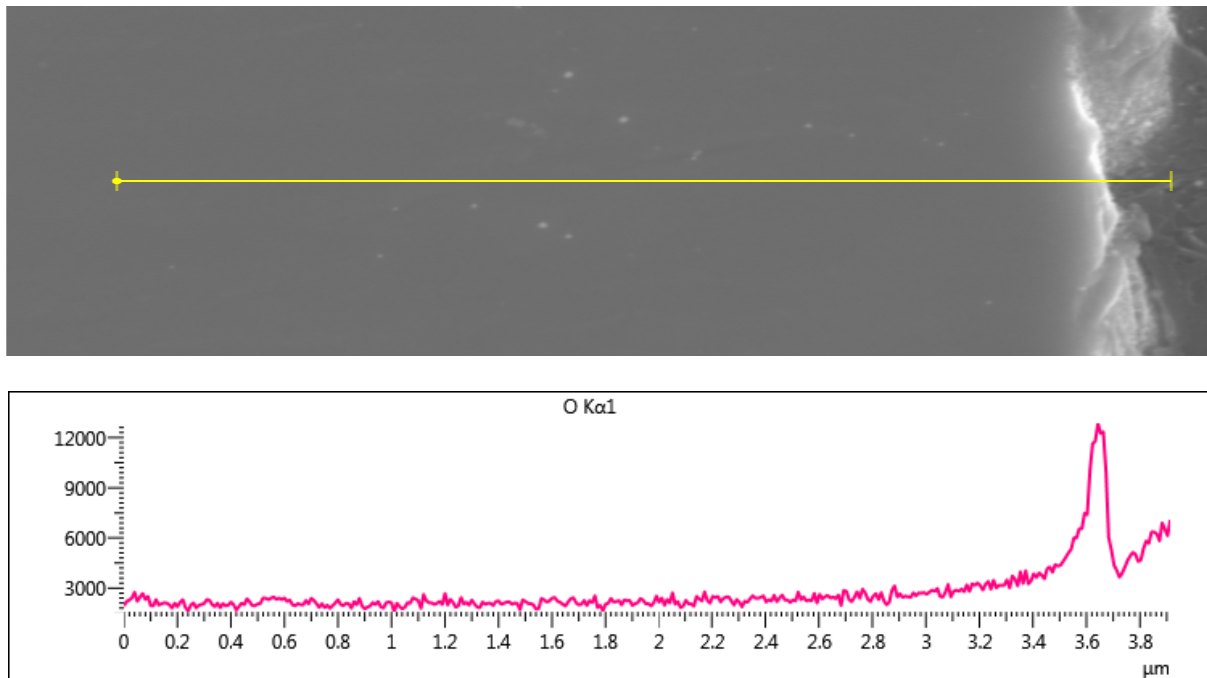
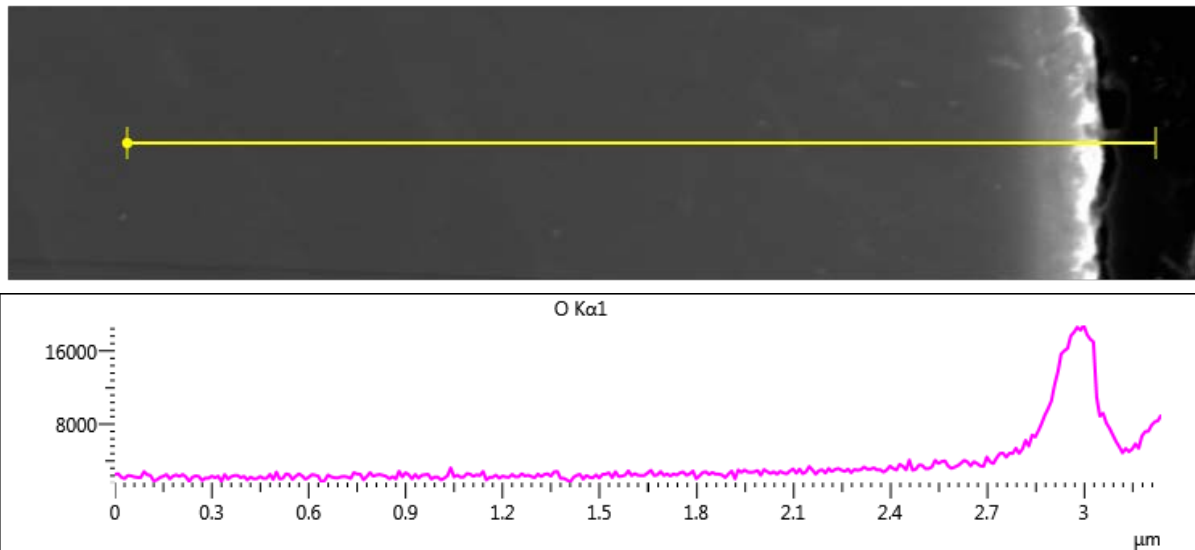


Figure 75: EDS line scan of 45 $\mu\text{m}$  blue Ti-6Al-4V powder particle cross section with elemental wt % tabulated.

Green:

Similar to yellow and blue, the oxygen content for the green 20 $\mu\text{m}$  powder particle remained consistent throughout the core material of the green particle (0 $\mu\text{m}$  -2.9 $\mu\text{m}$ ) and is significantly lower than the oxide layer as shown in Figure 76. The oxygen content begins to rapidly increase at 2.9  $\mu\text{m}$  as the line scan enters the oxide layer and peaks at 3.0  $\mu\text{m}$ . The oxygen peak rapidly decreases at 3.1 $\mu\text{m}$  as the scan enters the resin.



Element	O	Al	Ti	V
Wt %	6.23	5.54	85.54	2.7

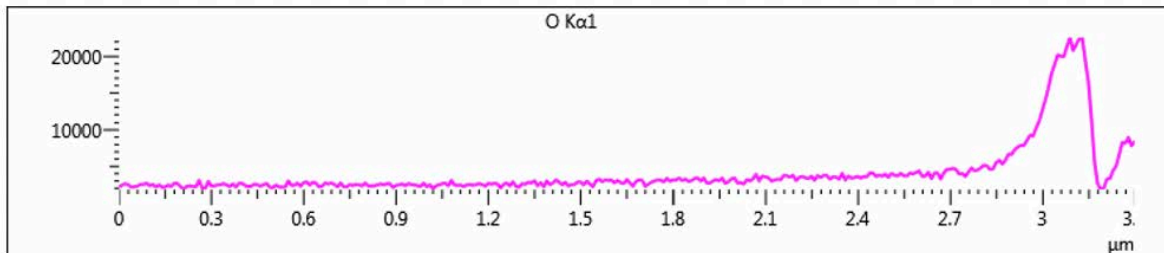
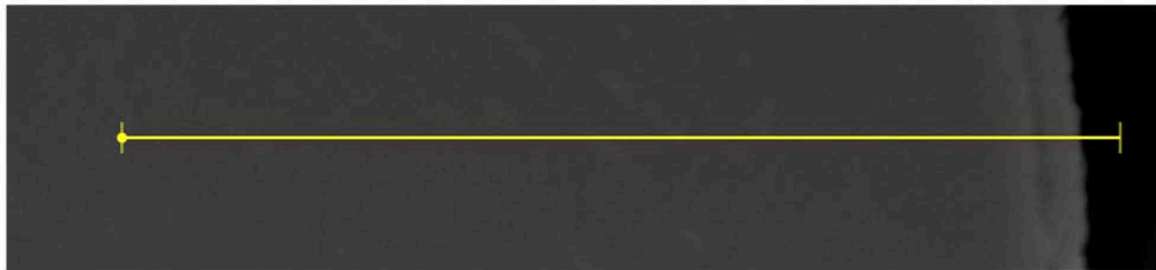
Figure 76: EDS line scan of 20µm green Ti-6Al-4V powder particle cross section with elemental wt % tabulated.

Similar to the green 20µm particle results in Figure 76, the line scan for a 45µm green particle in Figure 77 shows a consistent oxygen level throughout the core of the material (0µm-2.9µm) with no noticeable difference in CPS throughout the core material compared to the 20µm green particle.

The oxygen peak starts to increase around 3.0µm rising rapidly as the scan enters the oxide layer (3.0-3.15µm) and the material close to the oxide layer (2.9-3.0µm). The oxygen peak rapidly decreases around 3.7µm as the line scan leaves the oxide layer and enters the resin. By comparison with the results in Figure 76, there is no noticeable difference in the oxygen content within the core of particles material.

The results show a similar trend as the line scan approaches the oxide layer on both the 20µm and 45µm particle as the immediate surrounding material next to oxide layer shows a slight increase in oxygen content followed by a sharp oxygen peak as the scan enters the oxide layer. Additionally, the oxygen wt % for the 45µm (5.69 wt %) yellow particle is slightly lower than 20µm particle (6.23 wt %) showing a difference of 0.54 wt % between the two size classes.





Element	O	Al	Ti	V
Wt %	5.69	5.5	85.73	3.08

Figure 77: EDS line scan of 45 $\mu\text{m}$  green Ti-6Al-4V powder particle cross section with elemental wt % tabulated.

The EDS line scan data has significantly aided the understanding of where the main source of the oxygen contribution comes from within the coloured powder particles. The data suggests that the oxide layer is the main contributing factor for the oxygen measurement and the core only accounts for small amounts of oxygen, relative to the oxide film. An important finding from this data suggests that the oxygen does dissolve into the core material from the oxide layer, however, the distance over which the elevated oxygen levels are detected are relatively small in comparison to the diameter of the particle. It is also possible that this is a sampling volume effect, and potentially an effect of getting closer to the surface where x-rays can escape.

### 5.5 High resolution imaging of oxide layer

Scanning transmission electron microscopy was used to image and quantify the oxygen present in the oxide interface between core material and oxide shell in a blue Ti-6Al-4V particle with a diameter of 20  $\mu\text{m}$ . Utilising an in-situ FIB lift out process, TEM lamella samples were produced of the blue coloured Ti-6Al-4V powder particle

to understand the oxide structure on the particle surface and whether the oxide remains on the surface or diffuses into the core of the particle.

This information is essential in forming the failure hypothesis as it further aids understanding whether the majority of the oxygen contribution is from the oxide shell or the core material. A combination of high-resolution imaging on the aberration corrected JEOL 2100f, EDS mapping and EELS were utilised to analyse the interface between oxide shell and the core material.

### 5.5.1 Interface between oxide shell and core

Figure 78 displays a dark field (DF) and bright field (BF) micrograph of the particle core and oxide interface of the blue powder particle. The image displays a thin oxide layer present on the surface of the particle core.

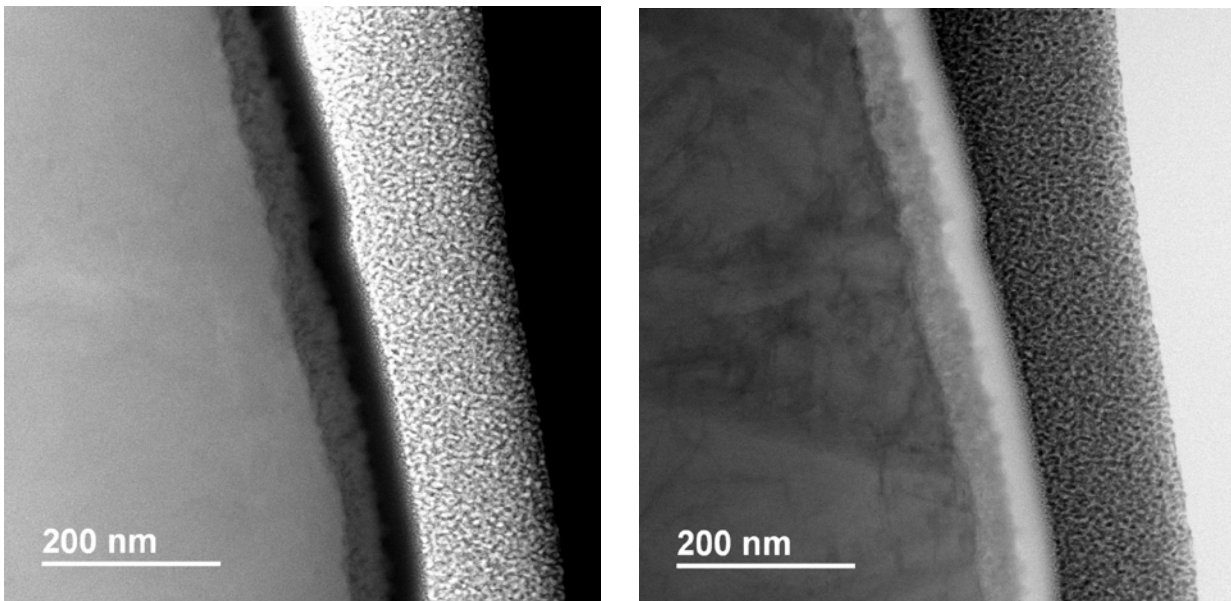


Figure 78: High resolution TEM micrograph of oxide interface of blue powder particle in both Annular dark field (ADF) and bright field (BF) illumination.

Figure 79 shows an EDX map of the elemental distribution of oxygen and aluminium in blue particle lamella. Figure 79A displays a distinct layer of oxygen atoms covering the surface of the lamella which is conclusive with the location of the oxide layer. Additionally, Figure 79A shows the presence of oxygen atoms distributed throughout the core material, suggesting that the oxygen is in solid solution with the alloying elements. Figure 79B shows the elemental distribution of aluminium, there is a varied distribution of Al elements present throughout the core in solid solution with the other elements. Interestingly, there is a distinct layer of Al on the oxide/gas surface, suggesting that the oxide is probably a mixed Ti-, Al-oxide. The presence of aluminium makes the oxide less likely to dissolve as  $\text{Al}_2\text{O}_3$  is more thermodynamically stable than  $\text{TiO}_2$ .

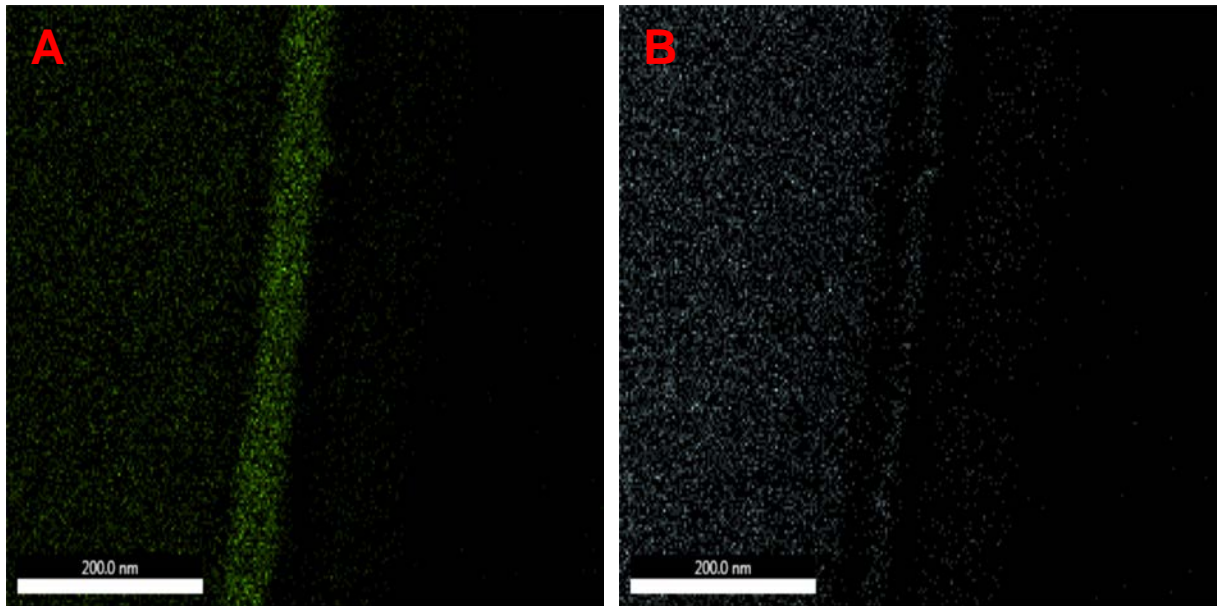
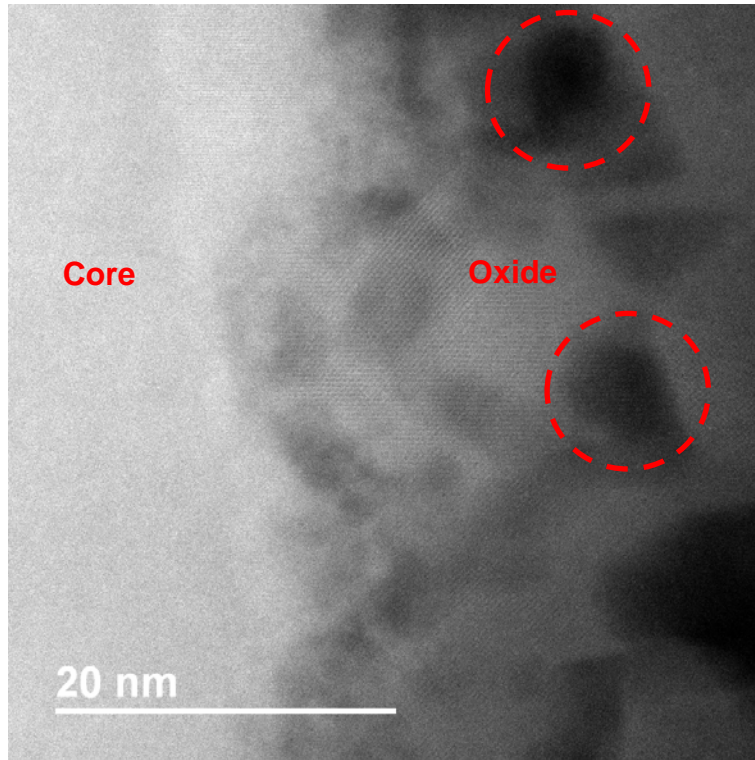


Figure 79: EDS mapping of the oxide interface showing oxygen (green) and aluminium (grey) mapping.

Figure 80 displays a high magnification micrograph of the blue particle oxide interface. The micrograph shows nano-pores across the oxide interface varying in size (5nm) as depicted by the red circles. This suggests that the density of the oxide may not be uniform. This may be an interesting finding as it may affect how the oxide breaks down under the laser interaction as the structural integrity of the oxide may be adversely affected resulting in oxide residue breaking off into the melt pool under the laser interaction. This would be detrimental to the build quality as the oxide residue may be stirred into the melt pool by Marangoni forces changing localised microstructure or acting as a mechanical flaw if the residue remains intact within the build layer. Alternatively, the oxide may vaporise into the gas flow instead of being stirred into the melt pool.



*Figure 80: TEM micrograph of oxide interface at high magnification showing nano-pores depicted by red circles.*

### 5.5.2 Electron energy loss spectroscopy (EELS) analysis

Figure 81 displays a high magnification micrograph of the interface between core material and oxide of the blue powder particles. Two regions of interest were selected to conduct electron energy loss spectrometry (EELS) in order to understand the elements, present and the phase of the oxide. Region A was selected as it represented the core Ti-6Al-4V material and region B was selected as it represented the oxide layer.

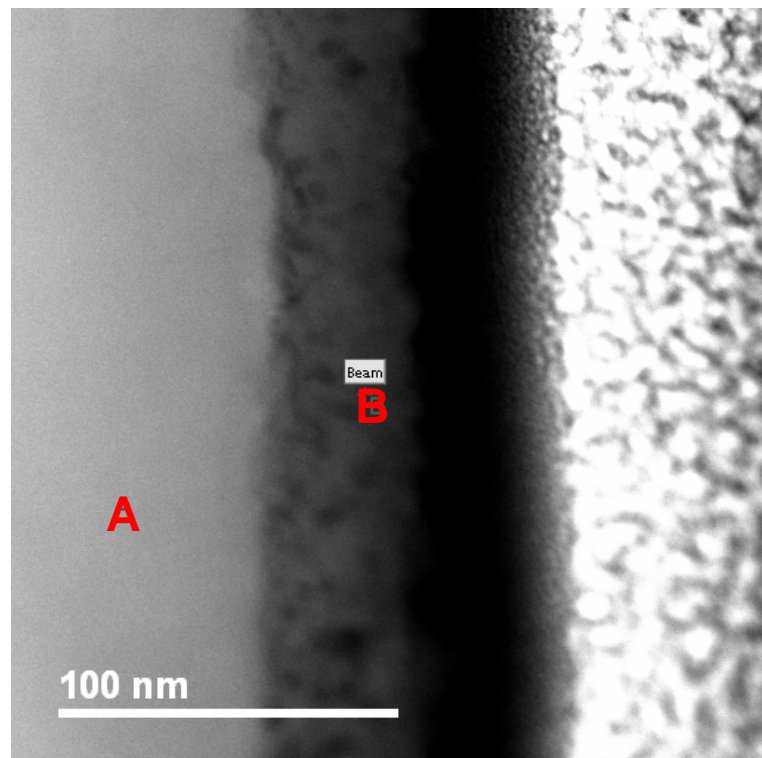


Figure 81: Micrograph of region of interest for EELS analysis; A is the core of material and B is the oxide layer.

It's important to note that although EELS analysis produces a better signal to noise ratio and higher spatial resolution for light elements in comparison to EDS, the analysis is limited to around 0.1 wt % for detecting elements such as oxygen similar to EDS. Additionally, the quality of the data is highly dependent upon the thickness of the sample. In the case of this experiment, the sample was around 40nm thick, a thinner sample would improve data accuracy however, further thinning of the sample risked damaging the Pt coating protecting the surface of the lamella which was essential for imaging the oxide interface.

The TEM cameras in the JEOL 2100F used for this analysis were calibrated using gold which has known lattice spacings. The diffraction ring pattern is used to identify the known crystal planes which is used to calibrate the camera length, and hence the scale bar that is present in the micrographs. Although this is an established accurate technique, there is a degree of error through the operation of the microscope due to potential defocus and stigmatism which can distort the lattice parameter measurements.

Figure 82 (Location A) illustrates the EELS spectra located in the core of the particle with no apparent oxide peak present. The sharp peak at 460eV suggests a Ti-L<sub>3,2</sub> edge. The remaining pattern shows no distinctive pattern conclusive with any known values for Titanium oxide and no distinctive O peak. Therefore, this suggests that although there no oxide phase present within the core of the shell and although oxygen may be present within the core material, it is not abundant enough to register a peak at the known value of O K-edge (532eV).

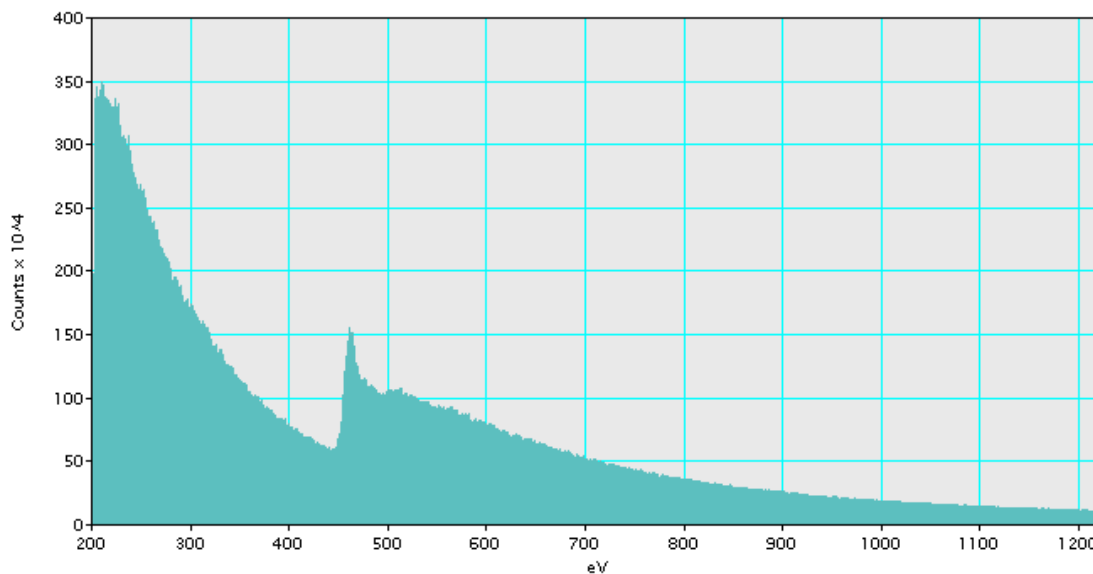


Figure 82: EELS spectra for location A (Material core)

Figure 83 (Location B) illustrates the EELS spectra obtained from the oxide layer. The sharp peak at 460eV suggests a Ti-L<sub>3,2</sub> edge. The O K-edge peak in Figure 83 is around 530eV which is conclusive with known value for Oxygen K-edge (532eV) in TiO<sub>2</sub>. This not only confirms the presence of oxygen within the region of interest but also suggests information on the phase of the oxide. The pattern displayed between 530eV and 600eV is similar with known patterns for TiO<sub>2</sub> (anatase and rutile) in a study of O K EELS spectra of titanium oxide phases by Stoyanov et al [164].

However due to extremely similar values of O K-edge values between rutile and anatase, atomic spacing measurements were used to try and determine which oxide phase was present. The atomic spacing measurements of the oxide at high resolution measured around 2.9 Å for the C-unit length suggesting the phase was indicative of rutile, however, the atomic spacing measurements vary across the oxide suggesting that the oxide phase was not uniform and potentially was a mixed Ti-Al oxide as previously suggested. Therefore, it is important to acknowledge a degree of uncertainty within the results in terms of quantifying the exact oxide species, however, the data suggests that there is a TiO<sub>2</sub> rutile phase present throughout the oxide but may vary in phase by location due to the alloying elements such as Aluminium. Stoyanov et al suggested that the Ti valence state for TiO<sub>2</sub> rutile is Ti<sup>4+</sup>[164].



Similar results were reported by Diamanti et al [150] investigating thermally oxidised titanium at 400°C, 500°C, 600°C and 700°C. The study found that for the 400°C and 500°C oxidised titanium powder, the dominant phase was anatase and the for the 600°C and 700°C titanium powder, the dominant phase was rutile. Figure 82 and 83 show the results for a blue powder particle which is oxidised at 650°C, the results suggest that it is likely that the blue powders dominant phase is rutile and based upon the similar findings from Diamanti et al [150] , it is likely that the yellow powders dominant phase is anatase. This is likely because macrocrystalline rutile is the thermodynamically stable structure of TiO<sub>2</sub>, whereas anatase a metastable phase and due to the nil transformation kinetics is stable at room temperature [165].

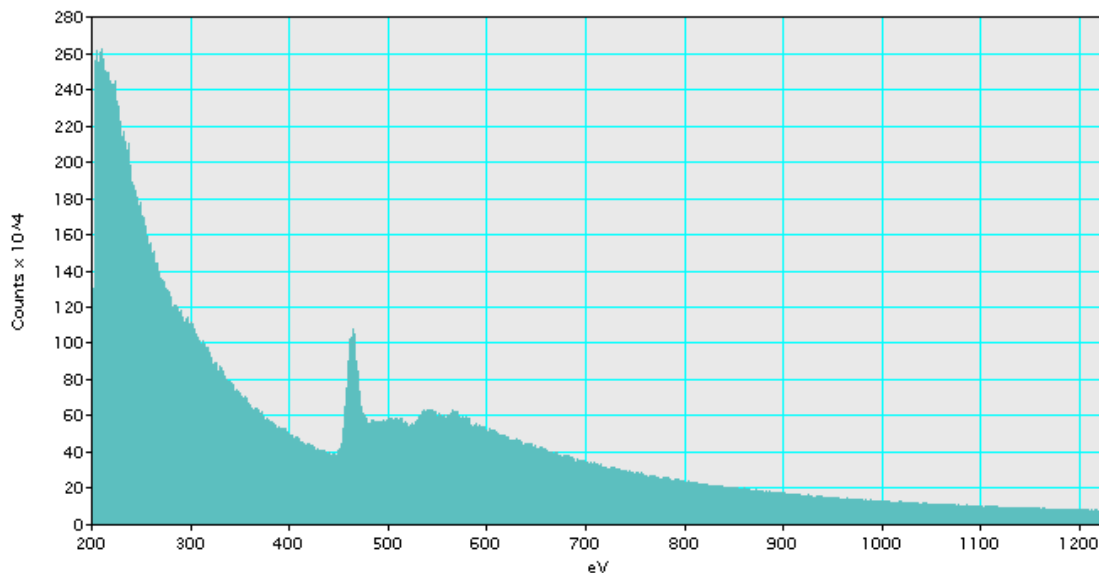


Figure 83: EELS spectra for location B (oxide layer)

## 5.6 Chapter summary

This chapter investigated the relationship between coloured particle size and the associated oxygen contribution. Additionally, the source of the oxygen contribution was investigated to understand whether the main oxygen contribution came from the oxide layer or the core and how significant the levels in each with respect to the particle size.

This data gathered in this chapter gives a better understanding of the oxygen contribution on a particle level, however, in terms of the powder bed, there will always be a distribution of different powder particles sizes and thus the number of particles from a particular size class may vary. Therefore, understanding the contribution of each size class was essential and the findings suggest that a higher distribution of smaller coloured particles could pose a significant problem in reused powder feedstock as the oxide layer is large relative to the particle size.

This could be detrimental to the build process as the oxide layer covering the particle could act as a mechanical flaw as the particle or oxide residue may remain unfused within the build layer as the laser beam interaction may not be sufficient to melt the powder particle, increasing the risk of porosity and crack initiation. Additionally, the oxide could pose a chemical flaw within the build if sufficient quantities of oxygen are dissolved into the surrounding build layers, locally changing the microstructure to the detriment of the build component.

These findings have been key to forming the failure hypothesis and suggest that although oxygen may dissolve into the core of the material, the oxide layer is likely to be more significant in terms of detrimentally effecting the build as opposed to the whole particle as it contains the largest quantity of oxygen. Particle size is a main consideration to the failure hypothesis and thus any quality control methodologies developed for post processed powder need to consider particle size distribution when assessing the impact, the coloured particles in reused feedstock.

To fully understand the impact that the oxidised particles have on the build process, a validation investigation is required using tensile builds with a doped layer of each coloured powder. The tensile builds will aid understanding of how the oxide layer acts under the laser beam interaction and whether it will evaporate, dissolve into the surrounding build layer (chemical flaw) or remain intact either in the form of oxide residue in the build layer or on the surface of the powder particle creating mechanical flaws.

## **6.0 Failure analysis**

This chapter highlights the failure hypothesis and discusses the validation investigation results of the control and doped tensile build specimens. In order to test and validate this hypothesis, tensile specimens were built with a doped layer of blended virgin + coloured particle to simulate an out of specification region within the build. (The details of how this was achieved in terms of loading the feeder, build methodology and oxygen calculations are explained in detail in section 3.5.1) Tensile testing was used to understand the mechanical properties of the control build compared to the doped builds. SEM imaging investigated the fracture surface to understand the type of failure mode, identify any areas of interest and investigate the microstructure. The findings of this chapter will test the failure hypothesis and try to establish the root cause of the tensile failure whether it agrees with the hypothesis or failure occurred due to a separate mechanism.

### **6.1 Failure hypothesis**

It is well known that most metal powder increases in oxygen as the number of reuses increase in the LPBF process [6]. Conventionally, this is measured using Inert gas fusion (IGF-IR spectroscopy) to monitor whether a powder batch is within specification. However, this process is a bulk analysis technique and cannot detect local variance in oxygen within the powder bed or quantify the presence of heavily oxidised particles. In reality, bulk powder measurements may disguise significant deviations from the acceptable limits and fail to detect heavily oxidised particles within the powder bed, which could have significant implication on build quality.

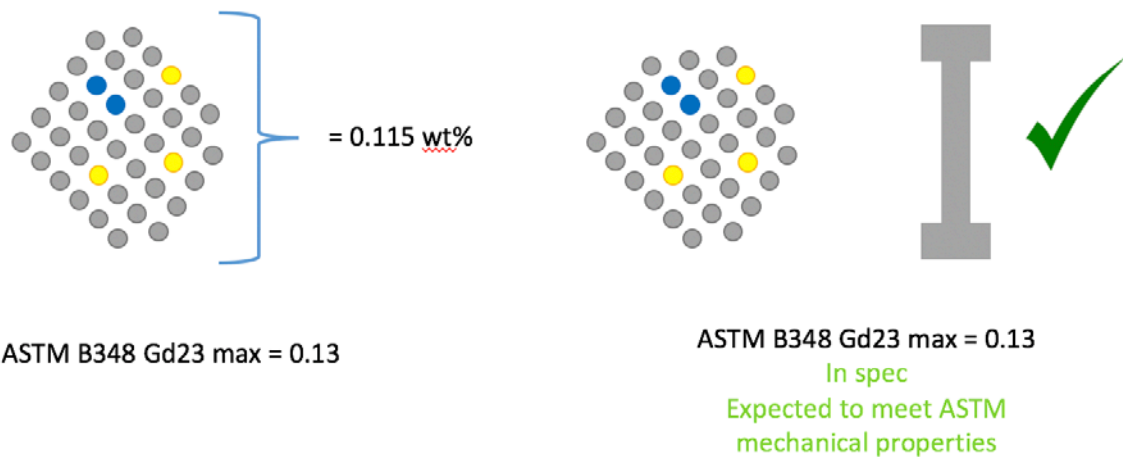


Figure 84: Schematic of how heavily oxidised particles can be present within a batch of powder, but the bulk powder measurement still be within specification

Figure 84 illustrates a situation where heavily oxidised particles are present within a bulk powder sample used for quantification by Inert gas fusion (IGF-IR spectroscopy). Within the whole sample analysed the number of oxidised particles is low enough for the powder to be in specification. However, if a smaller volume of powder was measured, it is possible that some local regions will be out of specification, and this may have implications for structural integrity of the final build. This effect would be most likely to have a significant effect where the oxidised material is incorporated into thin walled/small cross-section applications, causing a sudden change in microstructure and properties.

An example of this is shown in Figure 85, as built virgin Ti-6Al-4V tensile specimens with the heat affected zone powder still surrounding the parts. Virgin powder is compositionally homogenous when it enters the build chamber, however as the powder is reused, understanding the chemical homogeneity of the powder is critical to have consistent final built material properties. Figure 85 suggests that the powder is not compositionally homogenous as the heat affected zone around the built part shows discolouration suggesting that oxidised particles are present within the build.

If these particles can be removed, then the problem is less prominent. However, if the particles fall within the particle size distribution of the powder specification and are not removed by the manufacturers sieving process, these particles will be incorporated into subsequent builds and regions of inhomogeneity may lead to variation in material performance across the build.



*Figure 85: Image of heat affected zone powder surrounding Ti-6Al-4V parts inside the TRUMPF TruPrint 1000.*

NOTE: Figure 85 is from a Grade 23 Ti-6Al-4V powder degradation study conducted by Carpenter Additive in parallel to this project.

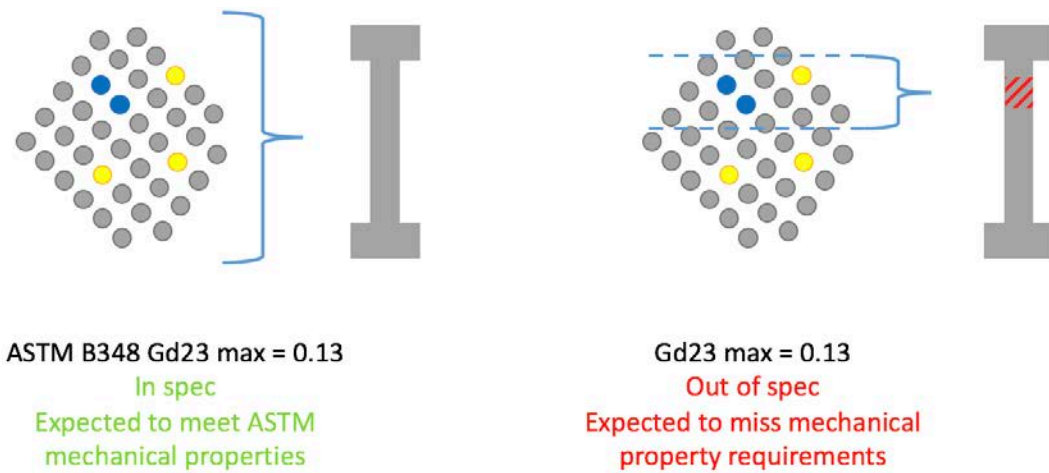


Figure 86: Schematic of out of specification region of powder within the build, the blue and yellow particles represent oxidised powder particles and the grey represent Ti-6Al-4V powder within ASTM limits.

Figure 86 illustrates an out of specification region within a tensile build that could lead to a local change in the material properties, generate structural defects and significantly affect the build mechanical properties, the oxidised particles creating unfused powder, oxide films or locally changing the chemical composition of the alloy. It is the testing of this idea that forms the basis for the work presented in this thesis. That a local, out of specification, region of powder within an SLM build can be as important to the mechanical properties of the final build as a general 'out of specification' powder, and that diluting used powder with fresh powder to put the bulk composition into specification may not avoid problems on powder reuse. Although the oxidised powder is diluted using virgin Ti-6Al-4V powder, there is still oxides present within the powder and they can become concentrated, in the case of a build with a thin-walled section or fine geometries, this would greatly change the material properties and could result in premature failure if subjected to loading conditions.

The hypothesis comes from the observation of oxide particles in recycled powder which are not removed by sieving. The hypothesis of this work is that the high oxygen content and oxide films on the particles locally alters the build layers, having a detrimental effect through two mechanisms; The first is a chemical flaw as oxygen dissolves into the surrounding material from the oxide film and remains interstitial within the localised build layer material decreasing ductility and increasing embrittlement. Secondly the laser beam may not have sufficient energy to melt or

vaporise oxide on the particle so it either remains unfused within the build or the particle melts and is incorporated but the oxide film is stirred into the melt pool in the form of oxide residue, creating problematic localised microstructures within the build.

## 6.2 Validation experiment and results

### 6.2.1 Tensile Build Methodology

Based upon industrial powder evolution studies and post processing optical images of Ti-6Al-4V powder from Carpenter Additive, oxidised particles of interference colour yellow and blue were chosen for further analysis as they occurred frequently within post processed powder and represent, in the context of this study, a low oxygen wt % (yellow) and a high oxygen wt % (blue). 100g of yellow and blue oxidised Ti-6Al-4V were manufactured to have sufficient powder for characterisation and tensile bar builds.

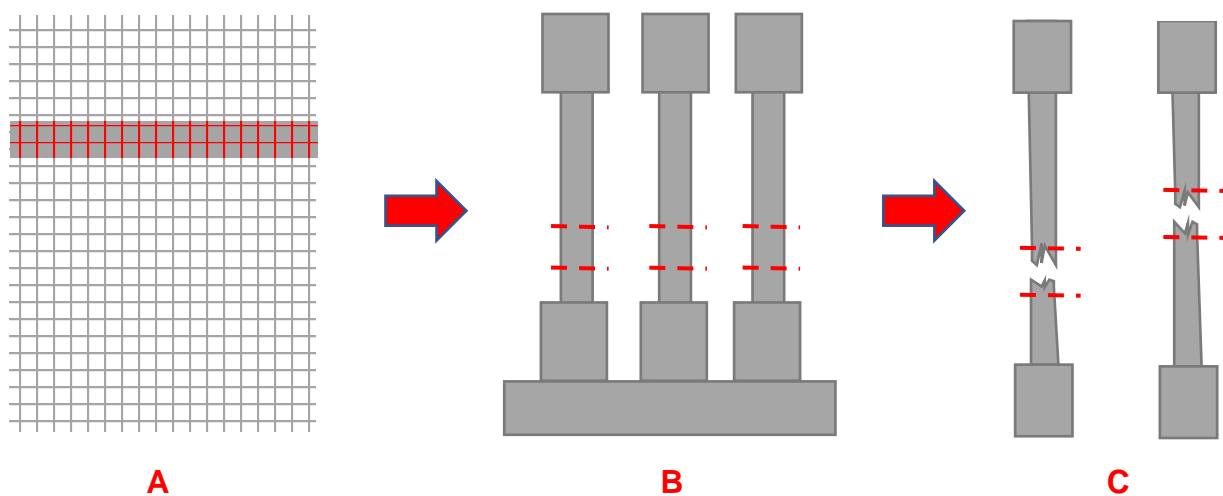


Figure 87: Diagram of experimental design to simulate local concentration of high oxygen wt% particles within volume of ASTM B348 Gr 23 Ti-6Al-4V powder

Figure 87 illustrates all the main stages of the experiment. Figure 87A shows a cross section of the powder bed with virgin Ti-6Al-4V (grey) and a 5mm layer (red) of virgin powder doped with oxidised particles at a known level in the build as shown in Figure 88. Doping of the oxidised powder in the feeder was performed in three stages; Firstly, the feed piston was dropped to a level required for the full build (a function available on the TruPrint 1000) and the piston was filled with virgin Ti-6Al-4V powder with a known quantity of powder shown in Table 5 and levelled so that the top of the volume was flat - as shown in Figure 87A. Secondly, the total mass of the blended coloured + virgin powder as shown in Table 5, was added into the piston and the powder levelled to ensure an even distribution of the doped layer. Lastly, the remaining volume of the feeder piston was topped up with virgin Ti-6Al-4V powder and levelled. The blended dope layer mass was pre-blended at a 70:30 mass of virgin to mass of colour ratio prior to adding it into the piston, Table 6 shows all the blending mass information. It is important to note, the doped layer thickness was determined by the mass of the doped blend added into the piston, the doped layer will be present across multiple build layers in the SLM build creating an out of specification region within the build to show the effect of oxidised particles on the final build quality.



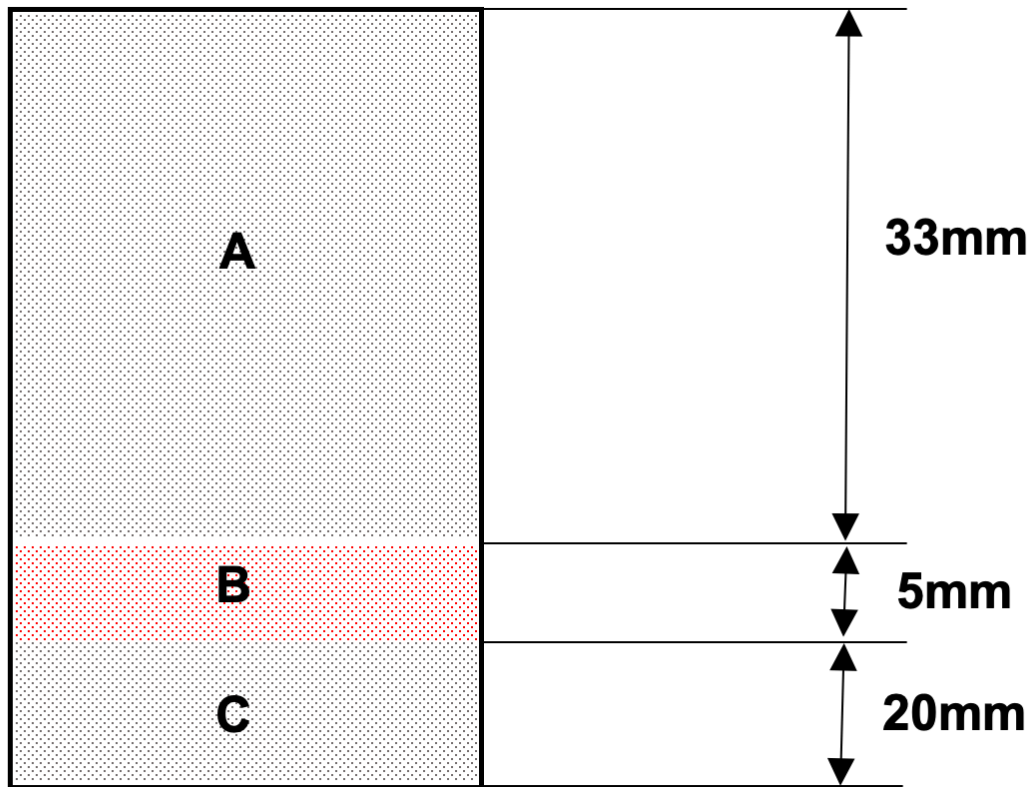


Figure 88: Stacking arrangement for doped tensile builds

Table 5: Minimum quantity of powder required for feedstock chamber to complete doped tensile builds

Section of Feedstock chamber	Volume (cm <sup>3</sup> )	Powder required (g)	Powder condition
A	157	394	Virgin
B (Doped layer)	40	100	Blended Virgin + Doped
C	259	651	Virgin

NOTE: Calculations for Table 5 are based on a build plate diameter of 100mm (TRUMPF TruPrint 1000) and a measured apparent density of 2.51g/cm<sup>3</sup> for virgin Grade 23 Ti-6Al-4V.

Figure 87B illustrates the tensile builds; The first production batch was the control and used virgin Ti-6Al-4V powder throughout the whole build to understand the mechanical properties of the virgin material. The second batch was the yellow doped layer build

(low wt % oxygen) and finally the third production batch was the blue doped layer build (high wt % oxygen).

Figure 87C illustrates the expected difference from the control build (failure within gauge length) compared to the doped layer builds (failure in doped layer). The tensile testing was conducted according to ASTM E8-16a [166], utilising a dual averaging extensometer at 21°C.

Table 6 displays the information on the oxygen wt % for each powder condition. The virgin powder was used for the control build and was also used for the doped layer builds. As shown in Figure 88, the feedstock chamber was layered in three stages, firstly virgin powder, secondly a doped layer with some oxidised powder, finally a layer of virgin powder. In Table 6, the weight percentage of oxygen was measured using the IGF combustion method, the values were obtained using triplicate testing to gain an average result for the oxygen wt %.

*Table 6: Oxygen wt % for doped powder layer blend.*

<b>Detail</b>	<b>IGF Value (wt %)</b>
O wt % of virgin	0.091
O wt % of Yellow powder	0.361
O wt % of Blue powder	0.737
Total bulk O wt % of virgin + Yellow (Whole build volume)	0.096
Total bulk O wt % of virgin + Blue (Whole build volume)	0.103

Table 7: Mass of powder required for blended oxidised powder layer.

Total mass of powder (Kg)		1.6		
Powder	Mass of oxidised powder (Kg)	Mass of virgin powder (Kg)	Mass of virgin required for blend (Kg)	Total mass of doped layer blend (Kg)
Yellow	0.030	1.50	0.070	0.100
Blue	0.030	1.50	0.070	0.100

As shown in Table 7, the total mass of powder for the whole build volume was 1.6kg. The doped layer was a fixed mass of 100g of blended powder, the mass of coloured powder was also fixed at 30g for both yellow and blue doped builds keeping the number of flaws in each build the same. The fixed mass of coloured powder enabled the total oxygen wt % for the whole build volume to be very similar (difference of 0.007 wt %) as shown in Table 7. The effect of the oxidised powder will be somewhat exaggerated as the doped regions are out of the powder specification, but a similar effect could occur in thin sections where a few oxidised particles are present. In effect, when considered at a bulk level the total powder volume would be within specification, however in a local region it is out of specification.

A dual averaging extensometer was used to conduct tensile testing at a temperature of 21°C. Tensile bars were tested from each build; control, yellow and blue which all adhered to ASTM E8-16a [166]. The specimens were tested in strain rate control at the first rate to beyond yield (0.005mm/mm/min), then the second rate was adopted (0.050 mm/mm/min) after the extensometer was removed.

The as-built tensile specimens were built using the dimensions illustrated in Figure 89, a cylinder was built using a TRUMPF TruPrint 1000, build parameters; laser power 175W, scan speed 900mm/s, hatch spacing 90µm, layer thickness 30µm and meander scan strategy. The oxygen level in the protective gas was kept below 100ppm throughout the build process.

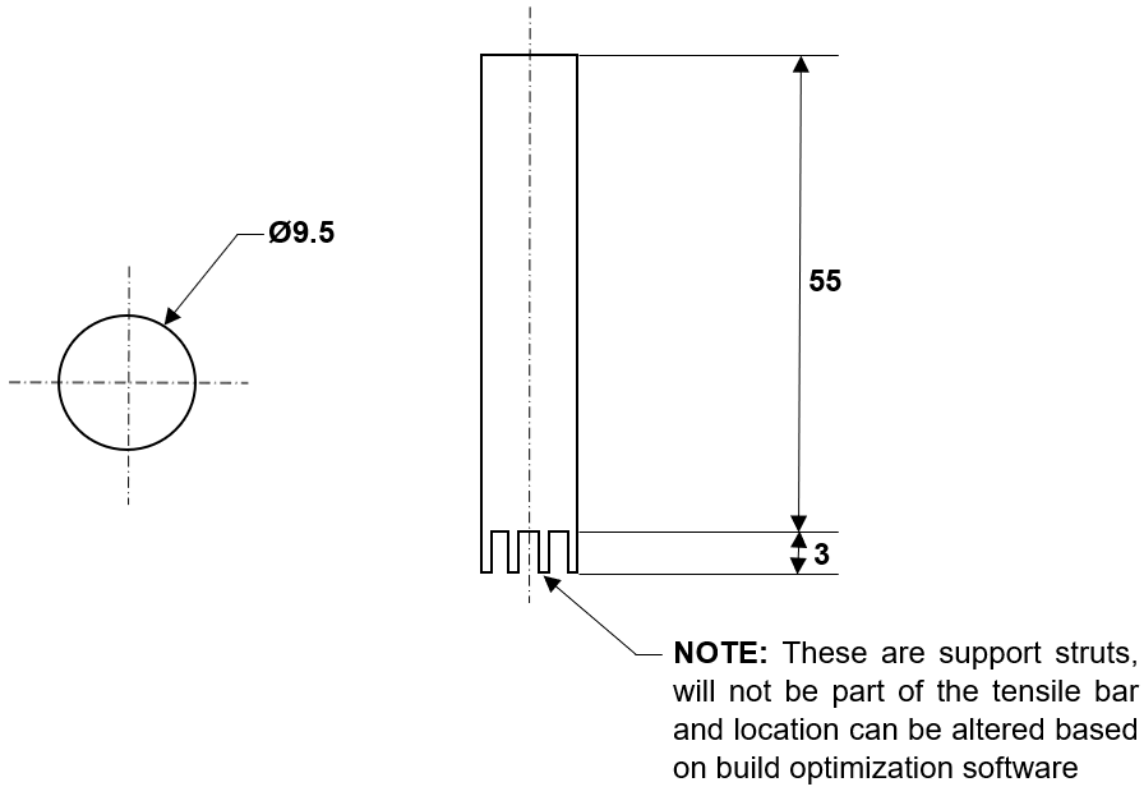
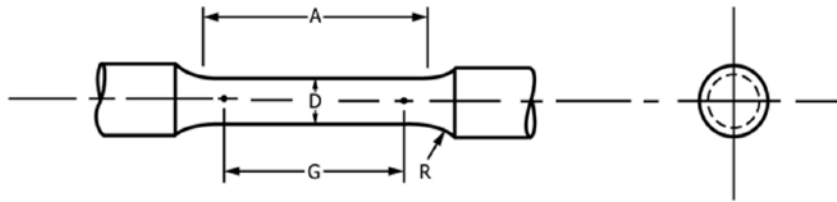


Figure 89: Technical drawing of cylindrical tensile bars

The as built tensile bars were machined, and heat treated by Westmooreland Mechanical testing and research Ltd adhering to ASTM E8-16a [166] as shown by Figure 90. The specification chosen for the tensile build is denoted by the red box in Figure 90. An M6 thread was machined onto the end of the shoulders to attach to tensile testing jaws, the total length of the tensile specimen was 55mm.

 **E8/E8M - 16a**



Dimensions, mm [in.]					
For Test Specimens with Gauge Length Four times the Diameter [E8]					
	Standard Specimen	Small-Size Specimens Proportional to Standard			
	Specimen 1	Specimen 2	Specimen 3	Specimen 4	Specimen 5
<i>G</i> —Gauge length	50.0 ± 0.1 [2.000 ± 0.005]	36.0 ± 0.1 [1.400 ± 0.005]	24.0 ± 0.1 [1.000 ± 0.005]	16.0 ± 0.1 [0.640 ± 0.005]	10.0 ± 0.1 [0.450 ± 0.005]
<i>D</i> —Diameter (Note 1)	12.5 ± 0.2 [0.500 ± 0.010]	9.0 ± 0.1 [0.350 ± 0.007]	6.0 ± 0.1 [0.250 ± 0.005]	4.0 ± 0.1 [0.160 ± 0.003]	2.5 ± 0.1 [0.113 ± 0.002]
<i>R</i> —Radius of fillet, min	10 [0.375]	8 [0.25]	6 [0.188]	4 [0.156]	2 [0.094]
<i>A</i> —Length of reduced parallel section, min (Note 2)	56 [2.25]	45 [1.75]	30 [1.25]	20 [0.75]	16 [0.625]

Figure 90: Schematic of tensile test specimen adhering to ASTM E8/E8M-16A, the red dashed box denotes the specimen dimensions chosen. [161]

Figure 91 displays an image of the control build on the TRUMPF TruPrint 1000 build plate. The ‘as built’ specimens are 55mm length and 9.5mm diameter cylinders which were machined post process and heat treated by Westmoorlands Mechanical Testing and Research Ltd into the dimensions as seen in Figure 91.

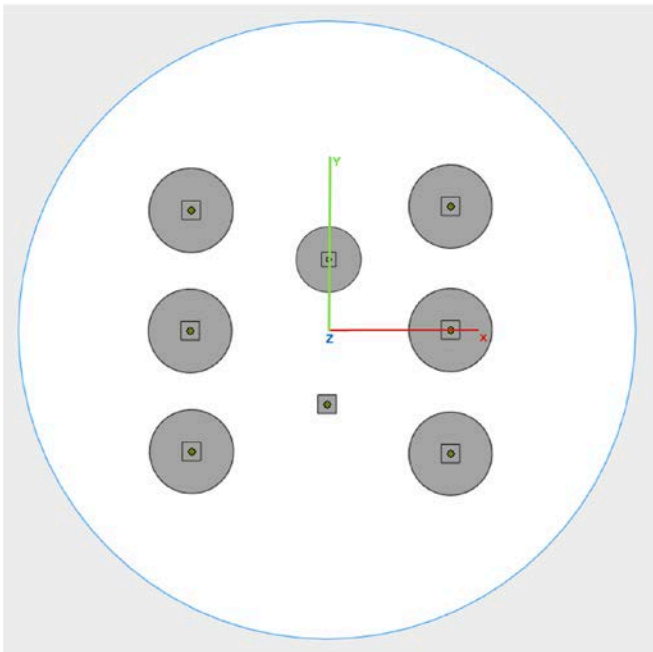


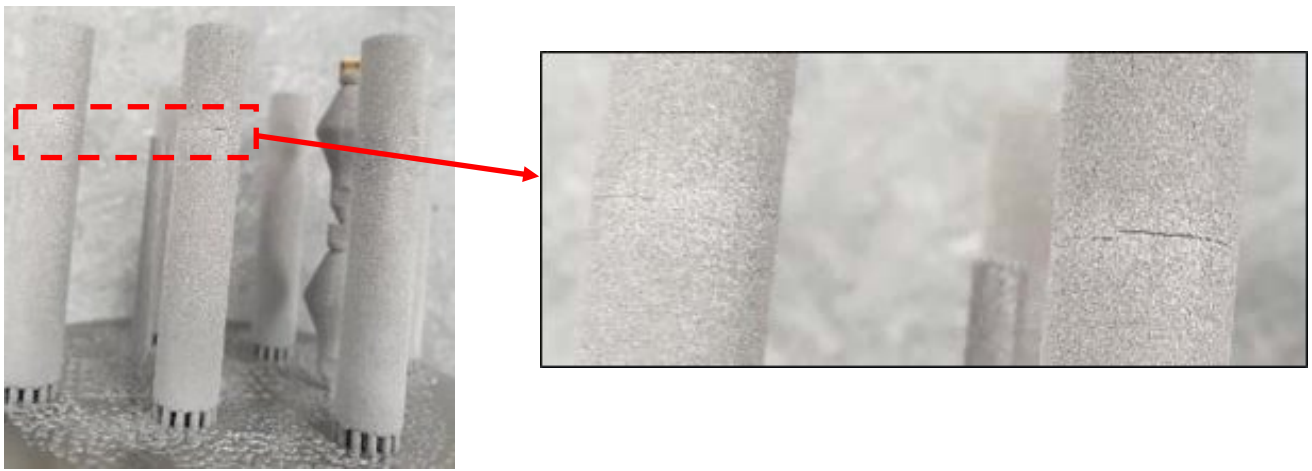
Figure 91: Image of build layout and control tensile build from the TRUMPF TruPrint 1000.

Figure 92 shows the results of the as built dimensions for the virgin tensile specimen. Figure 92A shows the total length of the as built tensile specimen excluding the support structures used in the build process displaying a length of 55.23mm compared to an expected length of 55mm. Figure 92B shows the total length of the as built specimen including the support structures displaying a value of 58.19mm compared to an expected length of 58mm. Finally Figure 92C shows the diameter of the as built specimen displaying a result of 9.8mm compared to an expected diameter of 9.5mm.



Figure 92: Dimensions of as built tensile bar: A) Length of bar excluding support, B) length of bar including support and C) diameter of bar

Figure 93 shows evidence of cracking offset from the centre point in the blue doped build. It is possible that this crack formation is due to the difference in material properties between the oxygen enriched doped layer and non-doped layer of the surrounding build layers. This would agree with the nano-indentation data found in chapter 7 and the oxide layers found on the fracture surface in chapter 6. More importantly, this gives an indication that the localised material properties have changed around or within the region of the doped layer.



*Figure 93: Image showing evidence of cracking in the approximated doped layer of the tensile build.*

### **6.2.2 Tensile test data**

Tensile testing was conducted to determine the mechanical properties of the different doped builds against the control build. Prior to tensile testing all tensile bar samples were stress relieved at 600°C for 4 hours under an argon atmosphere and then furnace cooled. The tensile testing adhered to ASTM E8-16a standards utilising a dual averaging extensometer at 21°C. A total number of six specimens were built and tested for each build, all built vertically and on the same machine, the TRUMPF TRUprint 1000; the specific build parameters can be found in Chapter 3.0. The specimens were tested in strain rate control at the first rate to beyond yield (0.005mm/mm/min), then the second rate was adopted (0.050 mm/mm/min) after the extensometer was removed. All tensile specimens were of nominal diameter (4mm), parallel length (25mm) and marked with a 16mm gauge length to determine the plastic

elongation post fracture. Table 8 displays the relevant tensile test data for control, yellow and blue builds adhering to ASTM E8-16a.

Table 8: Tensile test data for control, yellow and blue builds. Data provided by Westmoreland Mechanical Testing & Research, Ltd.

Tensile sample	0.2% PS [MPa]	UTS [MPa]	Elongation [%]	Reduction of area [%]	Failure in doped layer [Y/N]
Control build	1003 ± 2	1109 ± 14	2.7 ± 0.4	3.2 ± 0.7	N/A
Yellow build	1065 ± 3	1155 ± 36	1.8 ± 1	3.3 ± 0.9	Yes
Blue build	1050 ± 9	1127 ± 55	1.7 ± 0.6	2.4 ± 1.9	Yes

Figures 94 and 95 display the two failure modes from the tensile testing results. Figure 94 (the control build) suggests a ductile fracture as a cup and cone failure is present with an elongated fracture zone, the failure not being restricted to a limited number of build layers. Table 8 reiterates the ductile fracture with the highest observed elongation (2.7%) and reduction of area (3.2%). The failure occurs within the middle 50%-gauge length which is consistent with known virgin Ti-6Al-4V tensile testing failures.

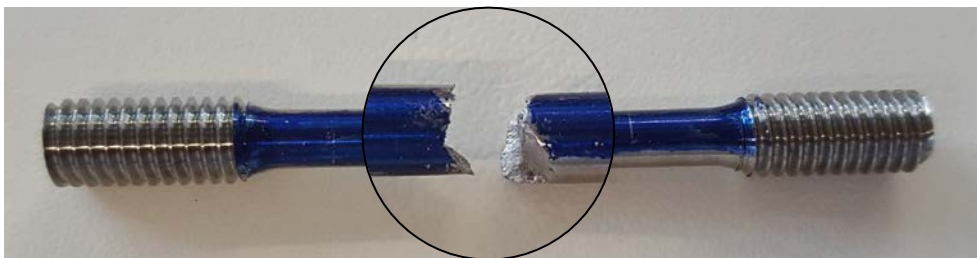


Figure 94: Optical image of ductile (control build) fracture.

In comparison Figure 95 shows a more brittle failure (blue doped build) with the fracture zone displaying a flat, sharp failure with little elongation (1.7%) and less reduction in area (2.4%). Figure 95 suggests that the fracture is at right angles to the build direction and thus indicates that the fracture is restricted to a few build layers.



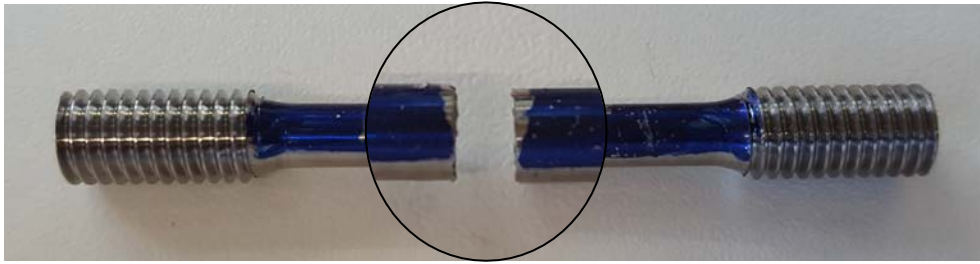


Figure 95: Optical image of brittle fracture (blue doped build).

Popovich et al [105] reported values of 2.4 % elongation prior to heat treatment at 20C and 8.3% elongation post heat treatment at 350C. The machine used for the manufacture of the tensile specimens was a SLM 280HL machine. All parts were manufactured using an argon shielding gas with the following process parameters- laser power – 275 W, scanning speed – 805 mm s<sup>-1</sup>, hatch distance – 120 μm, layer thickness - 50 μm, laser spot diameter - 81 μm, parts were manufactured in argon atmosphere. However, the build platform for this was kept at elevated temperature (200 ° C) during the process.

Chastand et al [167] reported values of 2.7% elongation after being heat treated at 640C for 4 hours and polished, however interestingly the ASTM F2924 achieved 10% elongation with no post heat treatment. All the LPBF samples were manufactured using a SLM 250HL machine with a layer thickness of 50 μm. All tensile samples were built in accordance with ISO/ASTM 52921.

Borisov et al [168] achieved an elongation of 10 % for Ti-6Al-4V samples fabricated using the SLM Solutions 280HL machine in an argon atmosphere (99.99% purity) on a Ti-6Al-4V built substrate. The process parameters used: scanning speed—805 mm/s, laser power—275 W, hatch distance—120 μm, layer thickness—50 μm. The laser beam size was approximately 80 μm. Heat treatment of the samples was performed adhering to AMS-H-81200A specification using a vacuum furnace at 10<sup>-3</sup>–10<sup>-4</sup> mbar at 950°C for 2 h, followed by furnace cooling.

Based on published literature values from numerous authors, the elongation in Table 8 is lower than expected for a virgin control build of Ti-6Al-4V. The root cause of the low elongation is likely a combination of numerous variables. The build plate in the TRUMPF TruPrint 1000 does not have the capability to preheat the bed which can result in induced thermal stresses throughout the build. Popovich et al [105] utilised a preheated build plate at 200°C resulting in better elongation values compared to the results in Table 8. Additionally, the heat treatment performed on the tensile specimens in Table 8 was slightly different to the various authors such as Borisov et al [168] suggesting that the heat treatment of the specimen may not have been optimal, and the formation of alpha phase may have increased which would result in lower elongation. Another consideration for the low elongation values is the poor/inconsistent laminar gas flow across the build plate as mentioned in section 3.3.1 as a limitation to the TRUMP TruPrint 1000. The inconsistent laminar gas flow can lead to poor removal of spatter from the fusion zone and result in the creation of pours in spatter is incorporate into fused material. Porosity was not measured throughout this study; therefore, it must be considered as a possible factor contributing to the low elongation values.

Table 9 shows the summary of where the specimen broke and how close the doped layer the failure occurs. The table shows results for only three fractured tensile bars as the remaining three bars are no longer available as they have been used for other analysis techniques such as FIB-SEM, TEM, and microstructure analysis. Length 1 shows the section of the fractured bar which would be the section of the build from the base plate upwards in the Y axis. Length 2 shows the section of the bar from the fracture location to the top of the tensile build in the Y axis.

*Table 9: Summary table of experimental data which demonstrates where each specimen broke and how close to doped band*

Sample	Fracture location (mm)		Expected location of doped layer (mm) from start of tensile build (mm)	Variation between length 2 and expected doped layer (mm)
	Length 1	Length 2		
Virgin	Length 1	Length 2	N/A	N/A
	29.98	25.02	N/A	N/A
	28.90	26.10	N/A	N/A
	26.46	28.54	N/A	N/A

Yellow	32.55	22.45	23	0.55
	31.90	23.10	23	0.10
	32.47	22.53	23	0.47
Blue	35.48	19.52	23	3.48
	34.69	20.31	23	3.69
	35.53	19.47	23	3.53

The results from Table 9 suggest that the virgin samples all fail within the gauge length and display a relatively central location for failure as expected. The yellow results suggest that the failure location is slightly offset of the centre point of the tensile specimen and may occur within the doped layer, however, this offset failure location could be from variation in the loading of doped layer in the build chamber. Similarly, the blue tensile specimen failure location suggests a greater offset location for failure and fails very close to the approximated location of the doped layer as opposed to inside the layer, this may be due to the difference in material properties and would agree with the nano-indentation results in Chapter 7.0. Refer to the Appendix for images of all the tensile specimen fractures with the relevant measurements.

Overall, it is difficult to make precise conclusions from this data as the accuracy of this data relies heavily on the skill of the operator when loading the feedstock chamber to ensure that the correct volume of powder is loaded precisely. Therefore, It's important to note that Table 9 gives an indication of the tensile fracture locations and in order to conclusively determine the failure mode and whether the failure occurs in the doped layer, SEM, TEM and EDX need to be utilised to identify evidence of oxide layers and oxidised particles within the fracture layer.

### 6.2.3 Fracture surface imaging

The tensile fracture surfaces show two main differences in failure type. Figure 96A (virgin control build) shows a large amount of deformed material between areas of what look like build defects. This surface is angled as in Figure 96A and is formed over many build layers, so the build defects are spread over many layers. This suggests that ductile fracture has occurred over most of the surface but that the build still has some defects. Figure 96B displays a higher magnification scanning electron

micrograph of a defect region, showing this material to be un-deformed and containing un-sintered powder particles and that full melting and fusion, between layers, has not occurred in some areas.

Figure 96C (yellow build) initially appears to display less pitted regions on the fracture surface but in this case, they are in a limited number of layers as the fracture surface is aligned with the build layers. The surface looks similar to the virgin material with evidence of plastic deformation even though the behaviour is different. The fracture surface morphology is characteristic of a failure that is restricted to a much narrower band of material. The fracture surface has a number of regions of what appear to be oxide films as shown in Figure 96D. These surface features were not observed within any of the control builds analysed.

Figure 96E (blue build) displays a smoother flatter fracture surface, restricted to a limited number of build layers, with characteristics of a less ductile failure. The fracture surface shows similar oxide film defects to the yellow build. Figure 96F shows a higher magnification micrograph of a large region which is indicative of an oxide film present on the fracture surface located at the edge of a large smooth plane. This region displays flow like characteristics as though the particle within the oxidised surface melted and stirred into the melt pool leaving the oxide film frozen in the material. This is likely due to the oxide film covering the particle surface has broken up and stirred into the melt pool under the Marangoni forces. This results in the metal fusing out and oxide is left flattened out on the surface.

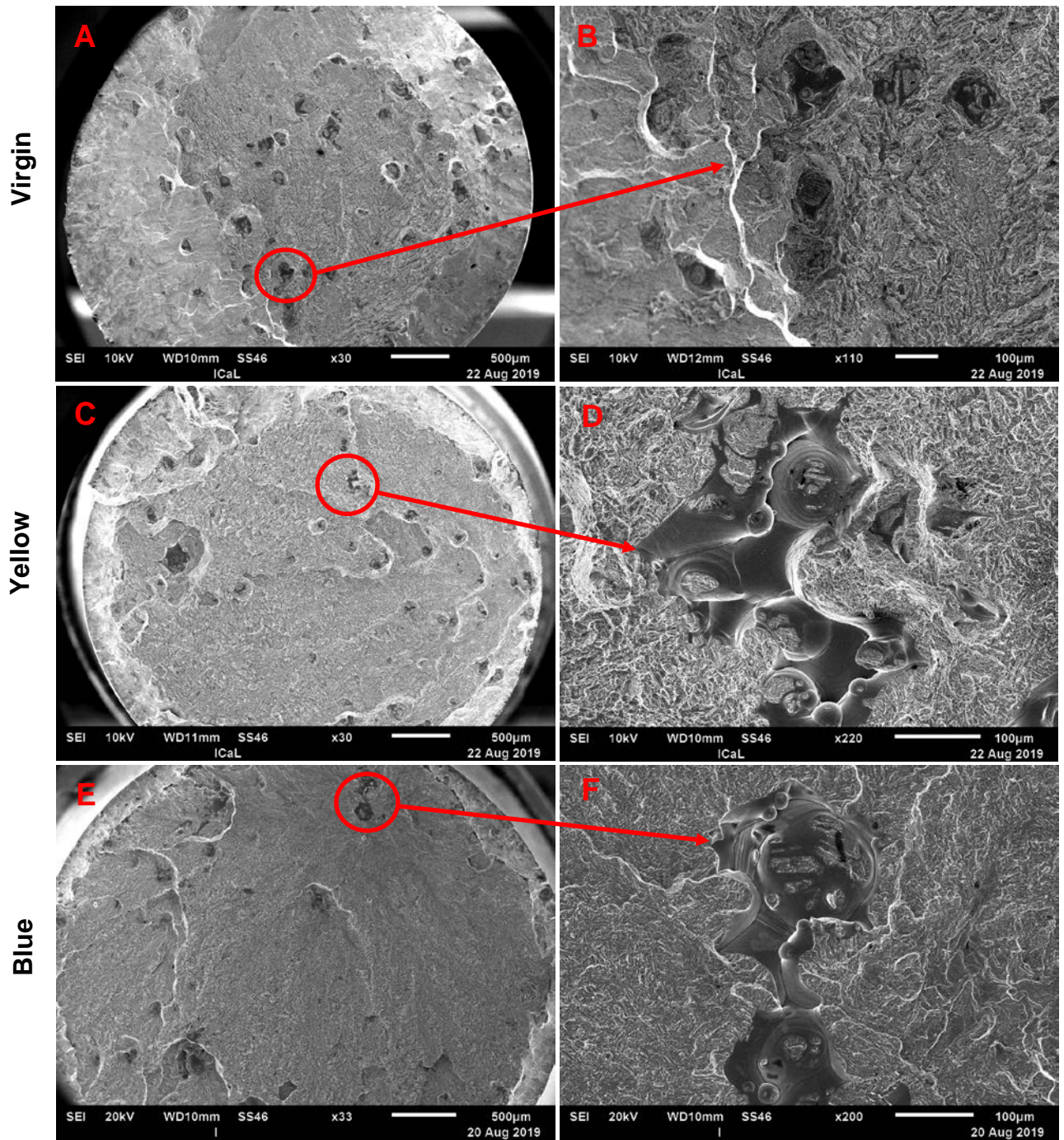


Figure 96: SEM micrograph of tensile fracture surface of A) Virgin C) Yellow and E) Blue, enhanced magnification micrographs of region of interest B), D) and F)

### **6.3 Oxide film/ residue formation in SLM**

Although SLM built parts are processed under an inert protective atmosphere, typically there is approximately 0.1% oxygen in the production process due to air filling in the spaces between powder particles. Oxide films usually arise from two different sources; the partial oxidation of the powder raw material or the oxygen entrapped from the atmosphere by the surface turbulent flow of the molten pool [169]. Louvis et al [160] showed that the oxide films on the upper surface of the molten pool in aluminium processed by SLM evaporate and form fumes which escape from the molten pool via the laser beam interaction. Additionally, the study showed that the oxide films on the lower surface of the molten pool are broken up by the Marangoni flow and are stirred up in the melt pool. The presence of oxides reduces the reactivity of the metal surface and therefore the wettability of the melt and substrates and thus the overlapping portions of the adjacent tracks can produce semi-closed or closed pores resulting in trapped un-melted particles. This increases the risk of porosity in the build and can form crack initiation points. Here the artificially oxidised Ti-6Al-4V has been blended with virgin powder to create a doped layer with a higher oxygen content which would be considered to be out of specification. The mechanical properties of the parts show that this doping has a significant effect. In the rest of the chapter the possible mechanism for this reduction in properties is investigated.

#### **6.3.1 Oxide film on fracture surface**

At 0° tilt the oxide region has features consistent with an oxide film and appears to be flat in nature as shown in both the yellow and blue doped specimens (Figures 96D and 95F), however, this was not observed in the virgin material builds. Figure 97A suggests that the oxide films appear to be in two forms, one where only the oxide film remains (fairly flat) and the other where the oxidised particle is still intact (curved), each forming part of the fracture surface.

The apparently un-fused embedded particles (blue) in Figure 97A are slightly larger than the nominal range for the Virgin powder (PSD 15-45µm). This may be because the formation of the oxide increases the particle size or simply because the PSD specifies the 95% range of the particle size class. It is also possible that they are not

intact particles surrounded by an oxide film, but remnants of oxide shells left intact when the particles melted, or fully oxidised material left within the melt pool, in both cases the oxide retaining the curved shape of the particle. However, the spherical shape and the pattern of the underlying grain structure seen in Figure 97A points to the oxide layer being thick enough to stop the particle breaking up in the melt pool and the oxide fragmenting or dissolving, so that the particle remains un-fused.

High resolution SEM imaging of the embedded oxidised particle clearly showed the microstructure of the underlying metal (under the oxide) which seems to have distorted the oxide as the metal contracted on cooling, the grain size of the metal being large as measured in the SEM (approx. 10  $\mu\text{m}$ ) compared to the oxide (Figure 97B). The grain structure of the metal under the oxide film is good evidence that these oxides were not well bonded to the metal above except in a few places where the layer can be seen to be damaged. This partial fusion of the Ti-6Al-4V oxidised particle to the substrate layer, upon successive depositions, would represent inhomogeneous inclusions that previous studies suggest would degrade the mechanical fatigue life of built parts [135].

The fracture behaviour in this region of the specimen is probably controlled by a combination of mechanical flaws (oxide films/particles) and local changes in chemistry, due to changes in oxygen content. The change in oxygen content will depend on if the films have time to dissolve during the fusion process. If there is, the higher oxygen content in the metal will make the alloy locally more brittle near where the oxide films had been. If, however, the oxide film was thicker it may not be broken up and dispersed into the surrounding metal, and so oxide films may be present in the build layer. With sufficient oxide thickness the oxide around the particles may remain unbroken and the intact particle may be left embedded within the build layer. If multiple particles are situated close together, they can act as one large mechanical flaw according to Griffith's crack criteria increasing the risk of crack propagation significantly. Also defect formation studies suggest that the presence of an oxide layer within the build decreases the wettability of the metal and blocks the flow of the molten metal resulting in poor bonding between the layers [170].

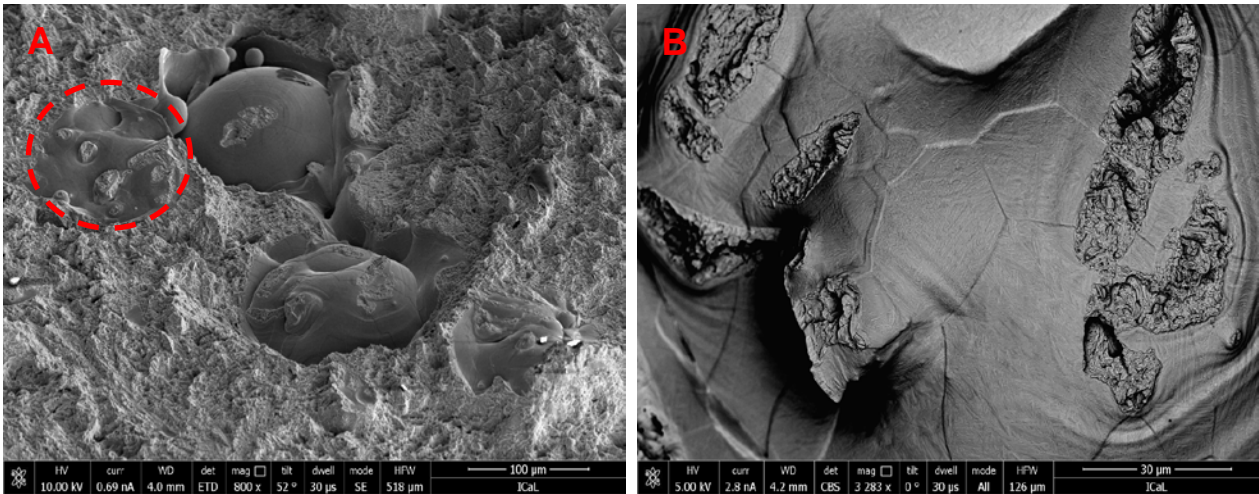


Figure 97: Non-melted oxidised Ti-6Al4V powder particle embedded into fracture surface B) high contrast solid-state backscatter electron detector (CBS) image of embedded oxidised particle surface in fracture surface

### 6.3.2 Microstructure analysis

Each tensile specimen was cross section and mounted in a thermo-setting phenol-urea based resin to be imaged in an JEOL 6610 scanning electron microscope (SEM) to understand a) the difference in microstructure between each build, and b) the difference in microstructure at the fracture surface (oxidised particle doped region), compared to a region not doped with oxide particles.



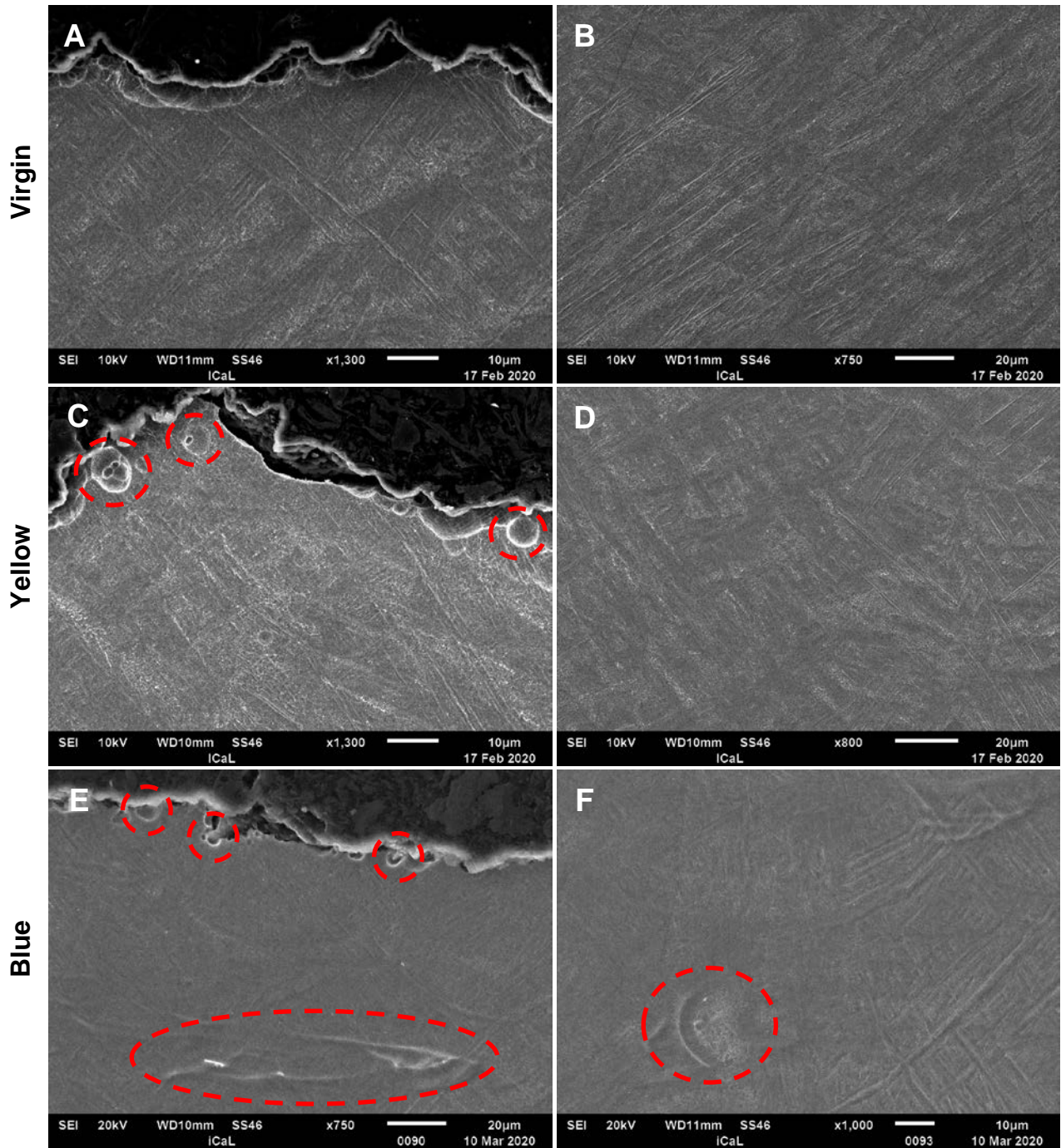


Figure 98: SEM micrograph of tensile build cross sections displaying fracture surface for A) Virgin, C) Yellow and E) Blue. Region of microstructure away from fracture surface for the three respective builds B), D) and F).

The virgin powder fracture surface cross section displays a ductile fracture with numerous elongated peaks in the fracture surface with a uniform cross hatching microstructure (Figure 98A). The fracture surface shows no evidence of any particles embedded into the fracture surface nor any obvious 'lack of fusion' sites along the fracture. Figure 98B displays the microstructure in a region ~80µm offset from the fracture surface and shows a uniform cross hatching microstructure.

Figure 98C shows a micrograph of one of the yellow particles fracture surfaces cross sectioned. It suggests a less ductile material with less evidence of deformation and less distinctive peaks compared to the fracture surface of the virgin sample. Figure 98C also shows three distinctive small particles (~5µm) embedded into the fracture surface. Figure 98D shows a region of microstructure ~80µm offset from the fracture surface layer and it displays a uniform cross hatching microstructure.

Figure 98E shows the microstructure of the cross section of the fracture surface of a blue tensile test sample. The image suggests a less ductile failure compared to the yellow sample, over most of the fracture surface. The fracture surface is predominantly flat and smooth but again it displays small distinctive particles (~5µm) within the fracture surface, similar to the yellow fracture surface. It is possible these are remnants of the oxide film that have balled up, as it is unlikely, they are metal powder particles at this size. Figure 98E (fracture surface) and, interestingly, Figure 98F (a region away from the fracture surface) suggests that not all the oxide dissolves, resulting in residual oxide films localised in the build. The image shows the cross-hatching microstructure observed elsewhere, but near the oxide swirls there are small voids of porosity (red highlighted circle Figure 98E). The oxide swirls are not observed in significant numbers near the actual fracture surface and are instead present in a region ~50µm below the surface. Figures 98E and 98F indicate that the oxide on the blue powder particles remains as films of oxide, probably due to the higher melting point of the oxides of TiO<sub>2</sub> (1843°C) and Al<sub>2</sub>O<sub>3</sub> (2072°C) compared to Ti-6Al-4V (1604-1660°C). It is likely that the oxide directly under the laser beam evaporated but the oxide below and on the sides of the particle did not and remained intact. The swirling of the oxide is an indication that the particle was melted but that it did not fuse with the rest of the material, nor was it significantly disrupted by the Marangoni forces stirring the melt pool. As there are relatively few oxide films observed it is likely that most are stirred

into the melt pool and broken up, either then dissolving in the metal or present as oxide fragments.

The presence of oxide remnants combined with the dissolved oxygen in the surrounding material seems to have a more significant affect than the intact oxide films, as it alters the localised mechanical properties to the detriment of the final build quality. This is likely because the oxide remnants behave as mechanical flaws, while the oxygen in the alloy from the dissolved oxide presents a chemical defect, hardening the material and reducing ductility making it easier for cracks to propagate. These observations point to oxidised particles having a deleterious effect even if the powder is brought back into specification by diluting the used powder with virgin material. Therefore, in order to re-use processed powder as feedstock, in safety critical situations, a method of identifying and removing heavily oxidised particles, of all sizes, is essential in order to avoid localised undesirable changes in mechanical properties. Additional research is also required to develop methods of controlling oxide formation, and how to disrupt any oxide films/residues present within build components. The removal of oxidised particles or the development of methods to modify the behaviour of oxidised particles would allow greater reuse of the powder in the SLM process.

#### **6.4 Chapter summary**

The tensile data suggested that although there wasn't a significant overall change in mechanical properties for the tensile build specimens, there was a local change in behaviour, the failure occurring within the doped layer for both the yellow and blue builds. Furthermore, the fracture surface imaging showed that for the control build, the failure was ductile and occurred over many layers with no evidence of defects but no apparent oxide films. However, the yellow build and in particularly the blue build displayed less ductile fractures occurring over fewer layer and oxide films were present within the fracture surface.

The findings in this chapter were important as the data suggests that failure may occur due to mechanical flaws within the build as the oxide film found on the fracture may

not have bonded significantly to its surroundings, most likely acting as a stress concentrator.

Further evidence of mechanical flaws was found in the microstructural analysis. The yellow and blue microstructure showed that small particles  $\sim 5\mu\text{m}$  in size were found near the fracture surface. It is possible that these are balled up oxide as the diameter of these particles are uncharacteristic of powder particles. Additionally, the blue build microstructure showed oxide swirls  $50\mu\text{m}$  below the fracture surface suggesting that not all the oxide dissolves, resulting in residual oxide films localised within the build layers.

However, this chapter did not investigate the dissolved oxygen content of the fracture surface and this still remains a possible failure mechanism as the particle oxides may have dissolved into the surrounding material, resulting in embrittlement in localised build layers. Therefore, failure due to chemical flaws cannot, at this stage, be ruled out as a possible failure mechanism. Thus, further analysis using S/TEM imaging of the fracture surface lamella was needed to quantify the oxygen content, the results of this analysis is discussed in greater in the chapter 7.0.

## **7.0 The effect of oxygen dissolution in the build**

Thus far, it has been established that mechanical flaws are present within the build in the form of oxide residue and evidence of oxide films on the fracture surface have been identified. This chapter investigates the influence of chemical flaws in the build and whether oxygen dissolution is a key factor in the reason for failure of the tensile specimens. Scanning transmission electron microscopy (S/TEM) was used in order to quantify the presence of oxygen within the fracture surface via high resolution EDX line scans and mapping, however oxygen concentration profiles given by the semi quantitative EDX analysis suggested that oxygen is being over detected.

Additionally, nano-indentation was used to compare the hardness values of the material near the fracture surface relative to the remaining layers of the build to understand if the inclusion of the oxidised particles changes the hardness of the surrounding material.

This chapter is the final investigation of experimental work for this project and attempts to determine if dissolved oxygen changes the local behaviour of the build material.

### **7.1 Quantification of oxygen in fracture surface**

The regions of interest (ROI) were selected because they would give greater understanding of the fracture surface morphology. Two regions of the blue build specimen were selected, one was postulated to be covered with an oxide film on an un-bonded particle (Figure 99A), the other a plastically deformed surface (Figure 99B). Additionally, a region of the yellow build was selected similar to Figure 99B to further understand the impact the oxidised particles had on the surrounding material not in contact with an oxide. It is not possible to confirm the nature of these regions using more conventional means such as SEM/EDX because the oxide thickness is much less than the sampling depth in SEM/EDX. The process parameters used to manufacture the lamella for each of the regions of interest are discussed in chapter 3.0.

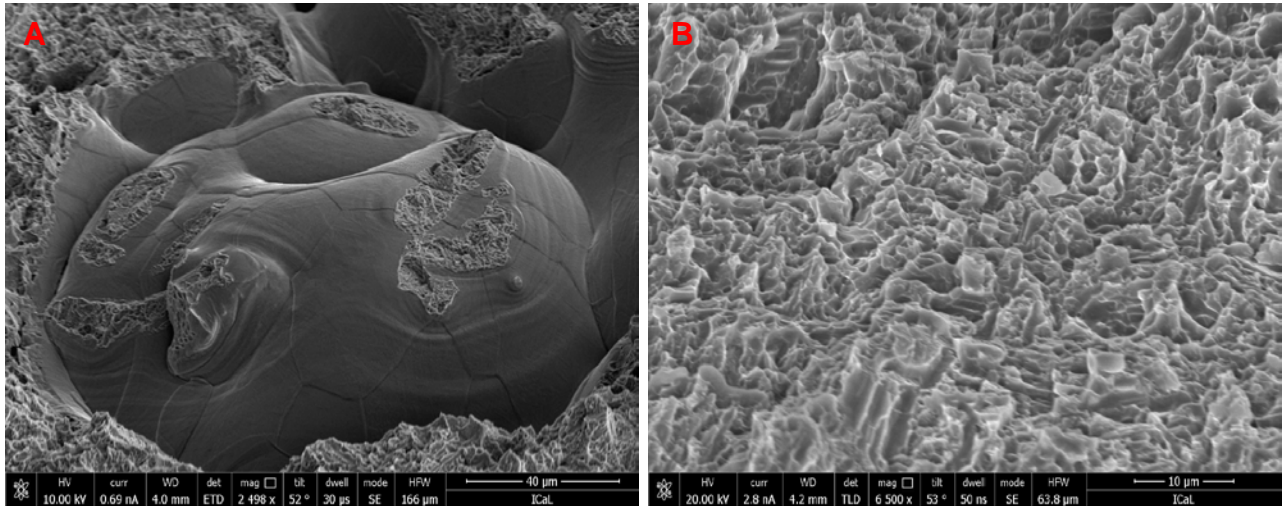


Figure 99: A) ROI with un-bonded particle in contact with oxide film, B) ROI plastically deformed region not in contact with an oxide film.

### 7.1.1 Oxide film on an unbonded particle (oxide region)

EDX mapping was used to determine the presence of oxygen and other elements within regions of the material. Figure 100 shows the EDX map for what was proposed to be an oxide film covered particle from the blue tensile fracture surface lamella sample. It shows the main elemental components; titanium (Ti), vanadium (V), aluminium (Al), oxygen (O) and Copper (Cu). The copper signal is attributed to the copper support grid as the alloy does not contain copper. Figure 100A shows the full elemental distribution within the region, while Figure 100B shows only the concentration of oxygen, the structure of the region being featureless.

Fracture surface

Fracture surface

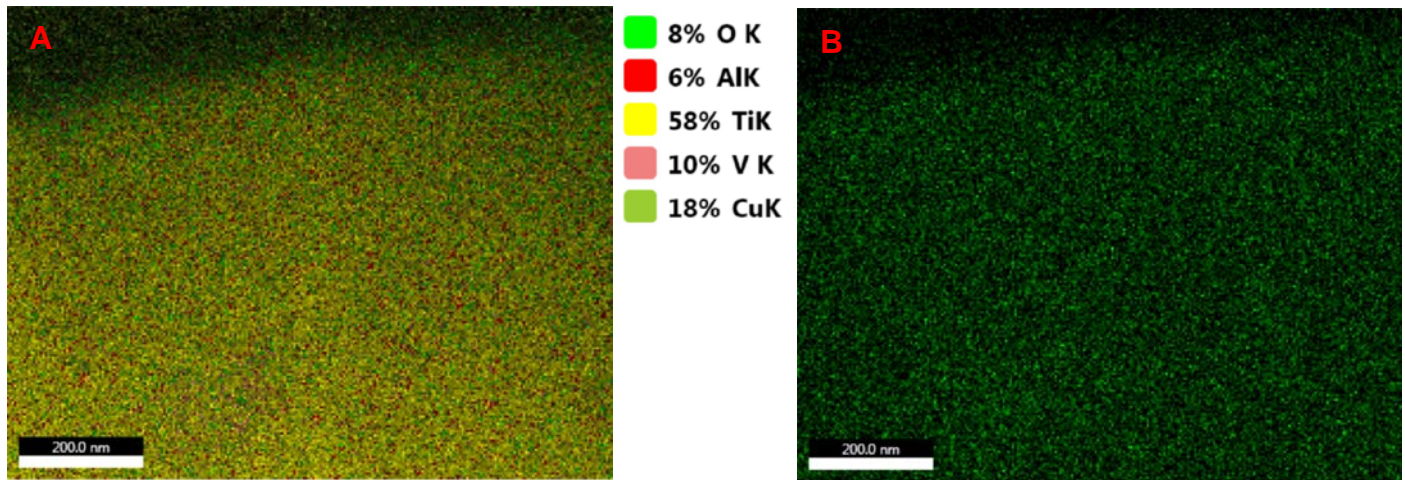


Figure 100: EDX elemental mapping of blue Ti-6Al-4V tensile build fracture surface lamella sample. A) EDX elemental overlay map B) Oxygen (O) element map

The analysis that produces these maps can also be used to produce concentration profiles like those seen in Figure 101 and Figure 103. Although these figures show the at. % composition for the different elements, it is worth remembering that the accuracy of EDX with light elements is limited, that contamination can occur during the ion beam thinning process and signals can be detected from the surroundings, as seen by the detection of copper. Therefore, what is important in these figures are the changes in concentration rather than the absolute values.

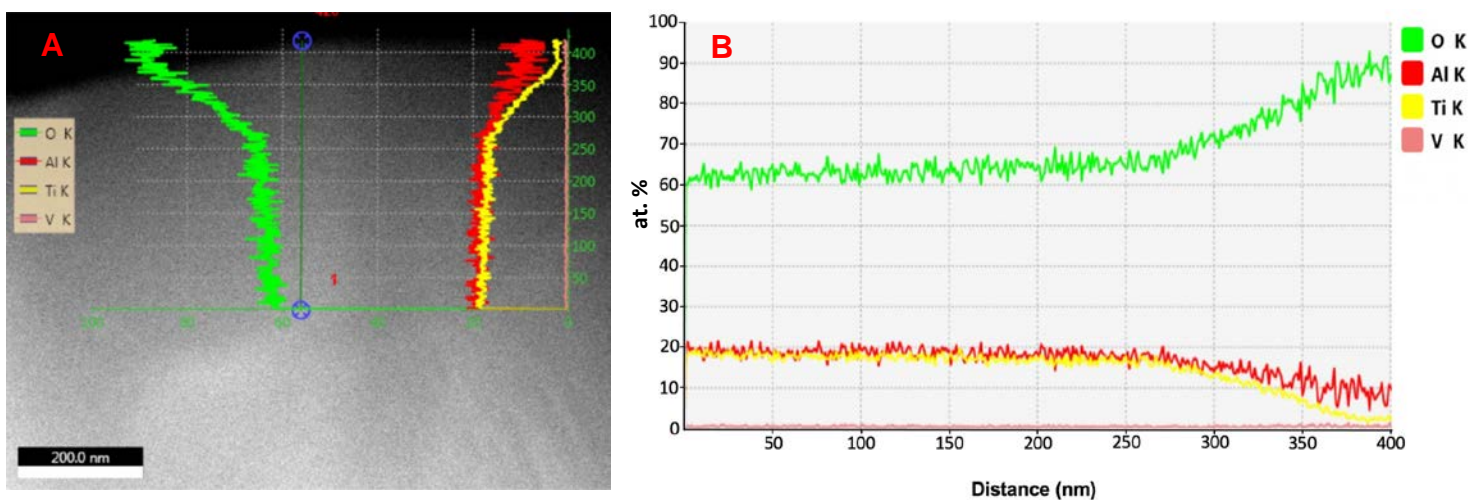


Figure 101: EDX elemental line scan of blue tensile build fracture surface lamella of embedded oxidised particle. A) HAADF-STEM image of lamella region of interest with graphing overlay B) Line scan graph

EDX line scans are in many ways more informative than maps especially if there are no discrete phases, as trends are easier to observe. The line scan displays elemental atomic % of the four main elements of interest: oxygen (O), aluminium (Al), titanium (Ti) and vanadium (V). The line scan in Figure 101A proceeds 400nm from the fracture surface and displays a consistent oxygen at. % of around 60 at. % between 0nm and 280nm, which is close to  $Ti_2O_3$  (60%) and  $TiO_2$  (67%) indicating this is a region of oxide, though possibly a non-equilibrium oxide that is not on the phase diagram as there are numerous titanium oxides that are very similar.

The oxygen concentration is well above the solubility limit of the titanium matrix at 34 at. % in the  $\alpha$ -phase [171] . This suggests that the line scan is only within the oxide and does not include any area of the underlying metal, although this would make the oxide thicker than predicted by the interference colour for this batch of powder, but that may be why the oxide on this particle survived intact, the thicker oxide being more robust.

Toward the outer edge of the specimen the oxygen at. % Increases between 280nm and the fracture surface peaking at 80 at. %, which is higher than is possible with any known titanium or aluminium oxide. There are two possible reasons this may have occurred, one that elements were lost during milling from the outer edge, but normally the element lost is oxygen, or that the values for oxygen concentration given by the semi quantitative EDX analysis are inaccurate, and oxygen is being over detected. In this second case the outer region is likely to be Al doped  $TiO_2$  while the inner region is an oxygen deficient oxide, and this would be consistent with the phase diagram. A rise in the aluminium content at the outer edge of the oxide is also observable in the line scans.

The presence of aluminium probably makes the oxide less likely to dissolve as  $Al_2O_3$  is more thermodynamically stable than  $TiO_2$ . The formation of the aluminium enriched oxide is also likely to reduce the oxygen dissolved in the metal but will also locally deplete the metal in aluminium. The observed vanadium content near this surface is low compared to the bulk and is uniform over the line scan, showing a surface depletion of vanadium.



The formation of an oxygen diffusion layer in the metal below the oxide is expected as the blue particles were oxidised at  $>600^{\circ}\text{C}$ , which combined with high processing temperatures in the SLM process should result in localised increases in oxygen content [172]. Kumar et al [173] suggested that as the oxide layer ( $\text{Al}_2\text{O}_3$  and  $\text{TiO}_2$ ) thickness increases, so does the oxygen content of the metal, resulting in an increase in hardness of the underlying metal. In the context of this study, an increase in hardness would be detrimental to the final build quality as this would result in a localised region of the build having significantly different mechanical properties and thus increase the risk of failure within this region.

### 7.1.2 Plastically deformed region (non-oxide region)

Using the same FIB-SEM in-situ lift out process, a plastically deformed region of the fracture surface was selected (Figure 99B). This region was chosen to quantify the oxygen concentration away from known oxide films and to look for evidence that some oxide films had dissolved into the surrounding metal. Similar FIB-SEM process parameters were used to those used for the embedded particle as discussed in chapter 3.0, with a  $4\mu\text{m}$  Pt layer thickness used to coat the more uneven surface.

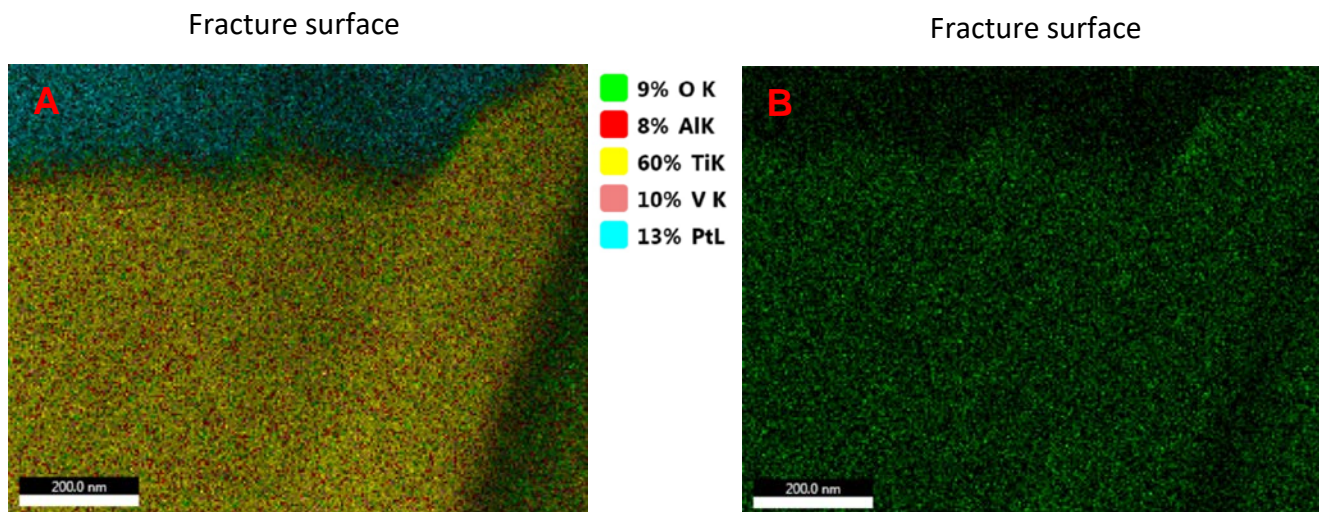


Figure 102: EDX elemental map of blue tensile non-embedded particle region of interest. A) EDX elemental overlay map B) EDX oxygen (O) map

Figure 102B shows the presence of oxygen and suggests a uniform distribution throughout the lamella, although the sample area is small. This suggests that there is some oxygen dissolution from the oxidised particles, which would be consistent with the low number of particles observed on the fracture surface compared to the number present in the doped powder. Even though the semi quantitative EDX (Figure 103) for this fracture surface region suggests an oxygen level that is within the solubility limit of the metal (34 at. %) it is higher than seems reasonable for metal not in direct contact with an oxide. It is, however, much less than in the sample seen in Figure 101. This would support the idea that the semi quantification carried out by the EDX system is over representing the oxygen concentration and although there is likely to be some oxygen dissolved in the metal it is not this high. The overall oxygen content of the powder from which this region was built is much lower than the value calculated by the system.

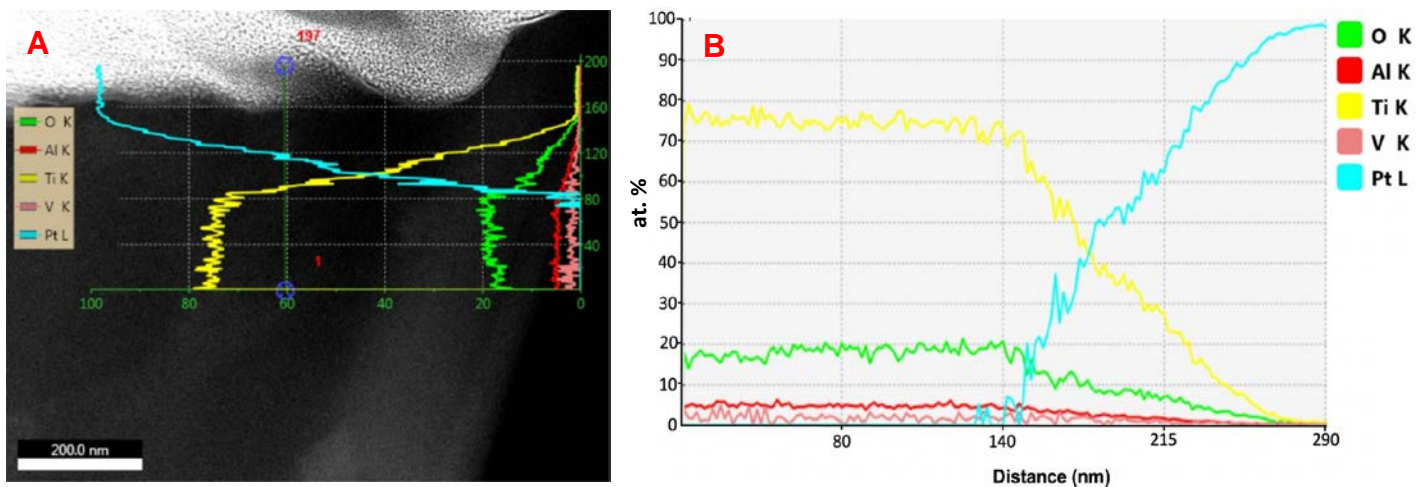


Figure 103: EDX elemental line scan of blue tensile build fracture surface lamella of non-embedded oxidised particle. A) TEM image of lamella region of interest with graphing overlay B) Line scan graph

Again, the EDX maps/images of the lamella show no particles or oxide films with significantly different compositions. The line scan displays at. % of the four main elements of interest: oxygen (O), aluminium (Al), titanium (Ti) and vanadium (V) and proceeds 290nm from the fracture surface displaying a consistent oxygen signal of around 20 at. % between 0nm and 150nm, the oxygen at. % decreasing rapidly upon contact with the Pt layer.

This line scan suggests that the fracture surface layer and subsequent layers surrounding the fracture surface may have a higher oxygen content but that there is no oxide film. The failure mechanism suggests that the oxygen content is raised in this region compared to the virgin material but that the amount cannot be quantified from this data. A higher oxygen content will create a region of the tensile bar with higher strength but lower ductility, but this cannot be proved from this experiment. Previous studies have shown that an ingress of oxygen into Ti-6Al-4V metal changes the ductile rupture mode to a brittle rupture mode. It was found that an oxygen content of 1 wt % is sufficient to embrittle the Ti-6Al-4V alloy [174].

NOTE: This stage of the project was significantly impacted by the COVID-19 pandemic, experiments could not be repeated, and different software was used because of the COVID-19 restrictions put in place to ensure the safety of staff and students.

Therefore, analysis of the yellow lamella was conducted by a JEOL S/TEM 2100+ which uses slightly different software and presents the results slightly different. The line scan data presents in the form of counts per second (CPS) and produces a data table with elemental at % and wt %. However, all the relevant data was obtained in order to discuss and analyse for the yellow lamella sample.

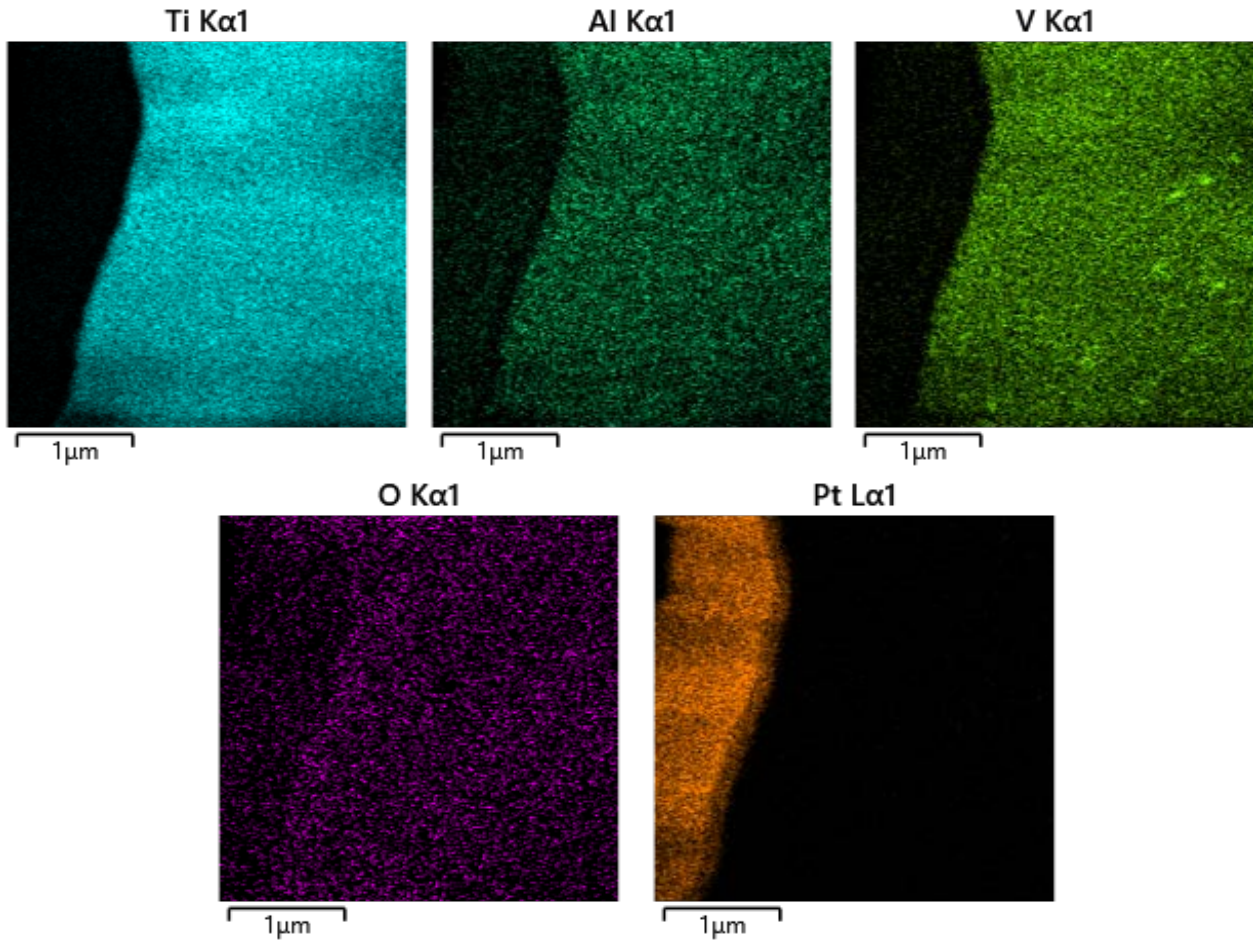


*Figure 104: EDX elemental map of the yellow build fracture surface lamella*

Figure 104 shows the elemental distribution of the yellow fracture surface lamella (not in contact with an oxide film). The oxygen map shows a uniform distribution of oxygen throughout the lamella, although the sample is small. This suggests that there is some oxygen dissolution from the yellow oxidised particles, but the elemental map is less dense in comparison to the Figure 102 for the blue specimen (not in contact with oxide film).

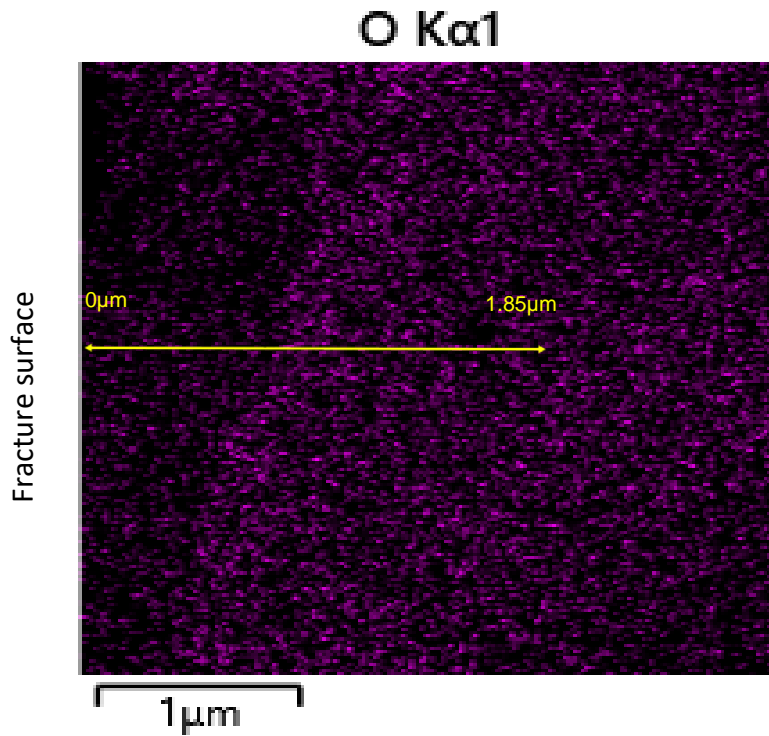


*Figure 105: EDX line scan of the yellow fracture surface lamella overlaid onto to the O elemental map*

Similar to the blue lamella analysis, a lamella sample was milled from the fracture surface of the yellow build fracture surface from a region of interest with no embedded particles. This was performed to make a comparison of the fracture surface layer localised oxygen content between the blue build and yellow build, this was, however, made more difficult by the Covid-19 restrictions forcing the use of different equipment. The EDX map in Figure 105 suggests an even oxygen distribution throughout the lamella sample suggesting that the oxygen dissolution from the embedded particles has increased the layers oxygen content, it is also a possibility that this could be noise from the peak overlap from different elements. The yellow build EDX map by comparison with the blue non embedded particle region of interest shows a lower density in oxygen throughout the lamella suggesting that the oxygen dissolution is less in the yellow build compared to that of the blue.

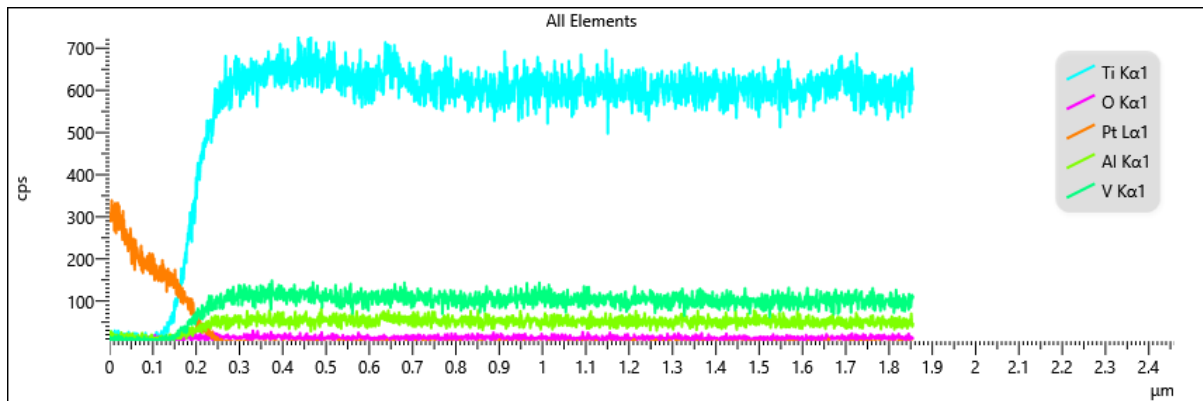


Figure 106: EDX line scan plot of elements for yellow non embedded particle region lamella.

The line scan spectrum results show the elements in the form of counts per second (CPS), it's important to note that CPS does not take into account coefficients and simply illustrates the presence of the element as opposed to a quantitative concentration. Due to software licensing constraints, CPS was the only available output plot, however the analysis still produced results for at % and wt % without the associated plot.

Results from the analysis showed an oxygen presence of 9 at % throughout the lamella. The oxygen dissolution is considerably lower at 9 at % compared to 20 at. % of the blue build tensile fracture lamella with the non-embedded particle region of interest. Even though the semi quantitative EDX (Figure 106) for this fracture surface region suggests an oxygen level of 9 at% is within the solubility limit of the metal (34 at. %) it is higher than seems reasonable for metal not in contact with an oxide. It is, however, much less than in the sample seen in Figure 101 and Figure 103 but still exceeds the allowable limits for ASTM oxygen standards for SLM built parts.

This suggests that the oxide layer present on the yellow particles within the melt pool may have dissolved into the surrounding layer increasing the localised oxygen content, however it is less than that of the blue build. This may be due to the lower oxygen content of the yellow particles compared to the blue, therefore there is less available oxygen to dissolve into the surrounding material. Another possibility is that the analysis may be wrong and not directly comparable as this analysis was completed on a different TEM and could not be repeated due to the time constraints and equipment availability due to the COVID-19 pandemic. It's important to note that the values

obtained from the EDX analysis cannot be taken as absolute values as this is a semi-quantitative technique, in this case, the trend shown is more significant as it shows where the oxygen is present and the relative concentrations across the lamella structure.

Between 0 $\mu\text{m}$  and 0.2 $\mu\text{m}$ , the line scan data suggests that the scan is in the platinum layer protective layer as Pt is the dominant peak with little counts from the other elements. However, at 0.25 $\mu\text{m}$ , the Pt peak decreases significantly, and oxygen content increases peaking at 50CPS and displays a constant trend throughout the lamella between 0.25 $\mu\text{m}$  and 1.85 $\mu\text{m}$ . This trend is significantly lower than that of the oxygen content within the blue specimen suggesting that the diffusion of oxygen into the surrounding layers of the build is less than that of the blue.

## **7.2 The effect of oxygen dissolution on the mechanical properties**

### **7.2.1 Nano-indentation hardness**

Nano-indentation was used to investigate the hardness of the material in the tensile specimen and compare the hardness of the material in the fracture surface and the surroundings layers to regions of no oxidised powder doping. The variation in hardness will aid in understanding the impact the oxidised particles have on the localised mechanical properties and whether the inclusion of oxidised particles, and dissolution of oxygen into the metal, increases hardness in the localised layers of the fracture and whether this has an impact on layers further away from the fracture surface.

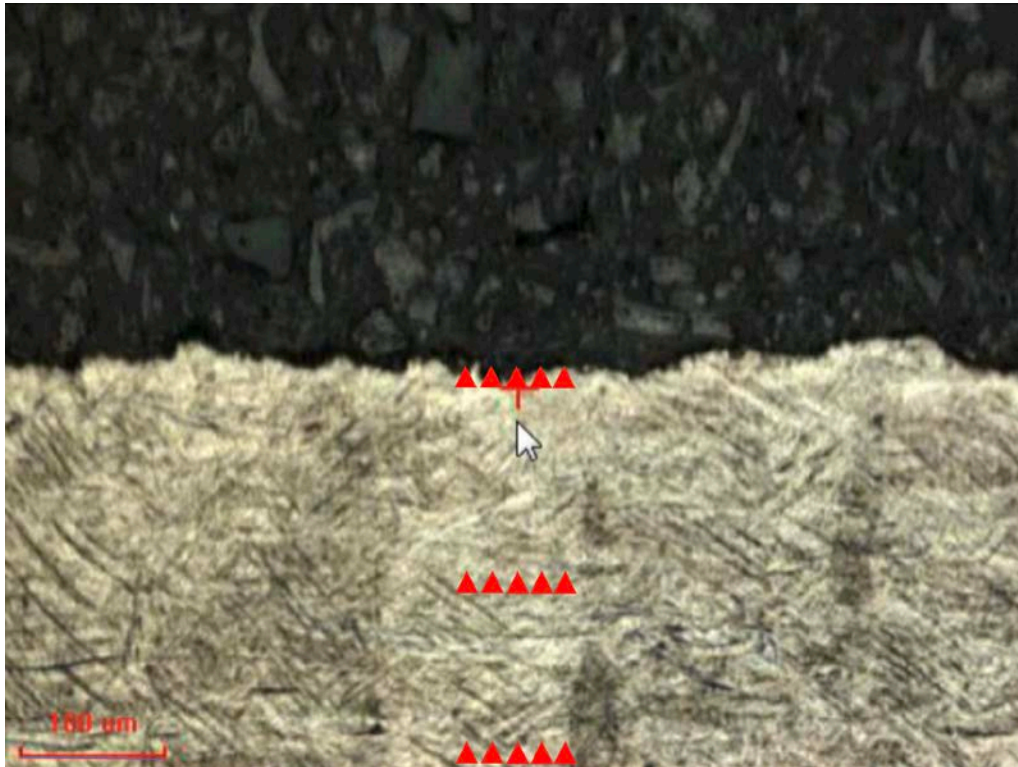


Figure 107: Indentation plan illustrated on SEM micrograph of tensile cross section sample

Figure 107 shows three indent arrays, normal to the tensile fracture surface, produced hardness profiles at three separate locations as they represented separate build layers; as the layer thickness for the build was set at  $150\mu\text{m}$ , a distance of  $300\mu\text{m}$  and  $100\mu\text{m}$  were chosen as they represented 5 layers and 10 layers succeeding the fracture layer respectively. For each distance point analysed, five locations parallel to the distance were chosen to gain an average result. It is important to note that  $0\mu\text{m}$  on the distance axis is defined at the fracture surface on the tensile specimen. The error bars in Figure 108 are calculated by standard deviation from the nano-indentation results for hardness.



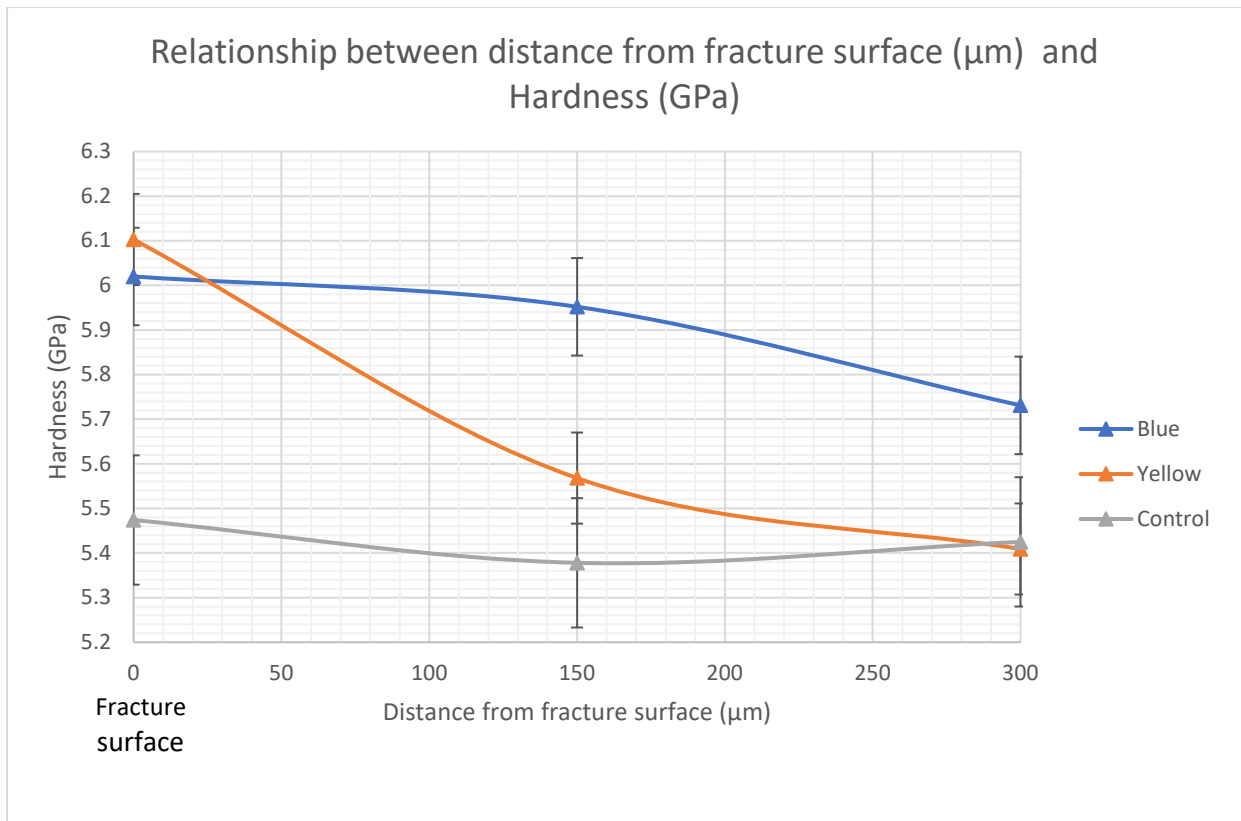


Figure 108: Relationship between hardness (GPa) and distance from the fracture surface (μm)

Figure 108 shows the relationship between hardness and distance from the fracture surface for each of the three tensile build specimens: blue, yellow and virgin (control). The data trend for the blue specimen shows that the sample had the overall highest hardness across the three data points at 5.901 GPa suggesting that the high oxygen content in the particles may have impacted the surrounding layers greater than the other two specimens as all three distances yield higher values for hardness for the blue sample compared to yellow and the control builds. Interestingly, the fracture surface of the blue specimen yields a similar result to the yellow with a difference of 0.1GPa indicating that the high oxygen content in the metal at the fracture surface may have a similar impact on hardness. The fracture surface of both the blue and yellow specimens display significantly higher values of hardness in comparison to the control build with a difference of around 0.6GPa which indicates that the oxidised particles significantly alter the localised hardness of the build which could lead to premature failure of the part subjected to loading conditions. A study by Tang et al [175] reported similar findings as they shown that increased oxygen content in Ti-6Al-4V built tensile

specimens resulted in increased values of hardness and elasticity modulus. Average nano-hardness value was reported to be 6.5GPa for 0.17 wt % oxygen, 7.5GPa for 0.2 wt % oxygen and 8.5GPa for 0.23 wt % oxygen.

However, at 150 $\mu$ m, the hardness value for the blue specimen is significantly higher than that of the yellow with a difference of 0.4GPa, indicating that the blue oxidised particles may have a greater impact on the surrounding layers in comparison to the yellow particles. Interestingly, at 150 $\mu$ m, the yellow specimen only has a difference of 0.19 compared to the virgin sample. At 300 $\mu$ m, approximately, ten build layers away from the fracture layer, the blue specimen again yielded the highest hardness at 5.7GPa, which was a difference of 0.3GPa compared the yellow and control. At 300 $\mu$ m, the yellow and control build both yields very similar value in hardness with a difference of 0.016GPa, indicating that the yellow oxidised particles have little effect on the hardness of the build layers at this distance. The thickness of the band of doped powder particles within the tensile build was approximately 500 $\mu$ m, the evidence suggests that the fracture occurs close to the interface between the doped and undoped regions.

Figure 108 suggests that the fracture is running close to where the hardness values changes rather than through the hardest layer. It is possible that the change in hardness is more significant than the oxide hardened material. The hardened material does not seem to lay equally across the two fracture surface of the yellow and blue tensile samples. This would also agree with the evidence found in chapter 6 as there is an oxide film present on the surface of the fracture sample, however there is no fracture running through the oxide and instead the fracture runs along the interface between the soft and hard material. This is likely due to the difference in hardness, the difference in the material properties which is making the fracture occur, not the presence of a harder brittle material, this likely creates a stress concentration due to the different material properties, this explains why the evidence in chapter 6 shows a ductile failure even though the fracture is fairly flat, the failure looks ductile because it is running between the softer and harder material instead of just the hardened material.

Overall, the nano-indentation data suggests that the impact of the oxidised particles is significant for the doped regions of the build and in the case of oxidised particles with

high oxygen content such as the blue build, the surrounding layers are also affected and see an increase in oxygen. This is also true of the yellow build, however, the effect on the hardness of the surrounding layer is less in comparison to the blue, it is also possible that the failure could be near the edge of the doped particle region. That being said, both the blue and yellow builds yielded higher value in comparison to the virgin build at both the fracture surface and 150 $\mu$ m which suggests that the oxidised particles do alter the localised mechanical properties of the build and the surrounding layers.

The addition of the oxidised particles into the doped layer has likely increased the amount of interstitial oxygen diffused into the surrounding build layers which impedes the dislocation motion resulting in a hardening of the material. In the HCP crystalline structure, the oxygen atoms are not free to move resulting in a reduction in atomic mobility of the interstitial region and thus an increase in hardness of the material [176]. Additionally, the presence of interstitial oxygen, particularly in the case of the blue build, facilitates the formation of martensitic phases due to distortion of the crystalline lattice by the oxygen resulting in crystallite micro-strain [177][178].

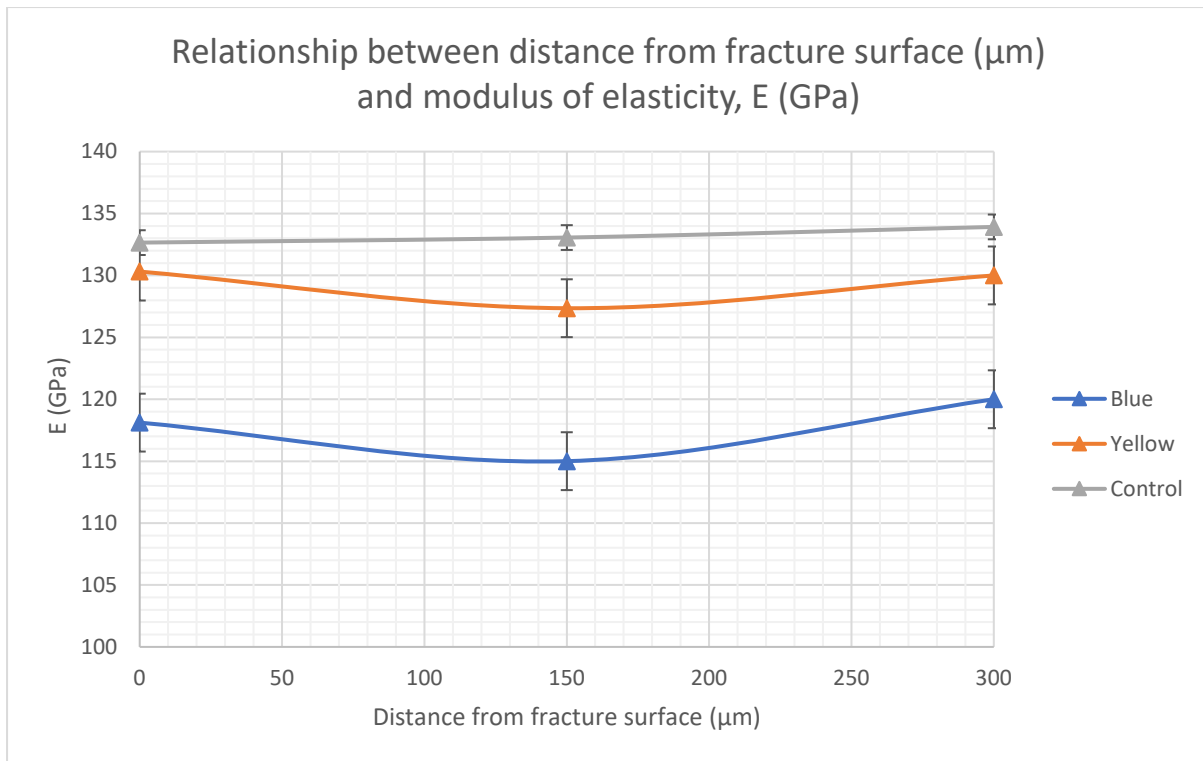


Figure 109: Relationship between distance from fracture surface ( $\mu\text{m}$ ) and modulus of elasticity,  $E$  (GPa) determined by the NanoSuite<sup>®</sup> software.

The relationship between the modulus of elasticity at max load,  $E$  (GPa) and the distance from the fracture surface ( $\mu\text{m}$ ) is shown in Figure 109. The errors bars in Figure 109 are calculated from the standard deviation of the nano-indentation results for modulus of elasticity at the maximum load. Similar to Figure 108,  $0\mu\text{m}$  is defined at the fracture surface for the tensile specimen. At the fracture surface ( $0\mu\text{m}$ ), the control build yields the highest modulus of elasticity at  $140\text{GPa}$  compared to lowest modulus at  $118\text{GPa}$  for the blue specimen, a difference of  $22\text{GPa}$ . The yellow tensile specimen produced results similar to the control build at the fracture surface with a slight reduction in the modulus of elasticity of  $2\text{GPa}$  at  $0\mu\text{m}$ .

The data trend across the three distances for the control build shows little variation with a difference of  $1\text{GPa}$  which is expected as the material properties throughout the specimen should be consistent as no oxidised particles have been added. Interestingly, the data trend across the yellow specimen illustrates a decline at  $150\mu\text{m}$  in the value of  $E$  (GPa) before trending back towards the virgin value at  $300\mu\text{m}$ . This suggests that yellow doped layer of oxidised particles may diffuse enough oxygen to

reduce the elasticity of the surrounding layers to the fracture surface, however as the distance from the fracture surface increases, the modulus of elasticity trends back towards the virgin values.

Similarly, the same trend can be observed for the blue specimen as the value of E (GPa) is 14 GPa lower at 0 $\mu$ m and drops slightly at 150 $\mu$ m to 115GPa (difference of 18GPa from control build) before trending back towards the virgin values at 300 $\mu$ m. This further suggests that doped blue particle layer in the fracture surface may diffuse a sufficient amount of oxygen to the surrounding layers that it reduces the elasticity, however as the distance increases from the fracture surface, the modulus of elasticity trends back towards the virgin values.

The results from Figure 109 shows the impact the doped oxidised particle layer has on the modulus of elasticity; the high oxygen content of the blue and yellow particles is sufficient enough to alter the modulus of elasticity of the built specimen.

Both the yellow and blue specimens show lower values of elastic modulus for all three distances compared to that of the control build. However, the yellow and blue builds both show that as the distance increases from the fracture surface (>200 $\mu$ m), the values of E (GPa) trend back towards the virgin values. The reduction in the modulus of elasticity is likely due to the interstitial oxygen diffusing into the surrounding localised layers during the melting of the doped layer within the build. The reduction in modulus of elasticity values can be related to the weakening of the atomic bond forces due to the presence of interstitial oxygen within the build layers [179][180]. In titanium alloys where the predominant phase is alpha or alpha prime, the oxygen atoms are not free to move, resulting in an decrease in elasticity modulus due to interstitial immobility [181]. The altering of the mechanical properties of the build through the reduction of elastic modulus may be considered detrimental build as it may result in premature failure under loading conditions.

### 7.3 Chapter summary

The data from the EDX analysis shows that the oxygen dissolution into the surrounding layers for both the yellow and blue doped tensile specimens is higher than the allowable limits for ASTM standards.

The oxygen dissolution from the doped oxidised layers has a significant impact on the nano-hardness of the part suggesting that the fracture surface layer (highest oxygen point) exhibit larger values of nano-hardness than anywhere else in the specimen. Interestingly, the fracture occurs along the interface of the soft and hard material instead of running through the hard oxide, this is likely due to the difference in material properties. Additionally, the blue and yellow builds also showed elevated values of hardness at distances of 150 $\mu\text{m}$  and 300 $\mu\text{m}$  away from the fracture surface suggesting that the oxygen dissolution may affect the mechanical properties of the surrounding layers, in particularly the blue tensile build.

The modulus of elasticity also showed the blue and yellow build had a lower elasticity modulus in comparison to the control build as the increase in oxygen content in the fracture surface and surrounding layers impedes dislocation movement. However, as the distance from the fracture surface increases (>200 $\mu\text{m}$ ), the modulus of elasticity trends back towards the virgin values.

Overall, the data from this chapter suggests that the oxygen dissolution from the doped regions during the melting process presents a significant chemical flaw within the build and changes the localised mechanical properties of both the fracture layer and the surrounding building layers. Additionally, the data suggests that the problem is more significant with the blue doped build in comparison to the yellow, however, the yellow oxidised particle still pose a significant risk as they detrimentally alter the mechanical properties of the final built part.

## 8.0 Conclusion

The main findings from this investigation suggest that oxidised particles incorporated into a Ti-6Al-4V SLM part will negatively impact the mechanical properties of that part, both because of mechanical defects (oxide films/residue) but also because of local chemical changes (interstitial impurities).

The dominant variable that most likely affects the local mechanical properties of an area is the local oxygen content. The local oxygen content being largely controlled by the oxide film present on the powder particles and the oxygen dissolved in the alloy. The nano-indentation data suggested that the change in hardness is more significant than the oxide hardened material as the fracture runs close to where the hardness values change rather than the hardest layer, this is likely to act as a stress concentrator that most likely causes the failure.

Particles with oxide layers/films and high oxygen content formed from prolonged heating or ejection from the melt pool, will both lead to unincorporated particles in the material or oxide films within the build layers. If the oxide is stable these will remain as mechanical defects. If the oxides are unstable and decompose, once incorporated into the melt pool, they will cause a local increase in oxygen, with the associated changes in mechanical properties as shown by the nano-indentation results in chapter 7.0.

Larger particles are likely to be removed via post process sieving or by the recoater in the SLM machine. However, smaller oxidised particles may remain in the powder after sieving and may be reused as feedstock for a new build. Particles in the range used by these machines pose a greater problem on powder reuse as they are not removed on recycling using sieving. They also have a higher surface area to volume ratio and are therefore likely to have higher oxygen levels.

Interference colours formed due to oxide layer thickness on Ti-6Al-4V powder surface proved to be a good indicator of the oxygen content of the powder particles. However, the exact oxygen concentration cannot be determined by this method, but an oxygen content range can be determined from each colour to give a good indication if a particle colour is likely to lead to significant change in materials properties of the build.

This research has shown that bulk measurement techniques cannot be used alone to measure the quality of a recycled powder as a local accumulation of oxidised powder will cause localised changes in properties. Therefore, robust quality control measures are essential in order to monitor or remove oxidised material in post processed powder. This would significantly boost user trust and confidence in reusing powder and allow wider adoption of powder such as titanium alloys for additive manufacturing across multi-disciplinary industries.

Further research is needed on the SLM of Ti-6Al-4V to understand methods of controlling oxide formation and disrupting the oxide films/residues formed within build components. This would improve the ability to reuse processed powder and reduce raw material costs, boosting cost efficiency for serial production.



## **9.0 Considerations and future work**

### **9.1 Considerations**

Similar to many projects, time constraints and cost inhibited the full investigation of all the objectives set out in the beginning of the project. Most notable the COVID-19 pandemic and the investigation into the impact of heat affected zone powder and investigation into the presence and formation of the oxidised particles within post processed powder. The COVID-19 pandemic delayed a lot of the intended work for the project and meant that the heat affected zone investigation could not occur and as such the artificially created powder particles had to be validated by means of tensile testing and full-scale investigation of post processed powder beds could not occur.

The level of validation that was originally intended for this project was not realised due to the COVID-19 pandemic, however, this does not diminish the novelty of the work conducted throughout this project which still yielded significant results. Below are the key areas which, based on the results from this investigation are key in the understanding and controlling the effects of oxidised Ti-6Al-4V powder particles in SLM process.

### **9.2 Future work**

#### **9.2.1 Modelling of Heat affected zone (HAZ) powder**

Ideally in order to validate the work completed throughout this project, a heat affected zone model could be created investigating the powder characteristics of the HAZ powder and the degradation mechanisms around different process parameters. Although it is known that oxidised particles occur in post processed powder, there is no definitive answer to at what powder reuse number or under what specific conditions we can expect to see such particles. Therefore, this work would further the understanding of the oxidised particles investigation conducted throughout this project and how they occur within post processed powder.

Varying the shape of the builds and the processing parameters would allow a model to be produced and validate how the powder degradation mechanisms occurs and how the oxygen content varies across the powder bed and the potential impact it has on build quality. A simple model could feature single track scan with varied process parameters such as energy density and progress onto complex geometries with thin and thick-walled applications.

### **9.2.2 The impact of sub yellow coloured powder on tensile properties**

Furthermore, this project specifically investigated the impact of three separate builds: control, yellow and blue. Further work would consider the impact of different oxygen content powder which have not produced an interference colours such as the sub yellow colours referred to throughout this research and investigate the impact of these particles within a doped layer of a tensile build. The sub yellow particles do not display a distinct colour as the oxide layer thickness is not large enough, however they have an increased oxygen content compared to virgin. The difference in oxygen content is small and is within ASTM limits, however, it is important to understand the impact of these particles if they are incorporated into a build as the majority of the post processed powder will consist of such particles. This will help define the lower limits of oxide level that are considered detrimental to the build.

Similar to the investigation conducted throughout this project, the powder could be thermally oxidised using a similar process used in this project. The powder could be blended with virgin to create a doped, out of specification layer within the build similar to that of the yellow and blue builds. Tensile testing would determine the mechanical properties and using electron microscopy, fracture analysis could determine the failure mode and nano hardness to determine changes in properties in the fractured area. It is important to note, additional analysis would be conducted that could not be done throughout this project due to machine constraints due to the COVID-19 pandemic. Micro-CT scanning could help understand the impact of porosity and lack of fusion within the 'as built' tensile specimens for the different oxygen content powders. This would have complemented the research within this project immensely as it would help understand whether the doped layer in the 'as built' part increased the localised

porosity of the doped and surrounding build layers. Additionally, more emphasis on the microstructure analysis would be conducted to understand the phase formed in the 'as built' part from the increased oxygen content powders. Electron backscatter diffraction (EBSD) would be used to understand the grain structure of the built part and electron probe micro analyser (EPMA) would be used to detect the elements present. EPMA would complement the EDX analysis well as measuring light elements such as oxygen quantitatively is extremely difficult, therefore having two separate analyses investigate the oxygen content within the titanium matrix increases the validity of the results.

### **9.2.3 Controlling oxide formation and disrupting oxide in the build process**

The results from this investigation have shown that oxidised particles can present both mechanical flaws as un-fused particles embedded within the build layers and can also present chemical flaws as it locally changes the mechanical properties of the build. Further work is required to understand methods to control oxide formation in Ti-6Al-4V SLM builds alongside understanding whether it is possible to negate the effects of the results shown in this project.

Understanding the impact of varied process parameters on the processing of powder beds with oxidised particles may be a good starting point into controlling the oxide formation and disruption within the build process. Higher energy density and low scan speeds potentially may vaporise some of the oxide layer on the particle surface and reduce the effects it may have as a mechanical and chemical flaw within the build. However, in order to fully understand and try to control oxide formation, further investigations of the powder feedstock, build environment and post processing operations need to take place to determine how best to control or remove problematic particles.

However, although important, the research work suggested here is both costly and time consuming, as the AM industry is moving fast towards serial production, a solution to monitor oxidised particles is needed. A potential solution for industry in the short term is to develop a method of imaging the powder bed and identifying particles that

are different from the bulk. This research has formed the basis for a quality control methodology through the use of interference colours to correlate an oxygen wt %, if a system can identify these coloured particles in post processed powder, then this would allow users to make decisions on whether or not to use the powder. That being said, further research would need to occur to find a solution to remove these individual particles and this may resort back to the earlier suggestion of understanding how to control the oxides once they occur within the post processed powder and finding ways to negate their effects.

### **9.3 Key contribution of the thesis**

Research into the impact of oxidised Ti-6Al-4V powder particles have on the final built part mechanical properties processed by SLM are best summarised in three main sections. Firstly, the characterisation of the thermally oxidised powder particles on both the bulk and particle level, as discussed in chapter 4 and 5, provides insights into how they differ from virgin powder and the problems they may present on a layer-by-layer basis within an SLM build. Secondly, the investigation of the fracture behaviour and microstructural changes present within the build, provides an insight into the impact the oxidised particles have as a mechanical flaw within the build, as discussed in chapter 6. Finally, the investigation into the effect the oxidised particles have as a chemical flaw within the build by understanding the oxygen dissolution of both the fracture and surrounding build layers, as discussed in chapter 7, give insights into localised changes in mechanical properties of the final built part.

This work has shown that oxidised particles are a real concern for the AM industry as they move towards the serial production of parts using Ti-6Al-4V as they can detrimentally affect the mechanical properties of the final built component. That being said, this work also highlights the fact that these problematic particles can be identified using interference colours as a reference point to correlate an oxygen wt % to them. This is highly important to the AM industry as quality control of powder is essential, especially for load critical parts where part consistency and predictability is crucial for safety standards. Therefore, the key contribution of this work is forming the basis for a quality control system to be developed based on the findings of the investigations

conducted throughout the project. Although further investigation of the powder chemical composition is needed to increase the statistical confidence of the oxygen wt % ranges, the interference colour can be used as a benchmark to identify problematic problems in post processed powder.




Ideally an in-situ system imaging system on a layer-by-layer basis would identify oxidised particles which could instruct the wiper blade to potentially remove the deposited layer prior to laser melting the respective layer and redeposit a fresh layer of feedstock powder. However, this would require significant research and collaboration from machine manufacturers to ensure all the relevant operations worked. It's worth noting that this will only work if the amounts of oxidised particles in the post processed powder is low enough.

On the other hand, a simpler solution would be to utilise a desktop imaging system where the powder sampling vials commonly used by industry now in recycling regimes is imaged using a camera system and software identifies the problematic particles.

In terms of the optimal action taken once the particles are identified is yet to be determined by further research, however, this forms the basis for the first quality control system for identifying oxidised particles in post processed powder without the time consuming and costly use of numerous SEM images and chemical analysis. This would further boost user confidence in processing Ti-6Al-4V for serial production by reducing the time needed to make decisions on powder quality and reduce the cost of various types of analysis typically conducted in current industrial powder recycling regimes.

# 10 Appendix

Table 10: Summary of pre-built tensile bars and measurement of fracture location

<p>As-built Virgin tensile bar</p>	 A photograph showing six cylindrical, grey, textured tensile bars arranged horizontally. Each bar has a slightly wider diameter at its ends, which are equipped with small metal grips for testing.
<p>As-built yellow tensile bar</p>	 A photograph showing six cylindrical, grey, textured tensile bars arranged horizontally. Each bar has a slightly wider diameter at its ends, which are equipped with small metal grips for testing.
<p>As-built blue tensile bar</p>	 A photograph showing six cylindrical, grey, textured tensile bars arranged horizontally. Each bar has a slightly wider diameter at its ends, which are equipped with small metal grips for testing.

Virgin tensile bar with fracture length measurement



Virgin tensile bar with fracture length measurement



Virgin tensile bar with fracture length measurement



Yellow tensile bar with fracture length measurement



Yellow tensile bar with fracture length measurement



Yellow tensile bar with fracture length measurement



Blue tensile bar with fracture length measurement



Blue tensile bar with fracture length measurement





Blue tensile  
bar with  
fracture  
length  
measurement



## 11 References

- [1] R. Bogue, "3D printing: the dawn of a new era in manufacturing?," *Assem. Autom.*, vol. 33, no. 4, pp. 307–311, Jan. 2013, doi: 10.1108/AA-06-2013-055.
- [2] A. Gisario, M. Kazarian, F. Martina, and M. Mehrpouya, "Metal additive manufacturing in the commercial aviation industry: A review," *J. Manuf. Syst.*, vol. 53, pp. 124–149, 2019, doi: <https://doi.org/10.1016/j.jmsy.2019.08.005>.
- [3] E. Larrañeta, J. Dominguez-Robles, and D. A. Lamprou, "Additive Manufacturing Can Assist in the Fight Against COVID-19 and Other Pandemics and Impact on the Global Supply Chain," *3D Print. Addit. Manuf.*, vol. 7, no. 3, pp. 100–103, Apr. 2020, doi: 10.1089/3dp.2020.0106.
- [4] M.J.Donachie, "Titanium: A Technical Guide," *ASM Int.*, 2000.
- [5] B. Meier *et al.*, "Effect of the reuse of powder on material properties of Ti6Al4V processed by SLM," *AIP Conf. Proc.*, vol. 2113, no. July, 2019, doi: 10.1063/1.5112682.
- [6] M. Velasco-Castro, E. Hernández-Nava, I. A. Figueroa, I. Todd, and R. Goodall, "The effect of oxygen pickup during selective laser melting on the microstructure and mechanical properties of Ti–6Al–4V lattices," *Heliyon*, vol. 5, no. 12, 2019, doi: 10.1016/j.heliyon.2019.e02813.
- [7] M. Shiomi, K. Osakada, K. Nakamura, T. Yamashita, and F. Abe, "Residual stress within metallic model made by selective laser melting process," *CIRP Ann. - Manuf. Technol.*, vol. 53, no. 1, pp. 195–198, 2004, doi: 10.1016/S0007-8506(07)60677-5.
- [8] N. J. Harrison, I. Todd, and K. Mumtaz, "Reduction of micro-cracking in nickel superalloys processed by Selective Laser Melting: A fundamental alloy design approach," *Acta Mater.*, vol. 94, pp. 59–68, 2015, doi: 10.1016/j.actamat.2015.04.035.
- [9] T. N. K. *et al.*, "Balling processes during selective laser treatment of powders," *Rapid Prototyp. J.*, vol. 10, no. 2, pp. 78–87, Jan. 2004, doi: 10.1108/13552540410526953.
- [10] M. Goldberg, M. Shunmugavel, R. Singh, A. Polishetty, and G. Littlefair, "A comparative study of mechanical properties and machinability of wrought and additive manufactured (selective laser melting) titanium alloy – Ti-6Al-4V," *Rapid Prototyp. J.*, vol. 23, no. 6, pp. 1051–1056, Jan. 2017, doi:

- 10.1108/RPJ-08-2015-0105.
- [11] H. Ali, L. Ma, H. Ghadbeigi, and K. Mumtaz, "In-situ residual stress reduction, martensitic decomposition and mechanical properties enhancement through high temperature powder bed pre-heating of Selective Laser Melted Ti6Al4V," *Mater. Sci. Eng. A*, vol. 695, no. April, pp. 211–220, 2017, doi: 10.1016/j.msea.2017.04.033.
  - [12] C. Y. Yap *et al.*, "Review of selective laser melting: Materials and applications," *Appl. Phys. Rev.*, vol. 2, no. 4, p. 41101, Dec. 2015, doi: 10.1063/1.4935926.
  - [13] D. W. Gibson, I., Stucker, B., Rosen, "Rapid prototyping to direct digital manufacturing," *Addit. Manuf. Technol.*, 2009.
  - [14] B. Vandenbroucke and J. Kruth, "Selective laser melting of biocompatible metals for rapid manufacturing of medical parts," *Rapid Prototyp. J.*, vol. 13, no. 4, pp. 196–203, Jan. 2007, doi: 10.1108/13552540710776142.
  - [15] D. Howie, "Big sister: High-powered Trent XWB-97," *the magazine Rolls Royce*, pp. 12–15.
  - [16] L. Thijs, F. Verhaeghe, T. Craeghs, J. Van Humbeeck, and J.-P. Kruth, "A study of the microstructural evolution during selective laser melting of Ti–6Al–4V," *Acta Mater.*, vol. 58, no. 9, pp. 3303–3312, 2010, doi: <https://doi.org/10.1016/j.actamat.2010.02.004>.
  - [17] I. Yadroitsev, P. Bertrand, and I. Smurov, "Parametric analysis of the selective laser melting process," *Appl. Surf. Sci.*, vol. 253, no. 19, pp. 8064–8069, 2007, doi: <https://doi.org/10.1016/j.apsusc.2007.02.088>.
  - [18] B. Liu, B.-Q. Li, and Z. Li, "Selective laser remelting of an additive layer manufacturing process on AlSi10Mg," *Results Phys.*, vol. 12, pp. 982–988, 2019, doi: <https://doi.org/10.1016/j.rinp.2018.12.018>.
  - [19] P. J. Withers and H. K. D. H. Bhadeshia, "Residual stress. Part 1 – Measurement techniques," *Mater. Sci. Technol.*, vol. 17, no. 4, pp. 355–365, Apr. 2001, doi: 10.1179/026708301101509980.
  - [20] M. Peter and K. Jean-Pierre, "Residual stresses in selective laser sintering and selective laser melting," *Rapid Prototyp. J.*, vol. 12, no. 5, pp. 254–265, Jan. 2006, doi: 10.1108/13552540610707013.
  - [21] R. J. Moat, A. J. Pinkerton, L. Li, P. J. Withers, and M. Preuss, "Residual stresses in laser direct metal deposited Waspaloy," *Mater. Sci. Eng. A*, vol. 528, no. 6, pp. 2288–2298, 2011, doi:

<https://doi.org/10.1016/j.msea.2010.12.010>.

- [22] N. Biswas, J. L. Ding, V. K. Balla, D. P. Field, and A. Bandyopadhyay, "Deformation and fracture behavior of laser processed dense and porous Ti6Al4V alloy under static and dynamic loading," *Mater. Sci. Eng. A*, vol. 549, pp. 213–221, 2012, doi: 10.1016/j.msea.2012.04.036.
- [23] Y.-L. Hao, S.-J. Li, and R. Yang, "Biomedical titanium alloys and their additive manufacturing," *Rare Met.*, vol. 35, no. 9, pp. 661–671, 2016, doi: 10.1007/s12598-016-0793-5.
- [24] L. Ciocca, M. Fantini, F. De Crescenzo, G. Corinaldesi, and R. Scotti, "Direct metal laser sintering (DMLS) of a customized titanium mesh for prosthetically guided bone regeneration of atrophic maxillary arches," *Med. Biol. Eng. Comput.*, vol. 49, no. 11, pp. 1347–1352, 2011, doi: 10.1007/s11517-011-0813-4.
- [25] R. Morgan, C. J. Sutcliffe, and W. O'Neill, "Density analysis of direct metal laser re-melted 316L stainless steel cubic primitives," *J. Mater. Sci.*, vol. 39, no. 4, pp. 1195–1205, 2004, doi: 10.1023/B:JMSE.0000013875.62536.fa.
- [26] K. A. Mumtaz, P. Erasenthiran, and N. Hopkinson, "High density selective laser melting of Waspaloy®," *J. Mater. Process. Technol.*, vol. 195, no. 1–3, pp. 77–87, 2008, doi: 10.1016/j.jmatprotec.2007.04.117.
- [27] H. Galarraga, D. A. Lados, R. R. Dehoff, M. M. Kirka, and P. Nandwana, "Effects of the microstructure and porosity on properties of Ti-6Al-4V ELI alloy fabricated by electron beam melting (EBM)," *Addit. Manuf.*, vol. 10, no. May 2018, pp. 47–57, 2016, doi: 10.1016/j.addma.2016.02.003.
- [28] T. Vilaro, C. Colin, and J. D. Bartout, "As-Fabricated and Heat-Treated Microstructures of the Ti-6Al-4V Alloy Processed by Selective Laser Melting," *Metall. Mater. Trans. A*, vol. 42, no. 10, pp. 3190–3199, 2011, doi: 10.1007/s11661-011-0731-y.
- [29] S. Tammam-Williams, H. Zhao, F. Léonard, F. Derguti, I. Todd, and P. B. Prangnell, "XCT analysis of the influence of melt strategies on defect population in Ti-6Al-4V components manufactured by Selective Electron Beam Melting," *Mater. Charact.*, vol. 102, pp. 47–61, 2015, doi: <https://doi.org/10.1016/j.matchar.2015.02.008>.
- [30] P.-H. Li, W.-G. Guo, W.-D. Huang, Y. Su, X. Lin, and K.-B. Yuan, "Thermomechanical response of 3D laser-deposited Ti-6Al-4V alloy over a

- wide range of strain rates and temperatures,” *Mater. Sci. Eng. A*, vol. 647, pp. 34–42, 2015, doi: <https://doi.org/10.1016/j.msea.2015.08.043>.
- [31] Y. Yang and H. C. Man, “Microstructure evolution of laser clad layers of W–C–Co alloy powders1This paper is sponsored by The Natural Science Foundation of Guangdong Province, China.1,” *Surf. Coatings Technol.*, vol. 132, no. 2, pp. 130–136, 2000, doi: [https://doi.org/10.1016/S0257-8972\(00\)00909-9](https://doi.org/10.1016/S0257-8972(00)00909-9).
- [32] L. Rickenbacher, T. Etter, S. Hövel, and K. Wegener, “High temperature material properties of IN738LC processed by selective laser melting (SLM) technology,” *Rapid Prototyp. J.*, vol. 19, Jun. 2013, doi: [10.1108/13552541311323281](https://doi.org/10.1108/13552541311323281).
- [33] S. Shrestha, T. Starr, and K. Chou, “A Study of Keyhole Porosity in Selective Laser Melting: Single-Track Scanning with Micro-CT Analysis,” *J. Manuf. Sci. Eng. Trans. ASME*, vol. 141, no. 7, 2019, doi: [10.1115/1.4043622](https://doi.org/10.1115/1.4043622).
- [34] G. Kasperovich, J. Haubrich, J. Gussone, and G. Requena, “Correlation between porosity and processing parameters in TiAl6V4 produced by selective laser melting,” *Mater. Des.*, vol. 112, pp. 160–161, 2016, doi: [10.1016/j.matdes.2016.09.040](https://doi.org/10.1016/j.matdes.2016.09.040).
- [35] J. P. Kruth, L. Froyen, J. Van Vaerenbergh, P. Mercelis, M. Rombouts, and B. Lauwers, “Selective laser melting of iron-based powder,” *J. Mater. Process. Technol.*, vol. 149, no. 1–3, pp. 616–622, 2004, doi: [10.1016/j.jmatprotec.2003.11.051](https://doi.org/10.1016/j.jmatprotec.2003.11.051).
- [36] D. Gu *et al.*, “Densification behavior, microstructure evolution, and wear performance of selective laser melting processed commercially pure titanium,” *Acta Mater.*, vol. 60, no. 9, pp. 3849–3860, 2012, doi: [10.1016/j.actamat.2012.04.006](https://doi.org/10.1016/j.actamat.2012.04.006).
- [37] M. Ikeda, S. Y. Komatsu, and Y. Nakamura, “Effects of Sn and Zr additions on phase constitution and aging behavior of Ti-50mass% Ta alloys quenched from  $\beta$  single phase region,” *Mater. Trans.*, vol. 45, no. 4, pp. 1106–1112, 2004, doi: [10.2320/matertrans.45.1106](https://doi.org/10.2320/matertrans.45.1106).
- [38] J. Liu, D. dong Gu, H. yu Chen, D. hua Dai, and H. Zhang, “Influence of substrate surface morphology on wetting behavior of tracks during selective laser melting of aluminum-based alloys,” *J. Zhejiang Univ. Sci. A*, vol. 19, no. 2, pp. 111–121, 2018, doi: [10.1631/jzus.A1700599](https://doi.org/10.1631/jzus.A1700599).
- [39] R. Li, J. Liu, Y. Shi, L. Wang, and W. Jiang, “Balling behavior of stainless steel

- and nickel powder during selective laser melting process,” *Int. J. Adv. Manuf. Technol.*, vol. 59, no. 9–12, pp. 1025–1035, 2012, doi: 10.1007/s00170-011-3566-1.
- [40] S. Das, “Physical Aspects of Process Control in Selective Laser Sintering of Metals,” *Adv. Eng. Mater.*, vol. 5, no. 10, pp. 701–711, Oct. 2003, doi: <https://doi.org/10.1002/adem.200310099>.
- [41] E. Santecchia, S. Spigarelli, and M. Cabibbo, “Material reuse in laser powder bed fusion: Side effects of the laser—metal powder interaction,” *Metals (Basel)*, vol. 10, no. 3, pp. 1–21, 2020, doi: 10.3390/met10030341.
- [42] C. L. A. Leung, S. Marussi, M. Towrie, R. C. Atwood, P. J. Withers, and P. D. Lee, “The effect of powder oxidation on defect formation in laser additive manufacturing,” *Acta Mater.*, vol. 166, pp. 294–305, 2019, doi: 10.1016/j.actamat.2018.12.027.
- [43] D. Powell, A. E. W. Rennie, L. Geekie, and N. Burns, “Understanding powder degradation in metal additive manufacturing to allow the upcycling of recycled powders,” *J. Clean. Prod.*, vol. 268, no. July, 2020, doi: 10.1016/j.jclepro.2020.122077.
- [44] M. Barclift, S. Joshi, T. Simpson, and C. Dickman, “Cost Modeling and Depreciation for Reused Powder Feedstocks in Powder Bed Fusion Additive Manufacturing,” 2016.
- [45] A. H. Maamoun, M. Elbestawi, G. K. Dosbaeva, and S. C. Veldhuis, “Thermal post-processing of AlSi10Mg parts produced by Selective Laser Melting using recycled powder,” *Addit. Manuf.*, vol. 21, pp. 234–247, 2018, doi: <https://doi.org/10.1016/j.addma.2018.03.014>.
- [46] L. Cordova, M. Campos, and T. Tinga, “Revealing the Effects of Powder Reuse for Selective Laser Melting by Powder Characterization,” *Jom*, vol. 71, no. 3, pp. 1062–1072, 2019, doi: 10.1007/s11837-018-3305-2.
- [47] R. Harkin, H. Wu, S. Nikam, J. Quinn, and S. McFadden, “Reuse of grade 23 ti6al4v powder during the laser-based powder bed fusion process,” *Metals (Basel)*, vol. 10, no. 12, pp. 1–14, 2020, doi: 10.3390/met10121700.
- [48] H. P. Tang, M. Qian, N. Liu, X. Z. Zhang, G. Y. Yang, and J. Wang, “Effect of Powder Reuse Times on Additive Manufacturing of Ti-6Al-4V by Selective Electron Beam Melting,” *Jom*, vol. 67, no. 3, pp. 555–563, 2015, doi: 10.1007/s11837-015-1300-4.

- [49] J. H. Martin, B. D. Yahata, J. M. Hundley, J. A. Mayer, T. A. Schaedler, and T. M. Pollock, "3D printing of high-strength aluminium alloys," *Nature*, vol. 549, no. 7672, pp. 365–369, 2017, doi: 10.1038/nature23894.
- [50] N. Kaufmann, M. Imran, T. M. Wischeropp, C. Emmelmann, S. Siddique, and F. Walther, "Influence of Process Parameters on the Quality of Aluminium Alloy EN AW 7075 Using Selective Laser Melting (SLM)," *Phys. Procedia*, vol. 83, pp. 918–926, 2016, doi: <https://doi.org/10.1016/j.phpro.2016.08.096>.
- [51] H. Zhang, H. Zhu, T. Qi, Z. Hu, and X. Zeng, "Selective laser melting of high strength Al–Cu–Mg alloys: Processing, microstructure and mechanical properties," *Mater. Sci. Eng. A*, vol. 656, pp. 47–54, 2016, doi: <https://doi.org/10.1016/j.msea.2015.12.101>.
- [52] T. Qi, H. Zhu, H. Zhang, J. Yin, L. Ke, and X. Zeng, "Selective laser melting of Al7050 powder: Melting mode transition and comparison of the characteristics between the keyhole and conduction mode," *Mater. Des.*, vol. 135, pp. 257–266, 2017, doi: <https://doi.org/10.1016/j.matdes.2017.09.014>.
- [53] Z. Sun, X. P. Tan, M. Descoins, D. Mangelinck, S. B. Tor, and C. S. Lim, "Revealing hot tearing mechanism for an additively manufactured high-entropy alloy via selective laser melting," *Scr. Mater.*, vol. 168, pp. 129–133, 2019, doi: 10.1016/j.scriptamat.2019.04.036.
- [54] H. Guleryuz and H. Cimenoglu, "Oxidation of Ti–6Al–4V alloy," *J. Alloys Compd.*, vol. 472, no. 1, pp. 241–246, 2009, doi: <https://doi.org/10.1016/j.jallcom.2008.04.024>.
- [55] H. P. TRIPP and B. W. KING, "Thermodynamic Data on Oxides at Elevated Temperatures," *J. Am. Ceram. Soc.*, vol. 38, no. 12, pp. 432–437, Dec. 1955, doi: <https://doi.org/10.1111/j.1151-2916.1955.tb14569.x>.
- [56] B. Sefer, "Oxidation and Alpha–Case Phenomena in Titanium Alloys used in Aerospace Industry: Ti–6Al–2Sn–4Zr–2Mo and Ti–6Al–4V," pp. 6–2, Accessed: Sep. 19, 2017. [Online]. Available: <https://www.diva-portal.org/smash/get/diva2:999194/FULLTEXT01.pdf>.
- [57] P. Kofstad, K. Hauffe, H. Kjoellesdal, P. Siekevitz, L. Ernster, and E. Diczfalusy, "Investigation on the Oxidation Mechanism of Titanium.," *Acta Chem. Scand.*, vol. 12, pp. 239–266, 1958.
- [58] B. G. Velasco and P. B. Aswath, "Microstructural stability, microhardness and oxidation behaviour of in situ reinforced Ti–8.5Al–1B–1Si (wt%)," *J. Mater.*

- Sci.*, vol. 33, no. 8, pp. 2203–2214, 1998, doi: 10.1023/A:1004395908966.
- [59] I. Gurrappa, D. Manova, J. Gerlach, S. Mändl, and B. Rauschenbach, “Influence of nitrogen implantation on the high temperature oxidation of titanium-base alloys,” *Surf. Coatings Technol. - SURF COAT TECH*, vol. 201, pp. 3536–3546, Dec. 2006, doi: 10.1016/j.surfcoat.2006.08.106.
- [60] S. Frangini, A. Mignone, and F. de Riccardis, “Various aspects of the air oxidation behaviour of a Ti6Al4V alloy at temperatures in the range 600–700 °C,” *J. Mater. Sci.*, vol. 29, no. 3, pp. 714–720, 1994, doi: 10.1007/BF00445984.
- [61] H. L. Du, P. K. Datta, D. B. Lewis, and J. S. Burnell-Gray, “Air oxidation behaviour of Ti6Al4V alloy between 650 and 850°,” *Corros. Sci.*, vol. 36, no. 4, pp. 631–642, 1994, doi: 10.1016/0010-938X(94)90069-8.
- [62] T. Mrowec, s. and Weber, *J. Electrochem Society*. 1970.
- [63] S. Van Gils, P. Mast, E. Stijns, and H. Terry, “Colour properties of barrier anodic oxide films on aluminium and titanium studied with total reflectance and spectroscopic ellipsometry,” *Surf. Coatings Technol.*, vol. 185, no. 2, pp. 303–310, 2004, doi: <https://doi.org/10.1016/j.surfcoat.2004.01.021>.
- [64] G. Napoli, M. Paura, T. Vela, and A. Di Schino, “Colouring titanium alloys by anodic oxidation,” *Anal. Zavoda za Povij. Znan. Hrvat. Akad. Znan. i Umjet. u Dubrovniku*, vol. 57, no. 1–2, pp. 111–113, 2018.
- [65] M. V. Diamanti, B. Del Curto, and M. P. Pedefferri, “Interference colors of thin oxide layers on titanium,” *Color Res. Appl.*, vol. 33, no. 3, pp. 221–228, 2008, doi: 10.1002/col.20403.
- [66] F. Bryant, “Snell’s Law of Refraction,” *Phys. Bull.*, vol. 9, no. 12, p. 317, 1958, doi: 10.1088/0031-9112/9/12/004.
- [67] J. Pojman *et al.*, “Snell’s law of refraction observed in thermal frontal polymerization,” *Chaos*, vol. 17, p. 33125, Oct. 2007, doi: 10.1063/1.2784386.
- [68] G. Lütjering and J. C. Williams, Eds., “Special Properties and Applications of Titanium BT - Titanium,” Berlin, Heidelberg: Springer Berlin Heidelberg, 2007, pp. 383–415.
- [69] M. Shao, S. Vijayan, P. Nandwana, and J. R. Jinschek, “The effect of beam scan strategies on microstructural variations in Ti-6Al-4V fabricated by electron beam powder bed fusion,” *Mater. Des.*, vol. 196, p. 109165, 2020, doi: <https://doi.org/10.1016/j.matdes.2020.109165>.



- [70] E. A. Bel'skaya and E. Y. Kulyamina, "Electrical resistivity of titanium in the temperature range from 290 to 1800 K," *High Temp.*, vol. 45, no. 6, pp. 785–796, 2007, doi: 10.1134/S0018151X07060090.
- [71] D. Eylon, S. Fujishiro, P. Postans, and F. Froes, "High-Temperature Titanium Alloys—A Review," *JOM*, vol. 36, pp. 55–62, Nov. 2013, doi: 10.1007/BF03338617.
- [72] D. Banerjee and J. C. Williams, "Perspectives on Titanium Science and Technology," *Acta Mater.*, vol. 61, no. 3, pp. 844–879, 2013, doi: <https://doi.org/10.1016/j.actamat.2012.10.043>.
- [73] H. Shao, D. Shan, Y. Zhao, P. Ge, and W. Zeng, "Accordance between fracture toughness and strength difference in TC21 titanium alloy with equiaxed microstructure," *Mater. Sci. Eng. A*, vol. 664, pp. 10–16, 2016, doi: <https://doi.org/10.1016/j.msea.2016.02.088>.
- [74] R. Banerjee, D. Bhattacharyya, P. C. Collins, G. B. Viswanathan, and H. L. Fraser, "Precipitation of grain boundary  $\alpha$  in a laser deposited compositionally graded Ti–8Al–xV alloy – an orientation microscopy study," *Acta Mater.*, vol. 52, no. 2, pp. 377–385, 2004, doi: <https://doi.org/10.1016/j.actamat.2003.09.038>.
- [75] T. Ahmed and H. J. Rack, "Phase transformations during cooling in  $\alpha+\beta$  titanium alloys," *Mater. Sci. Eng. A*, vol. 243, no. 1, pp. 206–211, 1998, doi: [https://doi.org/10.1016/S0921-5093\(97\)00802-2](https://doi.org/10.1016/S0921-5093(97)00802-2).
- [76] F. X. Gil Mur, D. Rodríguez, and J. A. Planell, "Influence of tempering temperature and time on the  $\alpha'$ -Ti-6Al-4V martensite," *J. Alloys Compd.*, vol. 234, no. 2, pp. 287–289, 1996, doi: [https://doi.org/10.1016/0925-8388\(95\)02057-8](https://doi.org/10.1016/0925-8388(95)02057-8).
- [77] U. Reisgen, S. Olschok, R. Sharma, and S. Gach, "Influence on martensite-start-temperature and volume expansion of low-transformation-temperature materials used for residual stress relief in beam welding," *Materwiss. Werksttech.*, vol. 48, no. 12, pp. 1276–1282, Dec. 2017, doi: <https://doi.org/10.1002/mawe.201700159>.
- [78] J. C. Lütjering, Gerd, Williams, "Titanium," *Eng. Mater. Process.*, no. 2nd ed, 2007.
- [79] N. Stanford and P. S. Bate, "The Martensitic Transformation Texture in Ti-6Al-4V," *Mater. Sci. Forum*, vol. 495–497, pp. 669–674, 2005, doi:

10.4028/www.scientific.net/MSF.495-497.669.

- [80] C. M. Lee, C. P. Ju, and J. H. Chern Lin, "Structure–property relationship of cast Ti–Nb alloys," *J. Oral Rehabil.*, vol. 29, no. 4, pp. 314–322, Apr. 2002, doi: <https://doi.org/10.1046/j.1365-2842.2002.00825.x>.
- [81] H. Y. Kim and S. Miyazaki, "Martensitic transformation and superelastic properties of Ti-Nb base alloys," *Mater. Trans.*, vol. 56, no. 5, pp. 625–634, 2015, doi: [10.2320/matertrans.M2014454](https://doi.org/10.2320/matertrans.M2014454).
- [82] M. Tahara, H. Y. Kim, T. Inamura, H. Hosoda, and S. Miyazaki, "Lattice modulation and superelasticity in oxygen-added  $\beta$ -Ti alloys," *Acta Mater.*, vol. 59, no. 16, pp. 6208–6218, 2011, doi: [10.1016/j.actamat.2011.06.015](https://doi.org/10.1016/j.actamat.2011.06.015).
- [83] M. Tahara, T. Inamura, H. Y. Kim, S. Miyazaki, and H. Hosoda, "Role of oxygen atoms in  $\alpha'$  martensite of Ti-20at.% Nb alloy," *Scr. Mater.*, vol. 112, pp. 15–18, 2016, doi: <https://doi.org/10.1016/j.scriptamat.2015.08.033>.
- [84] R. Salloom, D. Reith, R. Banerjee, and S. G. Srinivasan, "First principles calculations on the effect of interstitial oxygen on phase stability and martensitic transformation in Ti–Nb alloys," *J. Mater. Sci.*, vol. 53, no. 16, pp. 11473–11487, 2018, doi: [10.1007/s10853-018-2381-6](https://doi.org/10.1007/s10853-018-2381-6).
- [85] R. R. Boyer, "An overview on the use of titanium in the aerospace industry," *Mater. Sci. Eng. A*, vol. 213, no. 1, pp. 103–114, 1996, doi: [https://doi.org/10.1016/0921-5093\(96\)10233-1](https://doi.org/10.1016/0921-5093(96)10233-1).
- [86] M. Peters, J. Kumpfert, C. H. Ward, and C. Leyens, "Titanium Alloys for Aerospace Applications," *Titanium and Titanium Alloys*, pp. 333–350, Jul. 28, 2003, doi: <https://doi.org/10.1002/3527602119.ch13>.
- [87] N. Kherrouba, M. Bouabdallah, R. Badji, D. Carron, and M. Amir, "Beta to alpha transformation kinetics and microstructure of Ti-6Al-4V alloy during continuous cooling," *Mater. Chem. Phys.*, vol. 181, pp. 462–469, 2016, doi: <https://doi.org/10.1016/j.matchemphys.2016.06.082>.
- [88] S. L. Semiatin, S. L. Knisley, P. N. Fagin, D. R. Barker, and F. Zhang, "Microstructure evolution during alpha-beta heat treatment of Ti-6Al-4V," *Metall. Mater. Trans. A*, vol. 34, no. 10, pp. 2377–2386, 2003, doi: [10.1007/s11661-003-0300-0](https://doi.org/10.1007/s11661-003-0300-0).
- [89] S. S. Al-Bermani, M. L. Blackmore, W. Zhang, and I. Todd, "The Origin of Microstructural Diversity, Texture, and Mechanical Properties in Electron Beam Melted Ti-6Al-4V," *Metall. Mater. Trans. A*, vol. 41, no. 13, pp. 3422–3434,

- 2010, doi: 10.1007/s11661-010-0397-x.
- [90] M. Simonelli, Y. Y. Tse, and C. Tuck, "Effect of the build orientation on the mechanical properties and fracture modes of SLM Ti-6Al-4V," *Mater. Sci. Eng. A*, vol. 616, pp. 1–11, 2014, doi: <https://doi.org/10.1016/j.msea.2014.07.086>.
- [91] H. Beladi, Q. Chao, and G. S. Rohrer, "Variant selection and intervariant crystallographic planes distribution in martensite in a Ti-6Al-4V alloy," *Acta Mater.*, vol. 80, pp. 478–489, 2014, doi: <https://doi.org/10.1016/j.actamat.2014.06.064>.
- [92] M. Simonelli, Y. Tse, and C. Tuck, "Further understanding of ti-6al-4v selective laser melting using texture analysis," *23rd Annu. Int. Solid Free. Fabr. Symp. - An Addit. Manuf. Conf. SFF 2012*, pp. 480–491, Jan. 2012.
- [93] Y. Li and D. Gu, "Parametric analysis of thermal behavior during selective laser melting additive manufacturing of aluminum alloy powder," *Mater. Des.*, vol. 63, pp. 856–867, 2014, doi: <https://doi.org/10.1016/j.matdes.2014.07.006>.
- [94] M. Muhammad, "Small-Scale Characterization Of Additive Manufactured Ti-6al-4v Alloy Through Instrumented Indentation," 2018.
- [95] X. Wu, J. Liang, J. Mei, C. Mitchell, P. S. Goodwin, and W. Voice, "Microstructures of laser-deposited Ti-6Al-4V," *Mater. Des.*, vol. 25, no. 2, pp. 137–144, 2004, doi: <https://doi.org/10.1016/j.matdes.2003.09.009>.
- [96] F. Wang, J. Mei, H. Jiang, and X. Wu, "Laser fabrication of Ti6Al4V/TiC composites using simultaneous powder and wire feed," *Mater. Sci. Eng. A*, vol. 445–446, pp. 461–466, 2007, doi: <https://doi.org/10.1016/j.msea.2006.09.093>.
- [97] M. Simonelli, Y. Y. Tse, and C. Tuck, "On the Texture Formation of Selective Laser Melted Ti-6Al-4V," *Metall. Mater. Trans. A*, vol. 45, no. 6, pp. 2863–2872, 2014, doi: 10.1007/s11661-014-2218-0.
- [98] M. Simonelli, Y. Y. Tse, and C. Tuck, "Microstructure of Ti-6Al-4V produced by selective laser melting," *J. Phys. Conf. Ser.*, vol. 371, 2012, doi: 10.1088/1742-6596/371/1/012084.
- [99] L. Wang, C. Ma, J. Huang, H. Y. Ding, and M. Q. Chu, "Microstructure and tensile properties of Ti-6Al-4V alloys manufactured by selective laser melting with optimized processing parameters," *IOP Conf. Ser. Mater. Sci. Eng.*, vol. 265, no. 1, pp. 0–5, 2017, doi: 10.1088/1757-899X/265/1/012015.
- [100] H. Gong, K. Rafi, H. Gu, G. D. Janaki Ram, T. Starr, and B. Stucker, "Influence

- of defects on mechanical properties of Ti-6Al-4V components produced by selective laser melting and electron beam melting,” *Mater. Des.*, vol. 86, pp. 545–554, 2015, doi: <https://doi.org/10.1016/j.matdes.2015.07.147>.
- [101] W. Xu, S. Sun, J. Elambasseril, Q. Liu, M. Brandt, and M. Qian, “Ti-6Al-4V Additively Manufactured by Selective Laser Melting with Superior Mechanical Properties,” *JOM*, vol. 67, no. 3, pp. 668–673, 2015, doi: [10.1007/s11837-015-1297-8](https://doi.org/10.1007/s11837-015-1297-8).
- [102] J. Yang, H. Yu, J. Yin, M. Gao, Z. Wang, and X. Zeng, “Formation and control of martensite in Ti-6Al-4V alloy produced by selective laser melting,” *Mater. Des.*, vol. 108, pp. 308–318, 2016, doi: [10.1016/j.matdes.2016.06.117](https://doi.org/10.1016/j.matdes.2016.06.117).
- [103] D. K. Do and P. Li, “The effect of laser energy input on the microstructure, physical and mechanical properties of Ti-6Al-4V alloys by selective laser melting,” *Virtual Phys. Prototyp.*, vol. 11, no. 1, pp. 41–47, 2016, doi: [10.1080/17452759.2016.1142215](https://doi.org/10.1080/17452759.2016.1142215).
- [104] L. Parry, I. A. Ashcroft, and R. D. Wildman, “Understanding the effect of laser scan strategy on residual stress in selective laser melting through thermo-mechanical simulation,” *Addit. Manuf.*, vol. 12, pp. 1–15, 2016, doi: <https://doi.org/10.1016/j.addma.2016.05.014>.
- [105] A. Popovich, V. Sufiiarov, E. Borisov, and I. Polozov, “Microstructure and mechanical properties of Ti-6Al-4V manufactured by SLM,” *Key Eng. Mater.*, vol. 651–653, no. January 2016, pp. 677–682, 2015, doi: [10.4028/www.scientific.net/KEM.651-653.677](https://doi.org/10.4028/www.scientific.net/KEM.651-653.677).
- [106] A. International, “ASTM F2924 - 14 Standard Specification for Additive Manufacturing Titanium-6 Aluminum-4 Vanadium with Powder Bed Fusion,” 2014. .
- [107] A. M. Khorasani, I. Gibson, U. S. Awan, and A. Ghaderi, “The effect of SLM process parameters on density, hardness, tensile strength and surface quality of Ti-6Al-4V,” *Addit. Manuf.*, vol. 25, no. September, pp. 176–186, 2019, doi: [10.1016/j.addma.2018.09.002](https://doi.org/10.1016/j.addma.2018.09.002).
- [108] S. S. da Rocha, G. L. Adabo, G. E. P. Henriques, and M. A. de A. Nã\\textthreesuperiorbilo, “Vickers hardness of cast commercially pure titanium and Ti-6Al-4V alloy submitted to heat treatments,” *Braz. Dent. J.*, vol. 17, pp. 126–129, 2006, [Online]. Available: [http://www.scielo.br/scielo.php?script=sci\\_arttext&pid=S0103-](http://www.scielo.br/scielo.php?script=sci_arttext&pid=S0103-)

64402006000200008&nrm=iso.

- [109] A. International, "Standard specification for titanium and titanium alloy wire," *ASTM Int.*, vol. B863-10, 2010.
- [110] W. L. Finlay and J. A. Snyder, "Effects of three interstitial solutes (nitrogen, oxygen, and carbon) on the mechanical properties of high-purity, alpha titanium," *JOM*, vol. 2, no. 2, pp. 277–286, 1950, doi: 10.1007/BF03399001.
- [111] R. I. Jafee, "No Title," pp. 1665–1693, 1980.
- [112] J. M. Oh, B. G. Lee, S. W. Cho, S. W. Lee, G. S. Choi, and J. W. Lim, "Oxygen effects on the mechanical properties and lattice strain of Ti and Ti-6Al-4V," *Met. Mater. Int.*, vol. 17, no. 5, pp. 733–736, 2011, doi: 10.1007/s12540-011-1006-2.
- [113] S. Yamaguchi, "Interstitial Order-Disorder Transformation in the Ti-O Solid Solution. I. Ordered Arrangement of Oxygen," *J. Phys. Soc. Japan*, vol. 27, no. 1, pp. 155–163, Jul. 1969, doi: 10.1143/JPSJ.27.155.
- [114] I. I. Kornilov, "Effect of oxygen on titanium and its alloys," *Met. Sci. Heat Treat.*, vol. 15, no. 10, pp. 826–829, 1973, doi: 10.1007/BF00656056.
- [115] C. Wagner, *Diffusion in Solids, Liquids, Gases*, W. Jost, Ed. New York, 1952.
- [116] R. Gaddam, B. Sefer, R. Pederson, and M.-L. Antti, "Study of alpha-case depth in Ti-6Al-2Sn-4Zr-2Mo and Ti-6Al-4V," *IOP Conf. Ser. Mater. Sci. Eng.*, vol. 48, p. 12002, 2013, doi: 10.1088/1757-899x/48/1/012002.
- [117] R. Gaddam, B. Sefer, R. Pederson, and M.-L. Antti, "Oxidation and alpha-case formation in Ti-6Al-2Sn-4Zr-2Mo alloy," *Mater. Charact.*, vol. 99, pp. 166–174, 2015, doi: <https://doi.org/10.1016/j.matchar.2014.11.023>.
- [118] Y. Mishin and C. Herzig, "Diffusion in the Ti-Al system," *Acta Mater.*, vol. 48, no. 3, pp. 589–623, 2000, doi: 10.1016/S1359-6454(99)00400-0.
- [119] J. C. Slater, "Atomic radii in crystals," *J. Chem. Phys.*, vol. 41, no. 10, pp. 3199–3204, 1964, doi: 10.1063/1.1725697.
- [120] S. Dietrich, M. Wunderer, A. Huissel, and M. F. Zaeh, "A New Approach for a Flexible Powder Production for Additive Manufacturing," *Procedia Manuf.*, vol. 6, pp. 88–95, 2016, doi: 10.1016/j.promfg.2016.11.012.
- [121] A. J. Yule and J. J. Dunkley, *Atomization of melts for powder production and spray deposition*. Oxford; New York: Clarendon Press ; Oxford University Press, 1994.
- [122] A. S. Baskoro, S. Supriadi, and Dharmanto, "Review on Plasma Atomizer

- Technology for Metal Powder,” *MATEC Web Conf.*, vol. 269, p. 05004, 2019, doi: 10.1051/matecconf/201926905004.
- [123] A. Gatto, E. Bassoli, and L. Denti, “Repercussions of powder contamination on the fatigue life of additive manufactured maraging steel,” *Addit. Manuf.*, vol. 24, no. May, pp. 13–19, 2018, doi: 10.1016/j.addma.2018.09.004.
- [124] C. Pauzon, P. Forêt, E. Hryha, T. Arunprasad, and L. Nyborg, “Argon-helium mixtures as Laser-Powder Bed Fusion atmospheres: Towards increased build rate of Ti-6Al-4V,” *J. Mater. Process. Technol.*, vol. 279, no. December 2019, p. 116555, 2020, doi: 10.1016/j.jmatprotec.2019.116555.
- [125] T. Grünberger and R. Domröse, “Direct Metal Laser Sintering: Identification of process phenomena by optical in-process monitoring,” *Laser Tech. J.*, vol. 12, no. 1, pp. 45–48, 2015, doi: 10.1002/latj.201500007.
- [126] T. Fuhrich, P. Berger, and H. Hügel, “Marangoni effect in laser deep penetration welding of steel,” *J. Laser Appl.*, vol. 13, no. 5, pp. 178–186, 2001, doi: 10.2351/1.1404412.
- [127] E. Ahmadi and A. R. Ebrahimi, “Welding of 316L Austenitic Stainless Steel with Activated Tungsten Inert Gas Process,” *J. Mater. Eng. Perform.*, vol. 24, no. 2, pp. 1065–1071, 2015, doi: 10.1007/s11665-014-1336-6.
- [128] A. Kidess, S. Kenjereš, B. W. Righolt, and C. R. Kleijn, “Marangoni driven turbulence in high energy surface melting processes,” *Int. J. Therm. Sci.*, vol. 104, pp. 412–422, 2016, doi: 10.1016/j.ijthermalsci.2016.01.015.
- [129] B. J. Keene, K. C. Mills, and R. F. Brooks, “Surface properties of liquid metals and their effects on weldability,” *Mater. Sci. Technol.*, vol. 1, no. 7, pp. 559–567, Jul. 1985, doi: 10.1179/mst.1985.1.7.559.
- [130] T. N. Le and Y. L. Lo, “Effects of sulfur concentration and Marangoni convection on melt-pool formation in transition mode of selective laser melting process,” *Mater. Des.*, vol. 179, 2019, doi: 10.1016/j.matdes.2019.107866.
- [131] M. J. Matthews, G. Guss, S. A. Khairallah, A. M. Rubenchik, P. J. Depond, and W. E. King, “Denudation of metal powder layers in laser powder bed fusion processes,” *Acta Mater.*, vol. 114, pp. 33–42, 2016, doi: 10.1016/j.actamat.2016.05.017.
- [132] S. Ly, A. M. Rubenchik, S. A. Khairallah, G. Guss, and M. J. Matthews, “Metal vapor micro-jet controls material redistribution in laser powder bed fusion additive manufacturing,” *Sci. Rep.*, vol. 7, no. 1, p. 4085, 2017, doi:

10.1038/s41598-017-04237-z.

- [133] L. E. Criales, Y. M. Arisoy, B. Lane, S. Moylan, A. Donmez, and T. Özel, “Laser powder bed fusion of nickel alloy 625: Experimental investigations of effects of process parameters on melt pool size and shape with spatter analysis,” *Int. J. Mach. Tools Manuf.*, vol. 121, no. September 2016, pp. 22–36, 2017, doi: 10.1016/j.ijmachtools.2017.03.004.
- [134] A. T. Sutton, C. S. Kriewall, M. C. Leu, J. W. Newkirk, and B. Brown, “Characterization of laser spatter and condensate generated during the selective laser melting of 304L stainless steel powder,” *Addit. Manuf.*, vol. 31, no. March 2019, p. 100904, 2020, doi: 10.1016/j.addma.2019.100904.
- [135] M. Simonelli *et al.*, “A Study on the Laser Spatter and the Oxidation Reactions During Selective Laser Melting of 316L Stainless Steel, Al-Si10-Mg, and Ti-6Al-4V,” *Metall. Mater. Trans. A Phys. Metall. Mater. Sci.*, vol. 46, no. 9, pp. 3842–3851, 2015, doi: 10.1007/s11661-015-2882-8.
- [136] V. Gunenthiram, P. Peyre, M. Schneider, M. Dal, F. Coste, and R. Fabbro, “Analysis of laser–melt pool–powder bed interaction during the selective laser melting of a stainless steel,” *J. Laser Appl.*, vol. 29, no. 2, p. 022303, 2017, doi: 10.2351/1.4983259.
- [137] Y. Liu, Y. Yang, S. Mai, D. Wang, and C. Song, “Investigation into spatter behavior during selective laser melting of AISI 316L stainless steel powder,” *Mater. Des.*, vol. 87, pp. 797–806, 2015, doi: 10.1016/j.matdes.2015.08.086.
- [138] J. Yin *et al.*, “High-power laser-matter interaction during laser powder bed fusion,” *Additive Manufacturing*, vol. 29. 2019, doi: 10.1016/j.addma.2019.100778.
- [139] J. H. Tan, W. L. E. Wong, and K. W. Dalgarno, “An overview of powder granulometry on feedstock and part performance in the selective laser melting process,” *Addit. Manuf.*, vol. 18, pp. 228–255, 2017, doi: <https://doi.org/10.1016/j.addma.2017.10.011>.
- [140] L. Ji, C. Wang, W. Wu, C. Tan, G. Wang, and X.-M. Duan, “Spheroidization by Plasma Processing and Characterization of Stainless Steel Powder for 3D Printing,” *Metall. Mater. Trans. A*, vol. 48, no. 10, pp. 4831–4841, 2017, doi: 10.1007/s11661-017-4240-5.
- [141] A. D. Brandão *et al.*, “Challenges in Additive Manufacturing of space parts: Powder feedstock cross-contamination and its impact on end products,”

- Materials (Basel)*., vol. 10, no. 5, 2017, doi: 10.3390/ma10050522.
- [142] E. Santecchia, P. Mengucci, A. Gatto, E. Bassoli, S. Defanti, and G. Barucca, "Cross-Contamination Quantification in Powders for Additive Manufacturing: A Study on Ti-6Al-4V and Maraging Steel," *Materials* , vol. 12, no. 15. 2019, doi: 10.3390/ma12152342.
- [143] A. International, "ASTM E1409-13," *Standard Test Method for Determination of Oxygen and Nitrogen in Titanium and Titanium Alloys by Inert Gas Fusion*, 2013. .
- [144] M. Panalytical, "Mastersizer 3000," 2021.  
<https://www.malvernpanalytical.com/en/products/product-range/mastersizer-range/mastersizer-3000-version-B> (accessed Aug. 18, 2021).
- [145] F. A. S. Lucille A. Giannuzzi, *Introduction to Focused Ion Beams*. .
- [146] M. Schaffer, B. Schaffer, and Q. Ramasse, "Sample preparation for atomic-resolution STEM at low voltages by FIB," *Ultramicroscopy*, vol. 114, pp. 62–71, 2012, doi: 10.1016/j.ultramic.2012.01.005.
- [147] C. B. Williams, David B., Carter, *Transmission Electron Microscopy*. 2009.
- [148] W. C. Oliver and G. M. Pharr, "An improved technique for determining hardness and elastic modulus using load and displacement sensing indentation experiments," *J. Mater. Res.*, vol. 7, no. 6, pp. 1564–1583, 1992, doi: DOI: 10.1557/JMR.1992.1564.
- [149] A. T. Sidambe, "Biocompatibility of advanced manufactured titanium implants- A review," *Materials (Basel)*., vol. 7, no. 12, pp. 8168–8188, 2014, doi: 10.3390/ma7128168.
- [150] M. V. Diamanti, S. Codeluppi, A. Cordioli, and M. P. Pedferri, "Effect of thermal oxidation on titanium oxides' characteristics," *J. Exp. Nanosci.*, vol. 4, no. 4, pp. 365–372, 2009, doi: 10.1080/17458080902769937.
- [151] P. E. Carrion, A. Soltani-Tehrani, N. Phan, and N. Shamsaei, "Powder Recycling Effects on the Tensile and Fatigue Behavior of Additively Manufactured Ti-6Al-4V Parts," *JOM*, vol. 71, no. 3, pp. 963–973, 2019, doi: 10.1007/s11837-018-3248-7.
- [152] F. Malkin, J. A. Larkin, J. F. Verrill, and R. H. Wardman, "The BCRA–NPL Ceramic Colour Standards, Series II – Master spectral reflectance and thermochromism data," *J. Soc. Dye. Colour.*, vol. 113, no. 3, pp. 84–94, Mar. 1997, doi: <https://doi.org/10.1111/j.1478-4408.1997.tb01873.x>.



- [153] Y. Zhang, Q. Li, and H. Zhou, "Chapter 1 - Theoretical Foundation and Basic Properties of Thermal Radiation," Y. Zhang, Q. Li, and H. B. T.-T. and C. of H. T. in F. Zhou, Eds. Oxford: Academic Press, 2016, pp. 1–43.
- [154] O. Illies, G. Li, J.-P. Jürgens, V. Ploshikhin, D. Herzog, and C. Emmelmann, "Numerical modelling and experimental validation of thermal history of titanium alloys in laser beam melting," *Procedia CIRP*, vol. 74, pp. 92–96, 2018, doi: <https://doi.org/10.1016/j.procir.2018.08.046>.
- [155] S. A. Khairallah, A. T. Anderson, A. Rubenchik, and W. E. King, "Laser powder-bed fusion additive manufacturing: Physics of complex melt flow and formation mechanisms of pores, spatter, and denudation zones," *Acta Mater.*, vol. 108, pp. 36–45, 2016, doi: 10.1016/j.actamat.2016.02.014.
- [156] J. Yan, Y. Zhou, R. Gu, X. Zhang, W.-M. Quach, and M. Yan, "A Comprehensive Study of Steel Powders (316L, H13, P20 and 18Ni300) for Their Selective Laser Melting Additive Manufacturing," *Metals*, vol. 9, no. 1. 2019, doi: 10.3390/met9010086.
- [157] M. V. Diamanti, F. C. Spreafico, and M. P. Pedferri, "Production of anodic TiO<sub>2</sub> nanofilms and their characterization," *Phys. Procedia*, vol. 40, pp. 30–37, 2013, doi: 10.1016/j.phpro.2012.12.004.
- [158] M. V. Diamanti, B. Del Curto, V. Masconale, and M. Pedferri, "Production and Anodic Colouring of Newly-Designed Titanium Jewels," *Colour Des. Creat.*, vol. 5, no. 5, p. 16, 2010.
- [159] N. C. for B. Information, "Titanium-oxide," *PubChem Compound Summary for CID 162651*, 2021. .
- [160] E. Louvis, P. Fox, and C. J. Sutcliffe, "Selective laser melting of aluminium components," *J. Mater. Process. Technol.*, vol. 211, no. 2, pp. 275–284, 2011, doi: 10.1016/j.jmatprotec.2010.09.019.
- [161] S. Nasrazadani and S. Hassani, "Chapter 2 - Modern analytical techniques in failure analysis of aerospace, chemical, and oil and gas industries," A. S. H. Makhoul and M. B. T.-H. of M. F. A. with C. S. from the O. and G. I. Aliofkhazraei, Eds. Butterworth-Heinemann, 2016, pp. 39–54.
- [162] M. F. L'Annunziata, "Chapter 8 - Electromagnetic Radiation: Photons," M. F. B. T.-R. (Second E. L'Annunziata, Ed. Boston: Elsevier, 2016, pp. 269–302.
- [163] F. Eggert, P. P. Camus, M. Schleifer, and F. Reinauer, "Benefits from bremsstrahlung distribution evaluation to get unknown information from

- specimen in SEM and TEM,” *IOP Conf. Ser. Mater. Sci. Eng.*, vol. 304, no. 1, 2018, doi: 10.1088/1757-899X/304/1/012005.
- [164] E. Stoyanov, F. Langenhorst, and G. Steinle-Neumann, “The effect of valence state and site geometry on Ti L<sub>3,2</sub> and O K electron energy-loss spectra of Ti<sub>x</sub>O<sub>y</sub> phases,” *Am. Mineral.*, vol. 92, no. 4, pp. 577–586, 2007, doi: 10.2138/am.2007.2344.
- [165] O. Carp, C. L. Huisman, and A. Reller, “Photoinduced reactivity of titanium dioxide,” *Prog. Solid State Chem.*, vol. 32, no. 1, pp. 33–177, 2004, doi: <https://doi.org/10.1016/j.progsolidstchem.2004.08.001>.
- [166] A. International, “ASTM E8 / E8M-16ae1,” *Standard Test Methods for Tension Testing of Metallic Materials*, 2016. .
- [167] V. Chastand, P. Quaegebeur, W. Maia, and E. Charkaluk, “Comparative study of fatigue properties of Ti-6Al-4V specimens built by electron beam melting (EBM) and selective laser melting (SLM),” *Mater. Charact.*, vol. 143, Mar. 2018, doi: 10.1016/j.matchar.2018.03.028.
- [168] E. Borisov, I. Polozov, K. Starikov, A. Popovich, and V. Sufiiarov, “Structure and Properties of Ti/Ti64 Graded Material Manufactured by Laser Powder Bed Fusion,” *Materials* , vol. 14, no. 20. 2021, doi: 10.3390/ma14206140.
- [169] J. Zhang, B. Song, Q. Wei, D. Bourell, and Y. Shi, “A review of selective laser melting of aluminum alloys: Processing, microstructure, property and developing trends,” *J. Mater. Sci. Technol.*, vol. 35, no. 2, pp. 270–284, 2019, doi: 10.1016/j.jmst.2018.09.004.
- [170] B. Zhang, Y. Li, and Q. Bai, “Defect Formation Mechanisms in Selective Laser Melting: A Review,” *Chinese J. Mech. Eng. (English Ed.)*, vol. 30, no. 3, pp. 515–527, 2017, doi: 10.1007/s10033-017-0121-5.
- [171] S. Zabler, “Interstitial Oxygen diffusion hardening — A practical route for the surface protection of titanium,” *Mater. Charact.*, vol. 62, no. 12, pp. 1205–1213, 2011, doi: <https://doi.org/10.1016/j.matchar.2011.10.012>.
- [172] S. Becker, A. Rahmel, M. Schorr, and M. Schütze, “Mechanism of isothermal oxidation of the intermetallic TiAl and of TiAl alloys,” *Oxid. Met.*, vol. 38, no. 5, pp. 425–464, 1992, doi: 10.1007/BF00665663.
- [173] S. Kumar, T. S. N. Sankara Narayanan, S. Ganesh Sundara Raman, and S. K. Seshadri, “Thermal oxidation of Ti6Al4V alloy: Microstructural and electrochemical characterization,” *Mater. Chem. Phys.*, vol. 119, no. 1–2, pp.

- 337–346, 2010, doi: 10.1016/j.matchemphys.2009.09.007.
- [174] A. Casadebaigt, J. Hugues, and D. Monceau, “High temperature oxidation and embrittlement at 500–600 °C of Ti-6Al-4V alloy fabricated by Laser and Electron Beam Melting,” *Corros. Sci.*, vol. 175, no. April, 2020, doi: 10.1016/j.corsci.2020.108875.
- [175] L. Tang, J. Fan, H. Kou, B. Tang, and J. Li, “Effect of oxygen variation on high cycle fatigue behavior of Ti-6Al-4V titanium alloy,” *Materials (Basel)*., vol. 13, no. 17, pp. 1–16, 2020, doi: 10.3390/ma13173858.
- [176] J. I. Qazi, B. Marquardt, L. F. Allard, and H. J. Rack, “Phase transformations in Ti-35Nb-7Zr-5Ta-(0.06–0.68)O alloys,” *Mater. Sci. Eng. C*, vol. 25, no. 3, pp. 389–397, 2005, doi: <https://doi.org/10.1016/j.msec.2005.01.022>.
- [177] T. C. Niemeier, C. R. Grandini, and O. Florêncio, “Stress-induced ordering due heavy interstitial atoms in Nb-0.3wt.% Ti alloys,” *Mater. Sci. Eng. A*, vol. 396, no. 1, pp. 285–289, 2005, doi: <https://doi.org/10.1016/j.msea.2005.01.045>.
- [178] L. H. de Almeida, C. R. Grandini, J. P. B. Machado, and D. Rodrigues, “Stress induced ordering due interstitials in Nb-4.7at.%Ta,” *Mater. Sci. Eng. A*, vol. 412, no. 1, pp. 230–234, 2005, doi: <https://doi.org/10.1016/j.msea.2005.08.218>.
- [179] S. Li, M. Jia, F. Prima, Y. Hao, and R. Yang, “Improvements in nonlinear elasticity and strength by grain refinement in a titanium alloy with high oxygen content,” *Scr. Mater.*, vol. 64, pp. 1015–1018, 2011.
- [180] Y. T. Lee and G. Welsch, “Young’s modulus and damping of Ti-6Al-4V alloy as a function of heat treatment and oxygen concentration,” *Mater. Sci. Eng. A*, vol. 128, no. 1, pp. 77–89, 1990, doi: [https://doi.org/10.1016/0921-5093\(90\)90097-M](https://doi.org/10.1016/0921-5093(90)90097-M).
- [181] L. H. Almeida, C. R. Grandini, and R. Caram, “Anelastic spectroscopy in a Ti alloy used as biomaterial,” *Mater. Sci. Eng. A*, vol. 521–522, pp. 59–62, 2009, doi: <https://doi.org/10.1016/j.msea.2008.09.123>.





















